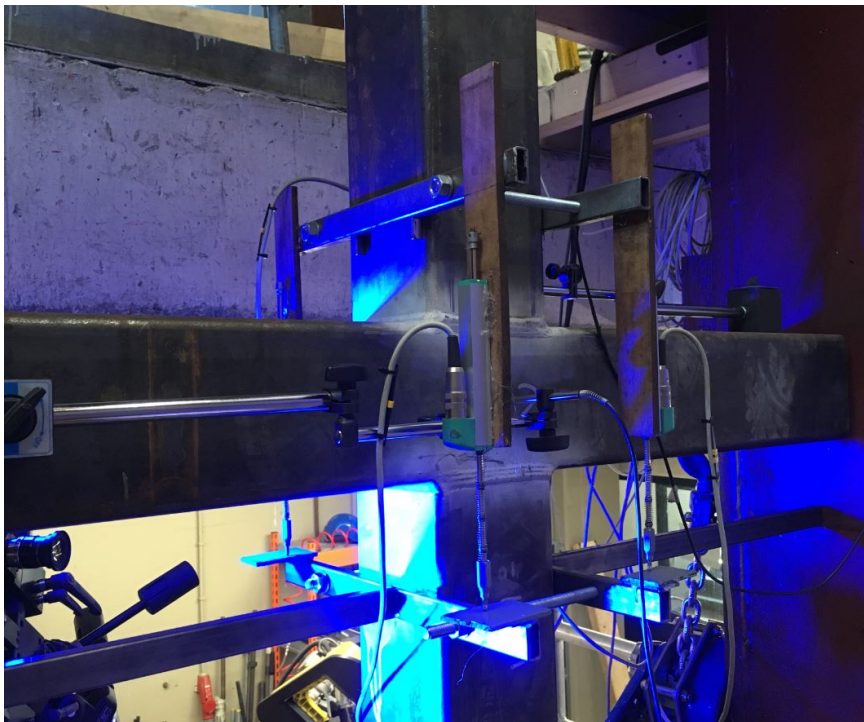


Material Factors for High Strength Rectangular Hollow Section X Joints

Bart Adegeest



[This page intentionally left blank]

Material Factors for High Strength Rectangular Hollow Section X Joints

by

Bart Adegeest

to obtain the degree of Master of Science
at the Delft University of Technology,
to be defended publicly on Wednesday July 8, 2020 at 2:00 PM.

Student number: 4297326
Thesis committee: Prof. Dr. M. Veljković Steel and Composite Structures, TU Delft, supervisor
Dr. C. L. Walters 3mE, TU Delft
Dr. H. Xin Steel and Composite Structures, TU Delft

An electronic version of this thesis is available at <https://repository.tudelft.nl/>.



[This page intentionally left blank]

Abstract

An increasing trend is occurring in the use of high strength steel (HSS) in tubular joints. Reason for this trend is the high yield strength of HSS which leads to reduced weights and costs. Characteristic for HSS is the reduced ductility in comparison to normal steels [43]. Therefore, Eurocode 3 part 1-8 (2020) [19] recommends material reduction factors (C_f) for the design of joints made of steel with a yield strength higher than 355 MPa. The standard includes steel grades up to S700. The material reduction factors need to be validated to ensure efficient design of tubular HSS joints.

This research intends to investigate the behaviour of X joints made from different kind of steel grades. The goal is to investigate if the material reduction factors for HSS, proposed in the new version of the Eurocode [19], are justified.

Coupon experiments are conducted to determine the material properties of the X joints. Two geometrically identical X joints with varying steel grades of S355 and S500 are experimentally tested. The conducted X joint experiments, which are evaluated by digital image correlation (DIC), provide the necessary evidence to understand the behaviour of the failure mode and the fracture strain. Finite element analysis confirms the experimental evidence. The results from both the experiments and finite element analysis are used to validate the Eurocode design resistance.

Furthermore, a parametric study is executed to investigate the influence of the material properties and the brace width over chord width ratio on the numerical resistance of X joints. This results in a total of 39 different X joint models that are included in this research. Lastly, the obtained numerical resistances are compared to the predicted design resistance according to Eurocode.

[This page intentionally left blank]

Preface

This thesis is written to obtain the degree of Master of Science in structural engineering at the Delft University of Technology. The goal is to investigate the material reduction factors applicable for high strength steel rectangular hollow section X joints according to the newly proposed Eurocode 3 part 1-8 (2020). Hopefully, will this thesis contribute to an increase in efficiency in the use of high strength steel in hollow section joints.

By this way I would like to show my gratitude to the people that helped me during my research. Firstly, I would like to specially thank MSc. R. Yan for helping me with my endless questions and guiding me throughout this whole process. Secondly, G. Stamoulis for guiding the experiments in the laboratory. Also, I want to show my gratitude to Prof. Dr. M. Veljković, Dr. C. L. Walters and Dr. H. Xin for the guidance during this thesis.

Last, but not least, I would like to thank my family for always supporting me during this period at the university.

*Bart Adegeest
Rotterdam, July 2020*

Contents

Abstract	II
Preface	IV
List of Figures	VIII
List of Tables	XII
Abbreviations and symbols	XIV
1 Introduction	1
1.1 Research objective and question	2
1.2 Research methodology	2
2 State of the art	3
2.1 High strength steel	3
2.2 Mechanical properties	5
2.2.1 Ductility limits	5
2.2.2 Toughness	6
2.2.3 Cold-forming	7
2.2.4 Stress triaxility	11
2.3 Welds	12
2.3.1 Fillet welds	12
2.3.2 Full-strength single-sided fillet welds	14
2.3.3 Butt welds	15
2.3.4 Welding topics that influence the joint strength	15
2.3.5 Heat affected zone (HAZ)	18
2.4 Hollow section joints EN1993-1-8:2020	25
2.4.1 Range of validity	26
2.4.2 Failure modes	31
2.4.3 Design equations	31
2.5 Previous research HSS hollow section joints	33
3 Coupon experiments	35
3.1 Curvature coupon specimens	37
3.2 Measuring methods	38
3.3 Modulus of elasticity	39

3.4	Yield strength	42
3.5	Engineering stress-strain curves	43
3.6	Standard material property based on correct gauge length	47
3.7	Second group coupon experiments	49
3.8	Ductility limits	52
3.9	Finite element analysis coupons	53
3.9.1	Implicit solver	53
3.9.2	Explicit solver	54
3.9.3	Model geometry coupons	54
3.9.4	Material input coupons	56
3.9.5	Other input parameters coupons	57
3.9.6	Results	57
3.10	Strain development along coupon specimen	64
3.10.1	X8-N-B - S355	66
3.11	Conclusions coupon experiments	68
3.11.1	Material properties FEM	69
4	X joint experiments	71
4.1	Test set-up and measuring methods	72
4.2	Results X joint experiments	75
4.2.1	Strain development joint X2	81
4.2.2	Strain development joint X8	83
5	Finite element analysis X2 and X8	85
5.1	Geometry properties	85
5.2	Boundary, loading and symmetry conditions	87
5.3	Material properties	88
5.4	Meshing	88
5.5	Results finite element analysis	90
5.5.1	Stress triaxiality	95
5.6	Conclusions finite element analysis and experiments X2 and X8	99
6	Parametric study	101
6.1	Parameters	101
6.2	Finite element model	102
6.2.1	Geometry	102
6.2.2	Boundary, loading and symmetry conditions	103
6.2.3	Material properties	104
6.2.4	Meshing	105
6.3	Finite element results	106
6.3.1	Effect of the material properties	106
6.3.2	Visual results	109
6.3.3	Comparison to the Eurocode prediction	111
6.4	Summary parametric study	113
6.4.1	Effect of the material properties	113
6.4.2	Comparison to the Eurocode prediction	114

7	Conclusions and recommendations	115
7.1	Conclusions	115
7.2	Recommendations	117
	Bibliography	118
A	Strain development along coupon specimen	123
A.1	X2-N-C - S500	124
A.2	T103-A - S700	126
B	Hand calculation according to EN1993-1-8:2020	128
B.1	Joint X2 (steel grade S500)	130
B.2	Joint X8 (steel grade S355)	131
C	Finite element analysis X joints	132
D	Stress triaxiality X joints	134
E	Parametric study	141

List of Figures

2.1	Wall thickness and weight reduction with increasing steel grades [53]	3
2.2	Historical development of HSS [53]	3
2.3	Schematic diagram (a) DQT and (b) QT [65]	4
2.4	Typical stress-strain curve [11]	5
2.5	Stress-strain curves of different steel grades [32]	5
2.6	Transition temperature curves of different steel grades [53]	6
2.7	Influence cold-forming process on the yield strength (f_y or σ_u) for a SHS [61]	7
2.8	Influence amount of cold-working on the stress-strain curve [28]	7
2.9	Tensile coupon locations Ma et al. [42]	8
2.10	Flat and corner stress-strain curves for S500MC and S700MC [60]	8
2.11	Stress-strain curves from flat and corner coupons of SHS 200x200x6 [47]	9
2.12	Stress triaxiality versus plastic deformation capacity [30]	11
2.13	Stress components [30]	11
2.14	Fillet weld stress components [16]	12
2.15	Double-sided end fillet weld [33]	14
2.16	Definition cold-formed zone according to EN1993-1-8:2020 [19]	16
2.17	Critical failure plane of 27° [7]	18
2.18	Critical failure plane asymmetric weld [7]	18
2.19	Subdivision HAZ [58]	19
2.20	Effect heat input on the hardness of TMCP HSS steel [51]	20
2.21	Effect heat input on the hardness of QT HSS steel [51]	20
2.22	Tensile strength of TMCP S500M steel as a function of peak temperature and cooling time [57, 58]	21
2.23	Tensile strength of TMCP S700M steel as a function of peak temperature and cooling time [57, 58]	22
2.24	HAZ modelling in DQ S960 RHS X joints [39]	23
2.25	Stress-strain curves base material and HAZ research Lan et al. [39]	23
2.26	Stress-strain curves for TMCP S385 (left) and RQT S690(right) [64]	24
2.27	Types of uniplanar hollow section joints [19]	25
2.28	Joint classification based on force transfer [19]	26
2.29	Joint parameters X joint [19]	27
2.30	Open end requirements [19]	28
2.31	Eccentricity of joints [19]	28
2.32	Failure modes of joints between RHS brace members and RHS chord members [19]	31
3.1	Lay-out coupon specimens first group	36
3.2	Coupon specimens T63-series	36

3.3	Initial curvature coupon specimens	37
3.4	Bending of the coupon grip section	37
3.5	Definition convex and concave side coupon specimen	38
3.6	Measuring methods coupon experiment	38
3.7	Stress-strain curve obtained from strain gauges (T93-B)	39
3.8	Stress-strain curve reloading part for determination E-modulus (T93-B)	40
3.9	E-modulus based on major strain points DIC (T93-C)	40
3.10	Offset unloading and reloading curve coupon experiment [40]	41
3.11	Yield strength determination (T103-A)	42
3.12	Stress-strain curves obtained from raw experimental data (T93-B)	43
3.13	Experimental data shift to yield point	44
3.14	Data shift T93-B	44
3.15	Data extraction DIC data from GOM Correlate (T93-B)	44
3.16	T63-series engineering stress-strain curves	45
3.17	T93-series engineering stress-strain curves	46
3.18	T103-series engineering stress-strain curves	46
3.19	Influence initial gauge length on engineering stress-strain curve T63-A	47
3.20	Correct engineering stress-strain curves T63-A, T93-B and T103-A	48
3.21	Locations of coupon specimens A-B (adjacent) and C-D (opposite) from RHS	50
3.22	X2-series engineering stress-strain curves	51
3.23	X8-series engineering stress-strain curves	51
3.24	Step definition implicit solver	53
3.25	Step and amplitude definition explicit solver	54
3.26	Eccentricity profile coupon specimen T63-A	55
3.27	Eccentricity profile coupon specimen T93-A and T103-A	55
3.28	Plastic material input properties FEM	56
3.29	FEM meshing T93-A	57
3.30	FEM results convex side T63-A	58
3.31	FEM results concave side T63-A	59
3.32	FEM results PEEQ strain (top) and DIC results equivalent Mises strain (bottom) T63-A (explicit/DIC based property)	59
3.33	FEM results convex side T93-B	60
3.34	FEM results concave side T93-B	61
3.35	FEM results PEEQ strain (top) and DIC results equivalent Mises strain (bottom) (explicit/DIC based property)	61
3.36	FEM results convex side T103-A	62
3.37	FEM results concave side T103-A	63
3.38	FEM results PEEQ strain (top) and DIC results equivalent Mises strain (bottom) (explicit/DIC based property)	63
3.39	Noise level observation specimen X8-N-B	65
3.40	Stress-strain curve X8-N-B with characteristic points (S355)	66
3.41	Section line along which the strains are extracted with length scale X8-N-B (S355)	66
3.42	Strain development X8-N-B for points 1 to 4 (S355)	67
3.43	Strain development X8-N-B for points 4 to 7 (S355)	67
3.44	Engineering stress-strain curves S355, S500 and S700 from coupon experiments	70
4.1	Joint X8 fixed into the test set-up	72
4.2	Schematic drawing locations LVDTs side view	73

4.3	Schematic drawing locations LVDTs top view	73
4.4	Positioning LVDTs on joint X2 during the experiment (1)	74
4.5	Positioning LVDTs on joint X2 during the experiment (2)	74
4.6	Brace failure joint X2	75
4.7	Chord side wall failure joint X8	75
4.8	Crack development in HAZ joint X2	76
4.9	Crack development in corner joint X8	76
4.10	Experimental results chord side wall displacement: overview (left) and detail (right)	77
4.11	Experimental results chord top face displacement	77
4.12	Experimental results axial displacement steel frame	78
4.13	Measuring points to compare to the 3% deformation limit [36]	78
4.14	DIC data points for comparison to the 3% deformation limit	79
4.15	Force-deformation curves X joints	80
4.16	Section lines and length scale joint X2	81
4.17	Strain distribution joint X2	82
4.18	Strain development along section lines joint X2	82
4.19	Section lines and length scale joint X8	83
4.20	Strain distribution joint X8	84
4.21	Strain development along section lines joint X8	84
5.1	FEM X joint	86
5.2	Joint X2	86
5.3	Boundary and loading conditions FEM X joint	87
5.4	Engineering stress-strain curves S355 and S500 from coupon experiments	88
5.5	FEM meshing X joint	89
5.6	FEM corner element	89
5.7	Force-displacement curves steel frame	90
5.8	Force-deformation curves joint X2	91
5.9	Force-deformation curves joint X8	92
5.10	Strain distribution joint X2 for experiment (left, equivalent Mises strain) and FEM (right, plastic equivalent strain)	93
5.11	Strain distribution joint X8 for experiment (left, equivalent Mises strain) and FEM (right, plastic equivalent strain)	94
5.12	Points at which stress triaxiality is extracted on the X joints	96
5.13	Stress triaxiality of joint X8	97
5.14	Force development against time steps FEM of joint X8	97
5.15	Stress triaxiality of joint X2	98
5.16	Force development against time steps FEM of joint X2	98
6.1	Boundary, loading and symmetry conditions FEM	103
6.2	FEM meshing of X joint with $\beta = 0,5$	105
6.3	Initial stiffness difference	108
6.4	Von Mises stress distribution at the governing load of steel grade S500-1 for $\beta=0,3$ (left), $\beta=0,5$ (centre) and $\beta=0,7$ (right)	109
6.5	Von Mises stress distribution at the maximum load of steel grade S500-1 for $\beta=0,3$ (left), $\beta=0,5$ (centre) and $\beta=0,7$ (right)	110
6.6	PEEQ strain distribution at the governing load of steel grade S500-1 for $\beta=0,3$ (left), $\beta=0,5$ (centre) and $\beta=0,7$ (right)	110

6.7	Results of material-1: FEM resistance over EC3 resistance	111
6.8	Results of material-2: FEM resistance over EC3 resistance	112
6.9	Results of material-c: FEM resistance over EC3 resistance	113
A.1	Stress-strain curve X2-N-C with characteristic points (S500)	124
A.2	Section line along which the strains are extracted with length scale X2-N-C (S500) .	124
A.3	Strain development X2-N-C for points 1 to 4 (S500)	125
A.4	Strain development X2-N-C for points 4 to 7 (S500)	125
A.5	Stress-strain curve T103-A with characteristic points (S700)	126
A.6	Section line along which the strains are extracted with length scale T103-A (S700) .	126
A.7	Strain development T103-A for points 1 to 4 (S700)	127
A.8	Strain development T103-A for points 4 to 7 (S700)	127
C.1	Axial displacement steel frame joint X2	132
C.2	Load-deformation curves joint X2	133
D.1	Stress triaxiality joint X8 (S355)	135
D.2	Force development against time steps FEM for joint X8 (S355)	135
D.3	Stress triaxiality distribution joint X8 (S355) for time step 20 (left) and 40 (right) .	136
D.4	Stress triaxiality distribution joint X8 (S355) for time step 60 (left) and failure (right)	137
D.5	Stress triaxiality joint X2 (S500)	138
D.6	Force development against time steps FEM for joint X2 (S500)	138
D.7	Stress triaxiality distribution joint X2 (S500) for time step 40 (left) and 50 (right) .	139
D.8	Stress triaxiality distribution joint X2 (S500) for time step 60 (left) and failure (right)	140
E.1	Engineering stress-strain curves mild strength steels	142
E.2	Engineering stress-strain curves high strength steels	142
E.3	Force-displacement curve material-1 for β equals 0,3: overview (left) and detail (right)	144
E.4	Force-displacement curve material-1 for β equals 0,5: overview (left) and detail (right)	144
E.5	Force-displacement curve material-1 for β equals 0,7	145
E.6	Force-displacement curve material-2 for β equals 0,3: overview (left) and detail (right)	145
E.7	Force-displacement curve material-2 for β equals 0,5: overview (left) and detail (right)	146
E.8	Force-displacement curve material-2 for β equals 0,7: overview (left) and detail (right)	146
E.9	Force-displacement curve material-c for β equals 0,3: overview (left) and detail (right)	147
E.10	Force-displacement curve material-c for β equals 0,5: overview (left) and detail (right)	147
E.11	Force-displacement curve material-c for β equals 0,7: overview (left) and detail (right)	148

List of Tables

1.1	Material reduction factors [19]	1
2.1	Impact toughness of different steel grades and delivery conditions [15]	7
2.2	Overview literature strength enhancements corner versus flat coupons cold-formed tubular sections	10
2.3	Overview scattering literature	10
2.4	Fillet weld correlation factor [19]	13
2.5	Filler metal properties [19]	13
2.6	Throat thickness for full-strength single-sided fillet welds	15
2.7	r/t -limitations welding in cold-formed zones [19]	16
2.8	Clarification abbreviations steel quality [17]	16
2.9	Recommended throat thickness for fillet welds according to Feldmann et al. [23]	18
2.10	Range of validity conditions for T, Y or X joints (A is Table 9.10 and B is Table 9.11 from EN1993-1-8:2020 [19])	30
2.11	Chord stress function [19]	32
2.12	Axial resistance welded T, Y and X joints between SHS braces and SHS chords (Table 9.12 of EN1993-1-8:2020 [19])	32
2.13	Axial resistance welded T, Y and X joints between RHS braces and RHS chords, (Table 9.13 of EN1993-1-8:2020 [19]) (1)	32
2.14	Recommended reduction factors according to Feldmann et al. [23]	33
3.1	Coupon geometry first group	35
3.2	E-modulus results	41
3.3	Yield strength results	42
3.4	Overview results coupon experiments first group	45
3.5	Overview results T63-A, T93-B and T103-A with correct initial gauge length	47
3.6	Coupon geometry second group	49
3.7	Results coupon experiments second group	50
3.8	Overview results coupon experiments first group	52
3.9	Overview results coupon experiments second group X2-series	52
3.10	Overview results coupon experiments second group X8-series	52
3.11	Geometry measurements ABAQUS models T63-A, T93-A and T103-A	55
3.12	Elastic and density material properties FEM	56
3.13	FEM results for specimen T63-A	58
3.14	FEM results for specimen T93-B	60
3.15	FEM results for specimen T103-A	62
3.16	Characteristic points	64

3.17	Results strain development along coupons	64
3.18	Overview results coupon experiments	68
3.19	Scatter coupon results for each steel grade	69
3.20	Characteristic values material properties used in FEM	69
4.1	X joint test program	71
4.2	X joint experimental results	75
4.3	Eurocode prediction for joint X2 and X8	80
5.1	Geometry parameters X joint FEM	85
5.2	Characteristic values material properties	88
5.3	Results steel frame	90
5.4	Results based on the 3% deformation limit	92
5.5	Failure mode obtained by experiment, FEM and Eurocode	93
5.6	Stress triaxiality coupon experiments	95
5.7	Overview results joints X2 and X8	99
5.8	Overview results X joint experiments compared to Eurocode [19] prediction	99
6.1	Parameters used in parametric study	101
6.2	Parametric study joint geometry	102
6.3	Full-strength weld calculation	102
6.4	Characteristic values material properties	104
6.5	FEM results influence of material property on numerical resistance	106
6.6	FEM results of material-2 and material-c compared to material-1	107
6.7	FEM results of the initial stiffness	108
6.8	Used material reduction factors for design strength Eurocode ($F_{EC3,Cf}$)	111
6.9	An overview of the resulted numerical resistance compared to the Eurocode	114
7.1	Results joints X2 and X8	115
7.2	Results parametric study	116
A.1	Characteristic points	123
B.1	Parameters X joint calculation	128
B.2	Range of validity check	129
B.3	Hand calculation results joint X2 and X8	129
E.1	Range of validity parametric study FEM [19]	141
E.2	Design resistances parametric study FEM according to EN1993-1-8:2020 [19]	143
E.3	Results FEM and Eurocode prediction for β equals 0,3	149
E.4	Results FEM and Eurocode prediction for β equals 0,5	150
E.5	Results FEM and Eurocode prediction for β equals 0,7	151

Symbols and abbreviations

Lower case symbols

Symbol	Description
a	throat thickness fillet weld
$b_{e,p}$	effective width for punching shear
b_{eff}	effective width for a rectangular hollow section brace member to chord connection
b_i	width of rectangular hollow section member i ($i=0,1$)
d_i	diameter of circular hollow section member i ($i=0,1$)
e	eccentricity of a joint in a hollow section lattice girder
e	initial eccentricity of coupon specimen
f_b	buckling strength of the chord side wall
$f_{u,FM}$	tensile strength of filler metal
$f_{u,PM}$	tensile strength of parent material
f_{ui}	ultimate or tensile strength of member i ($i=0,1$)
$f_{vw,d}$	design shear strength of a weld
f_{yi}	yield strength of member i ($i=0,1$)
g	gap between the brace member in a K or N joint
h_i	depth of the cross-section of member i ($i=0,1$)
l_{eff}	effective length weld
n	chord stress parameter for rectangular hollow section
r	corner radius rectangular hollow section
r_{in}	inner corner radius rectangular hollow section
r_{out}	outer corner radius rectangular hollow section
$t_{8/5}$	cooling time in the heat affected zone of a weld to cool down from 800°C to 500°C
t	thickness element
t_i	wall thickness of member i ($i=0,1$)
$t_{w,fillet}$	leg length fillet weld
w	width gauge section of coupon specimen

Upper case symbols

Symbol	Description
A_5	strain at fracture
A_c	cross-sectional area of coupon specimen
A_g	strain at maximum stress
A_i	cross-sectional area of member i (i=0,1)
C_1	exponent for chord stress factor
C_f	material reduction factor
E	modulus of elasticity
F_{EC3}	resistance predicted by Eurocode 3 part 1-8
$F_{3\%}$	resistance at 3% deformation limit
$F_{3\%,exp}$	resistance at 3% deformation limit obtained by experiment
$F_{3\%,fem}$	resistance at 3% deformation limit obtained by finite element model
F_{exp}	governing resistance obtained by experiment
F_{fem}	governing resistance obtained by finite element model
F_u	ultimate resistance
$F_{u,exp}$	ultimate resistance obtained by experiment
$F_{u,fem}$	ultimate resistance obtained by finite element model
$F_{w,Ed}$	design weld force per unit length
$F_{w,Rd}$	design weld resistance per unit length
L_0	initial gauge length coupon specimen
L_i	length of hollow section of member i (i=0,1)
$M_{ip,i,Ed}$	design in-plane internal moment in member i (i=0,1)
$M_{op,i,Ed}$	design out-of-plane internal moment in member i (i=0,1)
$N_{0,Ed}$	design axial force in the chord member which gives the lowest value of Q_f
$N_{i,Rd}$	design resistance of the joint, expressed in terms of the internal axial force in member i (i=0,1)
Q_f	chord stress factor
$W_{ip,pl,0}$	plastic section modulus of chord member in the plane of the joint
$W_{op,pl,0}$	plastic section modulus of chord member out of the plane of the joint
X_{sz}	ratio of the soft zone or heat affected zone width to the plate thickness

Greek symbols

Symbol	Description
α	critical failure plane angle fillet weld
β	the ratio of the mean diameter or width of the brace members to that of the chord member, for rectangular hollow section X joints: b_1/b_0
β_w	fillet weld correlation factor
$\beta_{w,mod}$	modified fillet weld correlation factor
γ	the ratio of the chord width to twice its wall thickness, for rectangular hollow section X joints: $b_0/2t_0$
γ_{m0}	partial factor for resistance of cross-sections
γ_{m2}	partial factor for resistance of welds
γ_{m5}	partial factor for resistance of joints in hollow section lattice girders
$\epsilon_{engineering}$	engineering strain
ϵ_f	strain at fracture
$\epsilon_{f,50}$	strain at fracture based on initial gauge length of 50 mm
$\epsilon_{f,70/80}$	strain at fracture based on initial gauge length of 70 or 80 mm
ϵ_{true}	true strain
$\epsilon_{true,plastic}$	true plastic strain
ϵ_u	strain at ultimate stress
ϵ_y	strain at the onset of yielding
η	the ratio of the brace member depth to the chord width, for rectangular hollow section X joints: h_1/b_0
η	stress triaxiality
θ_i	angle between brace member i and chord member (i=1)
λ_{ov}	overlap ratio
ν	Poisson's ratio
ρ	density
$\sigma_{0,2\%}$	0,2% proof stress
σ_1	stress in principal direction 1 ($\sigma_1 > \sigma_2 > \sigma_3$)
σ_2	stress in principal direction 2 ($\sigma_1 > \sigma_2 > \sigma_3$)
σ_3	stress in principal direction 3 ($\sigma_1 > \sigma_2 > \sigma_3$)
$\sigma_{engineering}$	engineering stress
σ_{eq}	von Mises stress
σ_m	mean or hydrostatic stress
σ_{\parallel}	normal stress along the axis of the weld

Symbol	Description
σ_{\perp}	normal stress perpendicular to throat section
σ_{true}	true stress
σ_u	ultimate or tensile stress
σ_y	yield stress
τ	thickness ratio: t_1/t_0
τ_{\parallel}	shear stress acting in the throat section parallel to axis of the weld
τ_{\perp}	shear stress acting in the throat section perpendicular to axis of the weld
χ	reduction factor for flexural buckling obtained from EN1993-1-1 using the relevant buckling curve and a normalised slenderness

Abbreviations

BF	for Brace Failure
CEV	for Carbon Equivalent Value
CFF	for Chord Face Failure
CHS	for Circular Hollow Section
CSWF	for Chord Side Wall Failure
DIC	for Digital Image Correlation
DQ	for Direct Quenching
EXT	for Extensometer
FEM	for Finite Element Model
GMAW	for Gas Metal Arc Welding
HAZ	for Heat Affected Zone
HSS	for High Strength Steel, steel grades from S460 up to and including S700
LVDT	for Linear Variable Differential Transformer
MPC	for Multi Point Constraint
MSS	for Mild Strength Steel, steel grades up to and including S460
PSF	for Punching Shear Failure
QT	for Quenching and Tempering
RHS	for Rectangular Hollow Section
RQT	for Reheated, Quenching and Tempering
SG	for Strain Gauge
SHS	for Square Hollow Section
TMCP	for Thermo-Mechanical Controlled Processing
UHSS	for Ultra High Strength Steel, steel grades higher than S700

Chapter 1

Introduction

An increasing trend can be seen in the interest of high strength steel (HSS). HSS are steel grades with yield strengths above 460 MPa. Reasons for this increase in interest is the high yield strength, which results in a high strength-to-weight ratio and reduction in costs [43]. The use of HSS is becoming standard in for example mobile cranes and long-span bridges. Higher stresses occur in HSS in comparison with mild strength steels (MSS). The modulus of elasticity is independent of the steel grade, which means that larger deflections can occur. For that reason, the serviceability needs be treated more carefully. Fatigue design becomes more relevant for HSS as a result of higher stress ranges that will occur in HSS structures. Welding has to be treated more carefully as well in comparison with MSS due to the higher stresses [26, 36].

In the current Eurocode 3 part 1-8 [16] design rules are included for hollow section joints with steel grades up to S460. For steel grades above S355, a material reduction factor (C_f) of 0,9 is introduced in the determination of the joint resistance. Additional rules for the use of HSS, Eurocode 3 part 1-12 [18], give a reduction factor of 0,8 on the joint resistance for steel grades above S460 up to S700. The scope of the newly proposed 2020 version of Eurocode 3 part 1-8 [19] includes steel grades from S235 up to and including S700. The material reduction factors that are proposed in the new standard are presented in Table 1.1. The design rules are validated for MSS. To make the rules applicable for HSS the material factors are introduced. Another criteria given in the new standard is that the design yield strength f_{yi} should not be larger than $0,8f_{ui}$ in the cases of chord punching shear and brace failure. This criteria is a result of the decreased ductility of HSS in comparison with MSS.

Table 1.1: Material reduction factors [19]

	$f_y \leq 355 \text{ N/mm}^2$	$C_f = 1,0$
$355 \text{ N/mm}^2 < f_y \leq 460 \text{ N/mm}^2$		$C_f = 0,9$
$460 \text{ N/mm}^2 < f_y \leq 550 \text{ N/mm}^2$		$C_f = 0,86$
$550 \text{ N/mm}^2 < f_y \leq 700 \text{ N/mm}^2$		$C_f = 0,8$

The material reduction factors are applied due to less rotation capacity of HSS [24]. According to Feldmann et al. [23], the material factors prevent the common use of HSS on the market. This research proposes different material factors based on experiments (1,0 for S500, 0,9 for S700 and

0,8 for S960). These material factors make the use of HSS more attractive. Wardenier and Puthli [62] analysed the research available regarding material reduction factors. Regarding RHS T and X joints loaded under tension, they noted that Australian and Finnish research led to contradicting conclusions and that the safety margin on brittle failure modes should be higher in comparison with ductile failure modes. It is observed that research results in a scattering in proposed material reduction factors in comparison with the factors that are proposed in the new Eurocode. Therefore, the aim of this research is to validate the material factors for HSS that are proposed in the new version of Eurocode 3 part 1-8 in a comparative experimental and numerical study of X joints loaded in tension.

1.1 Research objective and question

This research focuses on welded cold-formed rectangular hollow section X joints. The main objective is to investigate the behaviour of geometrically identical X joints made of different steel grades and determine if the material reduction factors of different grades of high strength steel, according to the new Eurocode, are justified. The research questions that will be investigated are:

1. What are the failure modes of HSS hollow sections and are there any differences in ductility between joints made of S355, S500 and S700? Is a difference influenced by stress-strain curves obtained in coupon tests?
 - (a) What are the failure modes for welded rectangular hollow section X joints? Does different steel grades influence the critical failure mode?
 - (b) Which requirements need to be met to perform accurate coupon tests? How to determine the characteristic and design material properties from coupon test results?
2. Are the material factors of different grades of high strength steel, when used in cold-formed squared hollow section X joints, justified? Or do they need to be adjusted to another value?
 - (a) How accurately are the design resistances of HSS X joints predicted according to Eurocode 3 part 1-8 (2020) in comparison with experimental and finite element analysis results?

1.2 Research methodology

The first part of the research consists of a literature survey to obtain the appropriate knowledge regarding HSS, hollow section joints, material reduction factors and welding. Coupon tests will be executed to obtain the proper material properties according to standardized testing procedures of the HSS hollow sections. These material properties will serve as input for the finite element analyses. Two full scale X joint experiments will be conducted and used to validate the finite element model and the material properties obtained from coupon experiments. The X joints have the same geometry and are made from steel grades S355 and S500. The X joints will be loaded under tension. There will be no loading applied on the chord of the specimen. To find a correct solution to the research question, the design method according to the new standard will be compared to results obtained from experiments and finite element analysis. Finite element models will be made in ABAQUS. At last a parametric study will be performed to investigate the influence of material properties and the brace width over chord width ratio (β) on the joint resistance. All the results will be analysed and conclusions will be drawn regarding the material reduction factors of the new Eurocode 3 part 1-8 (2020) [19].

Chapter 2

State of the art

2.1 High strength steel

The most commonly used steels are those with steel grades between S235 and S460, which are defined as mild strength steel (MSS). Steels with steel grades higher than S460 are defined as high strength steel (HSS), for which the spectrum runs up to S700. Steel grades higher than S700 are defined as ultra high strength steel (UHSS). Due to the high strength-to-weight ratio of HSS, lighter structures can be designed which reduces costs of resources, transportation and foundations. This results in an improvement of the carbon footprint of the particular structure [43]. Figure 2.1 shows that up to 70% weight reduction can be achieved when S690 steel is used instead of S235. HSS are used in civil applications such as long-span bridges and lattice girders [36]. The new standard, EN1993-1-8:2020 [19], includes hollow sections with MSS and HSS. UHSS is available on the market but is not included in the Eurocode.

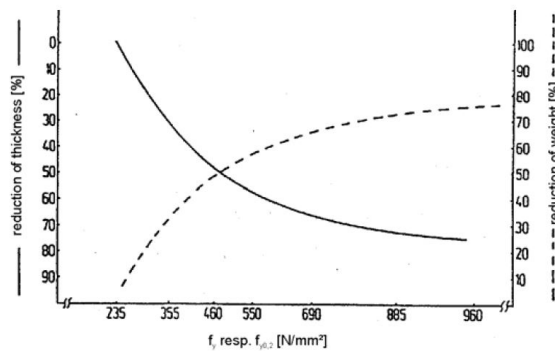


Figure 2.1: Wall thickness and weight reduction with increasing steel grades [53]

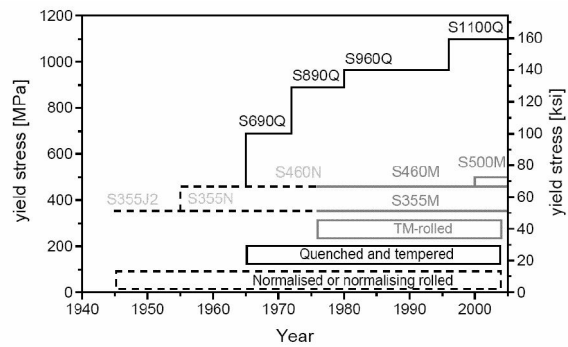


Figure 2.2: Historical development of HSS [53]

Different heat treatment techniques can be applied to produce HSS. Heat treatment influences the microstructure and grain size of the steel. A finer grained micro structure results in a higher strength and toughness.

The first heat treatment method, quenching and tempering (QT), is developed in the 1960's. In the quenching process the steel is rapidly cooled down, usually by water, around a temperature of 900°C to introduce martensite. Martensite is a crystalline structure with a hard form. Then, the steel is reheated to around 600°C for a specific time (tempering) before it is naturally cooled, usually by air. The schematic diagram is visible in Figure 2.3(b). The tempering process is applied to improve weldability and ductility [43, 53].

The second method, thermo-mechanical controlled processing (TMCP) is developed in the 1970's. TMCP uses a controlled rolling around a temperature of 700°C. This controlled rolling is followed up by an accelerated cooling process. Due to the minimal applied alloying elements in the TMCP technique, low carbon equivalent values (CEV) are achieved, which results in improved weldability in comparison with the QT technique [37, 43, 53]. CEV is determined according to equation 2.1 [43, 56].

$$CEV = C + \frac{Mn}{6} + \frac{Cr + Mo + V}{5} + \frac{Ni + Cu}{15} \quad (2.1)$$

Nowadays, TMCP is preferred by steel manufacturers because it results in a finer grained microstructure and good weldability, due to a reduction of CEV [43]. The historical development of HSS can be seen in Figure 2.2.

Currently, direct quenching (DQ) is another heat treatment method used to produce HSS. The difference with the QT method is that quenching is directly applied after the hot formation of steel. This difference is clearly visible in Figure 2.3, where (a) corresponds to the direct quenching and tempering method and (b) corresponds to the original quenching and tempering method [65].

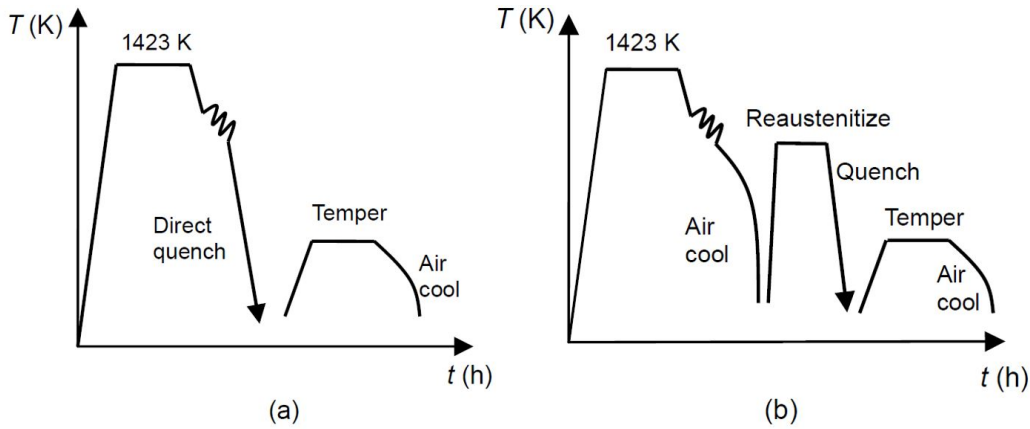


Figure 2.3: Schematic diagram (a) DQT and (b) QT [65]

Alloying is the process where alloys are added to change the chemical composition of steel. Nickel (Ni) and manganese (Mn) improve the tensile strength. Chromium (Cr) and vanadium (V) improve the hardness. These alloying elements result in beneficial effects on the material properties. Elements like phosphorus (P), nitrogen (N) and sulfur (S) results in an increase in brittle behaviour and therefore have a negative effect on the mechanical properties. Alloying generally results in an increase in material strength, but with a negative influence on the weldability due to an increase in CEV [43].

2.2 Mechanical properties

The mechanical properties of steel are commonly described by the stress-strain relationship. The stress-strain relationship in the elastic domain is described by the modulus of elasticity (E). The modulus of elasticity is independent of the steel grade and has a value of approximately 210.000 MPa. A significant difference exists between the stress-strain relationship of MSS and HSS. In ordinary MSS a clear yield plateau can be distinguished, see Figure 2.4. In the case of HSS, there usually is no yield plateau. Therefore, it is common practice to use the 0,2% proof stress as the yield stress for HSS [43]. Typical stress-strain curves for different steel grades can be seen in Figure 2.5.

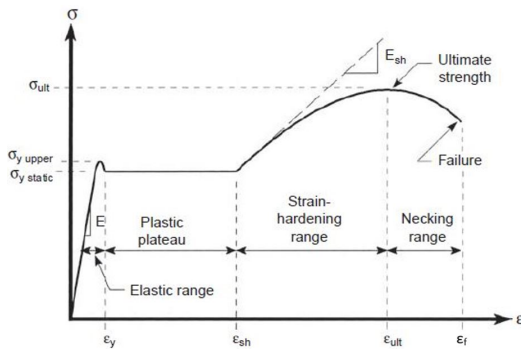


Figure 2.4: Typical stress-strain curve [11]

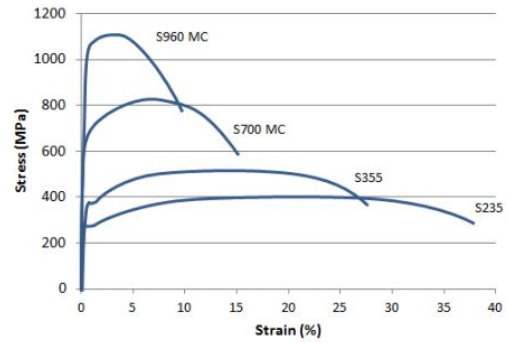


Figure 2.5: Stress-strain curves of different steel grades [32]

2.2.1 Ductility limits

To make sure that there is sufficient ductility, the Eurocodes give limitations for parameters that have an influence on the ductility of the material. The parameters that are used are the yield strength (σ_y), tensile strength (σ_u), strain at yielding (ϵ_y) and strain at fracture (ϵ_f). Eurocode 3 part 1-1 [14] provides the limitations for MSS (up to and including S460):

- $\sigma_u/\sigma_y \geq 1,10$ (actual values);
- $\epsilon_f \geq 15\%$;
- $\epsilon_f > 15\epsilon_y$, where $\epsilon_y = \sigma_y/E$.

Eurocode 3 part 1-12 [18] describes the additional rules for the use of the standards for HSS (S460 up to and including S700). This standard provides the following requirements for the ductility:

- $\sigma_u/\sigma_y \geq 1,05$ (actual values);
- $\epsilon_f \geq 10\%$;
- $\epsilon_f > 15\epsilon_y$, where $\epsilon_y = \sigma_y/E$.

As can be seen in Figure 2.5, the ductility of HSS is lower than the ductility of MSS. A lower ratio indicates less plastic capacity after yielding until (possible brittle) failure occurs. This additional plastic capacity after yielding is defined as the deformation capacity of the material.

2.2.2 Toughness

The ability of the material to avoid brittle failure is defined as toughness. Toughness is measured with the Charpy-V notch test. Which measures the impact energy at a predetermined test temperature [11]. To guarantee ductile behaviour, the impact energy has to be larger than 27J at the specified test temperature. Table 2.1 shows that the toughness of HSS is larger than the toughness of MSS for different delivery conditions and testing temperatures. These values are extracted from Eurocode 3 part 1-10 [15].

The toughness of steel is influenced by the temperature. Low temperatures result in more brittle failure of steel. The transition from ductile-to-brittle failure occurs at lower temperatures for HSS than for MSS [25]. This phenomena is also known as the transition temperature, see Figure 2.6. The lower shelf of the curves in Figure 2.6 are characterized by brittle failure for loading under tension. The upper shelf, on the contrary, is characterized by ductile failure. It can be seen that S355J2 will show brittle behaviour at a higher temperature in comparison with S460ML and S690QL, respectively around -40°C over -100°C [53]. This confirms the statement that the ductile-to-brittle failure transition occurs at lower temperatures for HSS. Increase of the thickness of the material and the rate of loading, results in an increase of the transition temperature and therefore has an influence on the toughness. It does not automatically mean that brittle failure is avoided when the operating temperature is higher than the transition temperature [6].

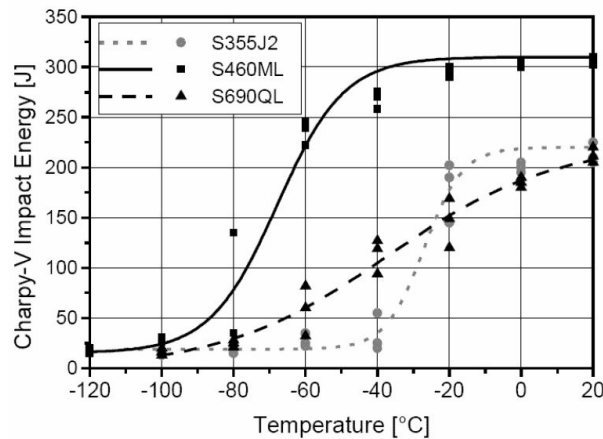


Figure 2.6: Transition temperature curves of different steel grades [53]

Ritakallio and Björk [52] looked into cold-formed hollow sections and its low temperature behaviour. This is done due to concerns regarding the loss of toughness in cold-formed corners, which is a result of strain ageing near welds. Strain ageing is the phenomenon where small elements, like nitrogen and carbon, diffuses to dislocations. The reduction of the toughness is reflected in the increase in the transition temperature. In the research is noted that a cold strain of 10% and accompanying ageing results in an increase in transition temperature in the range of 40°C to 80°C . This is applicable for most steels. However, it is observed that this increase is 25°C for TMCP steels, which indicates that finer grained steels are less sensitive to strain ageing. They reviewed a research regarding X and K joints made of S355, S420 and S460 steel. It is concluded that the effect of strain ageing is observed. However, the transition temperature remains below -50°C . This results in the conclusion that the reduction in toughness is not significant for X and K joints.

Table 2.1: Impact toughness of different steel grades and delivery conditions [15]

Steel grade	Subgrade	Test temperature [°C]	Impact energy [Jmin]
S355	JR	20	27
	J0	0	27
	J2	-20	27
S460	Q	-20	30
	M,N	-20	40
	QL	-40	30
	ML, NL	-50	27
	QL1	-60	30
S690	Q	-20	30
	QL	-40	30
	QL1	-40	40

2.2.3 Cold-forming

The cold-forming process to fabricate rectangular hollow sections (RHS) influences the mechanical properties differently than the hot rolled process. Cold-forming increases the yield strength of the material at the locations where the material is distorted (i.e. the corners of the RHS), see Figure 2.7. The ultimate strength of the material is increased as well, but to a lesser extent. This results in a decrease in the ratio σ_u/σ_y due to cold-working. Which means that the ductility is reduced.

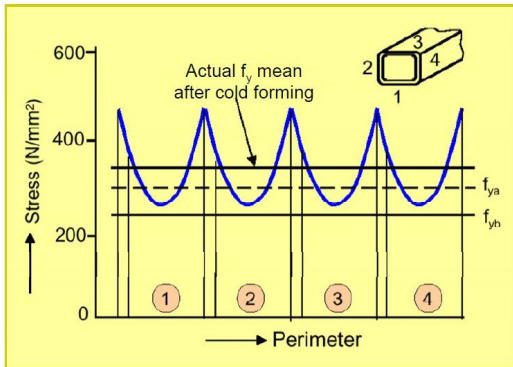


Figure 2.7: Influence cold-forming process on the yield strength (f_y or σ_u) for a SHS [61]

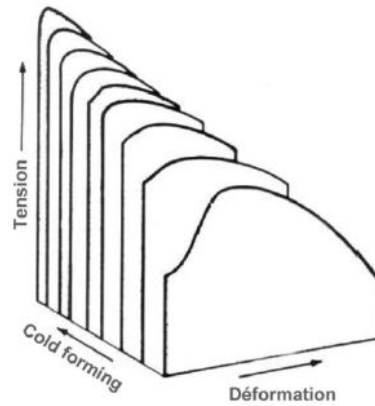


Figure 2.8: Influence amount of cold-working on the stress-strain curve [28]

When compared to the bilinear curve obtained from the hot rolling process, the cold-forming process generally results in a smoother transition between the elastic and yielding stage of the stress-strain curve [5]. This phenomenon is clearly visible in Figure 2.8, where stress-strain curves are shown in relation to the degree of cold-forming. It is observed that there is no clear-defined yield stress with a higher degree of cold-forming.

Ma et al. [42] looked into the material properties of cold-formed HSS hollow sections. They conducted coupon tests on specimens extruded from different locations of the tubular section, see Figure 2.9. For RHS, corner coupons are extracted and compared to flat coupon specimens from the same tubular section. For steel with a yield strength of 700 MPa, the corner coupons have a yield strength increase of 18%-34% compared to the flat coupons. The strain at fracture is decreased by 24%-40%. For steel with a yield strength of 900 MPa, the increase in yield strength is 14%-18% and the reduction in strain at fracture is 6%-13%. These results show the influence of work-hardening on these two steel grades. The production process of the steel tubes is not mentioned in the paper. These results support the statement that the cold-forming process increases the yield strength and decreases the strain at fracture at the distorted regions.

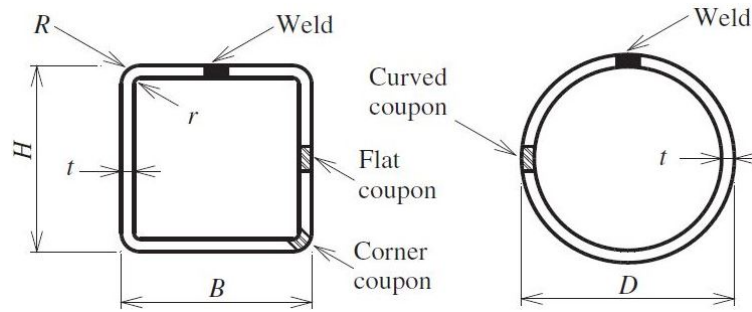


Figure 2.9: Tensile coupon locations Ma et al. [42]

Wang et al. [60] executed a similar experiment as Ma et al. [42] where they compared the results of flat coupon specimens to corner coupon specimens. The results for cold-formed S500MC and S700MC are of interest for this thesis and can be seen in Figure 2.10. It is observed that the yield strength increases in the range of 5%-15% and 8%-11%, for respectively S500MC and S700MC (this is the case for all the following results). The ultimate strength increases in the range of 13%-52% and 16%-27%. The strain at the ultimate stress is reduced in the range of 79%-83 % and 61%-85%. The strain at fracture is reduced in the range of 43%-68% and 43%-65%.

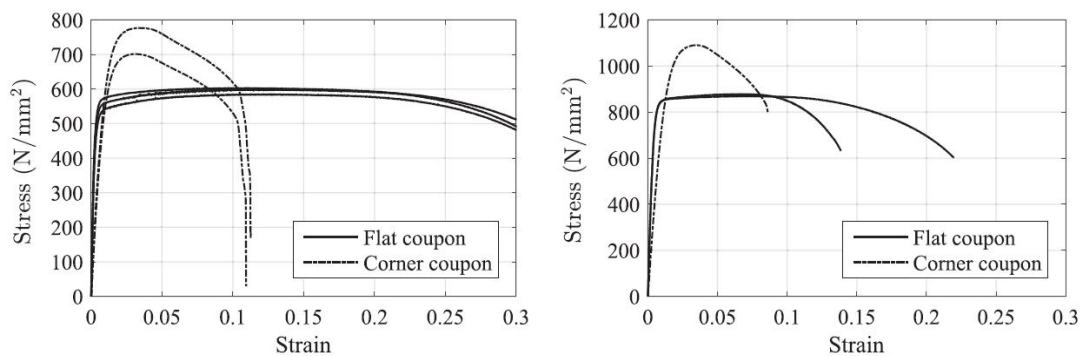


Figure 2.10: Flat and corner stress-strain curves for S500MC and S700MC [60]

Afshan et al. [1] investigated the strength enhancements in cold-formed sections. In their research they tested flat and corner coupon specimens of steel grade S355J2H. Flat coupons are extracted from three sides of the RHS. Where one coupon is taken from the side where the weld in longitudinal direction is located. The results are significantly higher than the results of the other two faces, which could be due to the over-strength of the weld material. A comparison is made between the results from the flat coupon specimens and the corner coupon specimens. The strength enhancement on the yield strength is in the range of 25%-51%. The ultimate strength is increased in the range of 19%-25%. The strain at ultimate strength is decreased in the range of 88%-95%. The strain at fracture is decreased in the range of 56%-65%.

The amount of cold-working is related to the strength in the heat affected zones (HAZ) of welds, when welded. A larger amount of cold-working results in a greater reduction in the strength of the HAZ. This is concluded by Hancock et al. [27] in their research regarding butt welded cold-formed C450 tubular joints.

Becque and Wilkinson [5] conducted coupon experiments on cold-formed tubular sections of grade C450. For each RHS two coupon specimens are extracted. One specimen from the side adjacent to the longitudinal seam weld and one specimen from the side opposite to the longitudinal seam weld. The yield strength of the adjacent side is divided by the yield strength of the opposite side, which resulted in a ratio in the range of 0,93 to 1,10, with an average value of 0,98. The ultimate strength of the adjacent side compared to the ultimate strength of the opposite side resulted in a range of 0,93 to 1,05, with an average value of 0,99. This indicates that there can be a difference up to 10% in the yield strength and up to 7% in the ultimate strength between the adjacent and the opposite side for coupon specimens of cold-formed C450 RHS.

Nseir [47] conducted coupon experiments from different sides of cold-formed SHS, the resulting stress-strain curves are presented in Figure 2.11. Four flat coupons and two corner coupons are extracted. The results include two cold-formed SHS made out of steel grade S355. The results from the four flat coupons are compared to each other. The maximum deviation for the yield stress and ultimate stress is 11% and 6%. The maximum deviation obtained for the fracture strain is 19%.

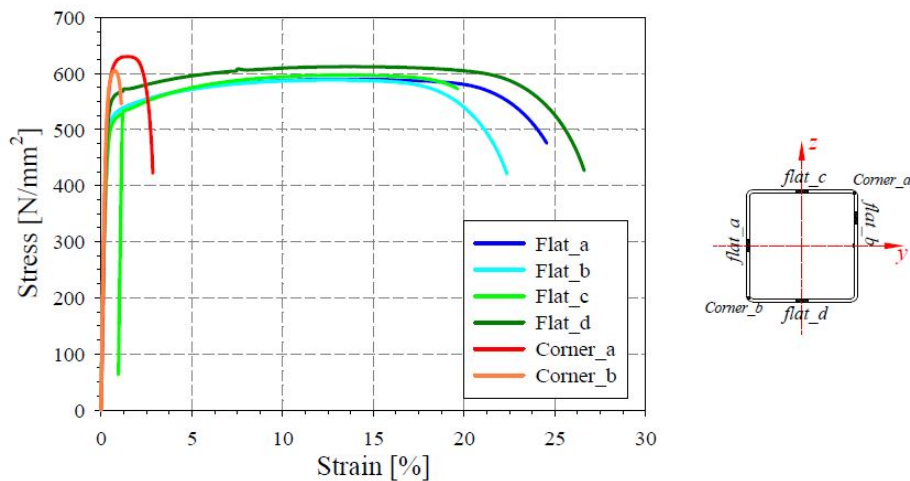


Figure 2.11: Stress-strain curves from flat and corner coupons of SHS 200x200x6 [47]

Chen and Young [21] investigated cold-formed tubular sections loaded under tension. The experimental program included normal and high strength steel sections. Flat coupon specimens are used from the side adjacent of the seam weld for SHS. For RHS is the flat coupon specimen extracted from the side with the longest depth. The tensile performance of full cross-section tubular sections is investigated and compared to tensile coupon tests from the same sections. The 0,2% proof stress increased with 8%, when comparing the full cross-section tensile test to the coupon tests. The ultimate stress increased with 6%. The strength increase of the 0,2% proof stress and ultimate stress is attributed to the strength increase in the corners of cold-formed sections. The research showed that the fracture strain of the tubular sections is lower than the fracture strain obtained by the coupon tests. No numbers are presented in the paper that describe the decrease of the fracture strain. Wang et al. [60] also investigated full cross-section tensile test and tensile coupon tests, only for hot-finished tubular sections. They also observed a lower fracture strain. However, they noted that there is no standard gauge length for full cross-section tensile tests. Therefore, the comparison between fracture strain of the full cross-section and the coupon tests has limited validity.

A summarizing table with values obtained from literature of the strength enhancement of corner coupons compared to flat coupons is presented in Table 2.2. The table presents the influence on the yield strength (σ_y), ultimate strength (σ_u), strain at ultimate stress (ϵ_u) and strain at fracture (ϵ_f). Table 2.3 represents the values observed in literature for the maximum scattering of flat coupon results between different sides of cold-formed sections. This table also shows the obtained results for the difference between full cross-section tensile tests and flat coupon tests.

Table 2.2: Overview literature strength enhancements corner versus flat coupons cold-formed tubular sections

	Steel grade	σ_y	σ_u	ϵ_u	ϵ_f
Afshan et al. [1]	S355J2H	+ 25%-51%	+ 19%-25%	- 88%-95%	- 56%-65%
Wang et al. [60]	S500MC	+ 5%-15%	+ 13%-52%	- 79%-83%	- 43%-68%
	S700MC	+ 8%-11%	+ 16%-27%	- 61%-85%	- 43%-65%
Ma et al. [42]	S700	+ 18%-34%	-	-	- 24%-40%
	S900	+ 14%-18%	-	-	- 6%-13%

Table 2.3: Overview scattering literature

Scatter between flat coupons from different sides RHS/SHS	Steel grade	σ_y	σ_u
Nseir [47]	S355	11%	6%
Becque and Wilkinson [5]	C450	10%	7%
Difference full cross-section tensile test and coupon tensile test	Material σ_y	σ_y	σ_u
Chen and Young [21]	235-795 MPa	+ 8%	+ 6%

2.2.4 Stress triaxiality

The stress triaxiality (η) for isotropic materials, see Equation 2.2, is described by the mean or hydrostatic stress (σ_m , see Equation 2.3) and the von Mises stress (σ_{eq} , see Equation 2.4). σ_1, σ_2 and σ_3 are the principal stresses and need to meet Equation 2.5 [3, 30].

$$\eta = \frac{\sigma_m}{\sigma_{eq}} \quad (2.2)$$

$$\sigma_m = \frac{\sigma_1 + \sigma_2 + \sigma_3}{3} \quad (2.3)$$

$$\sigma_{eq} = \frac{1}{\sqrt{2}} \sqrt{(\sigma_1 - \sigma_2)^2 + (\sigma_1 - \sigma_3)^2 + (\sigma_2 - \sigma_3)^2} \quad (2.4)$$

$$\sigma_1 \geq \sigma_2 \geq \sigma_3 \quad (2.5)$$

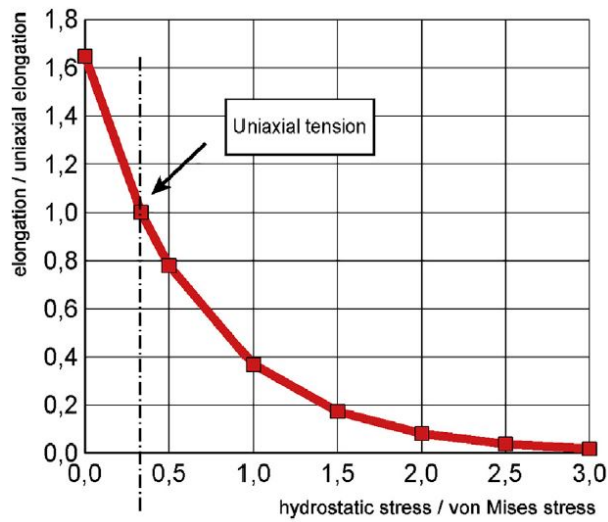


Figure 2.12: Stress triaxiality versus plastic deformation capacity [30]

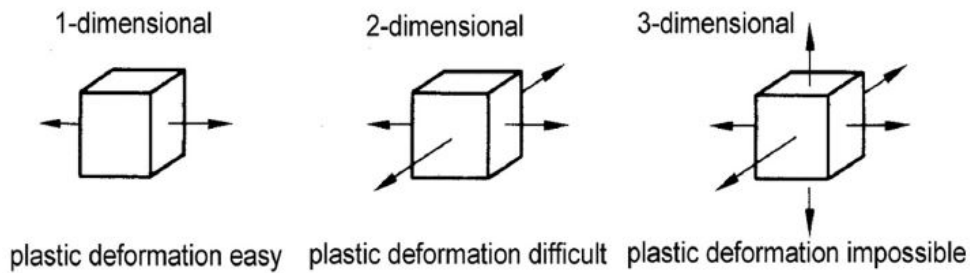


Figure 2.13: Stress components [30]

Figure 2.12 shows the relation between the stress triaxiality and the plastic deformation capacity. The plastic deformation capacity in this figure is expressed as the elongation divided by the uniaxial elongation. This means that the uniaxial elongation is expressed as 1,0. It can be seen that the deformation capacity decreases with an increase in stress triaxiality. This relationship can be explained by Figure 2.13. In the case of uniaxial tension, only σ_1 is unequal to zero, which corresponds to the '1-dimensional' case in Figure 2.13. The figure shows that an increase in principle stress components, which results in an increase in stress triaxiality, will result in a decrease in plastic deformation [30]. This corresponds with the relationship shown in Figure 2.12.

Research from Bao and Wierzbicki [4] resulted in a cut-off value for the stress triaxiality. This cut-off value is equal to -1/3. They analytically derived that below this value ductile fracture does not occur. The derivation is based on the experimental results reported in the book of Bridgman [10], which conducted over 350 tests of 20 different types of steels and heat treatments.

2.3 Welds

2.3.1 Fillet welds

Fillet welds are defined as triangular shaped welds that are located on the surface of the connected plates. Therefore, no plate or edge preparation is required. Fillet welds can be executed as single- or double-sided. Single-sided fillet welds result in additional forces and stresses due to local eccentricity. For this reason, single-sided fillet welds are not preferred to use but are only allowed in hollow section joints. Fillet welds are characterised by its effective throat thickness (a) and effective length (l_{eff}). The effective throat thickness is defined as the height of the largest triangle of the weld and should be at least 3 mm [16].

The Eurocode [16] provides two methods to determine the design resistance of a fillet weld. Respectively, the directional and simplified method. The directional method is the most economical method and results in a higher resistance. The forces are expressed into the following four components: normal stress perpendicular to the throat (σ_{\perp}), normal stress parallel to the axis of the weld (σ_{\parallel}), shear stress perpendicular to the throat (τ_{\perp}) and shear stress parallel to the axis of the weld (τ_{\parallel}). The stress components are presented in Figure 2.14.

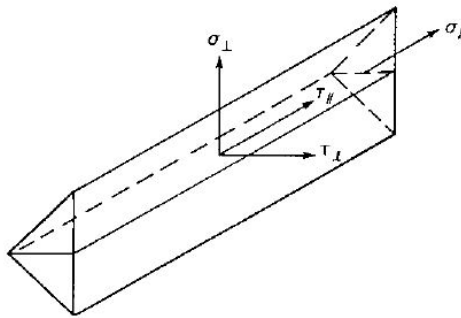


Figure 2.14: Fillet weld stress components [16]

Table 2.4: Fillet weld correlation factor [19]

Steel grade	S235	S275	S355	S420	S450	S460	S500	S550	S620	S690
β_w	0,80	0,85	0,90	0,88	1,05	0,85	0,90	0,95	1,05	1,10

The resistance of the fillet weld is checked with Equation 2.6 and 2.7. If both equations are satisfied, the design resistance of the weld is sufficient. Parameter f_u is the ultimate strength of the weaker part of the joint. Parameter β_w is the correlation factor and is related to the steel grade, see Table 2.4. Parameter γ_{m2} is the partial safety factor for welds with a value of 1,25 [14, 19].

$$[\sigma_{\perp}^2 + 3(\tau_{\perp}^2 + \tau_{\parallel}^2)]^{0,5} \leq \frac{f_u}{\beta_w \gamma_{m2}} \quad (2.6)$$

$$\sigma_{\perp} \leq \frac{0,9 f_u}{\gamma_{m2}} \quad (2.7)$$

For steel grades from S460 up and until S700, Equation 2.8 has to be satisfied to guarantee sufficient design resistance of the fillet weld. This equation takes the weakest parent ($f_{u,PM}$) and filler ($f_{u,FM}$) metal strengths into account. Parameter $\beta_{w,mod}$ is the modified correlation factor and is related to the filler metal strength, see Table 2.5.

$$[\sigma_{\perp}^2 + 3(\tau_{\perp}^2 + \tau_{\parallel}^2)]^{0,5} \leq \frac{0,25 f_{u,PM} + 0,75 f_{u,FM}}{\beta_{w,mod} \gamma_{m2}} \quad (2.8)$$

An alternative approach is the simplified method. The design resistance of the fillet weld is satisfied if Equation 2.9 is fulfilled. The equation assumes that the resultant of the forces of the weld does not exceed the design resistance of the weld per unit length. Parameter $F_{w,Ed}$ is the design value of the weld force per unit length. Parameter $F_{w,Rd}$ is the design weld resistance and is determined according to Equations 2.10, 2.11 and 2.12 [19].

$$F_{w,Ed} \leq F_{w,Rd} \quad (2.9)$$

$$F_{w,Rd} = f_{vw,d} a \quad (2.10)$$

$$\text{Steel grade} < S460 : f_{vw,d} = \frac{f_u / \sqrt{3}}{\beta_w \gamma_{m2}} \quad (2.11)$$

$$\text{Steel grade} \geq S460 : f_{vw,d} = \frac{0,25 f_{u,PM} + 0,75 f_{u,FM}}{\beta_{w,mod} \gamma_{m2}} \quad (2.12)$$

Table 2.5: Filler metal properties [19]

Filler metal strength class	42	46	69	89
Ultimate strength $f_{U,FM}$ [N/mm^2]	500	530	770	940
Correlation factor $\beta_{w,mod}$ [-]	0,89	0,85	1,09	1,19

2.3.2 Full-strength single-sided fillet welds

According to the directional and simplified method, design of fillet welds may lead to thin welds. This can result in low deformation capacity if the rupture strength of the weld is less than the yield strength of the connecting parts. Low deformation capacity of a joint can result in brittle failure. To guarantee ductile behaviour of a fillet welded joint, the welds should be designed according to the 'full-strength' concept. The rupture strength of the weld should be larger than the rupture strength of the connecting members to guarantee element failure in case of overloading. The full-strength fillet welds are usually expressed in a requirement of the throat thickness of the weld. Figure 2.15 and the directional method are used to obtain an expression for the full-strength double-sided fillet weld.

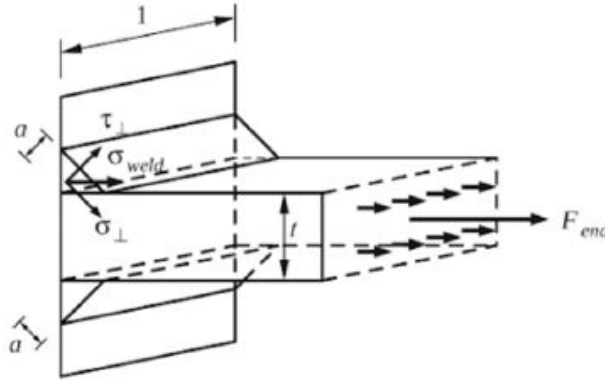


Figure 2.15: Double-sided end fillet weld [33]

$$[\sigma_{\perp}^2 + 3(\tau_{\perp}^2 + \tau_{\parallel}^2)]^{0,5} \leq \frac{f_u}{\beta_w \gamma_{m2}} \quad (2.13)$$

$$F_{end} = \frac{tlf_y}{\gamma_{m0}} \quad (2.14)$$

$$\sigma_{w,d} = \frac{F_{end}}{2al} \quad (2.15)$$

$$\sigma_{\perp} = \tau_{\perp} = \frac{\sigma_{w,d}}{\sqrt{2}}, \tau_{\parallel} = 0 \quad (2.16)$$

Combining Equations 2.13 - 2.16 results in the following expression:

$$a \geq \frac{t \beta_w \gamma_{m2} f_y}{\sqrt{2} \gamma_{m0} f_u} \quad (2.17)$$

The same derivation is performed for a single-sided full-strength fillet weld. Only Equation 2.15 is adapted into Equation 2.18.

$$\sigma_{w,d} = \frac{F_{end}}{al} \quad (2.18)$$

This results in the following expression for the required throat thickness of a full-strength single-sided fillet weld:

$$a \geq \frac{t\sqrt{2}f_y\beta_w\gamma_{m2}}{f_u\gamma_{m0}} \quad (2.19)$$

Parameter γ_{m0} , the partial safety factor for steel material, has a value of 1,0 [14]. The throat thickness a is dependent on the thickness t of the connecting element, the correlation factor β_w , the yield strength f_y of the weaker parent material and the ultimate strength f_u of the weld material. Table 2.6 shows the a/t -ratio that is required for a full-strength single-sided fillet weld. The minimum ductility limits are used, according to the standards [14, 18] for the different steel grades. For steel grade S960 is β_w linearly interpolated to a value of 1,24.

Table 2.6: Throat thickness for full-strength single-sided fillet welds

	β_w	f_y	f_u	a/t
	[–]	[MPa]	[MPa]	[mm]
S355	0,90	355	390,5	1,45
S460	0,85	460	506	1,37
S500	0,90	500	525	1,52
S700	1,10	700	735	1,85
S960	1,24	960	1008	2,09

2.3.3 Butt welds

Butt welds can be executed as full or partial penetration welds. When welding is executed properly, the filler metal of a butt weld may be considered as parent material. For full penetration butt welds, no calculation is needed when the filler metal strength is overmatching the parent metal strength [33]. When the filler metal is under-matching (possible for HSS), the strength of the filler metal according to Table 2.5 may be used. Edge preparation is required before welding of butt welds. Usually bevelled edges are used. This results in an increase in the fabrication costs in comparison with fillet welds.

2.3.4 Welding topics that influence the joint strength

A dominant part of the joint strength of brittle failure modes is related to the welding. Brittle failure modes are brace failure and punching shear failure, which requires sufficient weld strength for the failure modes to occur. Different topics regarding to welding that influence the joint strength will be discussed.

The toughness of steel in cold-formed zones is reduced during welding. Therefore, the Eurocode [19] prescribes limitations for welding in cold-formed zones in hollow sections. The cold-formed zone is defined in the standard as the corner area, including a distance of $5t$ at each side of the corner, see Figure 2.16. Welding in this zone is allowed for steel grades below S460. If the steel grades are equal to or above S460, r/t -ratio limitations according to Table 2.7 should be satisfied. In the case that these conditions are not met, welding still may be carried out if the thickness is below 12,5 mm, the steel is aluminium killed or the steel is of quality J2H, K2H, MH, MLH, NH or NLH (see Table 2.8 for the clarification of the steel quality abbreviations). However, according to Heinisuo et al. [29], welding of Domex S500 hollow sections is permitted in the cold-formed regions without taking into account the limitations given by the Eurocode.

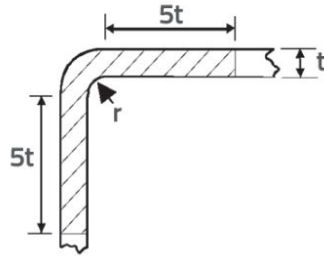


Figure 2.16: Definition cold-formed zone according to EN1993-1-8:2020 [19]

Table 2.7: r/t -limitations welding in cold-formed zones [19]

r/t	Strain due to cold forming [%]	Max. thickness under predominantly static loading [mm]
≥ 25	≤ 2	any
≥ 10	≤ 5	any
$\geq 3,0$	≤ 14	24
$\geq 2,0$	≤ 20	12
$\geq 1,5$	≤ 25	8
$\geq 1,0$	≤ 33	4

Table 2.8: Clarification abbreviations steel quality [17]

General	H	for Hollow section
Non-alloy steel	J2 or K2	for qualities with specified impact properties at -20°C
Fine grain steel	N	for Normalized
	M	for Thermomechanically rolled
	L	for qualities with specified impact properties at -50°C

A typical defect that can occur due to welding is hydrogen cracking (i.e. cold cracking). Hydrogen cracking increases the risk of brittle behaviour. This phenomenon can occur during the cooling process or in the first 72 hours after welding at a temperature below 200°C . Hydrogen cracking is related to the amount of alloying elements in the steel. The amount of alloying elements is described with the CEV of steel, see Equation 2.1. The amount of carbon in steel influences the hardness. Hydrogen cracking is more relevant for HSS because the hardness of the steel needs to be higher than 350 Hv (Hardness Vickers) for hydrogen cracking to occur. Under high temperatures, are the hydrogen elements more mobile, which results in more diffusion of the hydrogen elements through the steel surface. Therefore, under lower temperatures there is a higher risk that the hydrogen elements cannot diffuse. This leads to a higher risk of hydrogen cracking under lower welding temperatures.

EN1011-2 [13] recommends working temperatures to make sure that this type of cracking is avoided. The risk on hydrogen cracking increases by an increase of alloying content, plate thickness and hydrogen content. However, an increase in heat input reduces the risk on hydrogen cracking [9, 55, 56].

Another defect that may occur is hot cracking. Hot cracking is related to the amount of alloying elements and inclusions. There are two types of hot cracking, solidification- and liquation cracking. Solidification cracking occurs mainly in the centre of the weld and is associated with impurities like phosphorus and sulphur. Liquation cracking occurs in the HAZ. The cracks occur due to shrinkage during the cooling of steel. This shrinkage is a result of high local temperature differences and the corresponding difference in thermal expansion due to welding [9, 13, 55].

Lamellar tearing is a defect due to impurities in the steel. This defect is a result of a badly designed weld. The sulphur content is related to the risk of lamellar tearing. A higher amount results in a higher risk and vice versa. Cracking will occur due to shrinkage around the impurities [9, 55].

Fusion line failure is a phenomena occurring in HSS fillet welds. This failure is a result of less strength along the fusion line in relation to the strength of the base and weld material. This is a consequence of softening and other metallurgical effects. To avoid fusion line failure, the throat thickness could be increased. However, this is contradicting with the influence of the throat size on the softening effect. It is possible to avoid this problem by applying asymmetric welds [7].

Björk et al. [7] mentioned the additional capacity of a weld due to penetration of the weld material. The penetration of the weld increases the cross-section of the weld. The production process should be constant and without interruptions. It should be noted that the strength in the penetrated part is lower than the strength of the filler metal. An increasing degree of penetration results in a decrease in the average weld strength. The softening due to dilation should be taken into account when the additional capacity due to penetration is considered.

The critical failure plane or angle of rupture of a fillet weld is related to the weld strength and is assumed to be 45° in the current Eurocode. However, this assumption is only valid for the case of pure shear loading parallel to the weld. In the directional method is the critical failure plane the ratio between σ_\perp and σ_\parallel . For a symmetric fillet weld, with θ is 45° , the critical failure plane angle α is 27° , see Figure 2.17. This results in an increase in the required throat thickness of 8% compared to the method used in the standard. The critical failure plane can be optimized by applying asymmetric fillet welds (asymmetric leg lengths), see Figure 2.18. This will also improve the fatigue performance. The flank angle should be in the range of 30° - 40° to be optimal. The application of asymmetry results in an improvement of the weld performance [7, 9].

Many welding techniques are available on the market which can be used to weld HSS joints e.g. gas metal arc welding, manual metal arc welding, tungsten inert gas welding, laser welding, plasma welding and submerged arc welding. The most common used procedure today on the market is gas metal arc welding (GMAW) according to SSAB [55]. This is because the method is easy to automate, which results in high productivity.

The Eurocode describes the minimum required throat thickness for fillet welds. In the case of HSS joints, the current design rules are very conservative which leads to high welding costs. This is investigated by Feldmann et al. [23] through applying small weld sizes which resulted in failure in the welds before the full capacity of the joint could be reached. The final recommendations on the

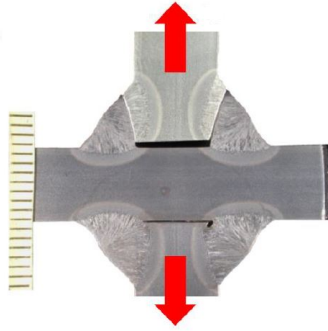


Figure 2.17: Critical failure plane of 27° [7]

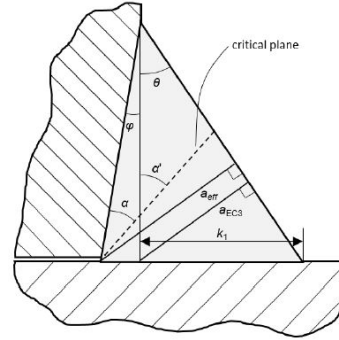


Figure 2.18: Critical failure plane asymmetric weld [7]

minimum applicable throat thickness can be seen in Table 2.9. Parameter t_i is the thickness of the brace member that will be connected by the fillet weld. The recommended throat thicknesses, which are smaller than the current Eurocode, result in a decrease in welding costs and an increase in weld performance due to a lower required heat input. It is observed that the reduction in strength in the softening zones increased significantly for higher steel grades. This effect resulted in some observed fusion line failures in the experiments.

Table 2.9: Recommended throat thickness for fillet welds according to Feldmann et al. [23]

Steel grade	Recommendation for throat thickness a			
	General min. allow. throat thickness [mm]	Min. allow. when brace force based design is used [mm]	Min. allow. when joint capacity based design is used [mm]	Current recommendation acc. EC3 [mm]
S500	3	$1,0t_i$	$1,0t_i$	$1,61t_i$
S700	3	$1,2t_i$	$1,2t_i$	$1,65t_i$
S960	3	x	$1,4t_i$	$1,73t_i$

2.3.5 Heat affected zone (HAZ)

The HAZ is the part of the parent material of which the properties are changed due to the high temperatures of the welding process, see Figure 2.19. As noted by Lan and Chan [37], welding of HSS hollow section joints is essential and the material properties of the HAZ are dependent on the steel production process (e.g. QT, DQ or TMCP), welding type, heat input and cooling time. The cooling time $t_{8/5}$ is the time needed for the joint to cool down from 800°C to 500°C and is related to the pre-heating temperature and the heat input. Where the heat input is dependent on the weld size [7]. A low heat input, for example achieved by multi-pass welding, results in a confined coarse-grained zone and therefore a satisfactory strength [55]. The thermal conductivity and shape

of the joint influences the cooling time. High thermal conductivity results in faster cooling and vice versa [9]. Björk et al. [7] mentioned that direct quenched HSS seem to have no upper limit for the maximum cooling time. An increase in steel grade results in a reduced maximum heat input due to the higher required strength of the weld [55, 56]. The strength of the welded joint is positively correlated to the hardness of the joint. The non-uniform material properties inside the HAZ are a result of complex welding thermal cycles and non-uniform cooling rates [20].

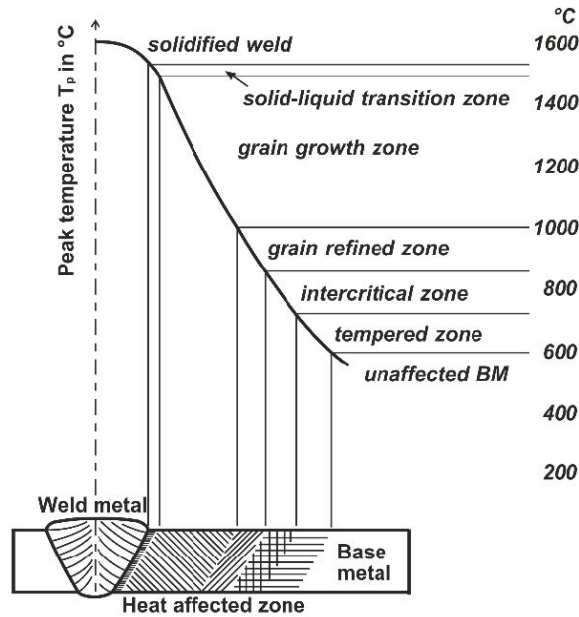


Figure 2.19: Subdivision HAZ [58]

Softening is the decrease of strength in the HAZ which can lead to failure in the HAZ. A small thickness and a high heat input results in a larger softening zone and a decrease in strength (hardness). The weakened area due to softening is supported by the surrounding base material due to the local 3D stress state at the weld toe, the constraint effect. The plastic deformations usually localize in the softening zone. The softening effect can decrease the material strength up to 25% [7]. The constraint effect can only prevent failure if the softening area is not through the thickness of the plate.

Asymmetry of the joint obstructs the softening effect (application of T instead of X). The softening effect can be avoided by welding techniques and proper weld design. Optimization of the joint dimensions (i.e. the lowest possible throat thickness) will increase the cooling rate which will result in a decrease in softening. For the welding techniques, multi-pass welding should be used instead of a single-pass welding with a larger throat thickness. During multi-pass welding, should the interpass temperature be considered to make sure that the temperature is dropped to an appropriate level before the next bead is welded. Also, laser and hybrid-laser beam processes help in getting the optimal cooling rate, which minimizes softening in the base plate.

For conventional steels, when the ratio between the width of the soft zone in relation to the thickness of the plate is below 0,25, the global strength is not necessarily decreased due to local softening. This

is due to the constraint effect of the unaffected base metal and the stronger weld metal [31, 44, 64].

Heinisuo et al. [29] mentioned in the SSAB handbook that for high strength hollow sections the use of butt welds over fillet welds (or the use of a combination of a partial butt weld and a fillet weld), results in a reduction of the amount of weld metal. This leads to a lower heat input and therefore reduces the softening in the HAZ. The maximum allowed cooling time for Domex 500ML and Strenx 700MLH is 20 seconds. There are no limits for the minimum cooling time.

Hancock et al. [27] noted in their research regarding butt welded cold-formed C450 tubular joints, that a higher heat input, which corresponds to a wider softening zone, results in a larger reduction in yield and ultimate strength in the HAZ.

Pirinen et al. [51] investigated the effect of the heat input on the mechanical properties for 8 mm thick but-welded HSS joints. They investigated a TMCP and QT steel with approximately the same mechanical properties, the tensile strength of both steels is in the range of 821-835 MPa. The influence for 3 different heat inputs (1,0, 1,3 and 1,7 kJ mm⁻¹) on the hardness is presented in Figure 2.20 for the TMCP and in Figure 2.21 for the QT steel. The figures show that an increase in heat input results in an increase of the HAZ/softening zone and therefore reduces the strength of the welded joint.

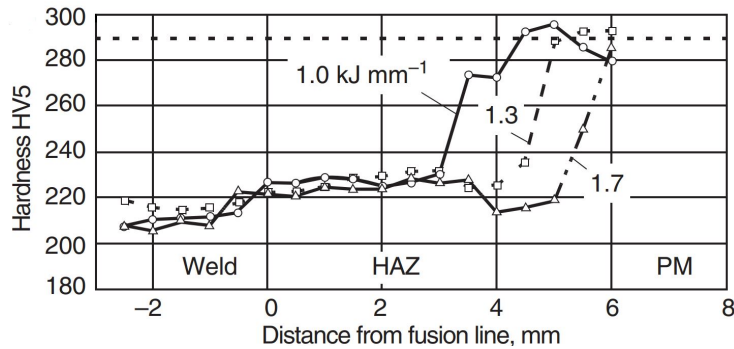


Figure 2.20: Effect heat input on the hardness of TMCP HSS steel [51]

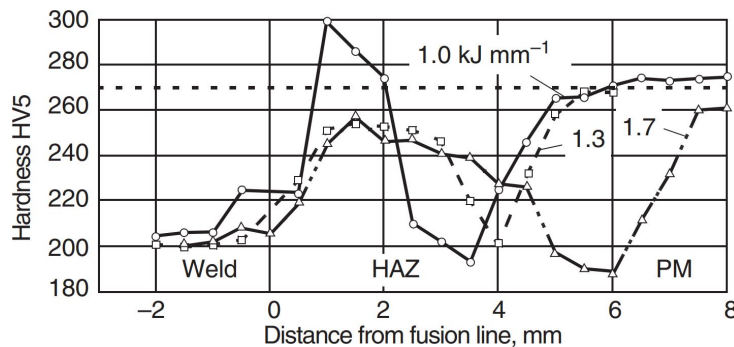


Figure 2.21: Effect heat input on the hardness of QT HSS steel [51]

Hochhauser et al. [31] investigated the influence of the softening on the properties of the HAZ for S700 TMCP steel. For different cooling times, the width of the HAZ (X_{sz} = ratio of width of the soft zone to the plate thickness of 6 mm) and the accompanying tensile strength reduction are determined. Cooling times of 5 to 18 seconds resulted in a width of the softening zone between X_{sz} of 0,33 and 0,6, with corresponding tensile strength reduction of 3% to 8%. It is noted that there is an almost linear increase between the width of the soft zone and the increase of the cooling time. It is concluded that low heat input during welding results in relatively small softening zones and higher strength of these zones.

Stroetmann et al. [57, 58] looked into the influence of the cooling time on the mechanical properties of welded HSS joints. The research included four steel grades which are produced by two different production processes, respectively TMCP (S500M and S700M) and QT (S690Q and S960Q). It is noted that TMCP steels contain lower carbon equivalents than QT steels, this means that TMCP steels can be welded at lower temperatures.

The HAZ is divided in the coarse and fine grained, intercritical and tempered zone, see Figure 2.19. Each zone experiences different peak temperatures during welding, respectively 1350, 1200, 1000, 800 and 600° Celsius. The influence of the cooling time on the tensile strength in the HAZ is investigated for the different peak temperatures. The cooling times are in the range of 1,5 to 25 seconds. The different peak temperatures correspond with the different zones of the HAZ. Figures 2.22 and 2.23 represent the results for TMCP S500M and S700M, which correspond with the steel grades used in this research. It is shown that the ultimate tensile strength of TMCP S500M is generally higher than the ultimate strength of the base material at room temperature (RT-line). These results are also obtained for QT S690Q and S960Q steel. However, for TMCP S700M is the ultimate strengths lower than the ultimate strength of the base material. The results for TMCP S700M are in accordance with the findings of Hochhauser et al. [31] and Javidan et al. [34]. Reason for this could be the optimised micro-alloying of TMCP steels. Figures 2.22 and 2.23 indicate a significant strength increase for lower cooling times.

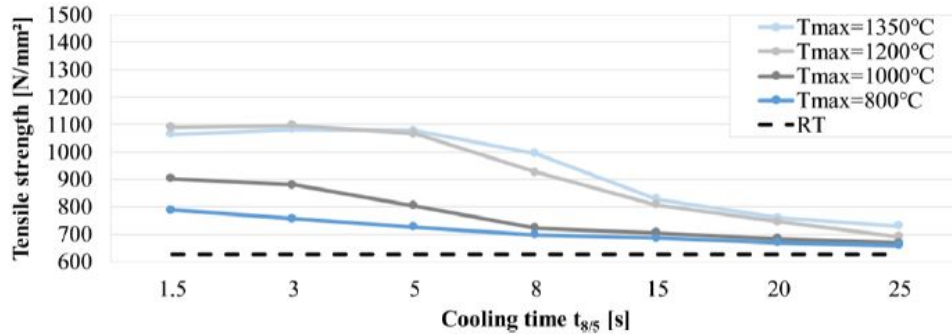


Figure 2.22: Tensile strength of TMCP S500M steel as a function of peak temperature and cooling time [57, 58]

Javidan et al. [34] looked into the influence of welding on the mechanical properties for mild steel (MSS, yield strength of 265 MPa), high strength steel (HSS, yield strength of 772 MPa) and ultra-high strength steel (UHSS, yield strength of 1247 MPa). HSS is produced by TMCP and UHSS is produced by DQ. The paper does not mention the production process of MSS. The influence on the

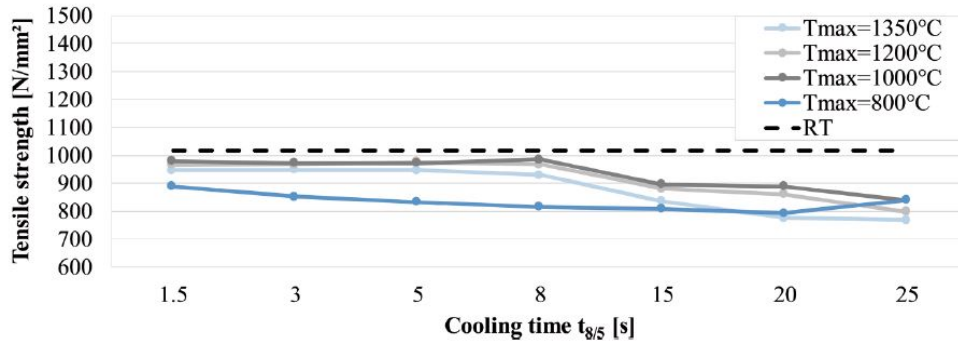


Figure 2.23: Tensile strength of TMCP S700M steel as a function of peak temperature and cooling time [57, 58]

tensile strength showed an increase of 13% and a decrease of 8% and 30%, respectively for MSS, HSS and UHSS. These results are for the steel material up to 4 mm distance from the weld. The ultimate strain is compared to the ultimate strain of the base material. This resulted in an increase of 2,5, 2,1 and 3,5 for MSS, HSS and UHSS.

Siltanen et al. [54] observed that the strength reduction for DQ S960 steel is around 20%. Although, the strength reduction for QT S960 steel is minor, these findings are in accordance with the results of Stroetmann et al. [57, 58]. These results are based on the reduction of the Vickers Hardness (VH) in the HAZ. There is a linear relationship between the increase of the VH-value and the increase in the yield and ultimate strength.

Amraei et al. [2] investigated the strength of cold-formed, butt-welded SHS. Coupon specimens are cut in half and welded together to determine the strength in comparison with non-welded coupon specimens. Steel with a yield strength of 780 MPa resulted in a strength reduction in the HAZ of 7%. The production process of the steel is not mentioned in the paper.

Lan et al. [39] looked into the structural behaviour of HSS RHS X joints. Eight RHS joints made of Q890 steel are tested under axial compression. Thereafter, a finite element model is built and validated against the test results. With this finite element model, the influence of the HAZ for DQ S960 steel is investigated. The tubular sections are produced by butt-welding plates to each other. Therefore, is the possible influence due to cold-forming excluded. The way the HAZ is modelled can be seen in Figure 2.24. For the red area a strength reduction of 20% (Siltanen et al. [54]) and ultimate strain increase of 2,1 (Javidan et al. [34]) times the value of the base material is applied. For the blue area a strength reduction of 10% is applied, the ultimate strain is identical to the ultimate strain of the base material. The same modulus of elasticity is adopted for the HAZ and the base material. The stress strain curves for the base material (black curve), blue area (blue curve) and red area (red curve) can be seen in Figure 2.25.

The numerical investigation showed a reduced static strength of 1% to 8% for the joints with small or large β -values (β is 0,2, 0,79 and 1,0). However, a strength reduction of 15% is obtained for a medium β -value of 0,5. This is due to the failure mode of chord face plastification. It must be noted that the influence for a β of 0,2 is less significant than the strength reduction for a β of 0,5. This can

be explained by the increasing under-utilisation of the increased yield strength for smaller β -values. The research shows that the joint strength reduction is less pronounced than the material strength reduction applied in the models. This indicates redistribution of plastic stresses in the HAZ to the base material.

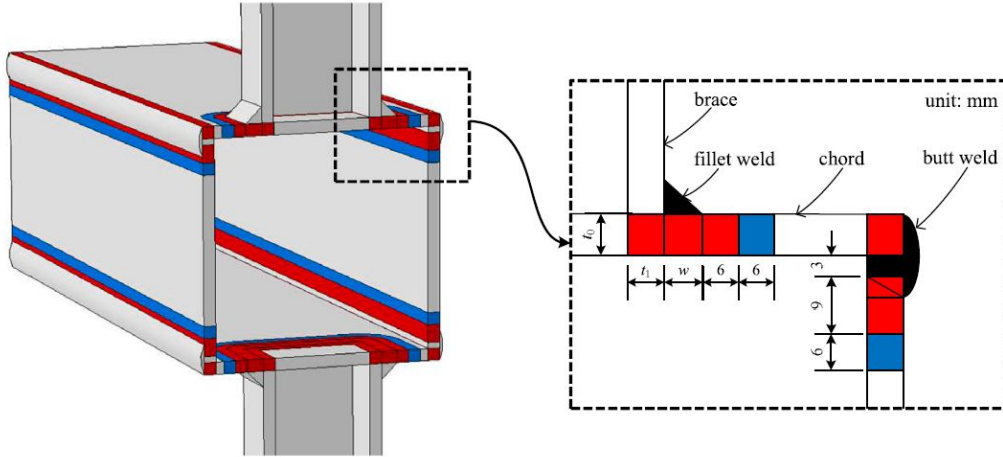


Figure 2.24: HAZ modelling in DQ S960 RHS X joints [39]

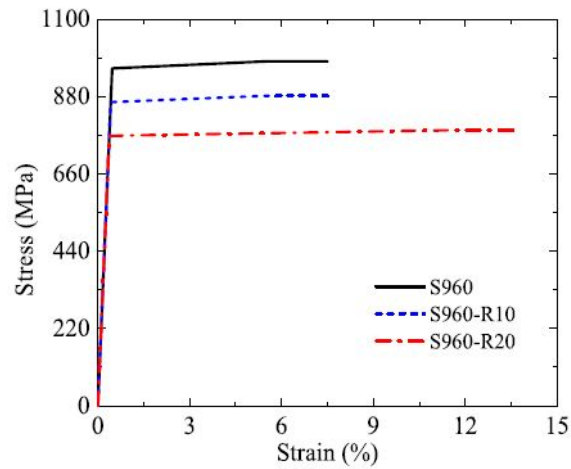


Figure 2.25: Stress-strain curves base material and HAZ research Lan et al. [39]

Lan et al. [38] applied the same HAZ modelling as Lan et al. [39] in their research regarding chord plastification in HSS CHS X joints subjected to axial compression. Steel grades S900 and S1100 are applied in the research. The same HAZ modelling visible in Figure 2.24 is applied for the brace-to-chord connection in this research. For the red area of S900 a strength reduction of 20% (Siltanen et al. [54]) and ultimate strain increase of 2,1 (Javidan et al. [34]) times the value of the base material are applied. For the blue area a strength reduction of 10% is applied, the ultimate strain is kept identical to the ultimate strain of the base material. This resulted in a joint strength reduction of

3% to 5%. For the red area of S1100 a strength reduction of 30% (Javidan et al. [34]) and ultimate strain increase of 3,5 (Javidan et al. [34]) times the value of the base material are applied. For the blue area a strength reduction of 15% is applied, the ultimate strain is kept identical to the ultimate strain of the base material. This resulted in a joint strength reduction of 5% to 7%. These results show that the reduction of joint strength is significantly lower than the reduction of material strength in the HAZ for CHS X joints made of S900 and S1100 steel loaded under axial compression. This difference is explained through redistribution of plastic stresses.

Maurer et al. [44] numerically investigated the effect of the HAZ on the static strength of butt welds. The investigated steel grade is TMCP S700MC. They concluded that the influence of the angle of bevel is negligible on the ultimate tensile strength of the weld.

Zhao et al. [64] investigated the impact of welding on T-stub joints. In their research, they first determined the material properties of weld-affected coupon specimens of reheated, quenched and tempered (RQT) S690 and TMCP S385 steel. The weld-affected coupons experienced a simulated thermal heat treatment to simulate the HAZ properties. Figure 2.26 shows the results for TMCP S385 and RQT S690. For TMCP S385, the strength is slightly increased by 5% to 8% due to welding. However, for RQT S690 steel the strength is significantly decreased by nearly 23%.

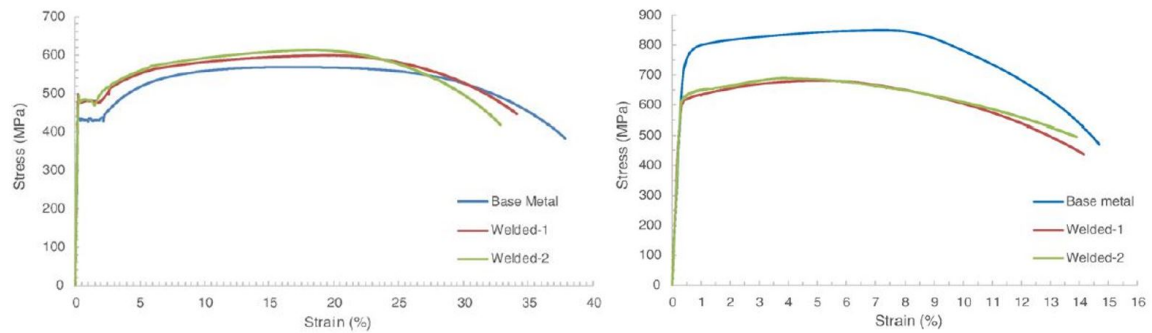


Figure 2.26: Stress-strain curves for TMCP S385 (left) and RQT S690(right) [64]

The researches done by Stroetmann et al. [57, 58], Javidan et al. [34], Siltanen et al. [54], Zhao et al. [64] show the importance of the production process and steel grade on the strength reduction in the HAZ. The strength reduction in the HAZ could be more significant for higher steel grades. Besides, the strength reduction could be more significant for TMCP and DQ HSS than for QT HSS

2.4 Hollow section joints EN1993-1-8:2020

In the design of hollow section joints, there are two main failure criteria described in literature, the ultimate load resistance and the deformation limit. Due to the multiple configurations, joints react differently to an increase in loading. Some joints have a clear ultimate force in the force-displacement curve, other joints have an increase in the capacity with large plastic deformations as a result. To avoid these large plastic deformations, a deformation limit is defined. In the case of a RHS chord, this limit is defined as 3% of the chord width ($0,03b_0$) [41]. The final ultimate resistance of the joint is governed by the lowest capacity of the ultimate load resistance or the deformation limit.

There are different kind of joint types as described in the newly proposed Eurocode [19], see Figure 2.27. The joint types are dependent on the force transfer and the geometry of the joint. The scope of this research includes only simple uniplanar X joints. Therefore, multiplanar joints are excluded in this section. The most simple type of connections are the T and Y joints, which both include one brace member. For T joints, the angle between the chord and the brace member is 90° (perpendicular). For Y joints, the angle between the chord and the brace member is unequal to 90° (inclined). X, K and N joints include two brace members. X joints consist of brace members that are located on opposite sides of the chord member and which transfers the force from one brace, through the chord member, to the opposite brace. The braces of X joints can be inclined or perpendicular to the chord member. K and N joints consist of two brace members located on the same side of the chord member. K joints have two inclined brace members, where N joints have one inclined brace and one brace that is perpendicular to the chord member. KT joints consists of three brace members and is a combination of a K and T joint. K, N and KT joints can be gapped or overlapped, this is an important parameter for the resistance of these joints.

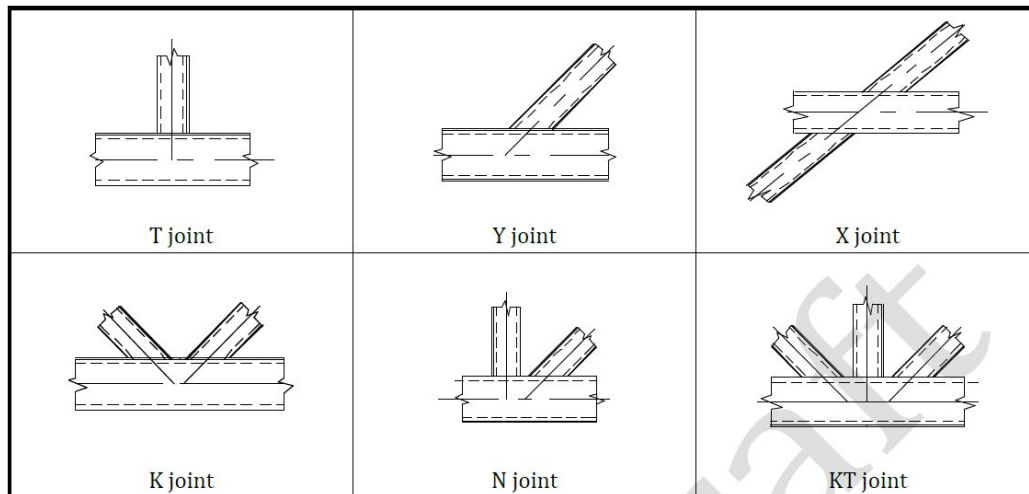


Figure 2.27: Types of uniplanar hollow section joints [19]

The classification of the joint of the above described types should be based on the method of force transfer, see Figure 2.28. The classification should not be based on the physical appearance of the joint. When the force from the brace is equilibrated by the beam shear force in the chord member, the joint is defined as T joint (brace perpendicular to the chord) or Y joint (inclined brace). When the brace forces (on one side of the chord member) are in equilibrium, within 20% of each other, the

joint is classified as K or N joint. When the brace force is transferred through the chord member to the brace member on the opposite side, it is classified as X joint.

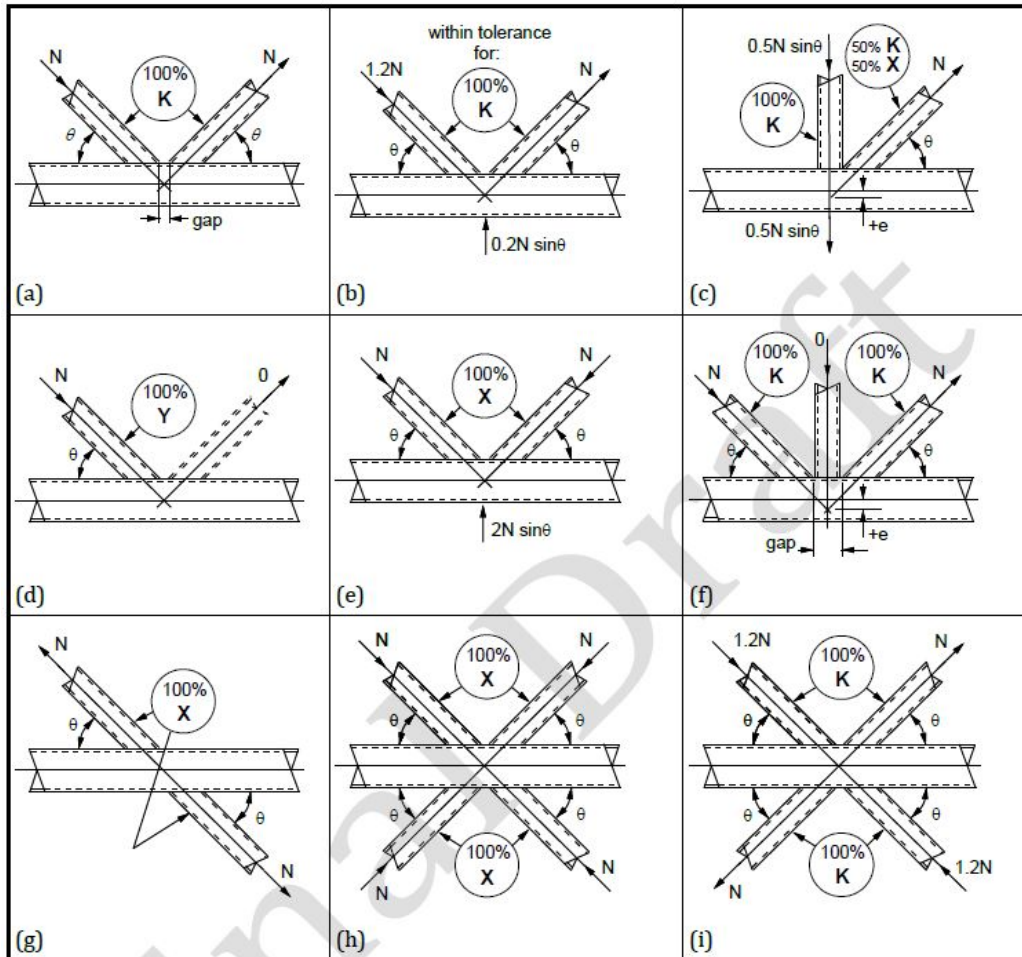


Figure 2.28: Joint classification based on force transfer [19]

2.4.1 Range of validity

The design equations proposed in the new version of Eurocode 3 part 1-8 are applicable for a certain range of validity. These range of validity equations are based on joint geometry parameters, see Figure 2.29. Index $i = 0$ is used for chord members, index $i = 1, 2$ are used for brace members. The X joint brace members used in the experiments consist of identical brace profiles for each joint. Therefore, both brace members are identified by index $i = 1$. The range of validity equations make use of certain non-dimensional parameters for RHS X joints, see equation 2.20, 2.21 and 2.22 [19].

$$\beta = \frac{b_1}{b_0} \quad (2.20)$$

$$\gamma = \frac{b_0}{2t_0} \quad (2.21)$$

$$\eta = \frac{h_1}{b_0} \quad (2.22)$$

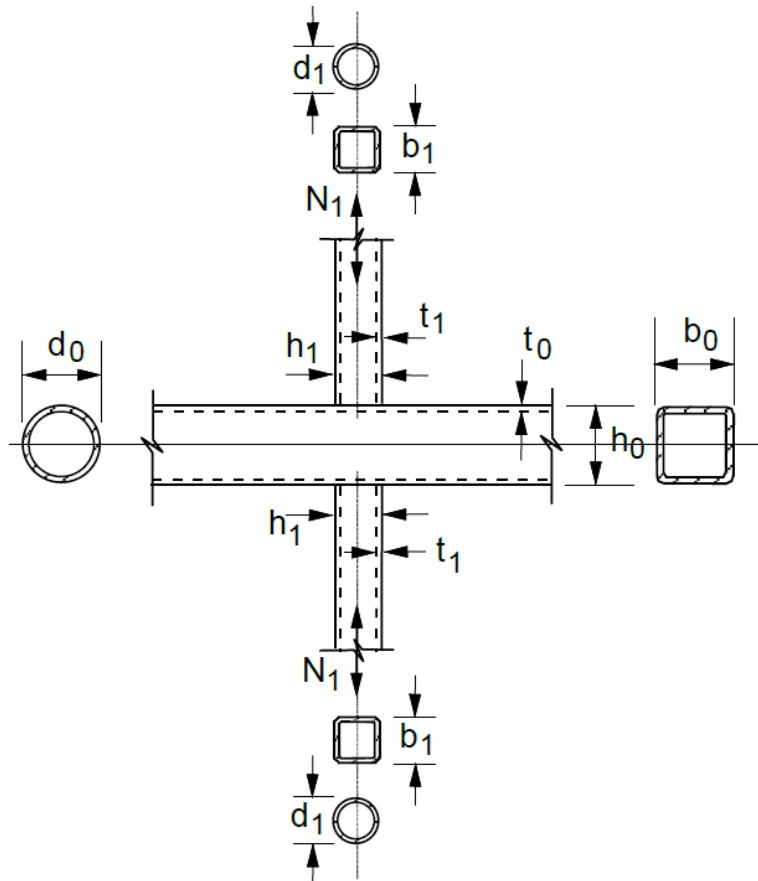


Figure 2.29: Joint parameters X joint [19]

Material

The new Eurocode includes steel grades S235 up to and including S700. UHSS are not included in the standard. The material factors for the different steel grades need to be taken into account, see Table 1.1. The design rules are applicable for both hot-finished hollow sections and cold-formed hollow sections conforming to EN10210 and EN10219, respectively.

Wall thickness

A minimum nominal wall thickness of 1,5 mm is required for the hollow section members.

Cross section classification

For compression members, the cross-section classification needs to be Class 1 or Class 2 according to Table 5.2 of EN1993-1-1:2005 [14].

Brace angle (θ_i)

To make sure that proper welds can be made, the brace angle should be at least 30° . Angles lower than 30° are allowed, but with the condition that the fabricator must show that proper welds can be made.

Gap (g)

The gap between two braces should be larger than the summation of the thickness of both braces ($t_1 + t_2$), see Figure 2.31 for definition gap (g). This space is required to make sure that proper welds can be made. This requirement is not relevant for X joints.

Overlap (λ_{ov})

The overlap in overlap type joints should be at least 25% to make sure that the shear transfer between the braces is sufficient. The brace member with the lowest $t_i f_{yi}$ -value should overlap the other brace member, in the case of different thicknesses and/or strength grades. In the case of brace members with different widths, the narrower brace member should overlap the wider one. This requirement is not relevant for X joints.

End requirements open chord

When a chord member is not connected to another member, an end distance is required of at least $\frac{2+\gamma}{10} d_0$, with an minimum value of $2,5d_0$. In the case of RHS, the largest value of b_0 or h_0 should be used as d_0 . Other requirements are applicable if a cap plate with a minimum thickness of $1,5t_0$ is welded to the open end. In that case the minimum distance has to be $0,5b_0(1-\beta)$ or $0,5d_0(1-\beta)$, see Figure 2.30.

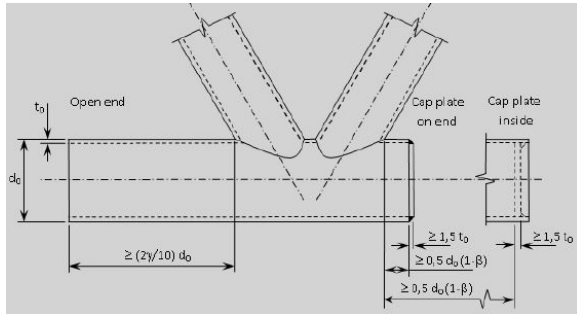


Figure 2.30: Open end requirements [19]

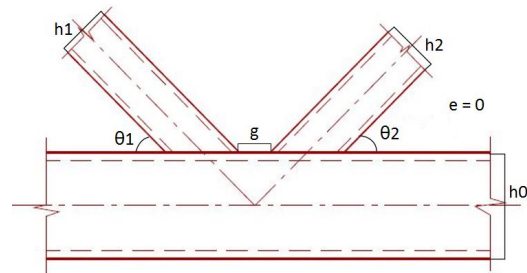


Figure 2.31: Eccentricity of joints [19]

Eccentricity (e)

The definition of the eccentricity can be seen in Figure 2.31. The eccentricity has to be in the range of $-0,55h_0 \leq e \leq 0,25h_0$ in the case of a RHS chord. In the case of a CHS chord the h_0 is replaced by d_0 . The value of the eccentricity can be determined by Equation 2.23 [61]. At an overlap joint,

the meeting point of the centre line of the braces is above the centre line of the chord member, this is defined as a negative eccentricity. At gap joints it is the other way around, the eccentricity is defined as positive. If the eccentricity is within this limits for steel grades below S460, the moments due to the eccentricity may be neglected. Otherwise the moments have to be included in the joint design.

$$e = \left(\frac{h_1}{2 \sin \theta_1} + \frac{h_2}{2 \sin \theta_2} + g \right) \frac{\sin \theta_1 \sin \theta_2}{\sin(\theta_1 + \theta_2)} - \frac{h_0}{2} \quad (2.23)$$

Range of validity equations

An overview of the range of validity requirements for welded T, Y and X joints between CHS or RHS brace members and RHS chord members is presented in Table 2.10. In this overview both conditions from Table 9.10 and 9.11 according to the new Eurocode [19] are summarised. The requirements for K joints are excluded because they are not in the scope of this research. The slenderness ratio (b/t) is limited. If these limits are met, the local buckling failure can be neglected.

There are different options possible regarding the range of validity and design tables that should be used:

1. RHS chord and braces: if the requirements of Table 2.10A are met, use the design equations according to Table 2.13.
2. SHS chord and braces: check requirements Table 2.10A and additional requirements of Table 2.10B. Following options are possible:
 - (a) If the conditions of both Tables 2.10A and 2.10B are met, use the design equations according to Table 2.12.
 - (b) If the conditions of only Table 2.10A are met, use the design equations according to Table 2.13.

Table 2.10: Range of validity conditions for T, Y or X joints (A is Table 9.10 and B is Table 9.11 from EN1993-1-8:2020 [19])

A		
General	General	$\theta_i \geq 30^\circ$ $e/h_0 \leq 0,25$
General	RHS braces	$b_i/b_0 \geq 0,1 + 0,01b_0/t_0$, but $\geq 0,25$ $0,5 \leq h_i/b_i \leq 2,0$
	CHS braces	$d_i/b_0 \geq 0,1 + 0,01b_0/t_0$, but $\geq 0,25$ $0,25 \leq d_i/b_0 \leq 0,80$
RHS chord	Tension	$b_0/t_0 \leq 35$ $h_0/t_0 \leq 35$
	Compression	Class 1 and 2 $b_0/t_0 \leq 35$ $h_0/t_0 \leq 35$
RHS braces	Tension	$b_i/t_i \leq 35$ $h_i/t_i \leq 35$
	Compression	Class 1 and 2 $b_i/t_i \leq 35$ $h_i/t_i \leq 35$
CHS braces	Tension	$d_i/t_i \leq 50$
	Compression	Class 1 and 2 $d_i/t_i \leq 50$
Conditions met?	Yes, apply rules Table 2.13	
B		
SHS braces and chord		$b_i/b_0 \leq 0,85$
Add. conditions met?	Yes, apply rules Table 2.12 No, apply rules Table 2.13 if conditions Table 2.10A are still met	

2.4.2 Failure modes

If all the requirements of the hollow section joints are met, the new version of the Eurocode provides tables with the possible failure modes that can occur. An overview of the possible failure modes is presented in Figure 2.32. The standard provides design equations for each failure mode to determine the resistance of the joint.

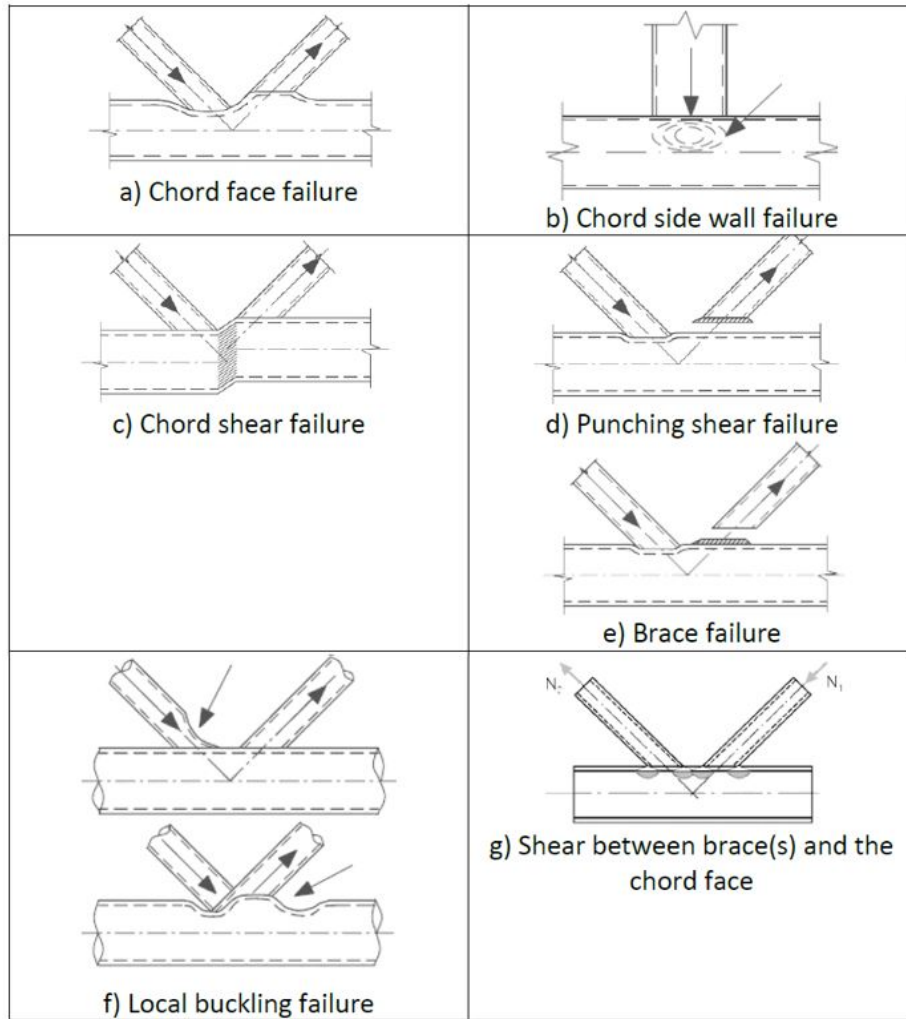


Figure 2.32: Failure modes of joints between RHS brace members and RHS chord members [19]

2.4.3 Design equations

A function in the design equations of chord face failure (CFF) and chord side wall failure (CSWF) is the chord stress function Q_f . The chord stress function can be determined according to Table 2.11. The parameter is related to the maximum chord load and depends on the chord stress parameter n for RHS, see Equation 2.24.

Table 2.11: Chord stress function [19]

Chord stress	Chord in compression: $n < 0$	$Qf = (1 - n)^{C_1}$, but $Qf \geq 0,4$ $C_1 = 0,6 - 0,5\beta$ for X joints
	Chord in tension: $n \geq 0$	$Qf = (1 - n)^{C_1}$, but $Qf \geq 0,4$ $C_1 = 0,10$

$$n = \frac{N_{0,Ed}}{A_0 f_{y0}} + \frac{M_{ip,0,Ed}}{W_{ip,pl,0} f_{y0}} + \frac{M_{op,0,Ed}}{W_{op,pl,0} f_{y0}} \quad (2.24)$$

Table 2.12: Axial resistance welded T, Y and X joints between SHS braces and SHS chords (Table 9.12 of EN1993-1-8:2020 [19])

Chord face failure: $\beta \leq 0,85$	$N_{1,rd} = C_f \frac{f_{y0} t_0^2}{\sin \theta_1} \left(\frac{2\eta}{(1-\beta) \sin \theta_1} + \frac{4}{\sqrt{1-\beta}} \right) \frac{Q_f}{\gamma_{m5}}$
---------------------------------------	---

Table 2.13: Axial resistance welded T, Y and X joints between RHS braces and RHS chords, (Table 9.13 of EN1993-1-8:2020 [19]) (1)

Chord face failure: $\beta \leq 0,85$	$N_{1,rd} = C_f \frac{f_{y0} t_0^2}{\sin \theta_1} \left(\frac{2\eta}{(1-\beta) \sin \theta_1} + \frac{4}{\sqrt{1-\beta}} \right) \frac{Q_f}{\gamma_{m5}}$
Chord side wall failure: $\beta = 1,0$ (2)	$N_{1,rd} = \frac{f_b t_0}{\sin \theta_1} \left(\frac{2h_1}{\sin \theta_1} + 10t_0 \right) \frac{Q_f}{\gamma_{m5}}$ for tension: $f_b = f_{y0}$ for compression: $f_b = \chi f_{y0}$, for T and Y joints $f_b = 0,8\chi f_{y0} \sin \theta_1$, for X joints
Brace failure	$N_{1,rd} = \frac{C_f}{\gamma_{m5}} f_{y1} t_1 (2h_1 - 4t_1 + 2b_{eff})$ $b_{eff} = \frac{10}{b_0/t_0} \frac{f_{y0} t_0}{f_{y1} t_1} b_1$, but $b_{eff} \leq b_1$
Punching shear failure: $\beta \leq (1 - 1/\gamma)$	$N_{1,rd} = \frac{C_f}{\gamma_{m5}} \frac{f_{y0} t_0}{\sqrt{3} \sin \theta_1} \left(\frac{2h_1}{\sin \theta_1} + 2b_{e,p} \right)$ $b_{e,p} = \frac{10}{b_0/t_0} b_1$, but $b_{e,p} \leq b_1$

(1) For X joints with $\cos \theta_1 > h_1/h_0$, check chord shear resistance with $\alpha = 1$ (Table 9.14)

(2) For $0,85 < \beta < 1,0$, linear interpolation may be applied between the governing resistances at $\beta = 0,85$ and $\beta = 1,0$

2.5 Previous research HSS hollow section joints

Lan and Chan [37] described a comprehensive overview of the recent research regarding hollow section joints made out of HSS.

Feldmann et al. [23] investigated the material reduction factors applicable for hollow section joints. Steel grades S500, S700 and S960 are investigated. During the time of this research, 2016, the applicable reduction factor for steel grades of S500 and above was 0,8. The newly proposed Eurocode makes a distinction between the reduction factors for steel grades S500 and S700, respectively 0,86 and 0,8. Steel grade S960 is excluded from the new standard. Welds are designed to be non-critical. Noteworthy is that in the S500 experiments, the failure modes obtained in the experiments often differed from the predicted failure modes according to the Eurocode [16]. The recommendations of the research can be seen in Table 2.14. It is concluded that steel grade S500 results in safe behaviour for room temperature and low ambient temperatures, which explains the recommended reduction factor of 1,0. Steel grade S700 showed an absence of deformation capacity which results in the 0,9 reduction factor. Steel grade S960 results in a recommended reduction factor of 0,8 and it is concluded that the material is not safe under low ambient temperatures. S960 joints should only be used under room temperature conditions to guarantee the safety.

Table 2.14: Recommended reduction factors according to Feldmann et al. [23]

Steel grade and reduction factor new EC	Proposed reduction factors for tested steel grades	
	Room temperature	Low temperature
S500 (0,86)	1,0	1,0 (-40°C)
S700 (0,8)	0,9	0,9 (-30°C)
S960 (0,8)	0,8	-

Becque and Wilkinson [5] executed an experimental research regarding the capacity of C450 cold-formed RHS T and X joints. The study is aimed to look at the influence of the cold-working process (increased yield stress, reduced ductility that can be seen in the strain at rupture, more rounded stress-strain curve, uneven work-hardening, increased residual stresses) on the static capacity of the joints. The material factor of 0,9 is also evaluated (for steel grades between S355 and S460). Welds are designed to be non-critical by using full penetration butt-welds with superimposed fillet welds. In the research T and X joints are tested that are located in- and outside the limits of the CIDECT guide. The newly proposed Eurocode prescribes material factors and a restriction that f_y should not exceed $0,8f_u$ in case of chord punching shear failure and brace failure (brittle failure modes). In the paper the CIDECT rules are applied and they prescribe the $0,8f_u$ -limit for all failure modes. The paper results in experimental evidence that for failure modes governed by fracture, reduction factors should be applied. On the other hand is there no experimental evidence for the 0,9 reduction factor and the limitation on the yield strength for ductile failure modes (chord face plastification and side wall buckling).

Kim [35] investigated HSS RHS X joints loaded under compression. The nominal yield stress of the joints is 650 MPa. Chord side wall buckling and chord face plastification are analysed. The tests showed that the design strength, according to EN1993-1-8:2005 [14], without application of the reduction factor is exceeded in all tests.

Pandey and Young [49] investigated the static capacity and load-deformation behaviour of T joints made of cold-formed S960 RHS joints. Aim of the research is to assess the applicability of the current EN1993-1-8:2005 and CIDECT rules for UHSS. The T joints are tested under axial compression. A wide range of test specimens with different geometrical parameters (β , τ , 2γ) are used. The results of the experiments are compared to the resistances given by the Eurocode 3 and CIDECT formulas, with and without the appropriate reduction factors for HSS. It is shown that the current design equations are not able to provide accurate results. For small β -values, chord face failure occurred and the results are unconservative. In this case is the deformation limit governing. For β -values between 0,74 and 1, a scatter of results is observed. The failure is mostly a combination of the chord face failure and chord side wall failure. The load-displacement curve mostly showed a gentle peak, but is still mostly governed by the deformation limit. For β is equal to 1, the results showed conservative results. An increase in chord side wall slenderness (h_0/t_0) leads to an increase in the conservatism of the results. The load-displacement curves shows a clear peak and governs the strength of the joints. This research shows that there is no reduction factor required for equal width RHS T joints made of S960 steel loaded under compression, when the current Eurocode formula is applied. However, a clear reduction factor is required in the case of small β -values. Possible reasons for this unconservatism is the reduced strain hardening of HSS and the large chord face deformation. These results show the clear influence of the β -factor on the design values according to the current Eurocode equations in relation to the experimental results.

Pandey and Young [48] also conducted a research regarding cold-formed S960 RHS X joints. The braces are loaded under axial compression. The results from the experiments are compared to the EN1993-1-8:2005 and the CIDECT design rules excluding the reduction factors. It is shown that for small β -values the design rules according to Eurocode and CIDECT are unconservative. The results become conservative for an increase in β -value. An increase in chord side wall slenderness (h_0/t_0) results in an increase in the conservatism for X joints with a β -value of 1 (equal width RHS). These observations are in line with the conclusions obtained in the investigation regarding the T joints [49]. The design equations for T and X joints in the design guides (Eurocode and CIDECT) are identical.

Mohan et al. [45, 46] numerically investigated the joint strength of axially loaded RHS T, X, K and N joints made out of C450 steel. They concluded that, without applying the reduction factor and the yield strength limit, the numerical joint strength is generally higher than the design strength according to the CIDECT design guide.

Wardenier and Puthli [62] conducted a survey regarding the available data for hollow section joints made of steel grades S420 up to and including S700. Regarding the RHS X joints loaded in tension, they noted that there are contradicting conclusions. They mentioned the research of Björk and Saastamoinen [8], who investigated 19 X joints made of cold-formed S420 steel. They concluded that there is no reason for a reduction factor below 1,0, this indicates that the design equations according to EN1993-1-8 are valid. Another research conducted by Tuominen and Björk [59] regarding S420 and S460 X joints resulted in the conclusion that there is no need for a material reduction factor. Contradicting are the above mentioned results according to Becque and Wilkinson [5], who proposed a reduction factor of 0,9 and a yield limit of $f_y \leq 0,8f_u$ for fracture based failure modes of C450 steel. They proposed a reduction factor of 1,0 for ductile based failure modes, see page 33.

Chapter 3

Coupon experiments

To obtain the material properties of the HSS, a total of 17 coupon experiments are conducted. These can be divided into two groups of experiments of 9 and 8 specimens. The first group of 9 specimens are extracted from additionally ordered tubular sections made of steel grades S500 and S700. The second group of 8 specimens are extracted from the full scale X joint specimens from the end of the chord member after the X joint experiment has taken place. These are made out of steel grades S355 and S500. The procedure and results of the first group of experiments will be discussed extensively. The second group of experiments is presented in section 3.7.

Table 3.1: Coupon geometry first group

	Steel grade	t [mm]	w [mm]	A [mm ²]	e [mm]	Side in cross-section
T63-A	S500	7,77	19,93	154,82	(1)	Adjacent
T63-B	S500	7,81	19,82	154,76	(2)	Opposite
T63-C	S500	7,80	19,90	155,22	3,95	Opposite
T93-A	S700	7,81	19,92	155,58	9,93	Adjacent
T93-B	S700	7,81	20,02	156,36	10,17	Adjacent
T93-C	S700	7,82	19,93	155,85	10,12	Adjacent
T103-A	S700	9,84	20,07	196,89	9,15	Adjacent
T103-B	S700	9,83	20,00	196,60	9,29	Adjacent
T103-C	S700	9,80	20,29	198,84	7,45	Opposite

(1) Complex geometry, will be discussed in FEM-section 3.9

(2) No initial eccentricity

The coupon specimens are extracted from cold-formed tubular RHS by waterjet cutting. The lay-out of the first group of coupon specimens is visible in Figure 3.1. The coupon specimens of the first group can be divided into three series: T63, T93 and T103. Each series consists of three specimens

(A, B and C). T63-series consists of steel grade S500 with a thickness of 8 mm, see Figure 3.2. T93-series consists of steel grade S700 with a thickness of 8 mm. T103-series consists of steel grade S700 with a thickness of 10 mm. Table 3.1 represents an overview of the test program of the first group with the following measured dimensions: thickness (t), width gauge section (w), cross-sectional area (A) and initial eccentricity (e). The initial eccentricity is a result of the residual stresses that occur in cold-formed tubular sections, details are provided in Section 3.1. The exact location of each coupon specimen in the cross-section is relevant and is presented in Table 3.1. The coupons are extracted from the centre of the adjacent or opposite side of the cross-section in relation to the side with the longitudinal weld.

The coupons are tested in a MTS hydraulic controlled testing machine. The loading rate used in the experiments is dependent on the elastic or plastic stage. The elastic loading rate used is 0,015 mm/s. For the coupon specimens made out of S500 steel (T63-series), the elastic loading rate of 0,015 mm/s is doubled twice to a final loading rate of 0,06 mm/s in the plastic stage. For the S700 specimens (T93- and T103-series), the elastic loading rate of 0,015 mm/s is doubled to a final loading rate of 0,03 mm/s in the plastic stage. This is in line with the recommendations of the standard [12].

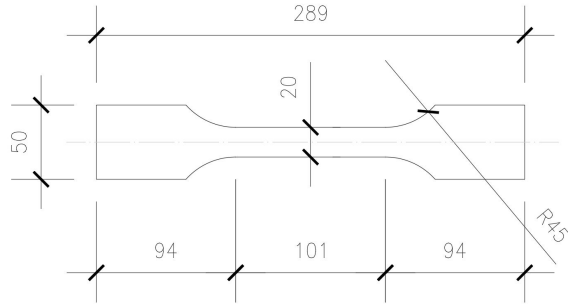


Figure 3.1: Lay-out coupon specimens first group



Figure 3.2: Coupon specimens T63-series

The original gauge length (L_0) is dependent on the cross-sectional area (A_c) of the coupon specimen, see Equation 3.1 [12].

$$L_0 = 5,65\sqrt{A_c} \quad (3.1)$$

The gauge width is 20 mm for all the specimens of the first group. The thickness for the T63- and T93-series is 8 mm, which results in an initial gauge length of 70 mm. The thickness for the T103-series is 10 mm, which results in an initial gauge length of 80 mm. The second group of coupons is designed in such a way, thickness of 6 mm and width of 13 mm, that the gauge length is equal to 50 mm, which corresponds to the range of the extensometer. The work presented below is based on an initial gauge length of 50 mm, this is due to the range of the extensometer for the first group of experiments and is not according to the standard [12]. Section 3.6 presents the material property for one of the specimens of each series based on the correct initial gauge length.

3.1 Curvature coupon specimens

The coupon specimens are extracted from cold-formed tubular RHS sections. Due to the residual stresses that occur in the sections, an initial curvature is observed in the coupon specimens. This curvature is defined by the initial eccentricity e , see Figure 3.3. The initial curvature resulted in problems with the fitting of the coupon specimens into the test machine. To overcome this problem, the grip section of the coupon specimen is bended by hand. The procedure visible in Figure 3.4 is used. First, the coupon specimen is clamped into a vice with only the grip section sticking out of the vice at the bottom. Then, the grip section is bended by hand, see right part Figure 3.4. Both grip sections are bended by this approach. This approach is applied to make sure that the properties and initial curvature of the gauge section remained untouched.

The curvature of the specimens is measured by the initial eccentricity as defined in Figure 3.3, the measurements are presented in Table 3.1. The T63-series is bended by the company who executed the waterjet cutting. This resulted in a complex geometry for specimen T63-A, this will be discussed in the finite element section 3.9. The gauge length of specimen T63-B is identified as straight.

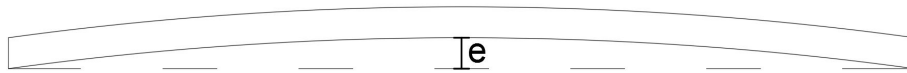


Figure 3.3: Initial curvature coupon specimens



Figure 3.4: Bending of the coupon grip section

3.2 Measuring methods

Before explaining which measuring methods are applied. It is important to define the orientation of the coupon specimen that is used in the test machine. Due to the curvature of the specimens, each specimen has a convex and concave side, see Figure 3.5.



Figure 3.5: Definition convex and concave side coupon specimen

Different measuring methods are adopted during the experiments. First of all, strain gauges of TML (FLAB-6-11) with a gauge length of 6 mm are applied for all the A- and B-specimens of each series. The strain gauges are not applied for the C-specimens. The strain gauges are applied on both the convex and concave side of the coupons in the centre of the gauge section, see 'SG' in Figure 3.6. The main reason for applying the strain gauges is proper measurement of the modulus of elasticity.

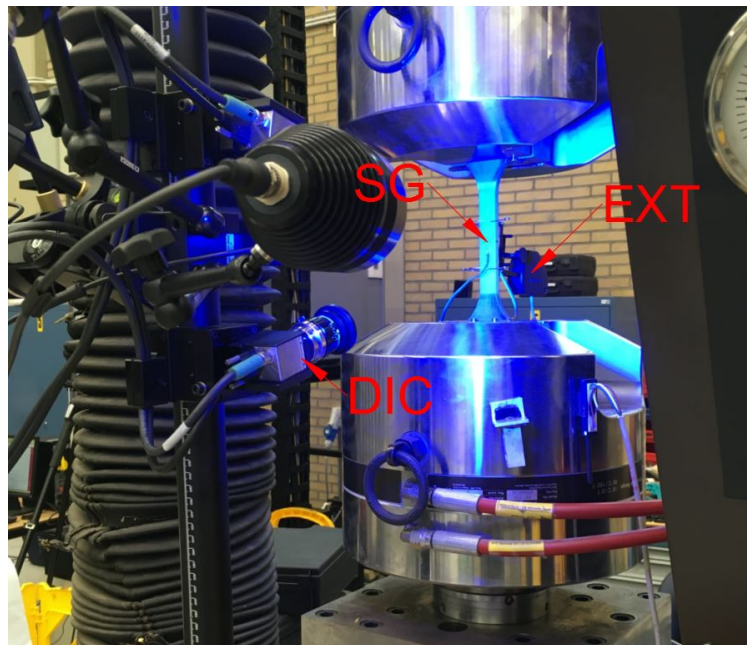


Figure 3.6: Measuring methods coupon experiment

Secondly, digital image correlation (DIC) is used to measure the strains and displacements on the surface of the coupon specimen. For the first experiment conducted, T93-A, only 2D DIC was available at that moment. Due to the out-of-plane deformation during the experiment, which is a result of the initial curvature of the coupon specimen, it is concluded that 3D DIC is more suitable. Therefore, 3D DIC is applied for all the other coupon specimens. The 3D DIC camera is positioned in such a way that it fully captures the coupon side facing the DIC camera, see Figure 3.6. There is a distinction made between which coupon side, convex or concave, is facing the DIC camera for specimens A, B and C:

- A : convex side facing the DIC camera;
- B : concave side facing the DIC camera;
- C : convex side facing the DIC camera.

The third measuring method is the application of an extensometer. The initial range of the extensometer is 50 mm. This range is not fixed to exactly 50 mm. Therefore, the distance between the clips of the extensometer is measured after the execution of the experiment, when the DIC data is processed through the GOM Correlate software. The extensometer is indicated with 'EXT' in Figure 3.6.

3.3 Modulus of elasticity

To obtain the modulus of elasticity, unloading and reloading is applied when the apparent yield of the coupon specimen appears during the experiments, this can be seen in Figure 3.7 which represents the stress-strain curve of coupon T93-B based on the strain gauges (SG) up to the moment that the strain gauges are broken. The total force is measured by the computer that controls the MTS test machine (MP3) and is converted to stresses by dividing it with the measured initial cross-sectional area. The strain measurements of the strain gauges and extensometer is directly linked to the MP3 force measurement. The approach of unloading and reloading is applied to eliminate the effects of the initial curvature.

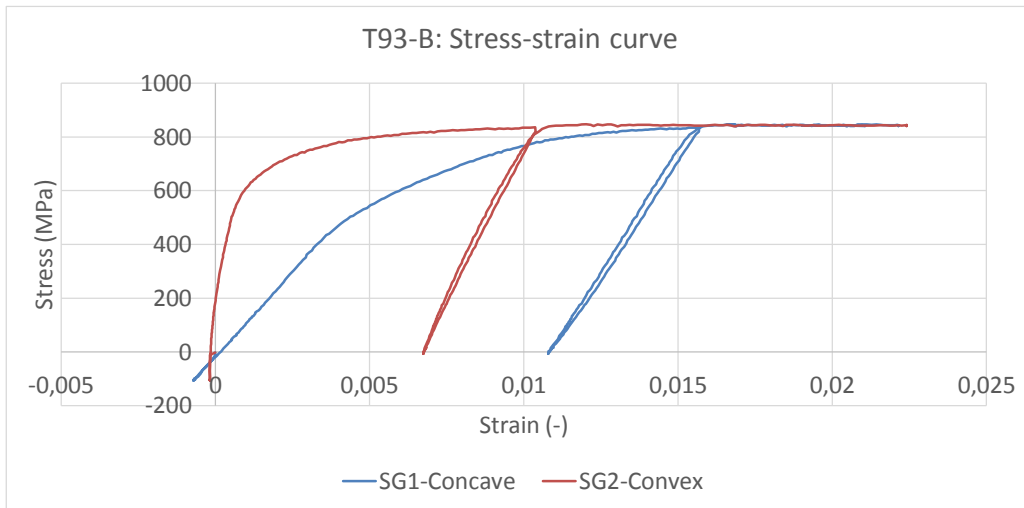


Figure 3.7: Stress-strain curve obtained from strain gauges (T93-B)

The results from strain gauges is used in the reloading part of the stress-strain curve to determine the Young's modulus. The linear part between 100 and 600 MPa is plotted in Figure 3.8. The purple line represents the average value of the strain measured by the strain gauges. A linear trend line is used to determine the slope of the purple line. This results into an E-modulus of 207 GPa for T93-B.

As mentioned before, there are no strain gauges applied for the C-specimens. For those coupon specimens, the E-modulus is determined by using the DIC data. It has to be noted that the recorded

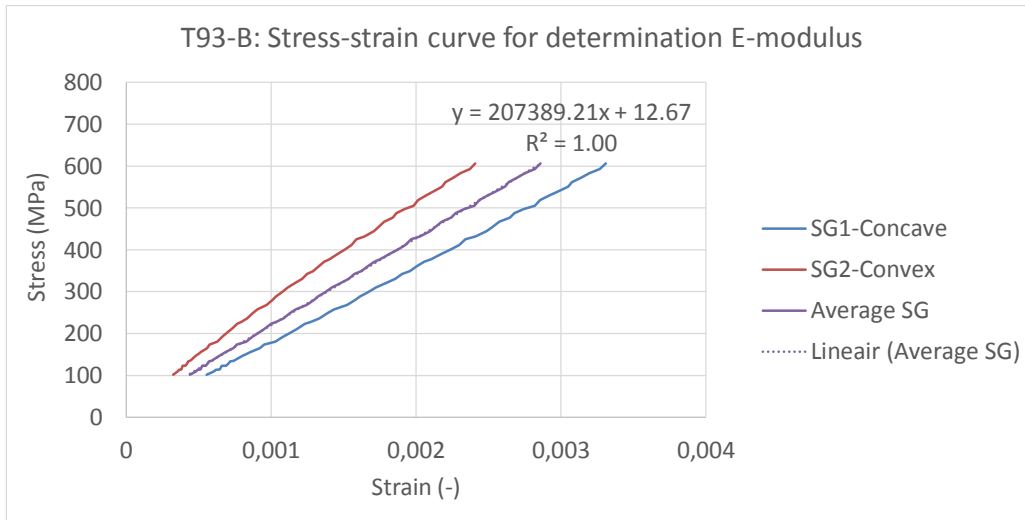


Figure 3.8: Stress-strain curve reloading part for determination E-modulus (T93-B)

force from DIC is less accurate than the recorded force from MP3. To eliminate the effects of the initial curvature, the reference stage is set at the onset of reloading. Then, 6 major strain points are defined to extract the strain alongside the specimen, see Figure 3.9 for the points selected for specimen T93-C. These major strain points are selected at the location where final fracture is occurring. There is chosen to average the data of 6 points to minimize the scattering in the data. The same procedure as shown in Figure 3.8 is applied to determine the E-modulus based on the reloading part of the DIC stress-strain curve.

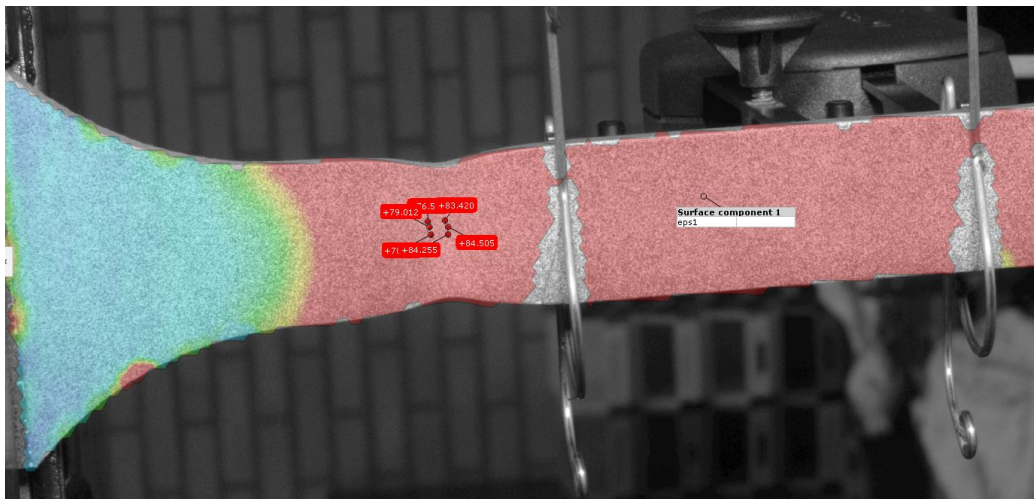


Figure 3.9: E-modulus based on major strain points DIC (T93-C)

The results of the E-modulus are presented in Table 3.2. For T63-A there is no reloading applied during the experiment. Therefore, the E-modulus of T63-B is assumed for T63-A. The E-modulus

Table 3.2: E-modulus results

[GPa]	T63-A	T63-B	T63-C	T93-A	T93-B	T93-C	T103-A	T103-B	T103-C
Strain gauges	(1)	190	-	195	207	-	196	197	-
DIC	-	204	197	209	194	197	193	211	198
Used E	190	190	197	195	207	197	196	197	198

(1) No reloading applied in the experiment, value of T63-B is assumed

is based on the value obtained by strain gauges if this value is available. Otherwise, the result based on DIC is used.

It is observed in Figure 3.7 that there is a difference between the unloading and reloading part of the stress-strain curve for both the concave and convex curves. It is observed that the concave curve (blue curve) seems to bend off a little bit before the specimen is fully unloaded. This is less the case for the convex curve (red curve). This phenomenon is noted in all experiments where unloading and reloading is applied. The strain difference between the curves is larger for the concave side in comparison to the results from the convex side. The offset between the unloading and reloading part of the curve can be explained by Figure 3.10. The small bend can be explained by the phenomenon that the specimen is not fully contracted at the moment the specimen is fully unloaded. This additional contraction after the load is removed, is due to effect that grains can produce small amount of plastic strains that are released after the load is fully removed [40]. The concave side undergoes more plastic deformation than the convex side, this explains the larger offset between the unloading and reloading curve for the concave side.

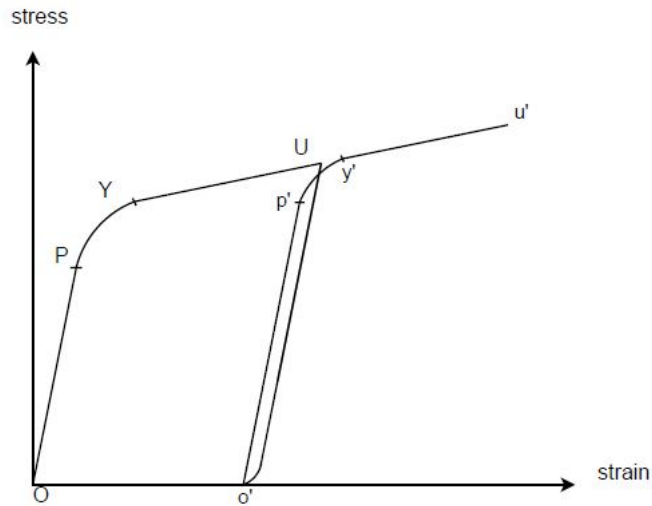


Figure 3.10: Offset unloading and reloading curve coupon experiment [40]

3.4 Yield strength

The yield strength is determined based on the 0,2% proof stress. The 0,2% proof stress is defined as the line that starts at 0,002 strain and linearly increases by the slope based on the obtained E-modulus (Table 3.2). The intersection between the 0,2% proof stress line and the experimental data is defined as the yield strength, see Figure 3.11. For specimen T103-A this resulted in a yield strength of 732 MPa.

For the experimental data, an assessment is made of the available data of each specimen. For the A- and B-specimens the average data of the strain gauges is used. For the C-specimens the data from DIC and extensometer is averaged, evidence for this approach is showed in the next indentation. An overview of the results is given in Table 3.3. This table shows the obtained yield strength (σ_y), E-modulus and the strain at yielding (ϵ_y).

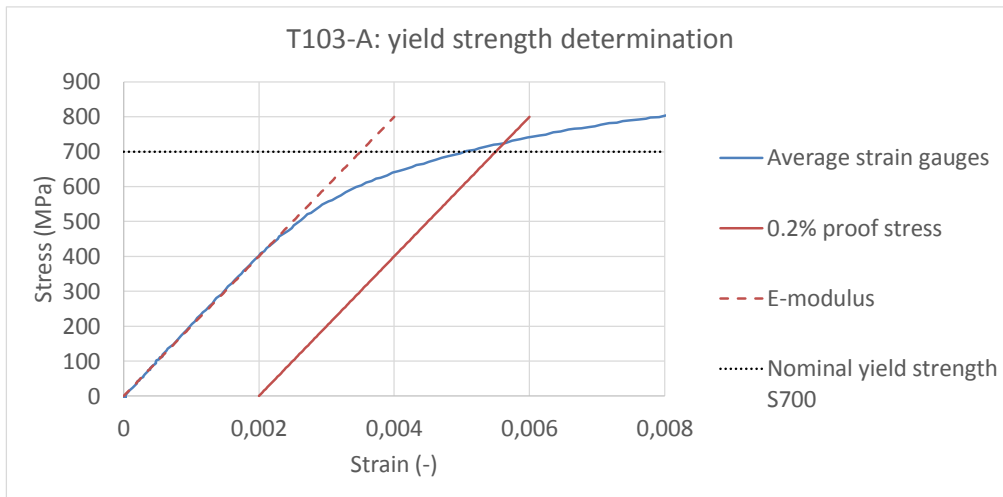


Figure 3.11: Yield strength determination (T103-A)

Table 3.3: Yield strength results

	T63-A	T63-B	T63-C	T93-A	T93-B	T93-C	T103-A	T103-B	T103-C
σ_y [MPa]	559	565	563	708	724	724	732	732	741
E [GPa]	190	190	197	195	207	197	196	197	198
$\epsilon_y = \sigma_y/E$ [-]	0,003	0,003	0,003	0,004	0,003	0,004	0,004	0,004	0,004

As mentioned before, the data is averaged from both strain gauges. One of the strain gauges is located on the convex side and one strain gauge is located on the concave side. By averaging the data from both sides the influence due to curvature is eliminated. However, for the C-specimens there are no strain gauges applied. During the data processing, it is observed that the results from the extensometer are in line with the results from the strain gauge located on the coupon side that is

facing away from the DIC camera. For specimen T93-B the concave side is facing the DIC camera. Figure 3.12 shows the good agreement between the strain gauges and the DIC and extensometer results. The strain gauge on the convex side is in agreement with the extensometer results. The results from the concave side are in line with the DIC results. This means that the extensometer is recording the data from the coupon side that is facing away the DIC camera. Therefore, the data from DIC and extensometer can be averaged if there are no strain gauges applied.

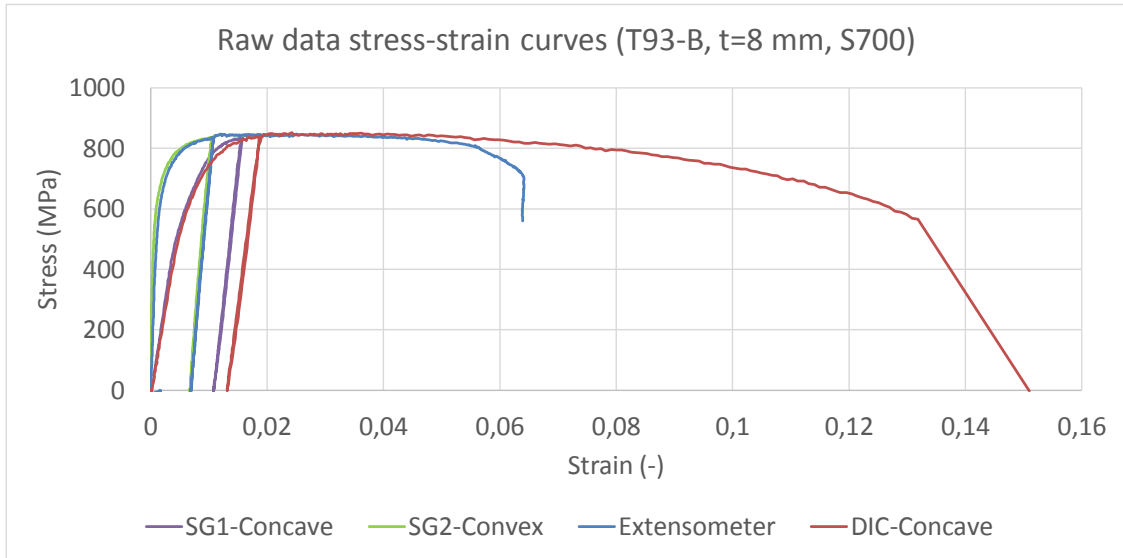


Figure 3.12: Stress-strain curves obtained from raw experimental data (T93-B)

3.5 Engineering stress-strain curves

The next step in the data processing is the engineering stress-strain curve. The elastic part of the engineering curve is based on the previous obtained yield strength, E-modulus and corresponding strain at yielding (Table 3.3). To eliminate the effects of the initial eccentricity on the results, the data from both sides of the coupon specimen is combined. However, 5 out of 9 of the coupon specimens of the first group resulted in failure outside the range of the extensometer, respectively specimens T93-A, T93-B, T93-C, T103-B and T103-C. Therefore, the raw experimental data obtained by DIC and extensometer is shifted to the determined yield point, see Figures 3.13 and 3.14 for the principle of the data shift. It is observed that the maximum strain shift is 1,4% of the fracture strain.

The 3D DIC results are processed in the GOM Correlate software. Firstly, the location of final fracture is determined. Based on the location of fracture, two data points are selected which have an initial distance of 50 mm, see Figure 3.15. The relative displacement between the data points is converted into strains by dividing it with the initial length between the data points. This approach is applied two times and the result is averaged to determine the strain obtained by DIC. As mentioned before, an initial gauge length of 50 mm is adopted in the determination of the stress-strain curves in this section which is not in line with the standard [12].

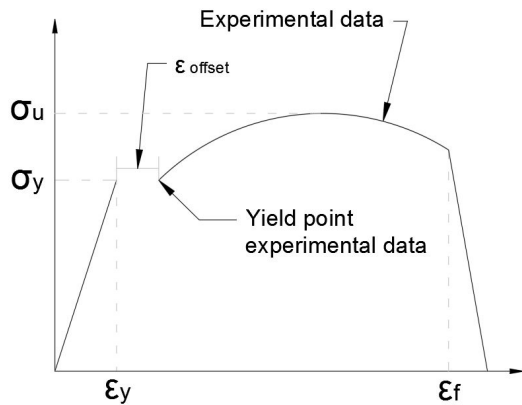


Figure 3.13: Experimental data shift to yield point

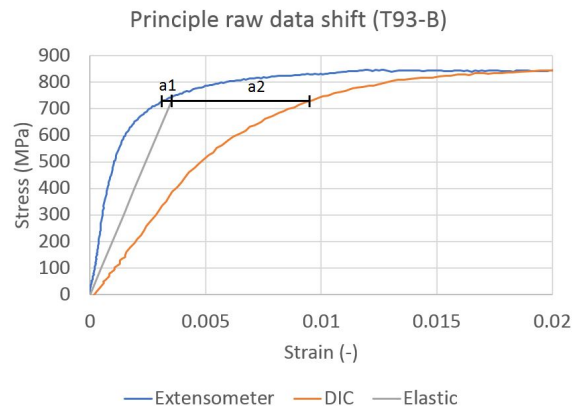


Figure 3.14: Data shift T93-B

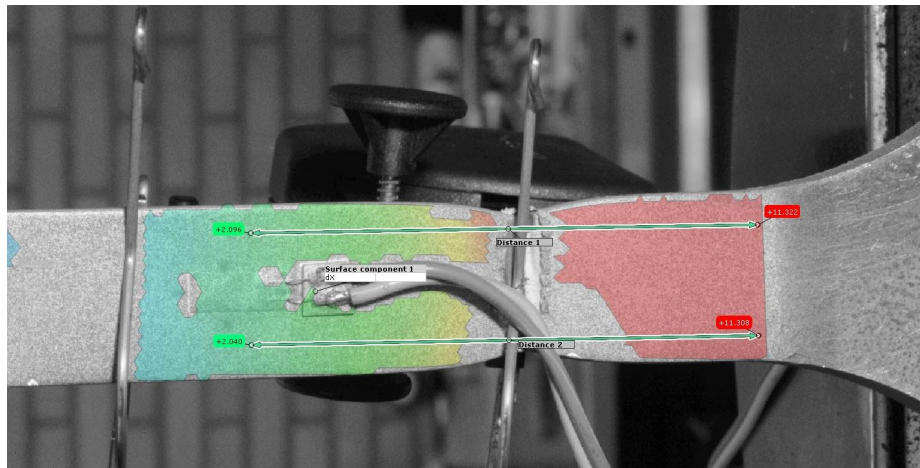


Figure 3.15: Data extraction DIC data from GOM Correlate (T93-B)

The extensometer measures the extension in the axial direction between the two clips of the extensometer. This data is converted into strains by dividing it with the initial length. The range of the extensometer is 50 mm.

The engineering stress-strain curves of T63-, T93- and T103-series are visible in respectively Figures 3.16, 3.17 and 3.18. The result based on extensometer data is shown with a dashed line, while the DIC data is shown with a solid line. An overview of the results from characteristic points of the engineering curves is presented in Table 3.4. σ_u represents the ultimate stress of the material and ϵ_f is the strain at fracture, see Figure 3.13 for definition σ_u and ϵ_f . The characteristic points are extracted from the engineering curves based on the extensometer (EXT) and DIC.

Important to note is that for specimen T93-A the result from 2D DIC is presented. Due to the

significant influence of the out-of-plane deformation on the 2D DIC results, only the data from the onset of reloading is extracted. It is assumed that the specimen is straight at this moment, which means that no additional out-of-plane deformation is occurring. The result is shown with the solid red line in Figure 3.17. The curve is shifted to the moment of reloading.

The average yield strength obtained is 562, 719 and 735 MPa for the T63-, T93- and T103-series, respectively. The average ultimate strength is 617, 850 and 883 MPa. The strain at fracture based on an initial length of 50 mm is 0,29, 0,15 and 0,17. The strain at fracture with the correct initial gauge length is discussed in Section 3.6.

Table 3.4: Overview results coupon experiments first group

	T63-A	T63-B	T63-C	T93-A	T93-B	T93-C	T103-A	T103-B	T103-C
Steel grade	S500	S500	S500	S700	S700	S700	S700	S700	S700
t [mm]	7,77	7,81	7,80	7,81	7,81	7,82	9,84	9,83	9,80
σ_y [MPa]	559	565	563	708	724	724	732	732	741
E [GPa]	190	190	197	195	207	197	196	197	198
σ_u (EXT) [MPa]	626	612	614	858	846	847	884	881	885
ϵ_f (EXT) [-]	0,31	0,24	0,30	-	-	-	0,17	-	-
σ_u (DIC) [MPa]	627	617	617	853	850	847	887	881	887
ϵ_f (DIC) [-]	0,29	0,29	0,29	0,15	0,16	0,15	0,18	0,17	0,17

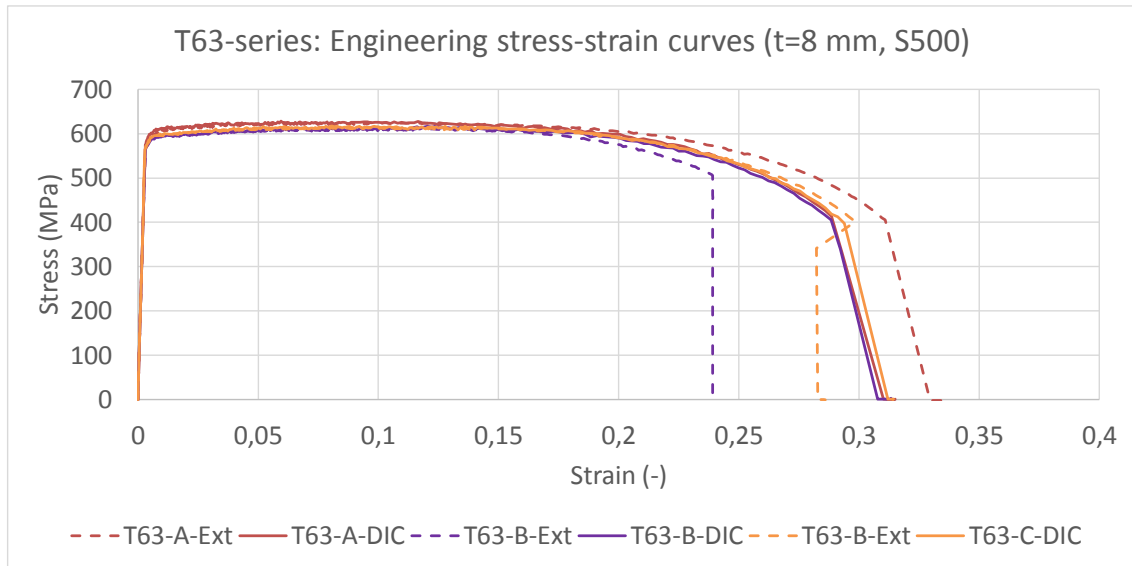


Figure 3.16: T63-series engineering stress-strain curves

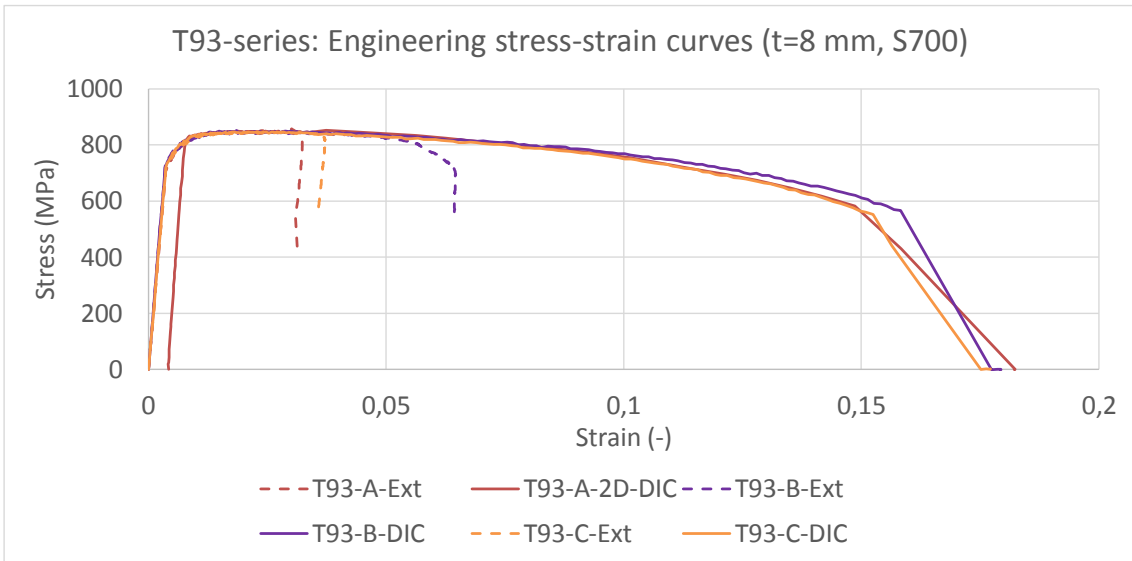


Figure 3.17: T93-series engineering stress-strain curves

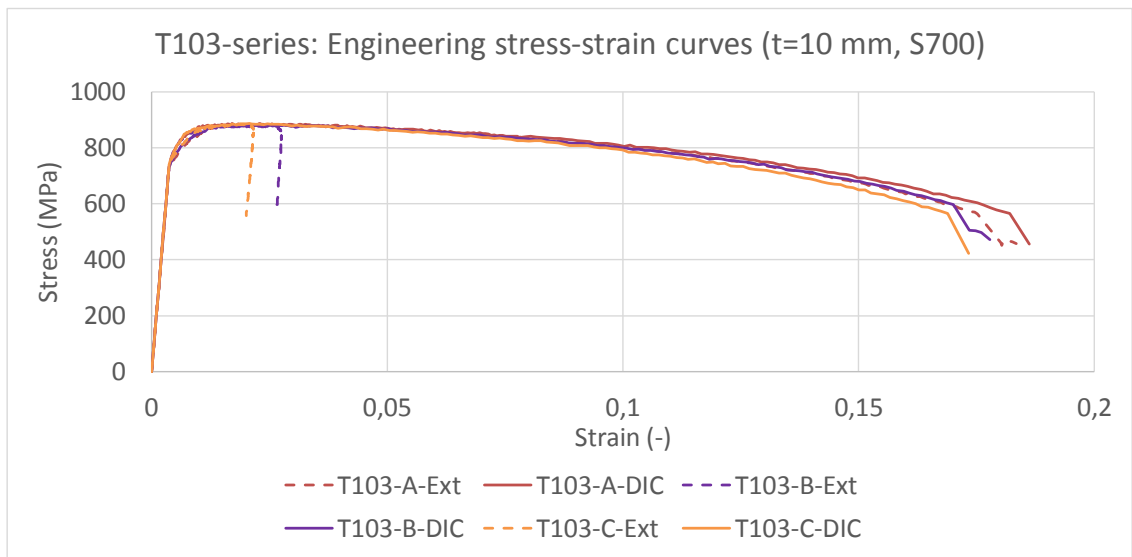


Figure 3.18: T103-series engineering stress-strain curves

3.6 Standard material property based on correct gauge length

The previously shown engineering stress-strain curves are based on an initial gauge length of 50 mm, which is not correct according to the standard [12]. It is essential that the fracture strain is checked according to the initial gauge length of the standard. For specimens T63-A, T93-B and T103-A the engineering stress-strain curves are obtained with the correct initial gauge length, respectively 70, 70 and 80 mm. The initial gauge length does not influence the results up to the point of necking. After the point of necking the influence of the initial gauge length becomes visible due to localization of the plastic deformation in a small area, see Figure 3.19 for the engineering stress-strain curve of specimen T63-A based on an initial gauge length of 50 and 70 mm. It is observed that with an increase of the initial gauge length, the ultimate strain becomes smaller. This effect is also noted in [32].

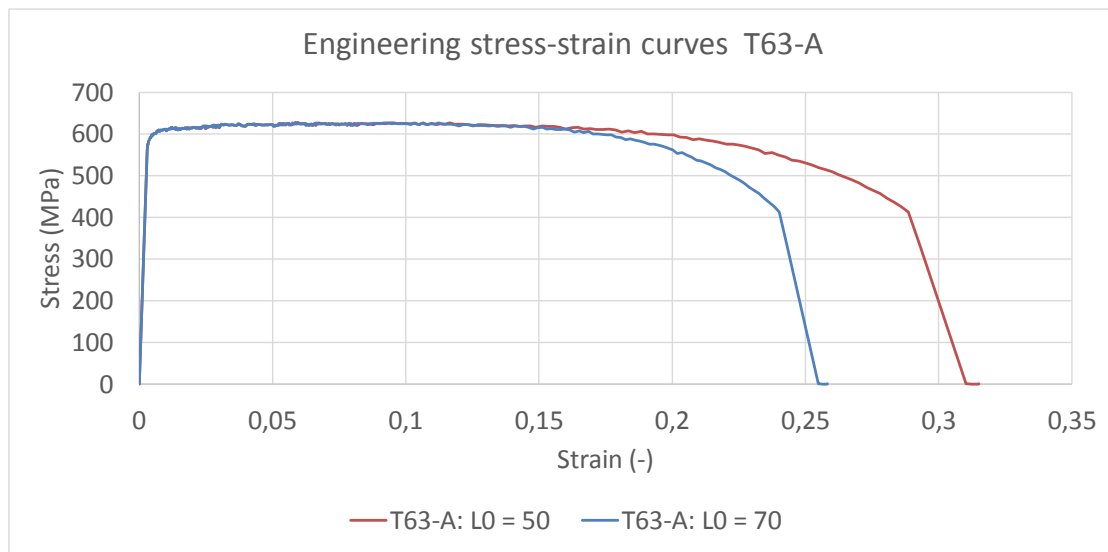


Figure 3.19: Influence initial gauge length on engineering stress-strain curve T63-A

Table 3.5: Overview results T63-A, T93-B and T103-A with correct initial gauge length

		T63-A	T93-B	T103-A
Steel grade		S500	S700	S700
E	[GPa]	190	207	196
σ_y	[MPa]	559	724	732
σ_u	[MPa]	626	846	884
$\epsilon_{f,50}$	[-]	0,287	0,157	0,181
$\epsilon_{f,70/80}$	[-]	0,243	0,126	0,128

The resulting engineering stress-strain curves with the correct initial gauge length for T63-A, T93-B and T103-A are presented in Figure 3.20. The characteristic values are presented in Table 3.5. Parameter $\epsilon_{f,50}$ is the strain at fracture based on an initial gauge length of 50 mm. Parameter $\epsilon_{f,70/80}$ is the strain at fracture with the correct initial gauge length for the specific coupon specimen according to the standard [12]. The fracture strain shows a better agreement between specimens T93-B and T103-A when the correct gauge length is considered with values of 0,126 and 0,128 when compared to the fracture strain obtained with an initial gauge length of 50 mm. The specimens are both steel grade S700 only with a different thickness of 8 and 10 mm.

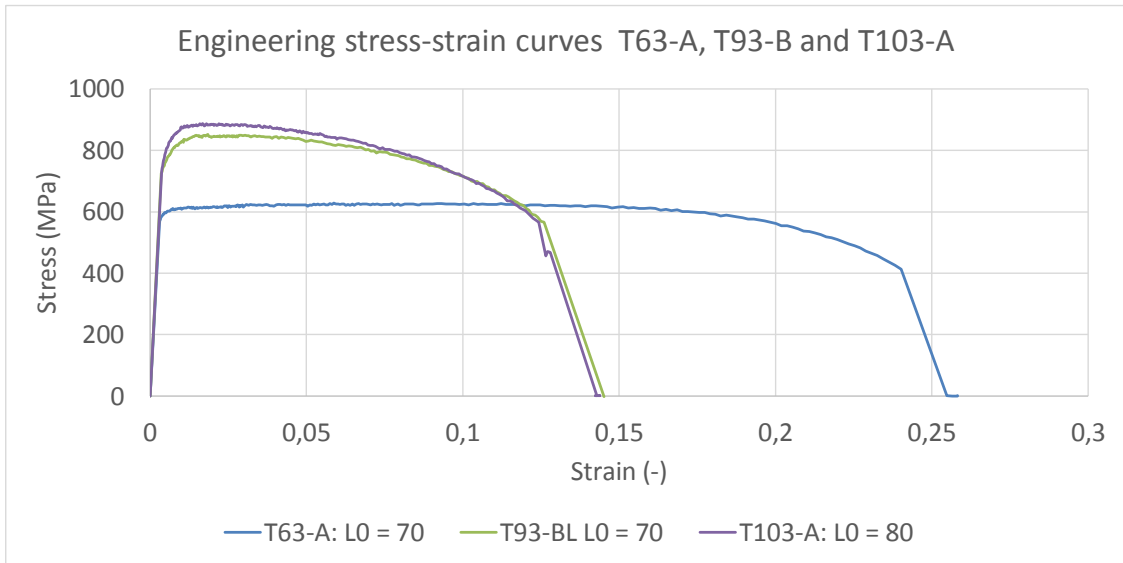


Figure 3.20: Correct engineering stress-strain curves T63-A, T93-B and T103-A

3.7 Second group coupon experiments

The second group of coupon experiments is extracted from joints X2 and X8. Joint X2 is made out of S500 with a thickness of 6 mm, while joint X8 is made out of S355 with a thickness of 6 mm. An overview of the geometry properties of the second group of experiments is presented in Table 3.6. The coupon specimens are in line with the standard [12]. The cross-section is chosen in such a way that the gauge length is 50 mm, which coincides with the range of the extensometer. The initial eccentricity of the second group is lower than the first group of experiments. There are no strain gauges applied in these experiments, only extensometer and 3D DIC. As shown before, the combination of DIC and extensometer capture the behaviour of both sides of the coupon specimen, because strain gauges are not applied there is chosen to combine the results from DIC and extensometer in the determination of the E-modulus in the reloading stage. The same approach, as described for the first group of experiments, is used. Good approximation is obtained between the extensometer and DIC results. All specimens failed inside the range of the extensometer. An overview of the results is presented in Table 3.7. The engineering stress-strain curves are presented in Figures 3.22 and 3.23.

Table 3.6: Coupon geometry second group

	Steel grade	t [mm]	w [mm]	A [mm ²]	e [mm]
X2-N-A	S500	5,91	12,98	76,71	3,76
X2-N-B	S500	5,90	12,69	74,87	4,18
X2-N-C	S500	5,90	13,01	76,76	3,89
X2-N-D	S500	5,87	13,01	76,37	3,80
X8-N-A	S355	5,91	12,99	76,77	3,83
X8-N-B	S355	5,90	13,16	77,64	4,63
X8-N-C	S355	5,95	12,95	77,05	3,84
X8-N-D	S355	5,92	12,86	76,13	3,92

The exact locations of the coupon specimens relative to the cross-section is shown in Figure 3.21. The longitudinal weld is indicated at the bottom. Specimens A and B are extracted from the side adjacent to the longitudinal weld. Specimens C and D are extracted from the side opposite to the longitudinal weld. This is the case for the specimens of both joints X2 and X8.

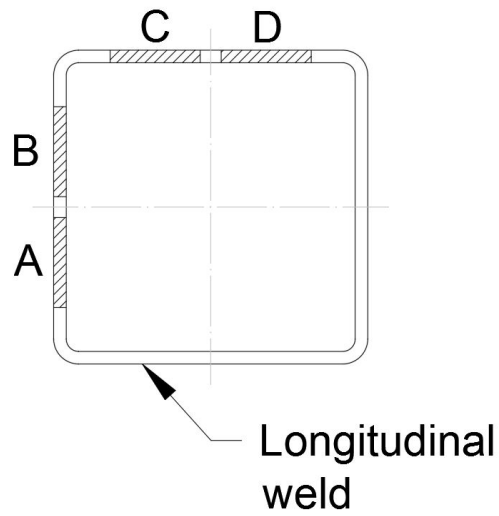


Figure 3.21: Locations of coupon specimens A-B (adjacent) and C-D (opposite) from RHS

Table 3.7: Results coupon experiments second group

	E [GPa]	σ_y [MPa]	σ_u [MPa]	σ_u/σ_y [-]	$\epsilon_y = \sigma_y/E$ [-]	ϵ_f [-]
X2-N-A	190	624	672	1,08	0,0033	0,22
X2-N-B	183	606	668	1,10	0,0033	0,21
X2-N-C	186	615	673	1,09	0,0033	0,22
X2-N-D	189	600	671	1,12	0,0032	0,24
Average	187	611	671	1,10	0,0033	0,22
X8-N-A	180	475	521	1,10	0,0026	0,26
X8-N-B	182	451	518	1,15	0,0025	0,28
X8-N-C	183	466	510	1,09	0,0026	0,28
X8-N-D	180	441	509	1,15	0,0024	0,29
Average	181	458	515	1,12	0,0025	0,28

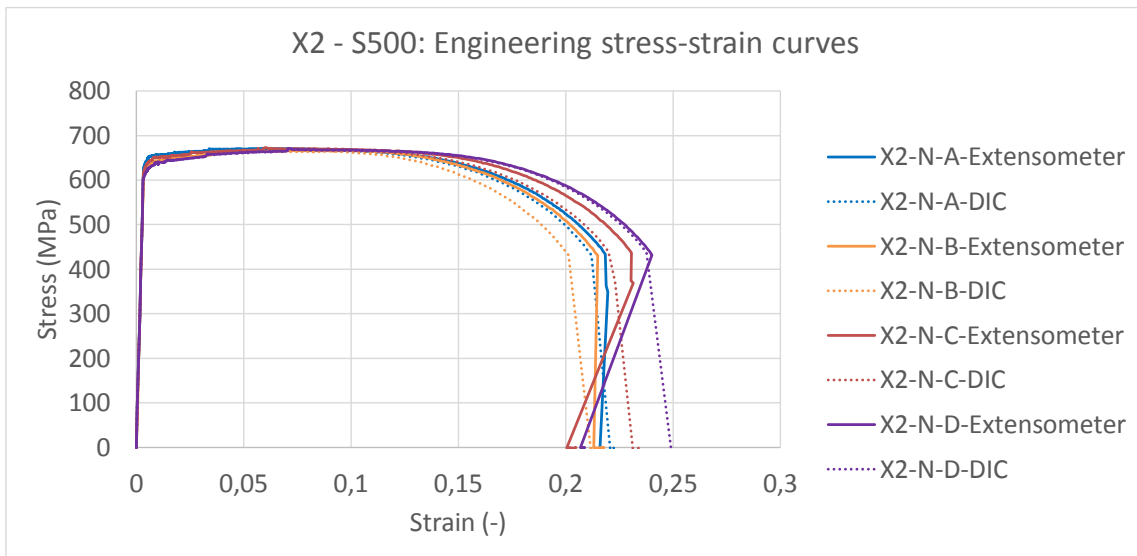


Figure 3.22: X2-series engineering stress-strain curves

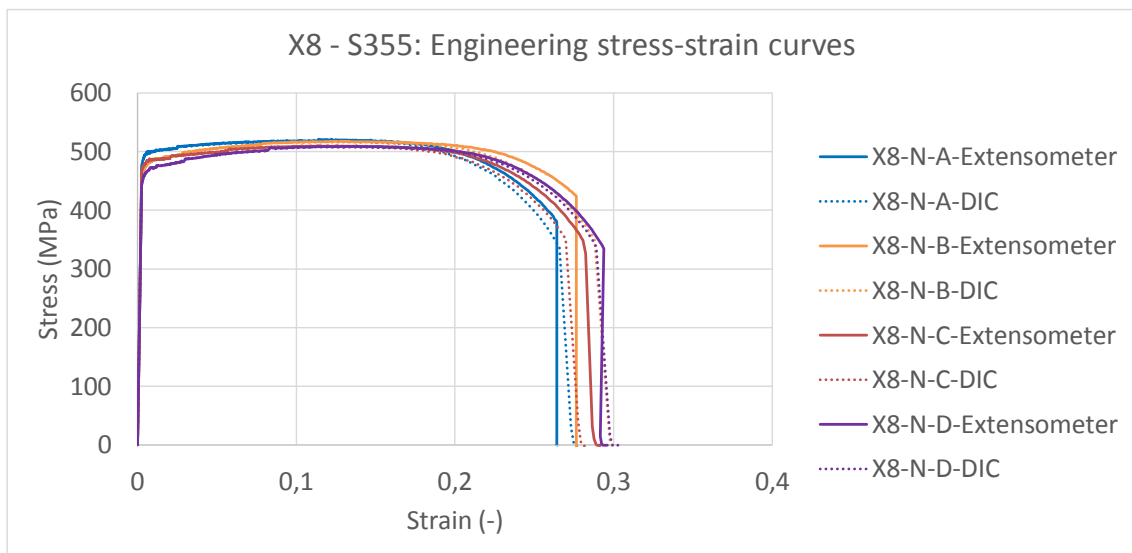


Figure 3.23: X8-series engineering stress-strain curves

3.8 Ductility limits

The minimum required ductility limits according to the standards [14, 18] are checked for the obtained stress-strain curves of the two groups of coupon specimens. The ductility limits are there to prevent sudden brittle failure. If the ductility limits are met, sufficient ductility is ensured and plastic design is allowed. The ductility limits are presented in Section 2.2.1. The results for the S500 and S700 coupons are presented in Tables 3.8 and 3.9. The results for the S355 coupons of joint X8 are presented in Table 3.10. The result of the first group of experiments are based on the results with an initial gauge length of 50 mm. When the correct gauge length is used, see Section 3.6, the strain at fracture becomes lower but still satisfies the minimum of 10%. The only coupon that does not fulfil the ductility limits is specimen X8-N-C due to a σ_u/σ_y -ratio of 1,09 where the minimum limit should be 1,10. It can be concluded that the provided S355, S500 and S700 materials satisfy the ductility limits according to the standards [14, 18], with one exception for steel grade S355.

Table 3.8: Overview results coupon experiments first group

	T63-A	T63-B	T63-C	T93-A	T93-B	T93-C	T103-A	T103-B	T103-C
σ_y [MPa]	559	565	563	708	724	724	732	732	741
σ_u [MPa]	626	612	614	858	846	847	884	881	885
$\sigma_u/\sigma_y \geq 1,05$	1,12	1,08	1,09	1,21	1,17	1,17	1,21	1,20	1,19
$\epsilon_f \geq 10$ [%]	29	29	29	15	16	15	18	17	17
$15^*\epsilon_y$ [%]	5	5	5	6	5	6	6	6	6
$\epsilon_f > 15^*\epsilon_y$	ok	ok	ok						

Table 3.9: Overview results coupon experiments second group X2-series

	X2-N-A	X2-N-B	X2-N-C	X2-N-D
σ_y [MPa]	624	606	615	600
σ_u [MPa]	672	668	673	671
$\sigma_u/\sigma_y \geq 1,05$	1,08	1,10	1,09	1,12
$\epsilon_f \geq 10$ [%]	22	21	22	24
$15^*\epsilon_y$ [%]	5	5	5	5
$\epsilon_f > 15^*\epsilon_y$	ok	ok	ok	ok

Table 3.10: Overview results coupon experiments second group X8-series

	X8-N-A	X8-N-B	X8-N-C	X8-N-D
σ_y [MPa]	475	451	466	441
σ_u [MPa]	521	518	510	509
$\sigma_u/\sigma_y \geq 1,10$	1,10	1,15	1,09	1,15
$\epsilon_f \geq 15$ [%]	26	28	28	29
$15^*\epsilon_y$ [%]	4	4	4	4
$\epsilon_f > 15^*\epsilon_y$	ok	ok	ok	ok

3.9 Finite element analysis coupons

To check if the engineering stress-strain curves are correct, three finite element models are created from coupon specimens T63-A, T93-A and T103-A. In ABAQUS the implicit and explicit solver can be used. The implicit solver is known for being more efficient in solving non-linear problems. However, the implicit method could have difficulties converging, which can result in long computation times due to the large number of iterations that are required. It is possible that the explicit method is more efficient in solving non-linear problems and requires less computation time [22]. First, the differences between the input parameters of the implicit and explicit solver are discussed.

3.9.1 Implicit solver

For the implicit method, two different material properties need to be defined: elastic and plastic properties. For the elastic properties, the E-modulus and Poisson's ratio need to be defined. The Poisson's ratio (ν) of 0,3 is consistently used throughout this thesis. To obtain the plastic input properties, the engineering stress-strain curve is converted into true stresses and true plastic strains by Equations 3.2, 3.3 and 3.4. Non-linear geometrical effects are included.

$$\sigma_{true} = (1 + \epsilon_{engineering})\sigma_{engineering} \quad (3.2)$$

$$\epsilon_{true} = \ln(1 + \epsilon_{engineering}) \quad (3.3)$$

$$\epsilon_{true,plastic} = \ln(1 + \epsilon_{engineering}) - \frac{\sigma_{true}}{E} \quad (3.4)$$

For the implicit solver the 'Static, General' step is introduced. The step definition for the implicit solver is presented in Figure 3.24.

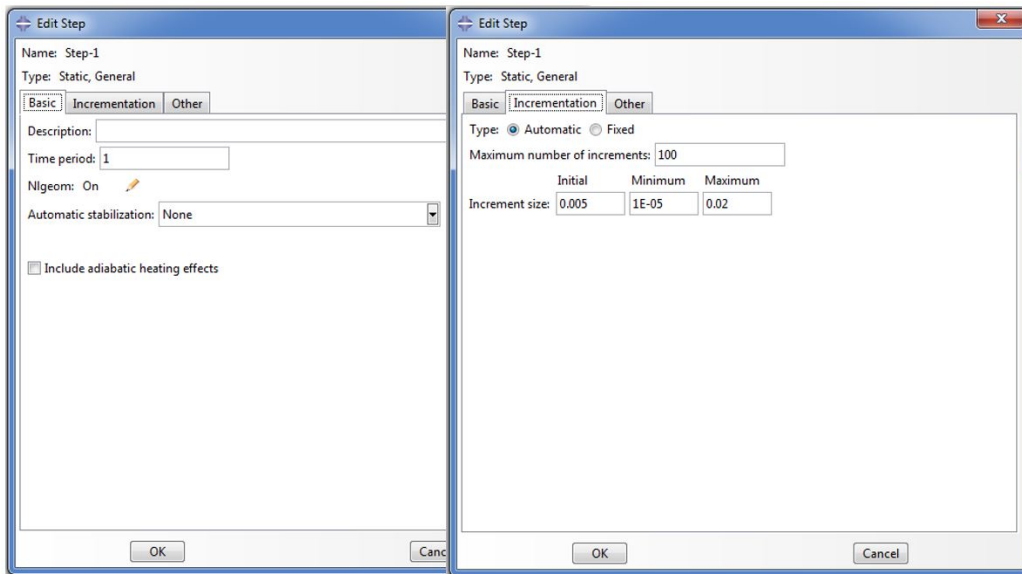


Figure 3.24: Step definition implicit solver

3.9.2 Explicit solver

For the material input of the explicit method, three different properties need to be defined: density, elastic and plastic properties. The elastic and plastic properties are defined in the same way as for the implicit method. The only difference is the definition of the density. The density (ρ) is defined at 7850 kg/m^3 and is consistently used throughout this thesis. Non-linear geometrical effects are included.

For the explicit solver, the 'Dynamic, Explicit' step is introduced. The definition of the explicit step and amplitude is presented in Figure 3.25. A time period of 200 seconds is introduced and is related to the definition of the amplitude. To reduce computation time mass scaling is applied, a target time increment of 0,0001 is defined.

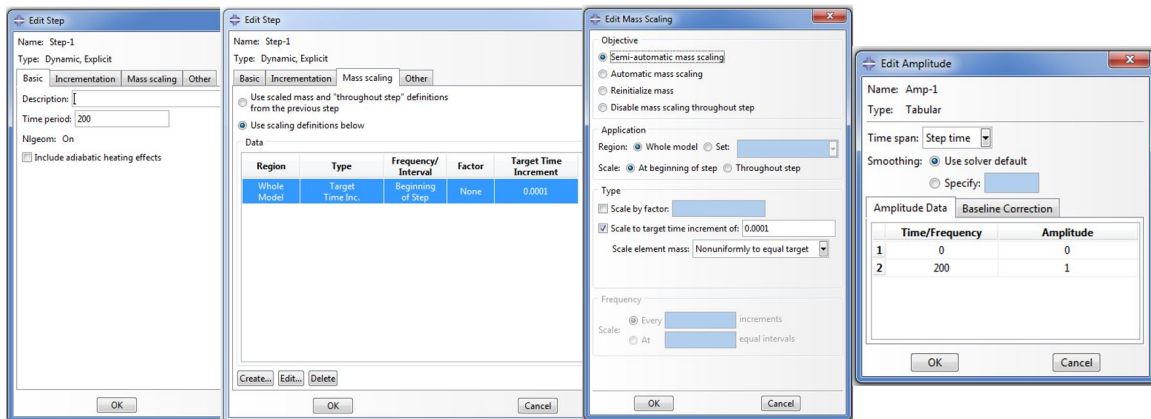


Figure 3.25: Step and amplitude definition explicit solver

3.9.3 Model geometry coupons

The measured thickness, width of the gauge section and eccentricity from Table 3.1 are applied in the models. An overview of the used dimension is given in Table 3.11. As noted in Table 3.1, the eccentricity geometry of specimen T63-A is complex. The specimen did not contain a perfect arc with one maximum eccentricity in the centre of the specimen. Therefore, is the eccentricity measured on five locations along the gauge length. The measurements are visible in Figure 3.26. This exact geometry is modelled in ABAQUS. Due to the bending of the grip section and the accurate placement of the grip section into the jaws of the testing machine, these sections are deleted from the ABAQUS model under the assumption that these grip sections are straight. By this method, the curved profile of the coupon specimen remains identical to the measured eccentricity profile. The eccentricity profile of specimens T93-A and T103-A is visible in Figure 3.27 and is based on one maximum measured eccentricity in the centre of the specimen.

Table 3.11: Geometry measurements ABAQUS models T63-A, T93-A and T103-A

	T63-A	T93-A	T103-A
t [mm]	7,77	7,81	9,84
w [mm]	19,93	19,92	20,07
e [mm]	see Figure 3.26	9,93	9,15

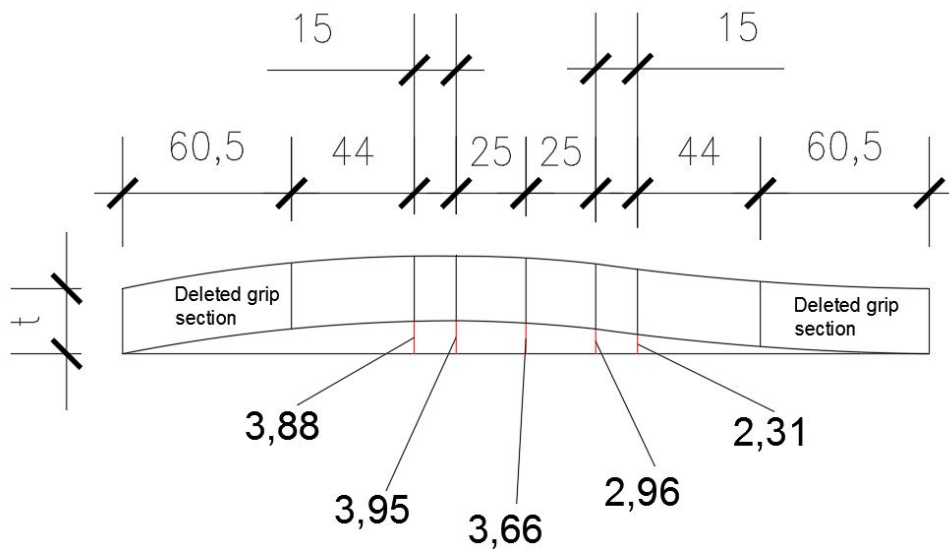


Figure 3.26: Eccentricity profile coupon specimen T63-A

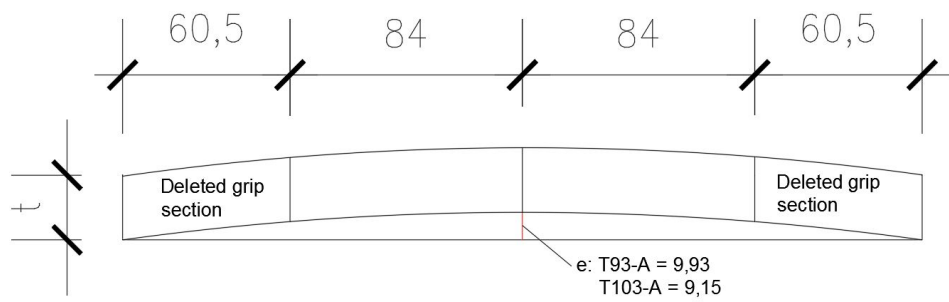


Figure 3.27: Eccentricity profile coupon specimen T93-A and T103-A

3.9.4 Material input coupons

The elastic and density properties used for the coupon models are presented in Table 3.12. The table indicates which property is used for which model (implicit or explicit). The plastic material properties are based on the engineering stress-strain curves, see Figures 3.16, 3.17 and 3.18. The engineering data is converted into true stresses and plastic strains by Equations 3.2, 3.3 and 3.4. The resulting curves of the plastic input is presented in Figure 3.28.

Table 3.12: Elastic and density material properties FEM

		T63-A	T93-B	T103-A	implicit/explicit
E	[GPa]	190	207	196	implicit and explicit
ν	[-]	0,3	0,3	0,3	implicit and explicit
ρ	[ton/mm ³]	7,85e-09	7,85e-09	7,85e-09	explicit

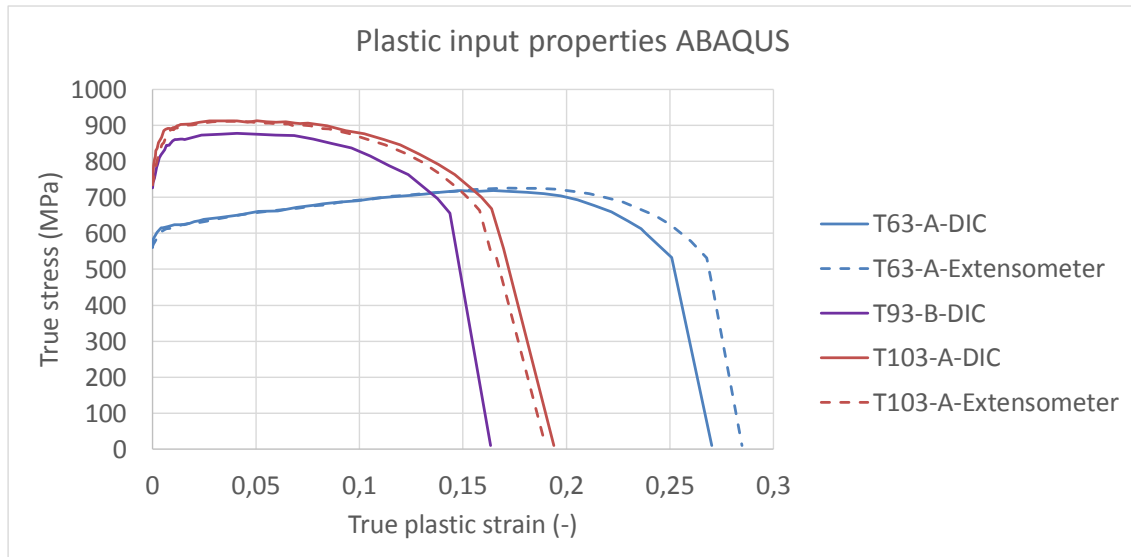


Figure 3.28: Plastic material input properties FEM

The data based on an initial gauge length of 50 mm is used to compare the finite element results to the experimental results. For specimen T63-A the material input properties are based on the 3D DIC and extensometer data. For specimen T93-A, there is chosen to apply the material properties of specimen T93-B, which is based on 3D DIC data. Reason for this choice is the use of 2D DIC for specimen T93-A. For specimen T103-A are the material input properties based on the 3D DIC and extensometer data.

3.9.5 Other input parameters coupons

For both the implicit and explicit method, 8-node linear brick elements (C3D8R) with reduced integration and hourglass control are applied. Elements of 2 mm are used with a through-thickness length of 1 mm. The mesh size is increased to 3 mm for the part of the coupon between the gauge length and the grip section. The meshing of model T93-A is visible in Figure 3.29.

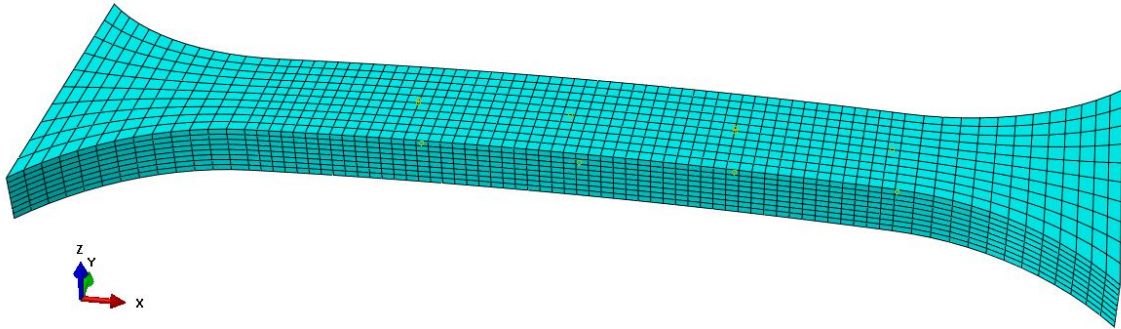


Figure 3.29: FEM meshing T93-A

Multi-point constraints (MPC) of the type BEAM are applied to define the boundary and loading condition. On the left side of the model, the displacement in X-, Y- and Z-directions and rotation in X- and Y-direction is fixed to simulate the clamping of the grip section into the test machine, see Figure 3.29 for the coordinate system. On the right side of the model, a displacement into X-direction is applied to simulate the movement of the jaw of the test machine.

3.9.6 Results

The results of the finite element analyses will be discussed for each model. The main criterion is the stress-strain curve up until the point of necking. After necking the ABAQUS model does not describe the damage development of the material properly. For each model, the stress-strain curve is obtained by extracting the displacement of two points, which have an initial distance of 50 mm, from both the convex and concave side. This displacement is converted into strains and compared to the corresponding experimental results (DIC or extensometer).

T63-A

The result for the convex side, which is recorded by the DIC during the experiment, is visible in Figure 3.30. The result from the concave side is visible in Figure 3.31. The results of four different models are shown, depending on the type of model (implicit or explicit) and the material input properties (DIC or extensometer based). An overview of the ultimate stress (σ_u) and corresponding strain (ϵ_u) is visible in Table 3.13. Figure 3.32 presents the PEEQ strain from FEM at the moment before failure (top) and the equivalent von Mises strain (bottom) from DIC.

Table 3.13: FEM results for specimen T63-A

Result	Property		Convex		Concave	
			σ_u [MPa]	ϵ_u [-]	σ_u [MPa]	ϵ_u [-]
Experiment	DIC	-	627	0,094	-	-
Experiment	Extensometer	-	-	-	626	0,106
FEM	Implicit	DIC based	627	0,091	627	0,094
FEM	Explicit	DIC based	627	0,091	627	0,096
FEM	Implicit	EXT based	626	0,096	626	0,102
FEM	Explicit	EXT based	626	0,099	626	0,104

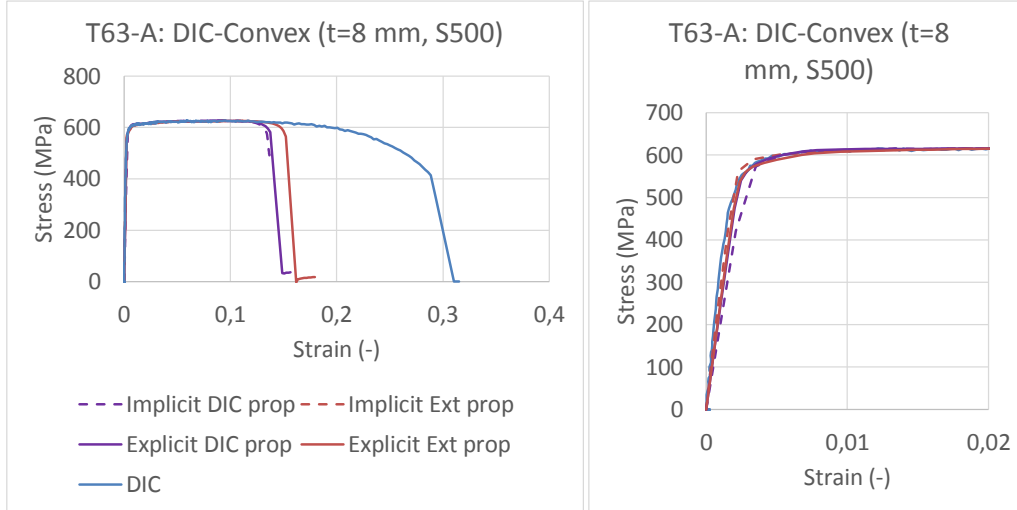


Figure 3.30: FEM results convex side T63-A

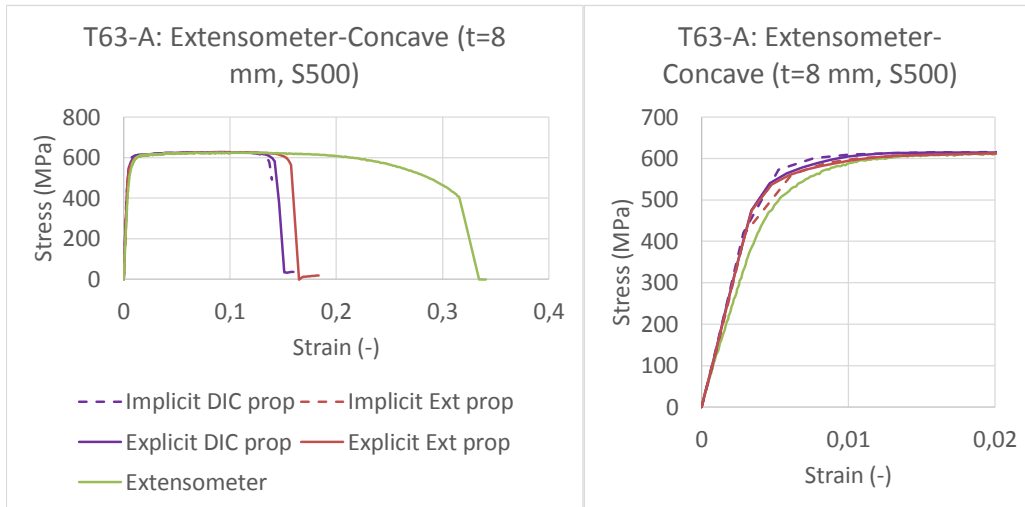


Figure 3.31: FEM results concave side T63-A

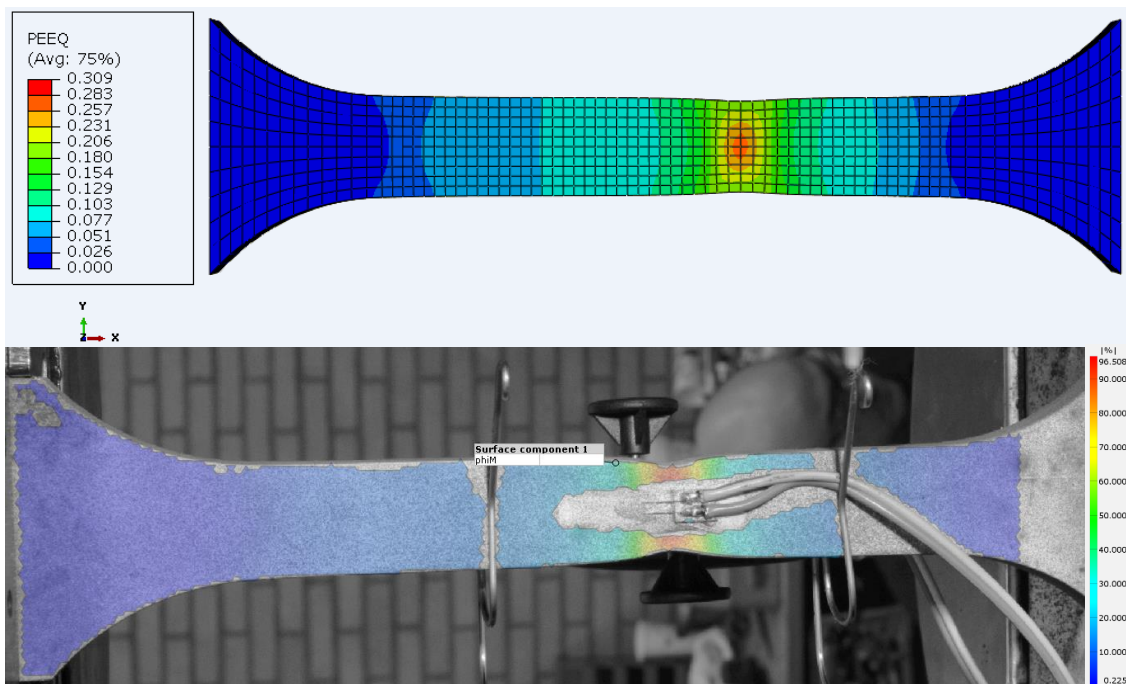


Figure 3.32: FEM results PEEQ strain (top) and DIC results equivalent Mises strain (bottom) T63-A (explicit/DIC based property)

T93-A/B

The experimental results of specimen T93-B are compared to the ABAQUS results. The concave side is facing the DIC camera in this experiment. The result of the convex side is visible in Figure 3.33. The result of the concave side is visible in Figure 3.34. For this model, only the explicit result is presented with the material property that is based on the DIC results. The implicit model resulted in a fracture at two locations. The full-scale X joint model is an explicit model, for that reason is the implicit result of T93-B disregarded and only the explicit result is shown. An overview of the ultimate stress and corresponding strain is visible in Table 3.14. Figure 3.35 presents the PEEQ strain from FEM at the moment before failure (top) and the equivalent von Mises strain (bottom) from DIC.

Table 3.14: FEM results for specimen T93-B

Result	Property		Convex		Concave	
			σ_u [MPa]	ϵ_u [-]	σ_u [MPa]	ϵ_u [-]
Experiment	Extensometer	-	846	0,026	-	-
Experiment	DIC	-	-	-	850	0,036
FEM	Explicit	DIC based	843	0,025	843	0,030

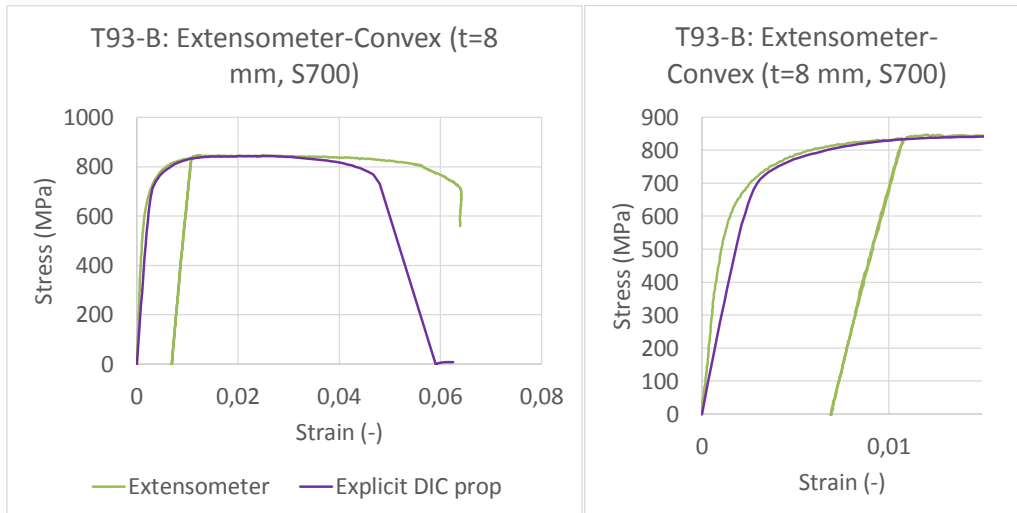


Figure 3.33: FEM results convex side T93-B

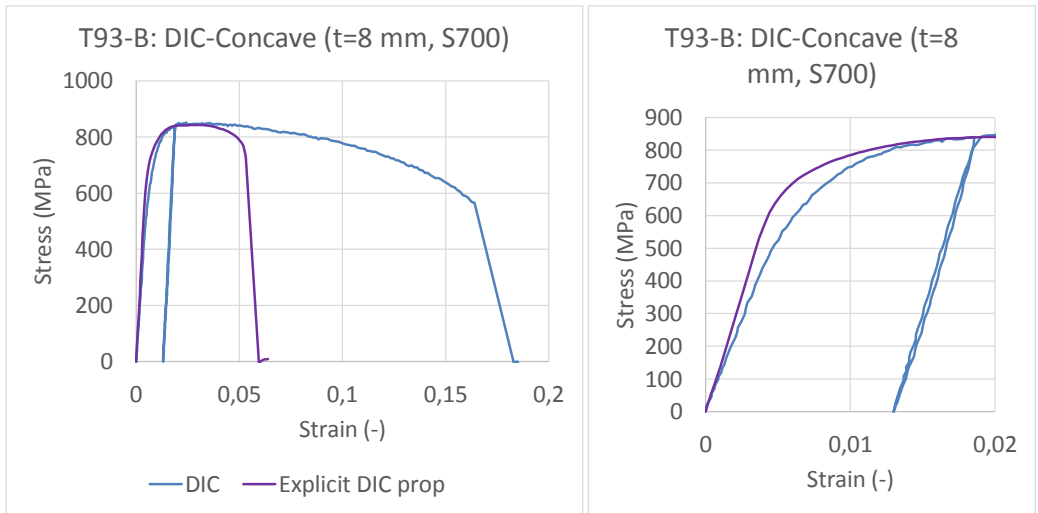


Figure 3.34: FEM results concave side T93-B

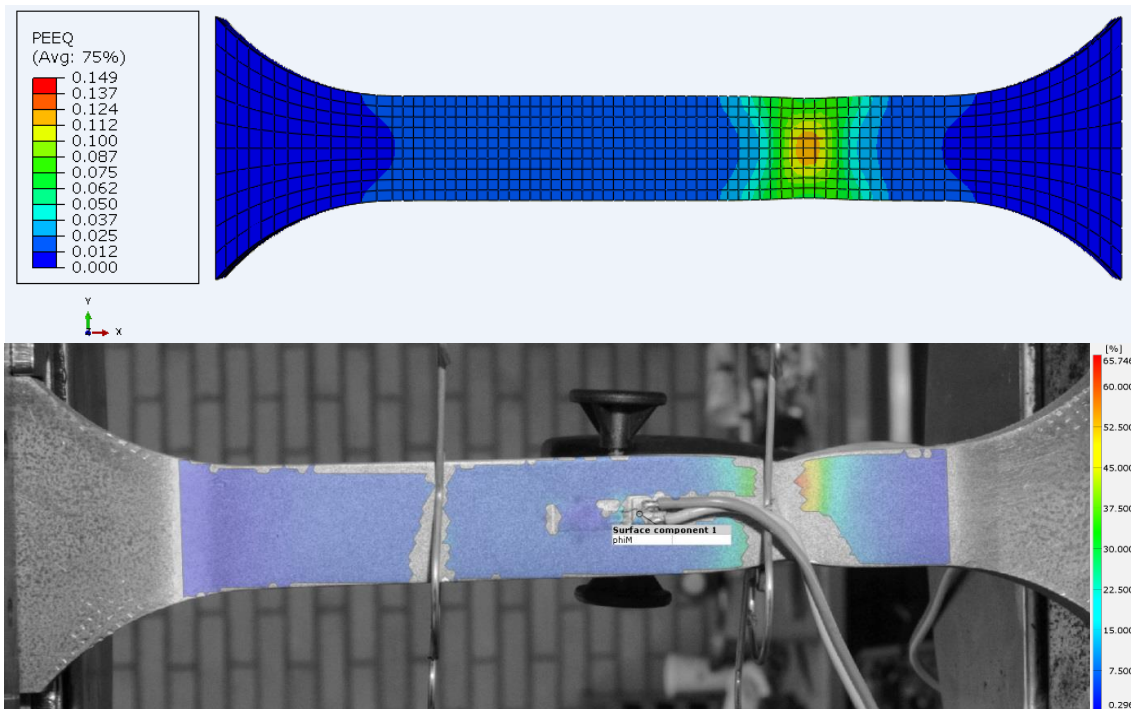


Figure 3.35: FEM results PEEQ strain (top) and DIC results equivalent Mises strain (bottom) (explicit/DIC based property)

T103-A

The result for the convex side is visible in Figure 3.36. The convex side is facing the DIC camera in the experiment. The result of the concave side is visible in Figure 3.37. The results of four different models are shown, depending on the type of model (implicit or explicit) and the material input properties (DIC or extensometer based). An overview of the ultimate stress and corresponding strain is visible in Table 3.15. Figure 3.38 presents the PEEQ strain from FEM at the moment before failure (top) and the equivalent von Mises strain (bottom) from DIC.

Table 3.15: FEM results for specimen T103-A

Result	Property		Convex		Concave	
			σ_u [MPa]	ϵ_u [-]	σ_u [MPa]	ϵ_u [-]
Experiment	DIC	-	887	0,022	-	-
Experiment	Extensometer	-	-	-	884	0,030
FEM	Implicit	DIC based	888	0,016	888	0,025
FEM	Explicit	DIC based	888	0,018	888	0,023
FEM	Implicit	EXT based	885	0,018	885	0,027
FEM	Explicit	EXT based	885	0,020	885	0,028

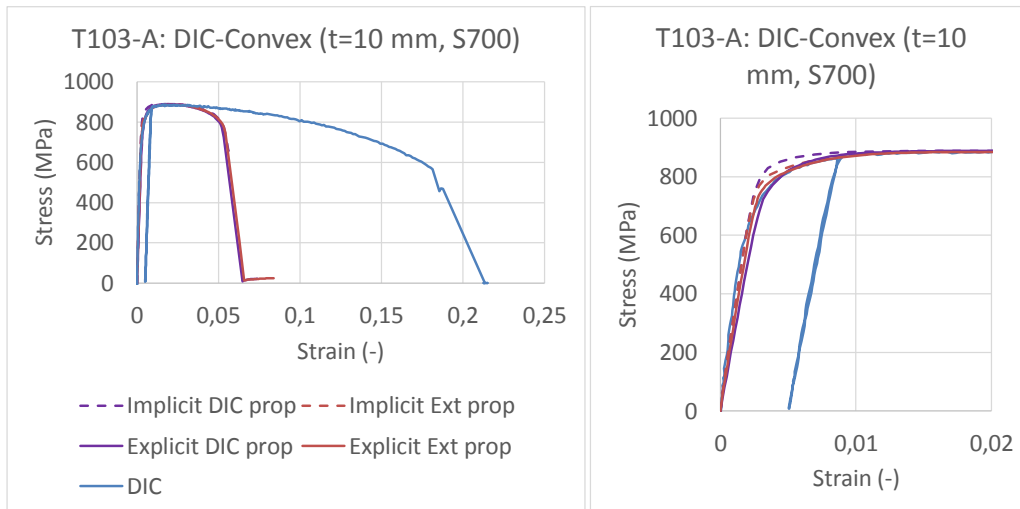


Figure 3.36: FEM results convex side T103-A

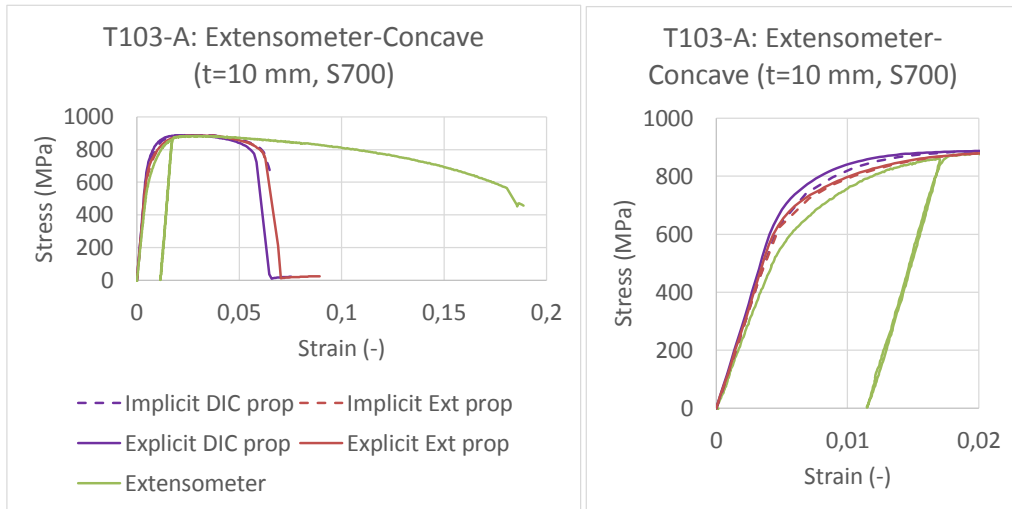


Figure 3.37: FEM results concave side T103-A

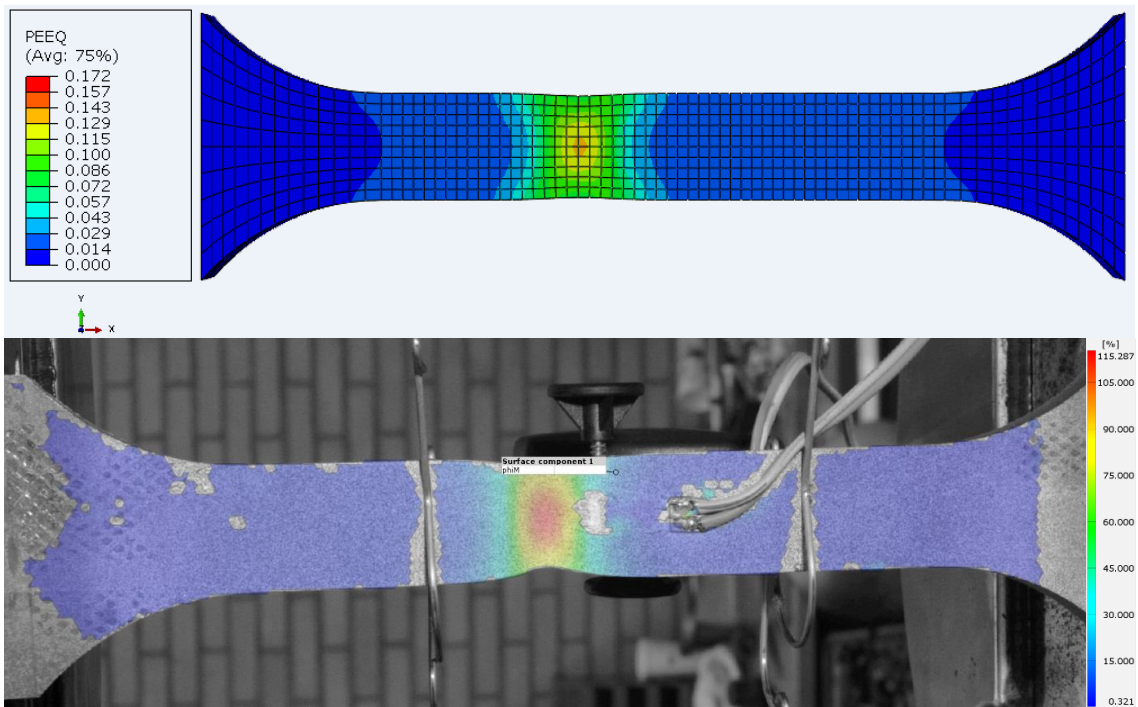


Figure 3.38: FEM results PEEQ strain (top) and DIC results equivalent Mises strain (bottom) (explicit/DIC based property)

3.10 Strain development along coupon specimen

The (major) strain development of three coupon specimens is evaluated for characteristic points of the stress-strain curves. The three specimens are chosen that are used as material input for the finite element model of joint X2 and X8 and for the parametric study further on in this thesis. The data is obtained by 3D DIC. Specimens X8-N-B, X2-N-C and T103-A are evaluated and correspond to steel grades S355, S500 and S700, respectively. The result for specimen X8-N-B (S355) is presented in Section 3.10.1. The result for X2-N-C (S500) and T103-A (S700) are presented in Appendix A. For each engineering stress-strain curve are seven characteristic points determined, see Table 3.16. Points 5 and 6 both represent points in the post-necking stage of the stress-strain curve and intent to show the localization of strains after necking.

Table 3.16: Characteristic points

1	Elastic stage
2	Yield point
3	Plastic behaviour
4	Ultimate stress
5	Post-necking behaviour
6	Post-necking behaviour
7	Fracture point

Table 3.17: Results strain development along coupons

	X8-N-B	X2-N-C	T103-A
Steel grade	S355	S500	S700
σ_y [MPa]	451	615	732
σ_u [MPa]	518	673	884
ϵ_u [%]	14	8,5	3
ϵ_f [%]	108	107	104

The results are summarized in Table 3.17. Figures 3.40, A.1 and A.5 present the engineering stress-strain curve with markers that represent the characteristic points, respectively for specimens X8-N-B (S355), X2-N-C (S500) and T103-A (S700). Figures 3.41, A.2 and A.6 show the section line along which the major strains are extracted with the corresponding length scale. The strain development is presented in three figures for each specimen. The first two figures show the results of the first four characteristic points up to the point of ultimate stress (i.e. necking), see Figures 3.42, A.3 and A.7. The second figure represents the results from the point of ultimate stress until fracture (points 4 to 7), see Figures 3.43, A.4 and A.8.

The figures do not show a continuous curve along the length of the specimen, see for example Figure 3.42 around 30 and 85 mm length. At the locations where there is a gap in the curve, the camera is not able to record the data. This is due to the clips of the extensometer.

For the sake of clarity, the results will be discussed based on the steel grade of each specimen and not the name of the coupon specimen. The strain at ultimate stress is 14%, 8,5% and 3% for steel grades S355, S500 and S700. The reduction of strain at ultimate stress is expected for increasing steel grades due to the reduction of ductility. The strain at fracture that is observed is for all three specimens in the range of 104% to 108%.

After the point of ultimate stress the strains are localized in a small area where necking is occurring, this phenomena is clearly visible by the increase of the height and reduction of the width of the peak of Figures 3.43, A.4 and A.8.

The strains after necking increase significantly. In the finite element analysis presented in Section 3.9, the results are accurate up to the point of necking. After the point of necking the results become inaccurate and show that significantly lower final displacements are observed in the FEM when compared to experimental results. The fracture strain used as input for the FEM is based on the engineering stress-strain curve, which is based on an initial gauge length that is in accordance with the standard. This means that the fracture strain is averaged over this initial gauge length. For example, for S355 is the fracture strain used in FEM around 28%, see Figure 3.40. Where the observed fracture strain by DIC is around 108%, see Figure 3.43. This supports the statement that lower fracture strains are used in FEM and give inaccurate results after necking, which could be solved by implementing damage modelling.

Noise is visible in the strain profiles of the coupon specimens. The noise is more clearly visible in the figures that represent characteristic points 1 to 4 in comparison to the figures that represent characteristic points 4 to 7, the reason for this difference is the scale of the Y-axis. It has been checked if the Lüders band phenomenon [63] is the reason of the noise. The Lüders band is a phenomena that can occur at the transition between the elastic and plastic stage at the yield point. It is observed that this is not the case. Prove for this is presented in Figure 3.39, which gives the strain profile for specimen X8-N-B for the second time step in DIC. At this time step, the specimen is only clamped at one side into the test machine. The other jaw still had to be clamped. This observation is made before the specimen is loaded. It is visible that a noise level is observed of around 0,1% strain.

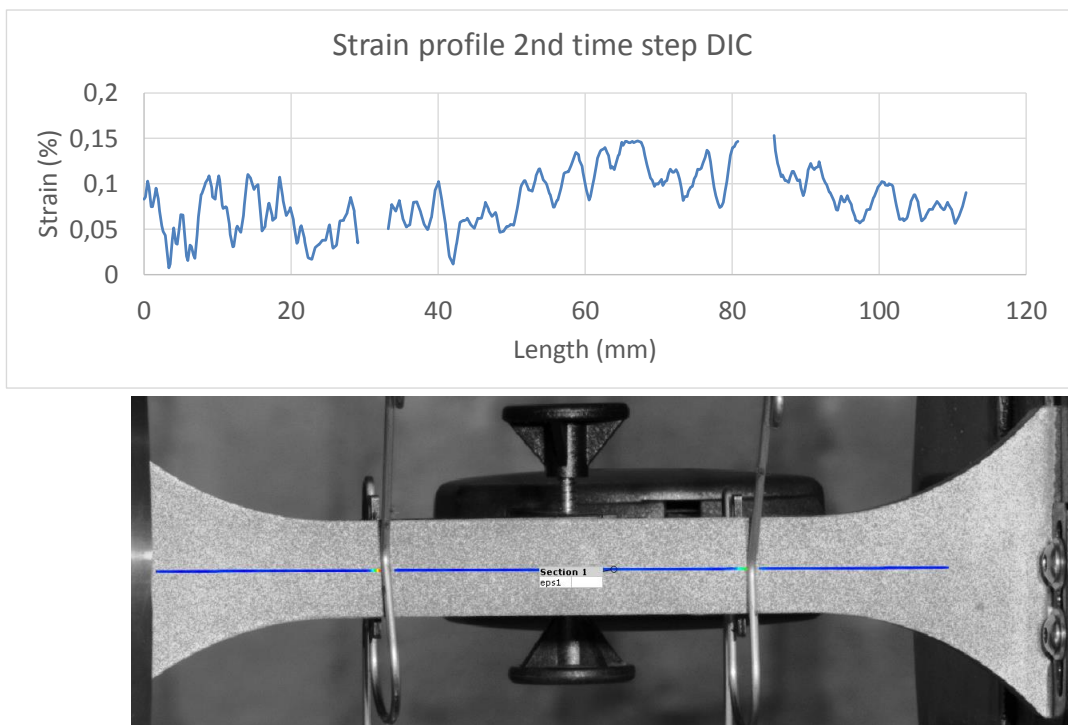


Figure 3.39: Noise level observation specimen X8-N-B

3.10.1 X8-N-B - S355

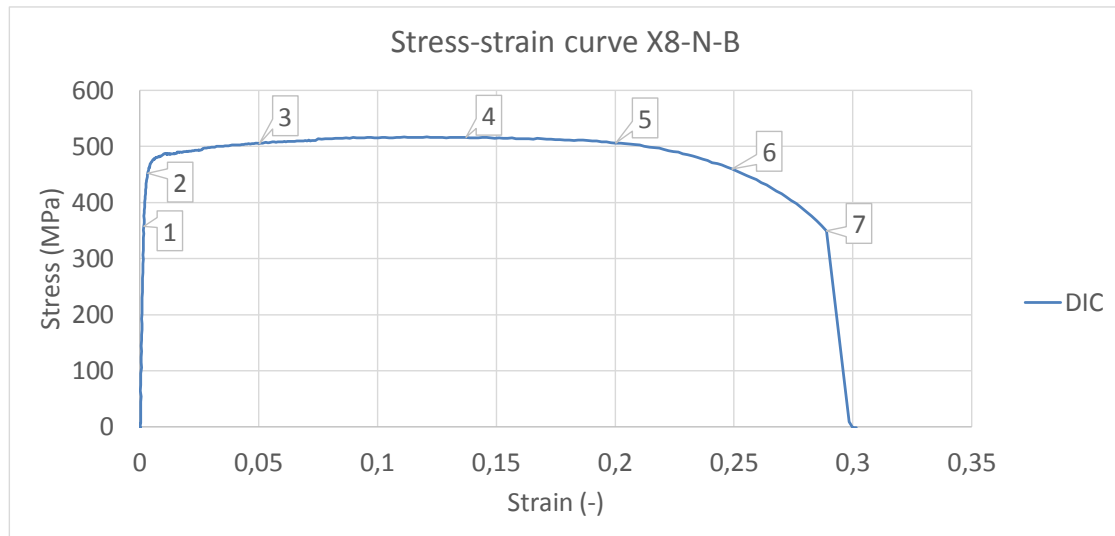


Figure 3.40: Stress-strain curve X8-N-B with characteristic points (S355)

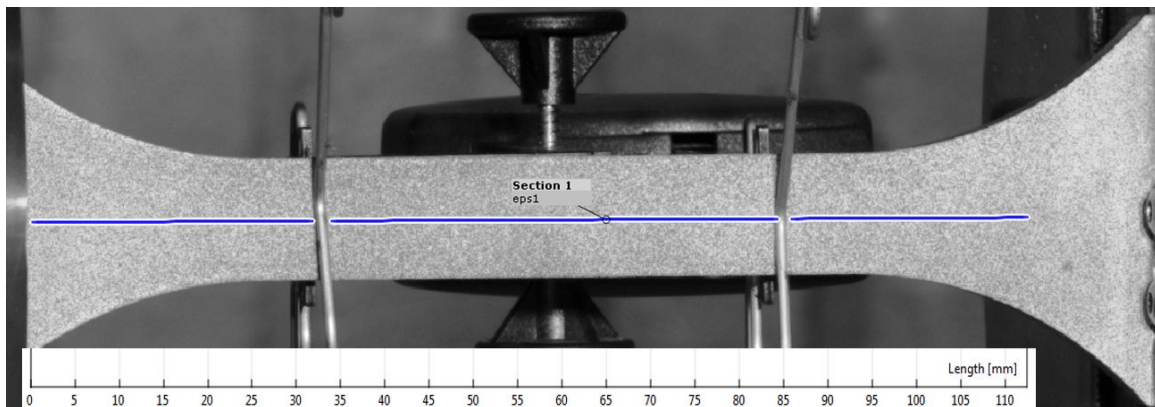


Figure 3.41: Section line along which the strains are extracted with length scale X8-N-B (S355)

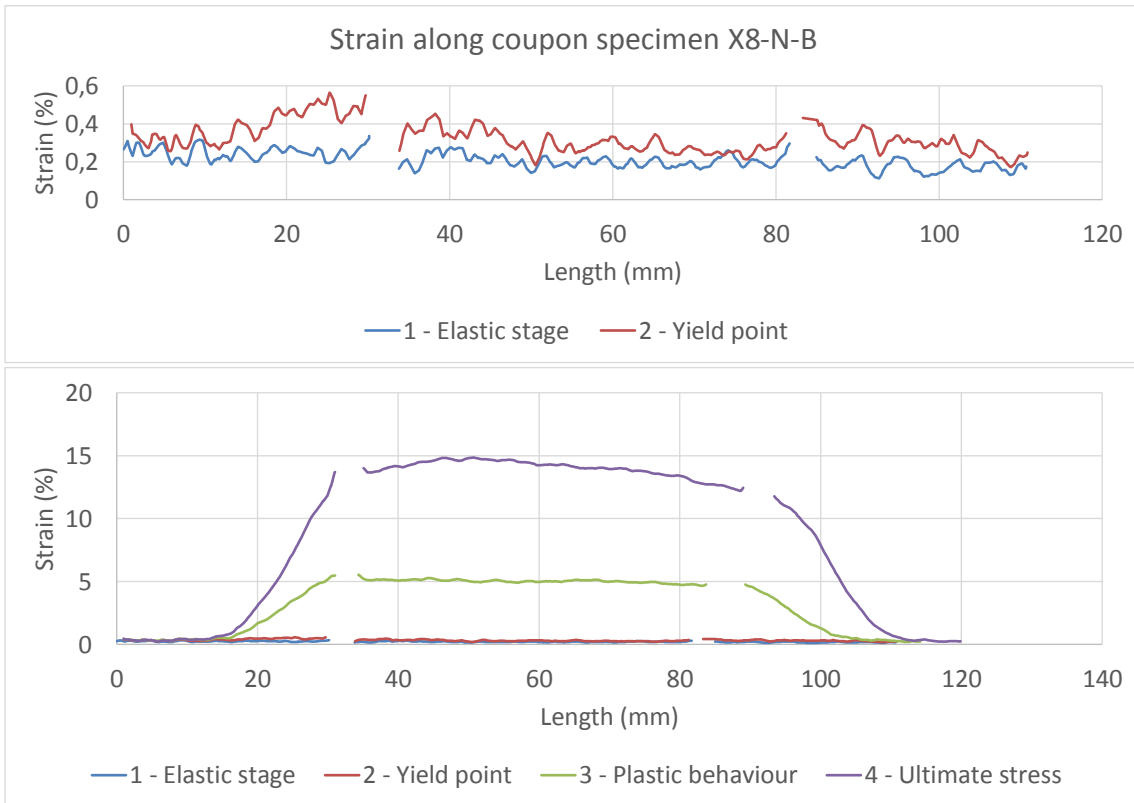


Figure 3.42: Strain development X8-N-B for points 1 to 4 (S355)

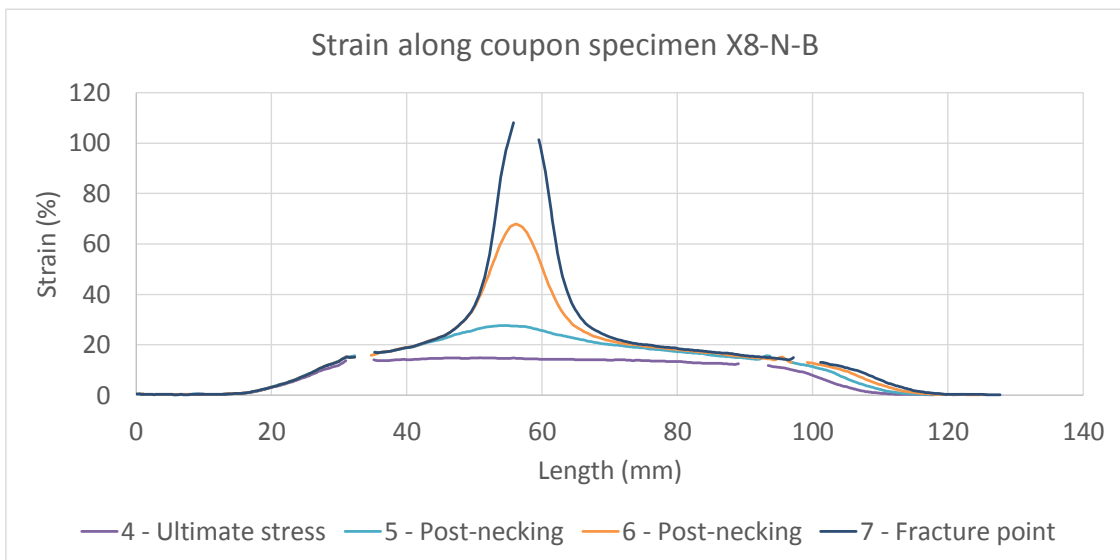


Figure 3.43: Strain development X8-N-B for points 4 to 7 (S355)

3.11 Conclusions coupon experiments

The results obtained from the coupon experiments are presented in Table 3.18. The results are presented for each series of coupon specimens and include the obtained scatter for the yield and ultimate stress.

Table 3.18: Overview results coupon experiments

		X8	X2	T63	T93	T103
Steel grade		S355	S500	S500	S700	S700
Quantity		4	4	3	3	3
t	[mm]	6	6	8	8	10
w	[mm]	13	13	20	20	20
σ_y	[MPa]	441-475	600-624	559-565	708-724	732-741
Scatter σ_y	[%]	7,7	4,0	1,1	2,3	1,2
σ_u	[MPa]	509-521	668-673	612-626	846-858	881-885
Scatter σ_u	[%]	2,4	0,7	2,3	1,4	0,5
ϵ_f	[%]	26-29	21-24	24	13	13

Coupon experiments X8 consists of steel grade S355 and a thickness of 6 mm. The yield stress is in the range of 441 to 475 MPa (scatter of 7,7%). The ultimate stress is in the range of 509 to 521 MPa (scatter of 2,4%). The strain at fracture is between 26% and 29%.

Coupon experiments X2 consists of steel grade S500 and a thickness of 6 mm. The yield stress is in the range of 600 to 624 MPa (scatter of 4,0%). The ultimate stress is in the range of 668 to 673 MPa (scatter of 0,7%). The strain at fracture is between 21% and 24%.

The T63-series consists of steel grade S500 and a thickness of 8 mm. The yield stress is in the range of 559 and 565 MPa (scatter of 1,1%). The ultimate stress is in the range of 612 and 626 MPa (scatter of 2,3%). The strain at fracture is 29% based on an initial gauge length of 50 mm. When the correct gauge length is used, is the strain at fracture 24% for specimen T63-A.

For steel grade S700 experiments are conducted with a thickness of 8 and 10 mm, respectively T93- and T103-series. The observed yield stress for the T93-series is in the range of 708 and 724 MPa (scatter of 2,3%). For the T103-series is the yield stress a little bit higher in the range of 732 and 741 MPa (scatter of 1,2%). The ultimate stress is in the range of 846-858 MPa and 881-885 MPa (scatter of 1,4% and 0,5%), respectively for T93- and T103-series. The strain at fracture for the T93-series and T103-series is in the range of 15% to 18% based on an initial gauge length of 50 mm. If the correct initial gauge length is used, is the strain at fracture approximately 13% for the T93- and T103-series.

The scatter observed for the yield and ultimate stress based on the steel grade is presented in Table 3.19. The scatter of the yield stress is 7,7%, 11,6% and 4,7% for steel grades S355, S500 and

S700. The scatter of the ultimate stress is 2,4%, 10,0% and 4,6% for steel grades S355, S500 and S700.

Table 3.19: Scatter coupon results for each steel grade

	σ_y	σ_u
S355	7,7%	2,4%
S500	11,6%	10,0%
S700	4,7%	4,6%

The material requirements according to the Eurocodes [14, 18] are satisfied with one exception, the σ_u/σ_y -limit of specimen X8-N-C is 1,09 where it should be at least 1,10.

The strain development along the coupon specimen is analysed by the use of DIC. The fracture strain observed at the final fracture location is in the range of 104% to 108% for steel grades S355, S500 and S700.

Finite element models are created for specimens T63-A, T93-B and T103-A. The maximum deviation in ultimate stress is 1, 7 and 4 MPa. The maximum deviation in the strain at ultimate stress is 1,2%, 0,6% and 0,7%, for respectively specimen T63-A, T93-B and T103-A. The FEM shows accurate results up to the point of necking. After the point of necking the results become inaccurate. Reason for this is that the used fracture strain in FEM is lower than the observed fracture strain in the experiment by DIC. This could be solved by implementing damage modelling.

3.11.1 Material properties FEM

For the validation of the X joint finite element model against the experiment, the material properties of the second group (S355 and S500) are used. These properties are also included in the parametric study. Steel grade S700, from the first group of coupon experiments, is also included in the parametric study. The engineering stress-strain curves that will be used later on in this thesis are presented in Figure 3.44. The characteristic values of these curves are presented in Table 3.20.

Table 3.20: Characteristic values material properties used in FEM

Steel grade	E [GPa]	σ_y [MPa]	σ_u [MPa]	ϵ_f [%]
S355	182	451	518	28
S500	186	615	673	22
S700	196	732	884	13

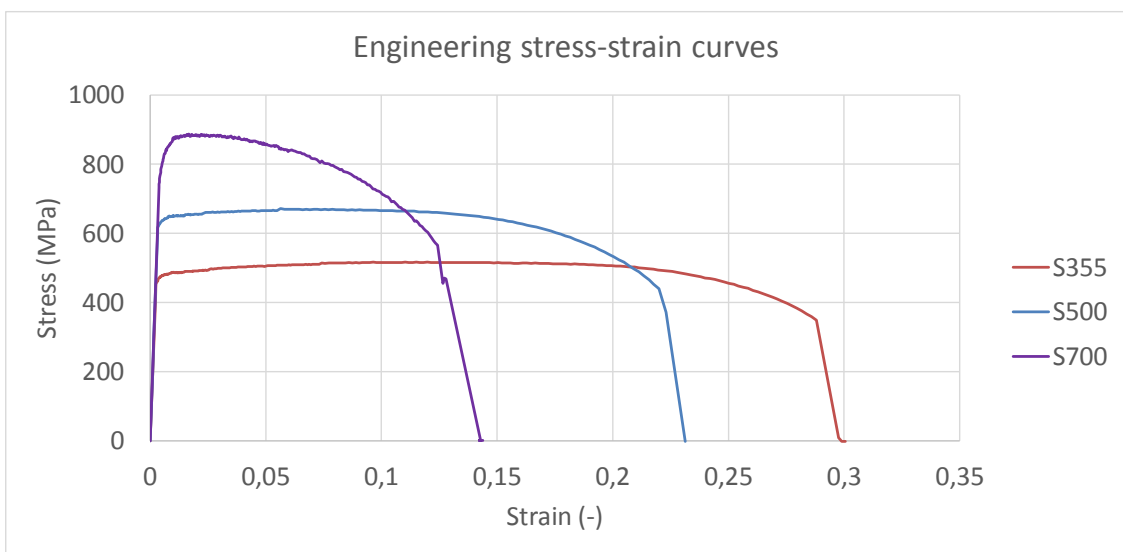


Figure 3.44: Engineering stress-strain curves S355, S500 and S700 from coupon experiments

Chapter 4

X joint experiments

To verify the material reduction factors applicable for HSS, full-scale X joint experiments are executed. An extensive test program is created which includes nine different X joints, with different configurations and steel grades (S355, S500 and S700). However, due to long production and delivery times only two joints are included in this thesis. The two joints that are included both have chord and brace members that exist of 150x150x6 mm tubular sections. The joints are labelled as X2 and X8, this designation is based on the designation of the full test program. Joint X2 consists of steel grade S500, while X8 consists of steel grade S355. The details of the joints and measured dimensions are presented in Table 4.1. Figure 2.29 shows the definition of the geometry parameters. The table shows the geometric parameters β , 2γ and τ . The length of the chord and braces is described by L_0 and L_1 . The inner and outer radius of the chord and brace members are described by the parameters r_{in} and r_{out} .

Table 4.1: X joint test program

Joint	Chord	Brace	Steel grade	β	2γ	τ	L_0	L_1
	[mm]	[mm]	[-]	$= b_1/b_0$	$= b_0/t_0$	$= t_1/t_0$	[mm]	[mm]
X2	150x150x6	150x150x6	S500	1	25	1	1500	752
X8	150x150x6	150x150x6	S355	1	25	1	1500	752
	h_0	b_0	t_0	h_1	b_1	t_1	r_{in}	r_{out}
	[mm]	[mm]	[mm]	[mm]	[mm]	[mm]	[mm]	[mm]
X2	150,22	150,66	6,02	150,30	150,46	5,99	7,00	13,00
X8	149,93	150,47	6,06	150,40	149,91	5,99	4,97	11,00

4.1 Test set-up and measuring methods

The test set-up that is used for the experiment has a maximum capacity of 10.000 kN. The loading rate that is applied in the experiments is 0,01 mm/s.

Sloth holes are fabricated in the brace members. Tail plates are located in these sloth holes and welded to the brace members. The sloth hole has a depth of 250 mm. The weld between the sloth hole and brace member is designed to be non-critical. The tail plate contains a circular pin hole to fix the X joint into the test set-up. Figure 4.1 shows joint X8 that is fixed into the test set-up, the tail plates of the bottom brace member are visible.

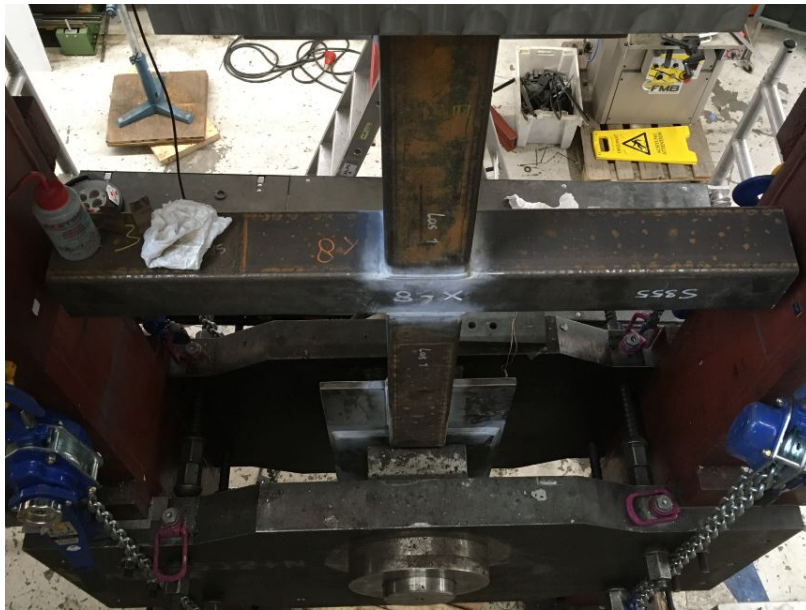


Figure 4.1: Joint X8 fixed into the test set-up

Different measuring methods are used during the experiments. Firstly, 3D DIC is used to measure the strain development on one side of the joint. Secondly, six linear variable differential transformers (LVDTs) are used to measure three different type of displacements:

1. Axial displacement of specific points on the brace members. A steel frame is fixed onto the top and bottom brace members, with a spacing of 380 mm. Four LVDTs, respectively LVDT 7, 8, 9 and 10, are glued to this steel frame to measure the axial displacement. These measurements are used to calibrate the finite element model.
2. Chord side wall indentation. LVDT 11 is located in the centre of the chord side wall to measure the inward displacement of the chord side wall. This LVDT is located on the other side than the side that is captured by the DIC camera.
3. Indentation of the chord top face. LVDT 12 is located in the centre of the chord top face at a distance of 30 mm from the brace surface.

Schematic drawings with the exact locations of the LVDTs are presented in Figures 4.2 and 4.3. The red squares represent the LVDTs. For LVDT 11 and 12, the base is located at a distance of 425

mm and is shown with the black squares. Figures 4.4 and 4.5 show the positioning of the LVDTs during the experiment.

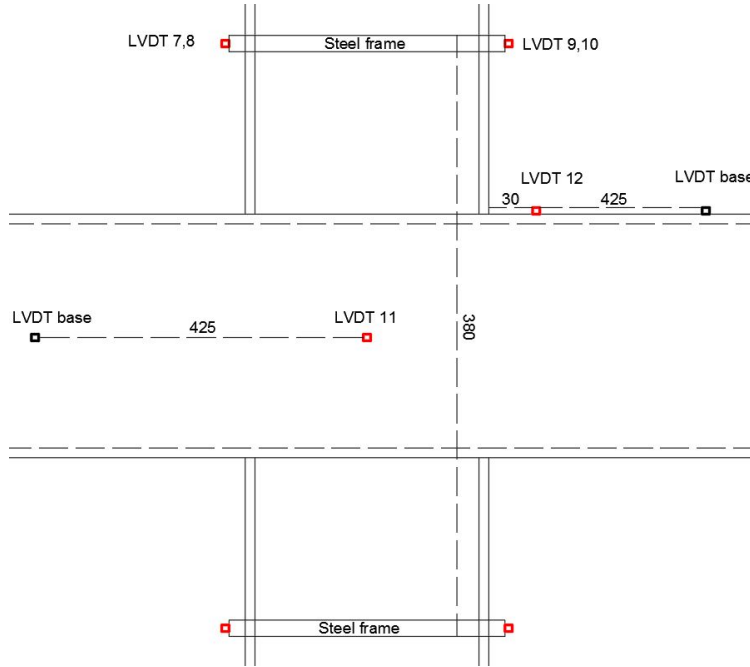


Figure 4.2: Schematic drawing locations LVDTs side view

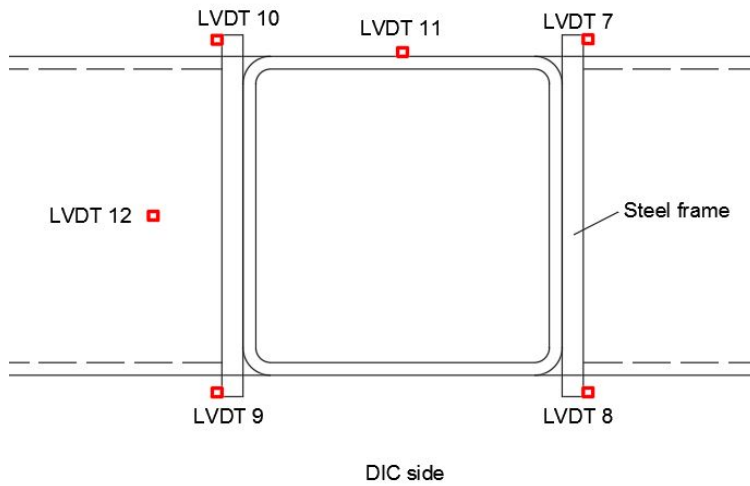


Figure 4.3: Schematic drawing locations LVDTs top view



Figure 4.4: Positioning LVDTs on joint X2 during the experiment (1)

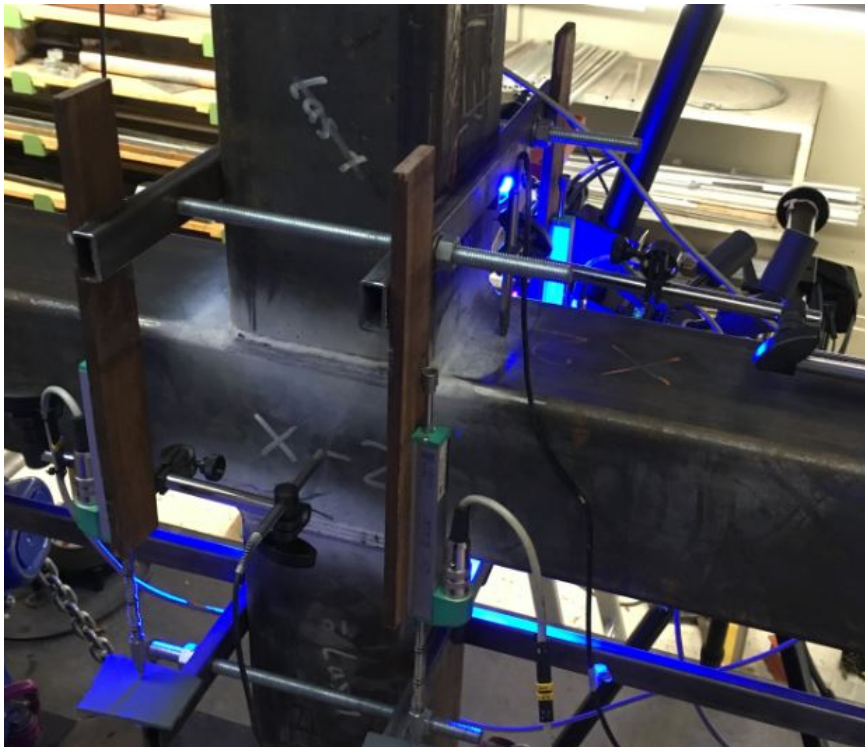


Figure 4.5: Positioning LVDTs on joint X2 during the experiment (2)

4.2 Results X joint experiments

An overview of the experimental results is given in Table 4.2. F_u represent the ultimate resistance. $F_{3\%}$ represents the resistance at the 3% deformation limit, if this limit is reached. Joint X2 resulted in an ultimate resistance of 1713 kN with brace failure as the failure mode, see Figure 4.6. Joint X8 resulted in an ultimate resistance of 1374 kN with a chord side wall failure, see Figure 4.7. Both failures occurred on the side where the DIC is positioned. The brace failure of joint X2 is located right above the weld material inside the heat affected zone.

Table 4.2: X joint experimental results

	Steel grade	F_u [kN]	$F_{3\%}$ [kN]	Failure mode
X2	S500	1713	Not reached	Brace failure
X8	S355	1374	1362	Chord side wall failure

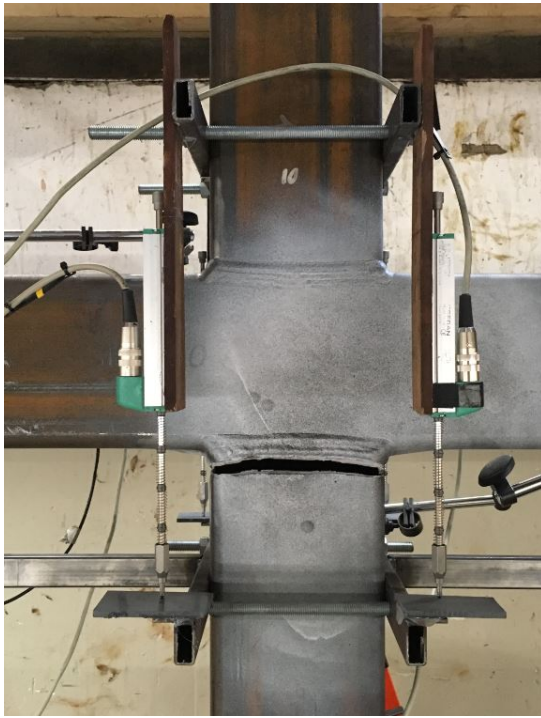


Figure 4.6: Brace failure joint X2



Figure 4.7: Chord side wall failure joint X8

The crack development of joint X2 is presented in Figure 4.8, the crack develops in the heat affected zone of the brace member. The crack development of joint X8 is presented in Figure 4.9, the crack initiates in the corner.

The chord side wall displacement, see Figure 4.10, that is measured by LVDT 11 is observed to be 1,05 mm for joint X8. This displacement is 0,88 mm for joint X2.

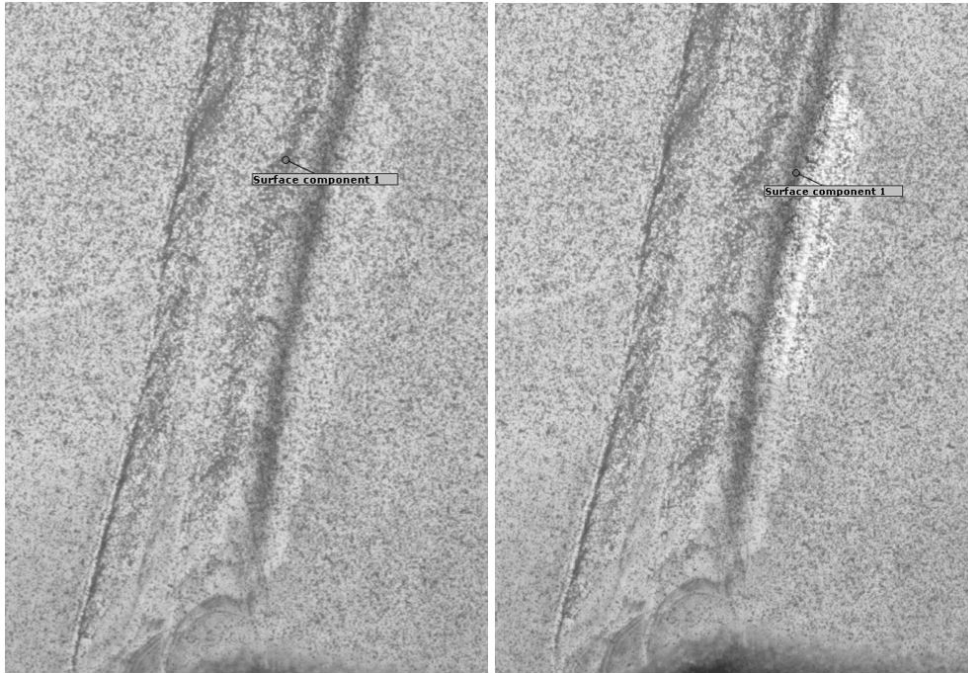


Figure 4.8: Crack development in HAZ joint X2

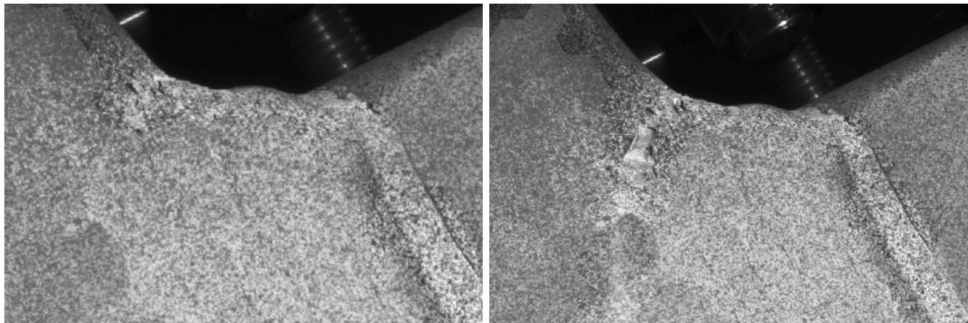


Figure 4.9: Crack development in corner joint X8

Figure 4.11 shows the results from LVDT 12, which is located on the top of the chord face at a distance of 30 mm from the brace surface. For both joints a short yielding plateau is visible at approximately 800 and 1050 kN for joints X8 and X2. There is no data available from LVDT 12 that describes the downward part of the curve.

Figure 4.12 shows the results of the four LVDTs located on the steel frame. The four displacement measurements are averaged. The increased yield strength and reduced ductility of steel grade S500 in comparison to S355 is clearly visible.

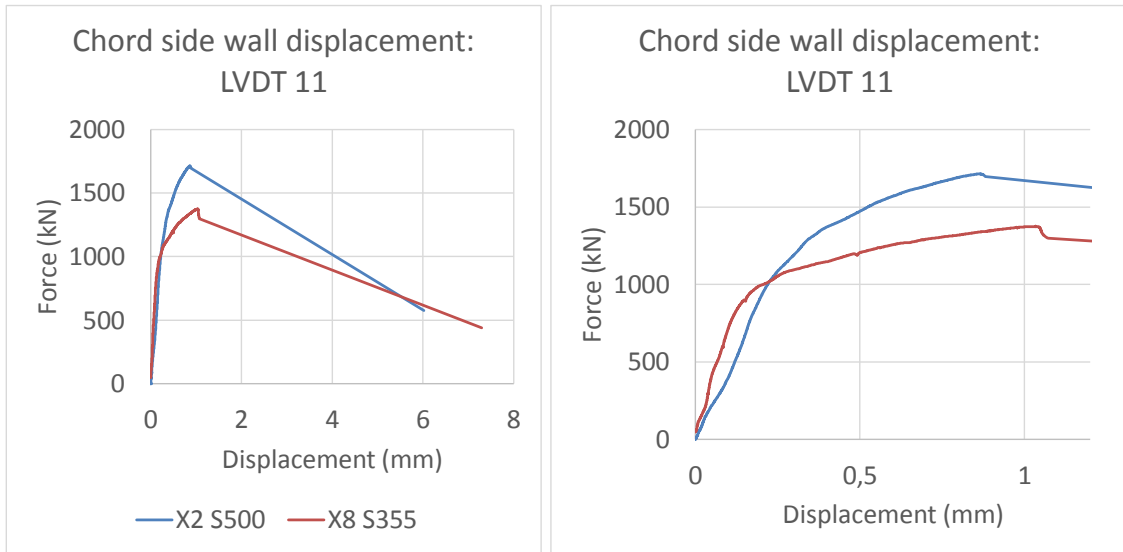


Figure 4.10: Experimental results chord side wall displacement: overview (left) and detail (right)

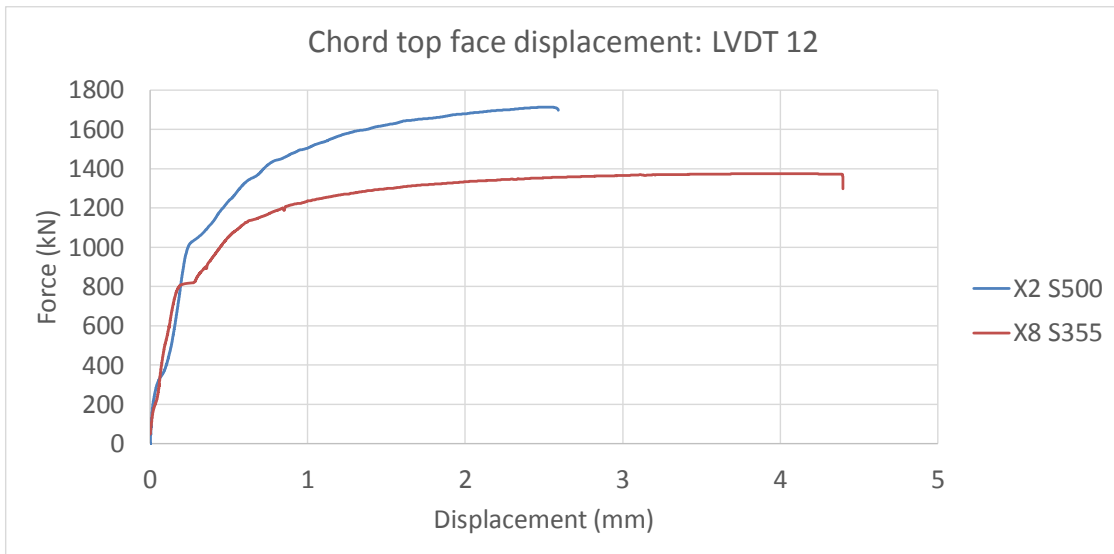


Figure 4.11: Experimental results chord top face displacement

The steel frame has an initial spacing of 380 mm. Literature commonly describes the 3% deformation limit based on the chord width b_0 . However, for X joints the displacement is based on the vertical displacement of the two black points shown in Figure 4.13, which is in the same direction as h_0 . Therefore, it is more reasonable to use h_0 instead of b_0 . Joints X2 and X8 are both SHS which

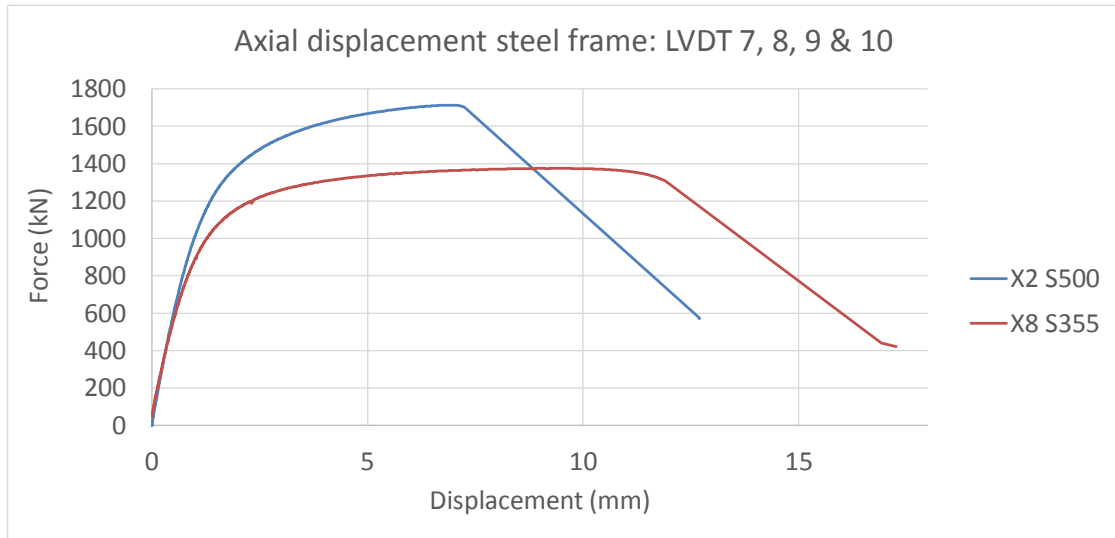


Figure 4.12: Experimental results axial displacement steel frame

means that h_0 is equal to b_0 in this case. To include the 3% deformation limit based on the steel frame LVDTs, the distance between the measuring points should be 2 times h_0 for X joints, which results in a distance of 300 mm for both joints. Therefore, the LVDT data of the steel frame cannot be used to compare against the 3% deformation limit. To compare the experimental results to the 3% deformation limit, the results from DIC are used.

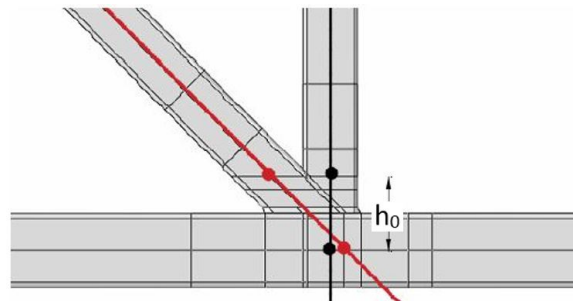


Figure 4.13: Measuring points to compare to the 3% deformation limit [36]

To obtain the results from DIC, 2 points are defined with an initial distance of 150 mm (h_0), which is in agreement with Figure 4.13. The 2 points that are defined for joint X8 are visible in Figure 4.14. The coordinate axis is transformed in such a way that the axial displacement of the braces is in X-direction, see left bottom of Figure 4.14 for the coordinate system. The results are presented in Figure 4.15. It has to be noted that the force obtained through DIC is 17,5 kN (1%) lower for joint X2 compared to the force that is recorded through the test set-up. This difference is 1,3 kN (0,1%) for joint X8. Joint X2 fails before the 3% limit is reached, while joint X8 reaches the 3%

deformation limit at a force of 1362 kN. The plastic deformation in the chord side wall of joint X8 is represented by the horizontal plateau in Figure 4.15.



Figure 4.14: DIC data points for comparison to the 3% deformation limit

Table 4.3 shows the predicted resistance from Eurocode (F_{EC3}) [19]. This prediction is based on the real measured yield strength (real σ_y) including and excluding the material reduction factor (C_f), and the nominal yield strength (nominal σ_y) according to the standard including and excluding the material reduction factor. These values are presented by the horizontal dashed lines in Figure 4.15.

In literature [5, 35, 39, 49] LVDT measurements are commonly used to compare against the 3% deformation limit. In the experiments of joints X2 and X8, is the observed chord side wall displacement around 1 mm and therefore not close to the 3% deformation threshold of 4,5 mm. This limit is therefore not governing. The chord top face displacement of LVDT 12 is included in Figure 4.15 for the sake of comparison to the results of the 3% deformation limit based on Figure 4.13.

Table 4.3: Eurocode prediction for joint X2 and X8

	X2 - S500			X8 - S355		
	σ_y	C_f	F_{EC3}	σ_y	C_f	F_{EC3}
	[MPa]	[-]	[kN]	[MPa]	[-]	[kN]
real σ_y , incl. C_f	615	0,8	1169	451	0,9	964
real σ_y , excl. C_f	615	1,0	1328	451	1,0	974
nominal σ_y , incl. C_f	500	0,86	1022	355	1,0	767
nominal σ_y , excl. C_f	500	1,0	1080	355	1,0	767

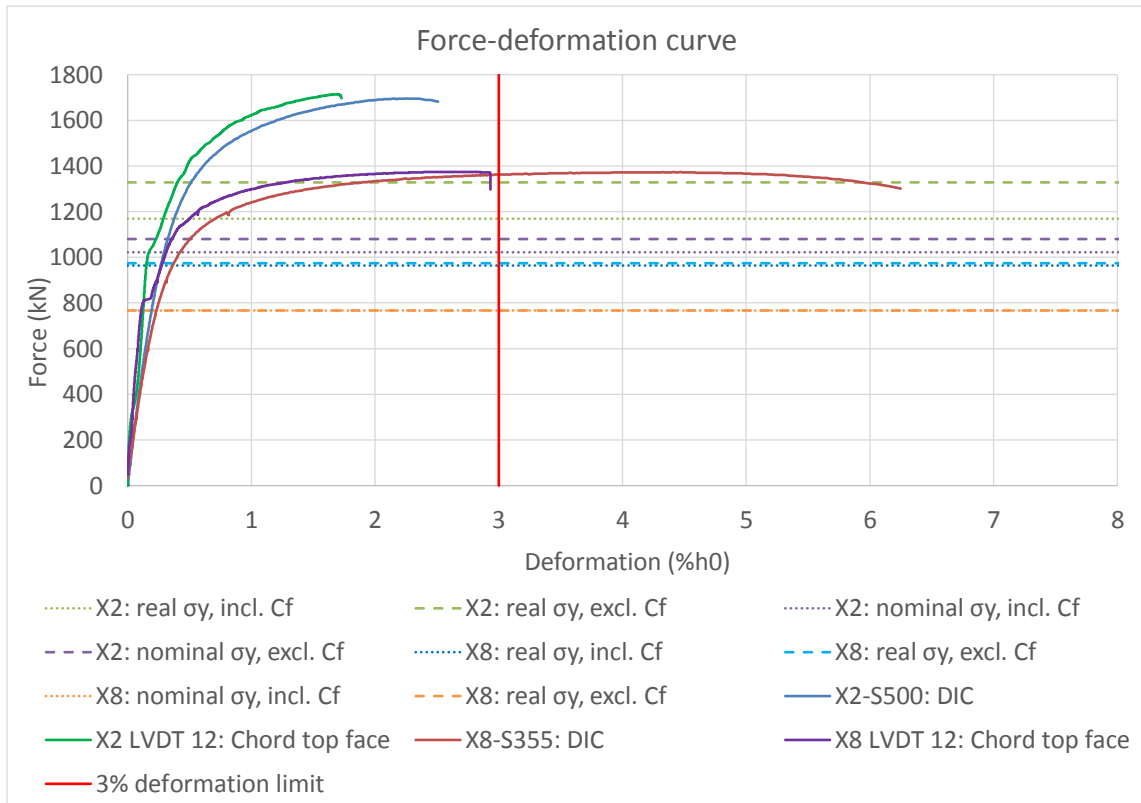


Figure 4.15: Force-deformation curves X joints

4.2.1 Strain development joint X2

The strain development is analysed by DIC along two section lines. The section lines (section 1 and section 2) are presented in Figure 4.16. The strain is obtained from four points along the force-deformation curve: deformation at $1\%h_0$, $1,5\%h_0$, $2\%h_0$ and at failure (see Figure 4.15). The strain development is presented in Figure 4.18. Characteristic areas in the strain development along the joint are indicated. The strain distribution of joint X2 is presented in Figure 4.17, with an indication of the characteristic areas observed in Figure 4.18. The legend of Figure 4.17 is set to 10% strain to make the characteristic areas along the section lines clearly visible.

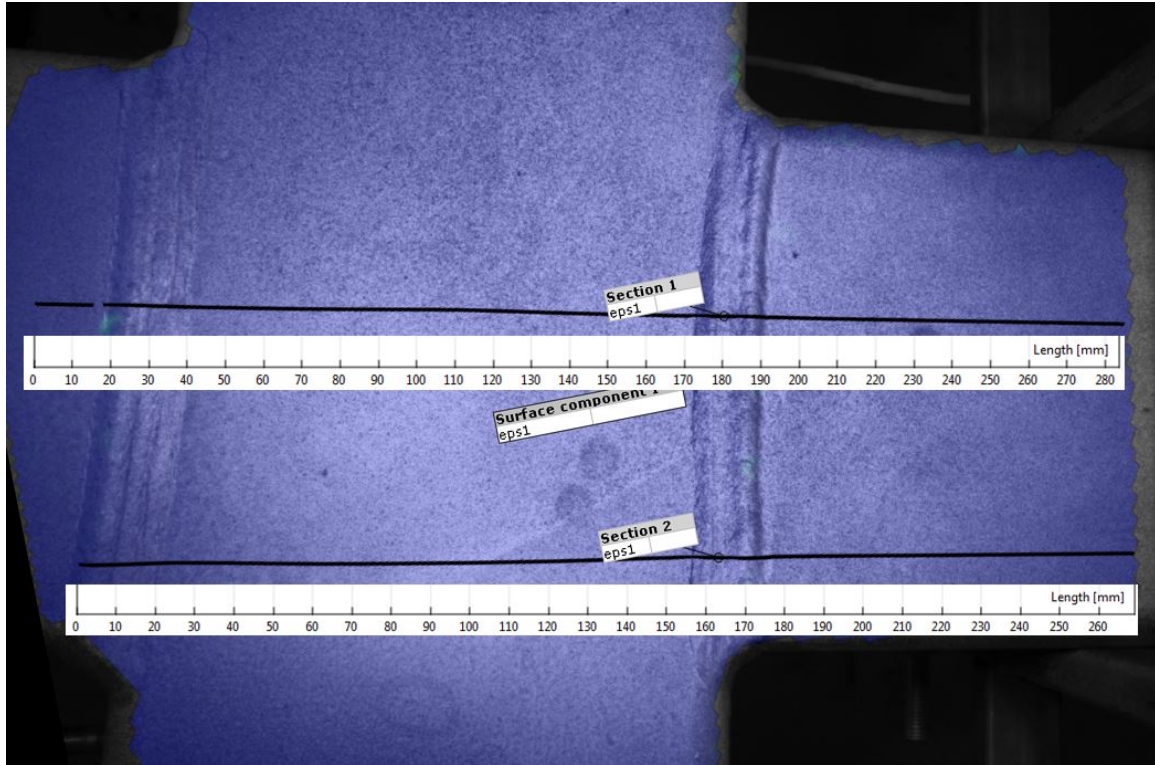


Figure 4.16: Section lines and length scale joint X2

The strain profiles show that strain is developing at certain areas along the section lines, see Figures 4.17 and 4.18. Around the weld areas strains are developing on both sides of the filler metal, respectively the chord and brace member side. Higher strains are observed on the sides of the brace members compared to the sides of the chord member. Brace failure (BF) is occurring in the heat affected zone of the right brace member. In section 1, strains are occurring in the centre of the chord side wall with a maximum value of 5%. Two small peaks are visible in section 2 which represent the strain distribution in the chord side wall with values close to 5%. The observed strain at fracture is 17%.

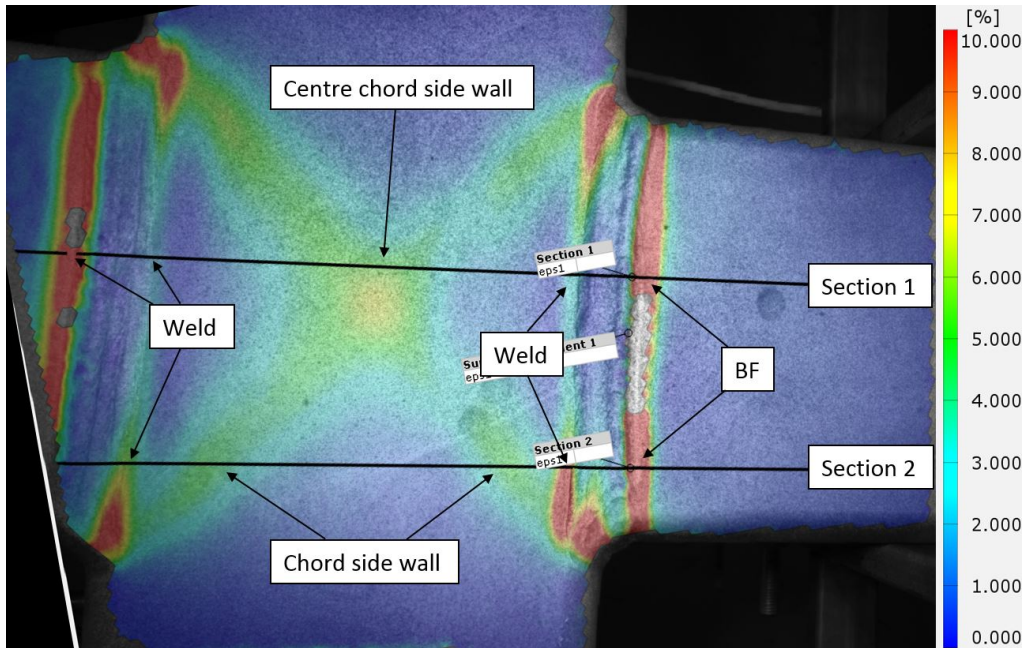


Figure 4.17: Strain distribution joint X2

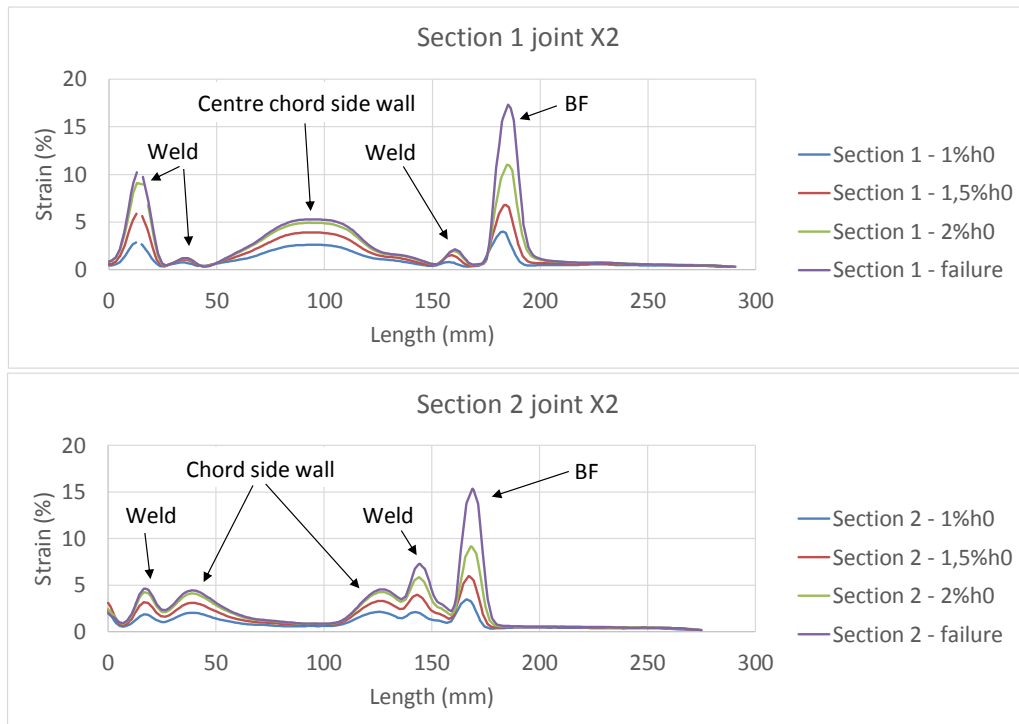


Figure 4.18: Strain development along section lines joint X2

4.2.2 Strain development joint X8

The same analysis procedure to obtain the strain development of joint X2 is applied for joint X8. The section lines (section 1 and section 2) are presented in Figure 4.19. The strain is obtained from four points along the force-deformation curve: deformation at $3\%h_0$, $4\%h_0$, $5\%h_0$ and at failure (see Figure 4.15). The strain development is presented in Figure 4.21. Characteristic areas in the strain development along the joint are indicated. The strain distribution of joint X8 is presented in Figure 4.20, with an indication of the characteristic areas observed in Figure 4.21. The legend of Figure 4.20 is set to 10% strain to make the characteristic areas along the section lines clearly visible.

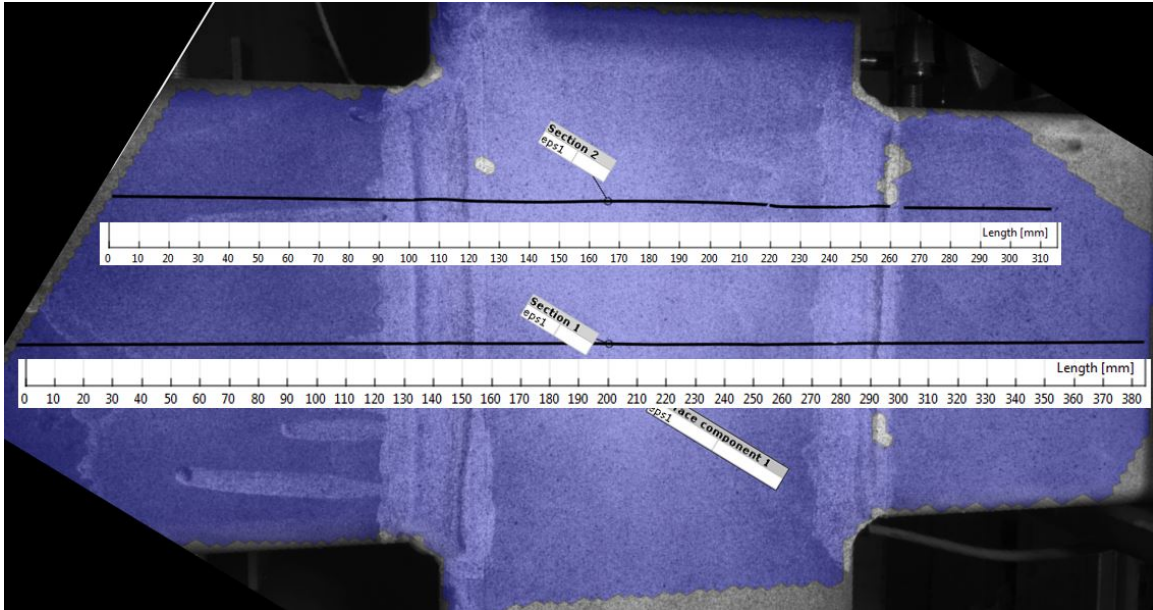


Figure 4.19: Section lines and length scale joint X8

The strain profiles show that strain is developing at certain areas along the section lines, see Figures 4.20 and 4.21. Around the weld areas strains are developing in the range of 3%-6% on the brace member sides of the filler metal. This is different in comparison with joint X2, where strains are developing on both sides of the filler metal. Two small peaks, with strain values of 3%-4%, are visible in section 2 which correspond to the chord side wall. In section 1, strains are occurring in the centre of the chord side wall with a maximum strain level close to 10%. This area is close to the final fracture area. Chord side wall failure (CSWF) is the governing failure with an observed fracture strain of 38%.

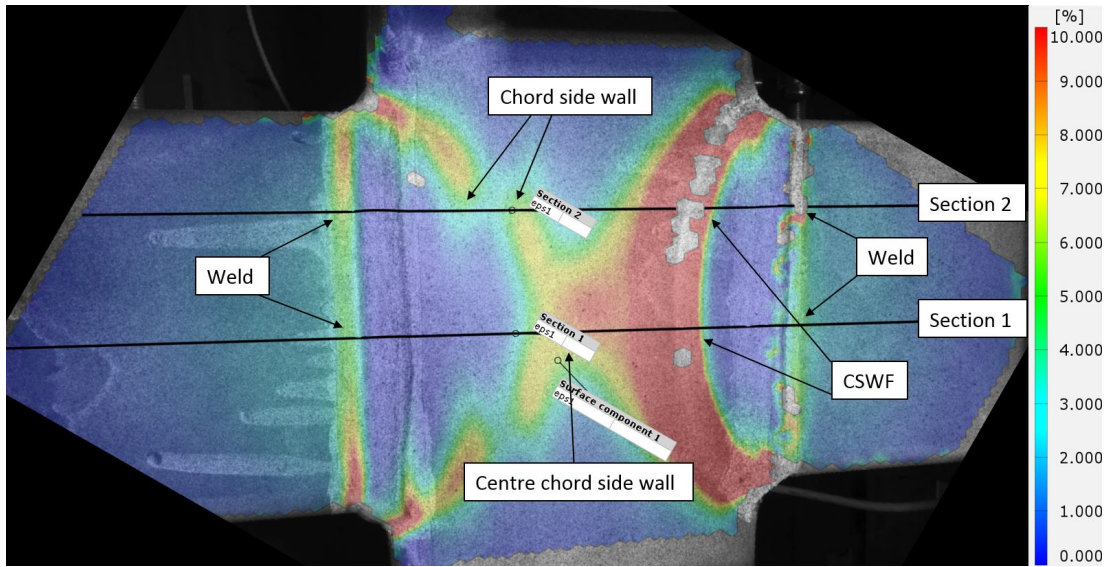


Figure 4.20: Strain distribution joint X8

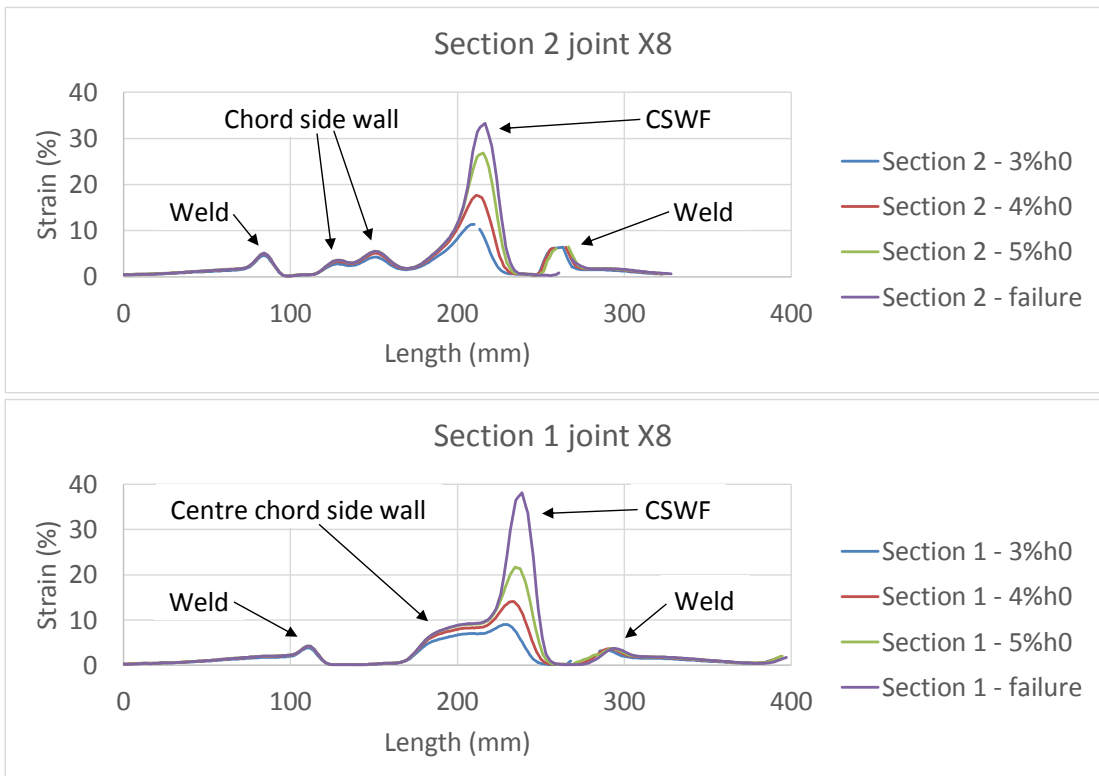


Figure 4.21: Strain development along section lines joint X8

Chapter 5

Finite element analysis X2 and X8

The X joints that are tested, X2 and X8, are modelled by finite element method in the ABAQUS software. The experimental results of joint X2 and X8 are used to validate the finite element model (FEM). In order to save calculation time, one quarter of the full X joint is modelled. The explicit solver is applied in this analysis. Reason for the use of the explicit solver are convergency problems observed in the modelling process, these problems are due to the complexity of the X joint model. The implicit solver gives the same result as the explicit solver. Proof for this statement is presented in Appendix C.

5.1 Geometry properties

The geometry parameters of the chord and brace members can be seen in Table 5.1. The finite element model is presented in Figure 5.1. r_{in} is the inner radius of the chord and brace member. r_{out} is the outer radius of the chord and brace member. $t_{w,fillet}$ is the leg length of the additional fillet weld, the fillet weld is modelled as a triangle. r_{in} , r_{out} and $t_{w,fillet}$ are based on the measurement dimensions of joint X2. In the real X joints, there is some additional filler material on the weld that connects the chord side wall to the brace member, see Figure 5.2. This additional material is disregarded in the finite element model. L_0 and L_1 represent the length of the chord and brace members.

Table 5.1: Geometry parameters X joint FEM

Parameters	[mm]
t_0/t_1	6
$h_0/h_1/b_0/b_1$	150
r_{in}	7
r_{out}	13
L_0	1500
L_1	752
$t_{w,fillet}$	7

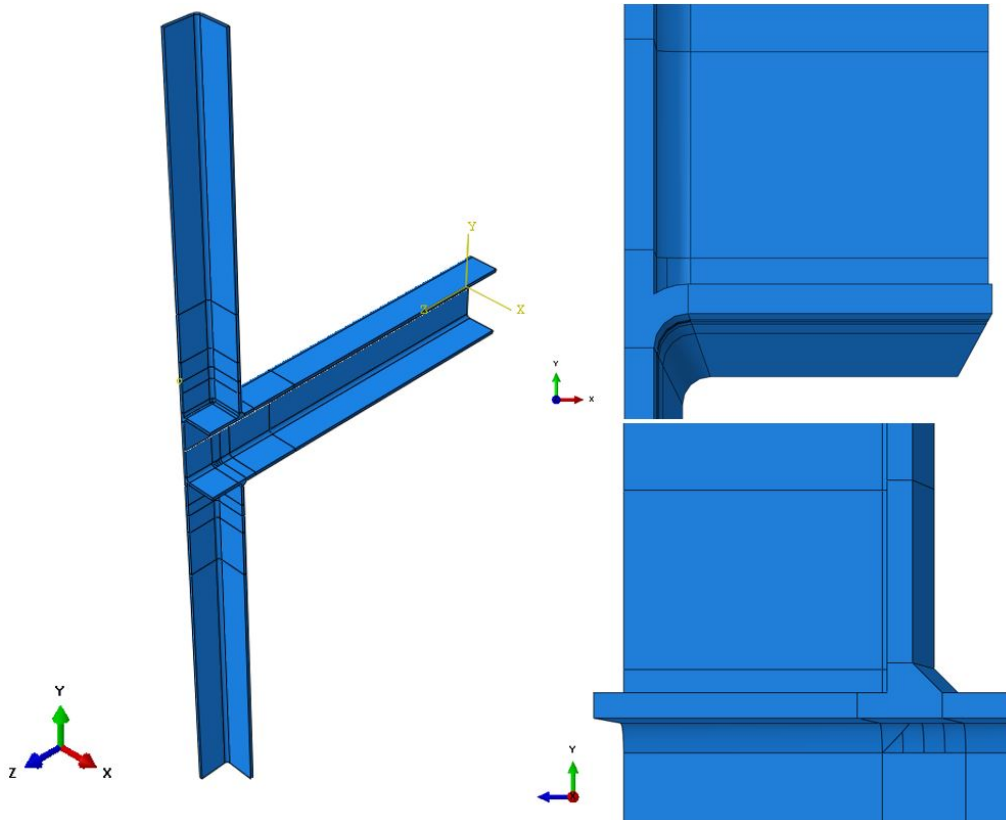


Figure 5.1: FEM X joint



Figure 5.2: Joint X2

5.2 Boundary, loading and symmetry conditions

Figure 5.3 shows the boundary conditions of the FEM. The boundary and loading condition are applied using a MPC constraint of type BEAM. A reference point at the centre location of the full brace member is used. The surface of the brace member is used as slave surface. At the bottom brace member, a pinned boundary conditions is applied. At the top brace member, is the loading condition modelled by applying a displacement in Y/U2-direction. All the other degrees of freedom (U1, U3, UR1, UR2, UR3) at the reference point where the load is applied are set to zero, to make sure that the load is applied correctly on the quarter model. Symmetry conditions are applied to assure that the quarter model represents the full X joint connection. These conditions are applied in X-direction ($U1=UR2=UR3=0$) and Z-direction ($U3=UR1=UR2=0$). The X-direction symmetry conditions are applied on the through-thickness surfaces where the X-axis is located in normal direction, see green surfaces Figure 5.3. For the Z-direction symmetry conditions, is the Z-axis located in normal direction on the through-thickness surfaces, see red surfaces Figure 5.3.

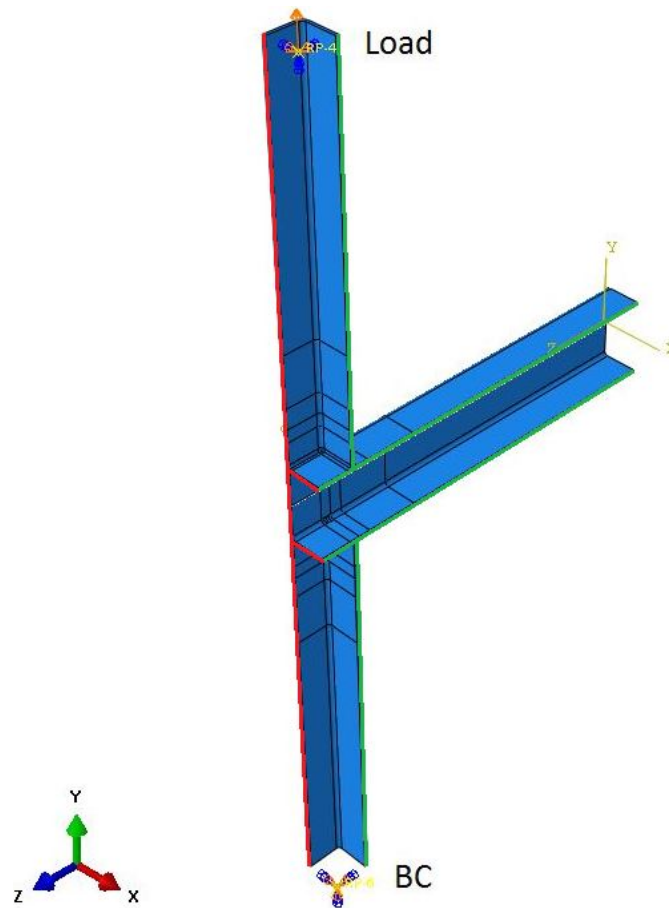


Figure 5.3: Boundary and loading conditions FEM X joint

5.3 Material properties

The material properties are obtained from coupon experiments, see section 3.11.1. Table 5.2 represents the characteristic values of the materials S355 and S500. Figure 5.4 represents the engineering stress-strain curves. The curves are first transformed to true plastic strains and stresses by Equations 3.2, 3.3 and 3.4 before it is implemented in ABAQUS. Poisson’s ratio of 0,3 and mass density of 7850 kg/m³ is introduced. Non-linear geometry effects are included in the analysis.

Table 5.2: Characteristic values material properties

Steel grade	E [GPa]	σ_y [MPa]	σ_u [MPa]	ϵ_f [-]
S355	182	451	518	0,28
S500	186	615	673	0,22

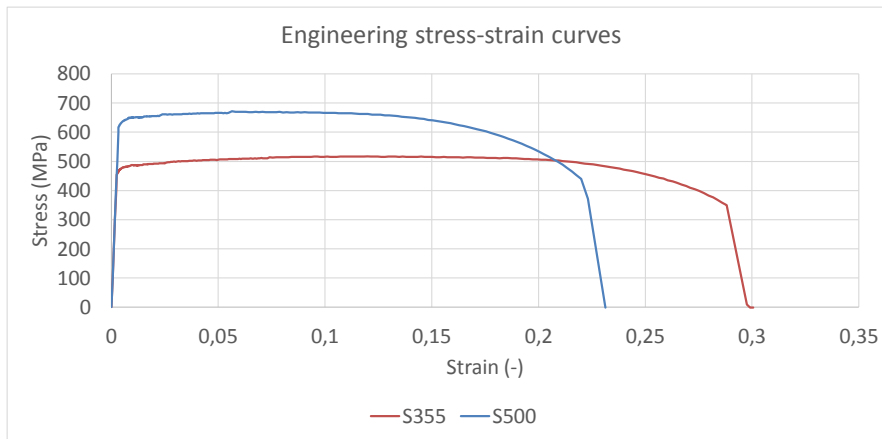


Figure 5.4: Engineering stress-strain curves S355 and S500 from coupon experiments

5.4 Meshing

For the meshing, linear 8-node brick elements with reduced integration (C3D8R, hex-elements) and 10-node modified quadratic tetrahedron (C3D10M, tet-elements) are applied. Partitioning is applied to gradually increase the mesh size to save calculation time. The fine mesh contains elements of 3 mm. In the brace member, regions are introduced with tet-elements to create a transition between the fine and coarse mesh to reduce the number of elements. The meshing is visible in Figure 5.5.

To make a smooth transition between the additional fillet weld and the chord/brace side wall, a corner element is created. This corner element with meshing is visible in Figure 5.6. The corner element contains a complex geometry. For that reason, partitioning is applied to make sure that hex-elements could be applied for the meshing of the corner.

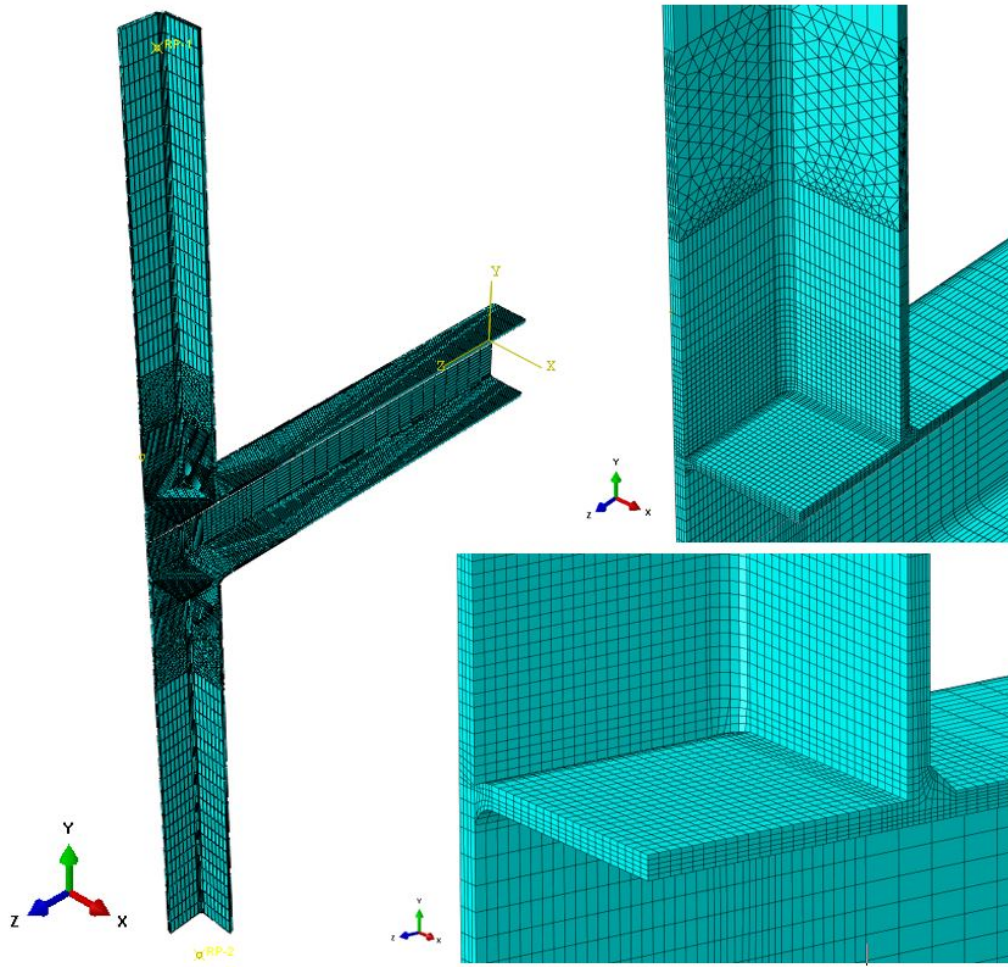


Figure 5.5: FEM meshing X joint

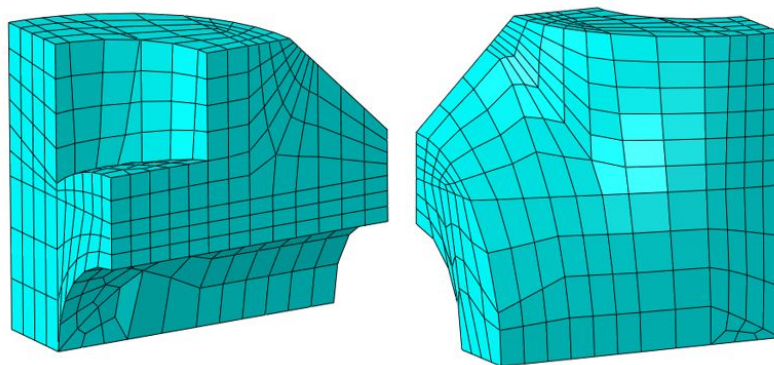


Figure 5.6: FEM corner element

5.5 Results finite element analysis

The results of the finite element models are compared to the results from experiments X2 and X8. Firstly, the measurements of the four LVDTs, that are attached to the steel frame with an initial distance of 380 mm, are compared to the FEM results, see Figures 4.4 and 4.5 for the steel frame. The resulting force-displacement curves for the experiment and the FEM are presented in Figure 5.7. The characteristic values are presented in Table 5.3. The governing design resistance based on the real yield strength and including the material reduction factor is presented in this table by F_{EC3} . The full Eurocode 3 prediction is presented in Table 4.3. The calculation of the design resistance according to the Eurocode is presented in Appendix B.

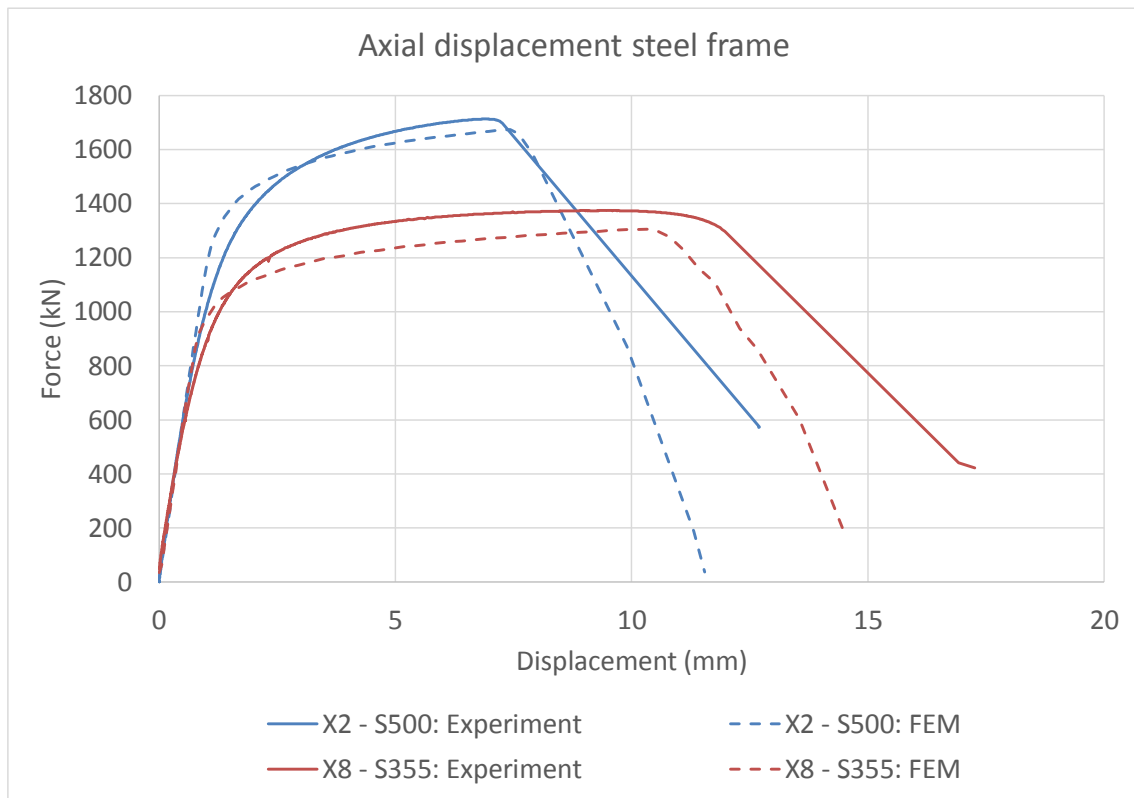


Figure 5.7: Force-displacement curves steel frame

Table 5.3: Results steel frame

Joint	Steel grade	$F_{u,exp}$ [kN]	$F_{u,fem}$ [kN]	F_{EC3} [kN]	$F_{u,exp}/F_{u,fem}$ [-]
X2	S500	1713	1674	1169	1,023
X8	S355	1374	1305	964	1,053

The results show a good agreement between the ultimate resistance of the experiment ($F_{u,exp}$) and the finite element model ($F_{u,fem}$). The ratio $F_{u,exp}/F_{u,fem}$ is 1,023 and 1,053 for X2 and X8. The force-displacement curves show a proper initial stiffness prediction of the connection for both X2 and X8.

The above described results show a good agreement between FEM and the experiments. In the next step the FEM results will be compared to the 3% deformation limit according to Figure 4.13. The results will be compared to the force-deformation curves obtained by DIC. $F_{3\%,exp}$ represents the force at the 3% deformation limit of the experiment, while $F_{3\%,fem}$ represents the limit obtained by FEM. Table 5.4 gives an overview of the results. It has to be noted that the force measurements from DIC are less accurate than the force recordings from the test machine. The ultimate recorded force by DIC is lower than the actual ultimate force, respectively 17,5 kN (1%) and 1,3 kN (0,1%) lower for X2 and X8.

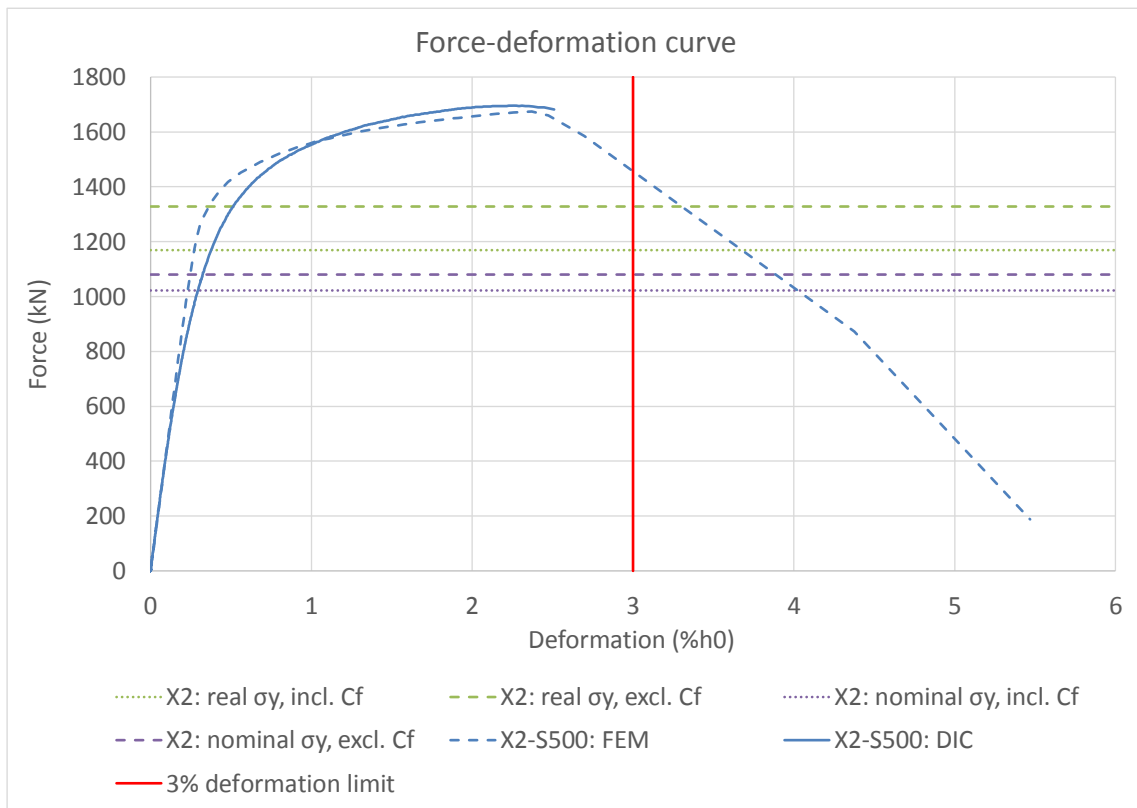


Figure 5.8: Force-deformation curves joint X2

The curves show a good agreement for joint X2, see Figure 5.8. The 3% deformation limit is not reached before fracture occurs. For joint X8, see Figure 5.9, is the result in agreement up to around 3,5% deformation, after that point the FEM fails while the experiment undergoes more plastic deformation before final fracture. The ratio $F_{3\%,exp}/F_{3\%,fem}$ results in a value of 1,048 for joint X8. The horizontal lines in Figures 5.8 and 5.9 represent the Eurocode predictions according to Table 4.3.

Table 5.4: Results based on the 3% deformation limit

Joint	Steel grade	$F_{3\%,exp}$ [kN]	$F_{3\%,fem}$ [kN]	F_{EC3} [kN]	$F_{3\%,exp}/F_{3\%,fem}$ [-]
X2	S500	-	-	1169	-
X8	S355	1362	1300	964	1,048

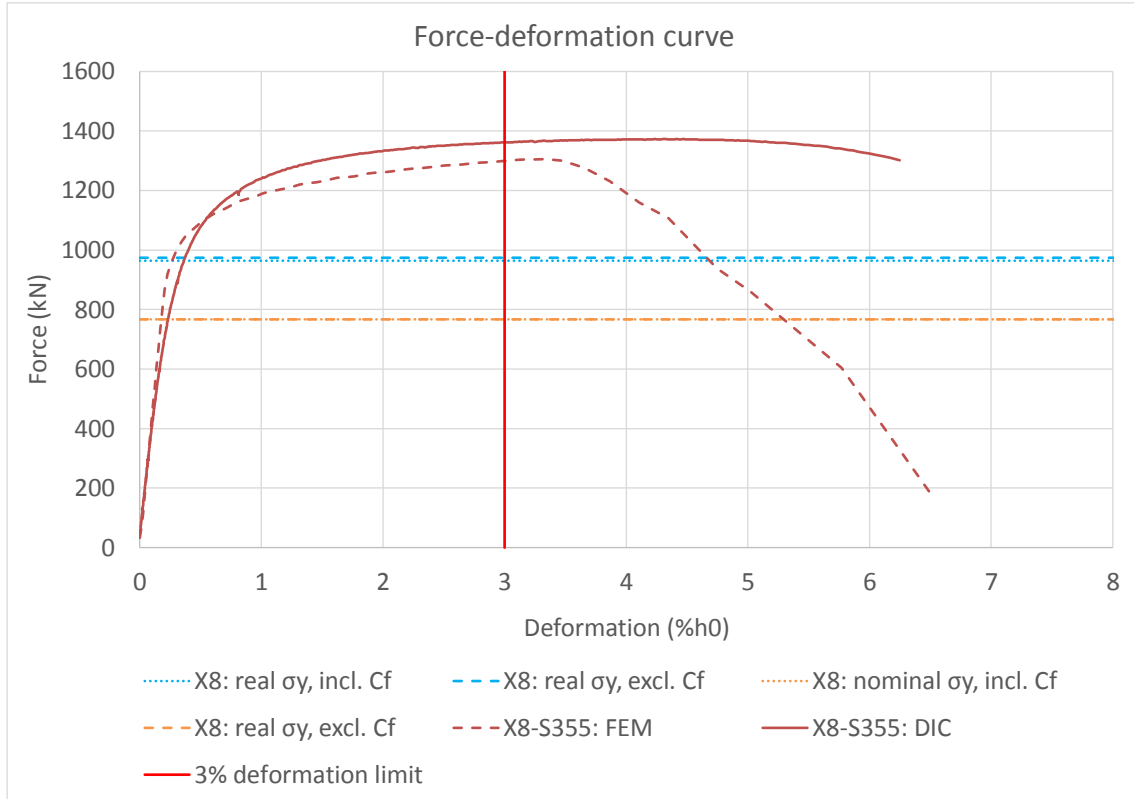


Figure 5.9: Force-deformation curves joint X8

The failure modes occurring in the experiments are compared to the failure modes from FEM. An overview table of the failure modes, brace failure (BF) or chord side wall failure (CSWF), is given in Table 5.5. For joint X8, the Eurocode predicts a resistance of 964 kN for BF and 974 kN for CSWF. The design resistances are so close to each other that it is possible that either one of the failure modes can occur. For joint X2 is BF predicted. For CSWF there is no material reduction factor included in the design equation. However, this is the case for BF.

Joint X2 resulted in BF in the experiment. The FEM resulted in CSWF. The strain distribution at the moment before failure for experiment and FEM is visible in Figure 5.10. During the experiment the failure occurred in the heat affected zone above the weld material in the brace mem-

ber. In the model is one material property applied for the full model. There is no distinction made between the material properties of the base material, heat affected zone and weld material. This is disregarded due to the complexity of the corner element of the model, see Figure 5.6. This could be the reason why the failure mode of the experiment does not agree with the failure mode of the FEM. Joint X8 resulted in CSWF for both the experiment and FEM, see Figure 5.11.

Table 5.5: Failure mode obtained by experiment, FEM and Eurocode

Joint	Steel grade	Experiment	FEM	EC3
X2	S500	BF	CSWF	BF
X8	S355	CSWF	CSWF	BF/CSWF

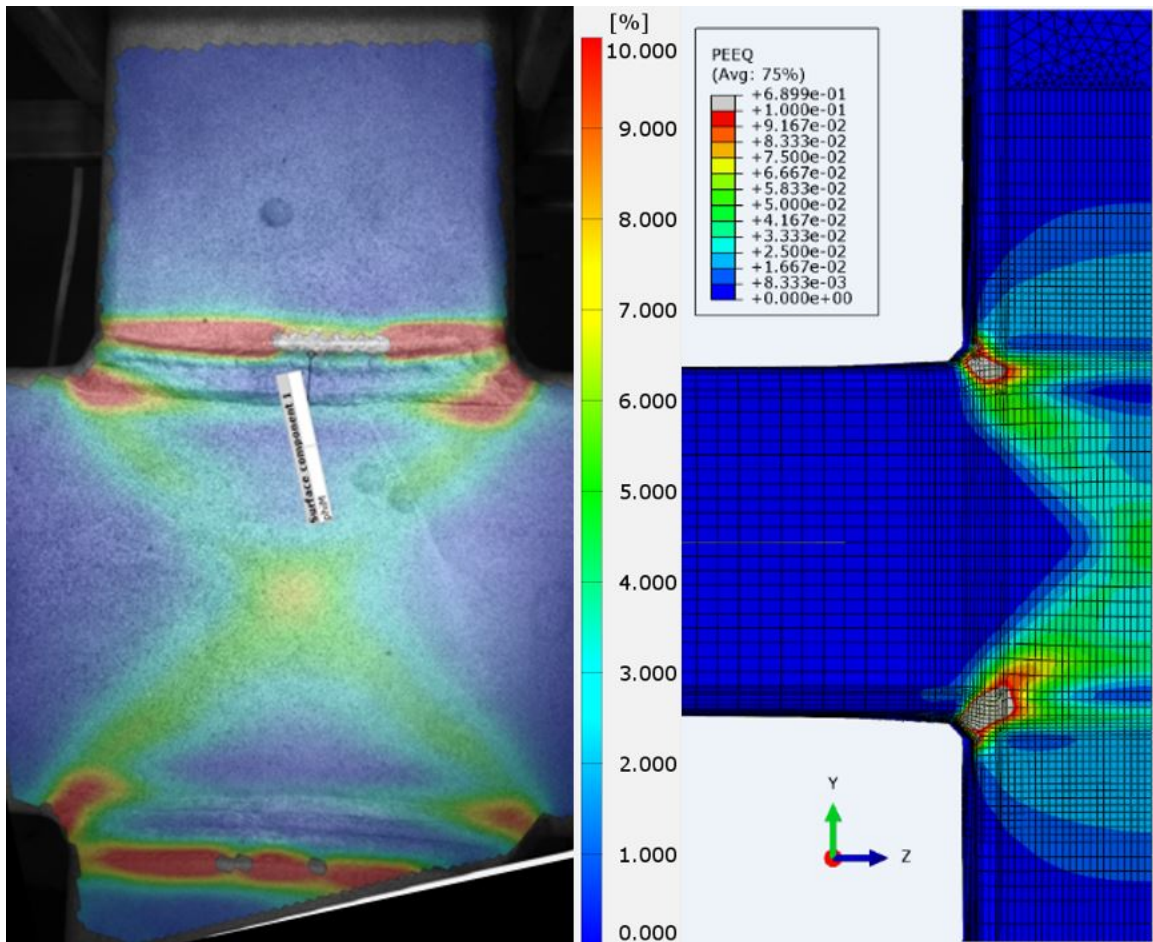


Figure 5.10: Strain distribution joint X2 for experiment (left, equivalent Mises strain) and FEM (right, plastic equivalent strain)

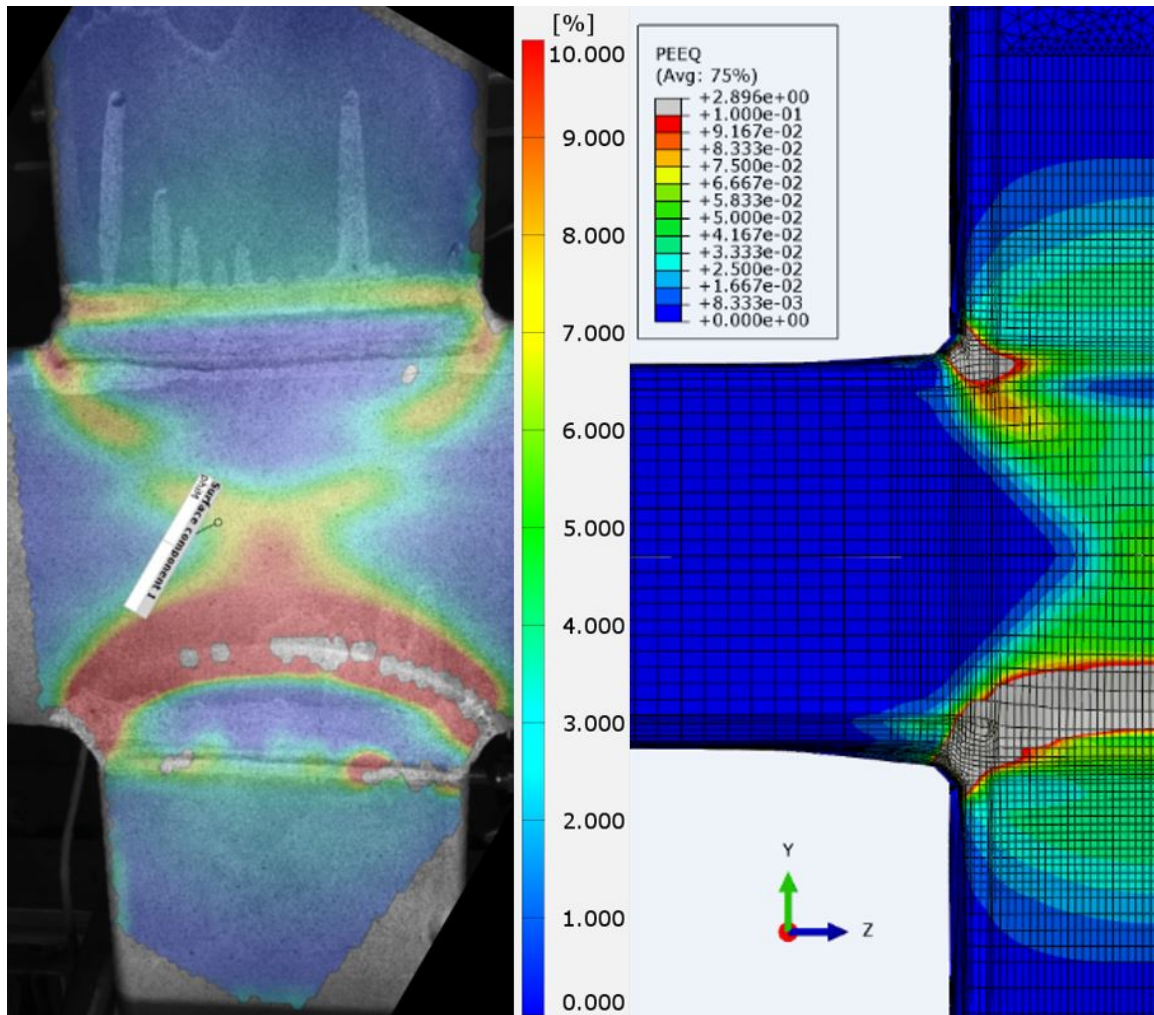


Figure 5.11: Strain distribution joint X8 for experiment (left, equivalent Mises strain) and FEM (right, plastic equivalent strain)

The fracture strain applied for the material property in FEM, see Table 5.2, is lower than the real observed fracture strain during the coupon experiments, see Table 3.17. The material property after necking is not correctly implemented in FEM. This is the reason why the deformation of the coupon FEM results turned out to be lower than the experimental coupon results, see Section 3.9.6. Therefore it is expected that the deformation of the full scale X joints FEM would be lower than the observed results during the experiments. For joint X2, see Figure 5.8, the deformation of the FEM is close to the deformation observed by the experiment. For joint X8, see Figure 5.9, the deformation of the FEM is lower when compared to the experimental result. An explanation for this is the contribution of the localized deformation in the fracture zone to the total deformation. It is observed that the contribution of the deformation in the localized region contributed to 13% of the total deformation for joint X2. For joint X8 is this contribution 30%. The reason for this significant difference is that joint X2 failed by brace failure, which is a brittle failure mode and localized plastic

deformation occurred in the small region of the heat affected zone in the brace member. While joint X8 failed by chord side wall failure, which is a ductile failure mode and local plastic deformations occur in a larger region when compared to the failure of joint X2. This means that the influence of the properties after necking on the FEM result is more significant for joint X8 in comparison to joint X2. This explains the good deformation prediction of the FEM for joint X2 and the difference observed for joint X8.

5.5.1 Stress triaxiality

The fracture strain is observed through evaluation of DIC and results in fracture strains of 38% for joint X8 (S355) and 17% for joint X2 (S500). For the coupon experiments is the observed fracture strain in the range of 104%-108%. It is investigated if this difference can be explained by the stress triaxiality (η).

For the coupon experiments the stress triaxiality is determined based on the FEM results, see Section 3.9. The stresses in the three principal directions are extracted from the fracture location in the model and the triaxiality is determined according to Equations 2.2, 2.3, 2.4 and 2.5. The results are presented in Table 5.6. The results show that the stress triaxiality for the tensile coupons is around 0,33, which is in agreement with Figure 2.12. This indicates that uniaxial tension is occurring.

Table 5.6: Stress triaxiality coupon experiments

Coupon specimen	Stress triaxiality [-]
T63-A	0,32-0,35
T93-B	0,31-0,33
T103-A	0,32-0,34

To determine the stress triaxiality of the X joints, the models are implemented in the 2019 version of ABAQUS, where the triaxiality can be selected as one of the output options. The results of the stress triaxiality is extracted for the following four points on the X joint:

1. Brace side wall;
2. Brace side wall above the weld;
3. Chord side wall where failure is occurring in the model;
4. Corner element where failure starts.

The points are indicated in Figure 5.12. The extracted stress triaxiality for the four points is plotted against the time steps of the model. The result for joint X8 is shown up to the moment of failure and is presented in Figure 5.13. For the sake of clarity is the force development in relation to the time steps of the model presented in Figure 5.14. Contour plots of joint X8 are presented in Appendix D in Figures D.3 and D.4 for time steps 20, 40, 60 and at failure.

As expected, the result for the brace side wall (point 1) gives values around 0,33, which means that at this location only tension stresses occur. This point is shown for the sake of comparison.

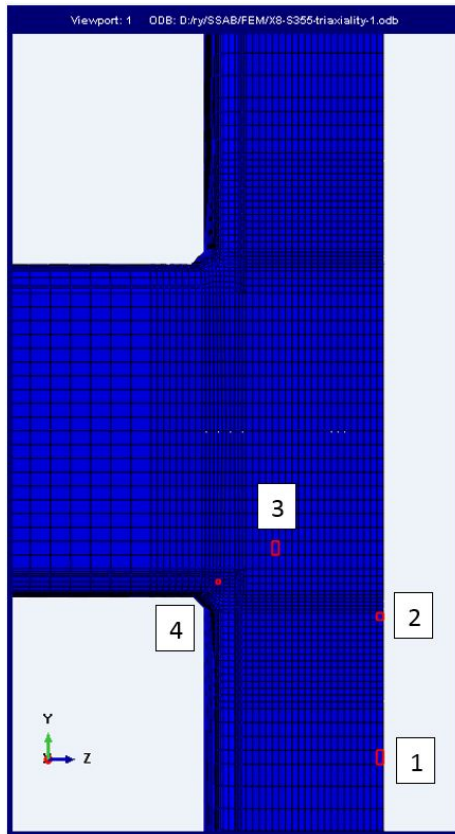


Figure 5.12: Points at which stress triaxiality is extracted on the X joints

The values obtained for points 2, 3 and 4 are slightly higher with values around 0,5. This means that the loading conditions are going towards biaxial tension ($\eta = 0,66$). For joint X8 is fracture starting at the corner (point 4) and extending through the chord side wall (point 3). The observed larger stress triaxiality of these points in comparison with the result of point 1 indicate a higher complexity of the stress state.

The result of joint X2 is presented in Figure 5.15. The force development against the time step in FEM is presented in Figure 5.16. Contour plots of joint X2 are presented in Appendix D in Figures D.7 and D.8 for time steps 40, 50, 60 and at failure. The result of joint X2 is approximately the same as the result obtained for joint X8. This can be explained by the similar observed failure mode of chord side wall failure in FEM. While in the experiment of joint X2 brace failure occurred in the heat affected zone, which results in the small fracture strain of 17%.

When looking at the fracture strains of the coupon specimens (104%-108%) and joints X8 (38%) and X2 (17%), it is clear that the fracture strain observed in the X joints is less in comparison with the coupon specimens. The higher stress triaxiality at the fracture locations of joint X8 supports the decrease in fracture strain observed in the X joint experiment. The small fracture strain of joint X2 is dedicated to the failure in the heat affected zone.

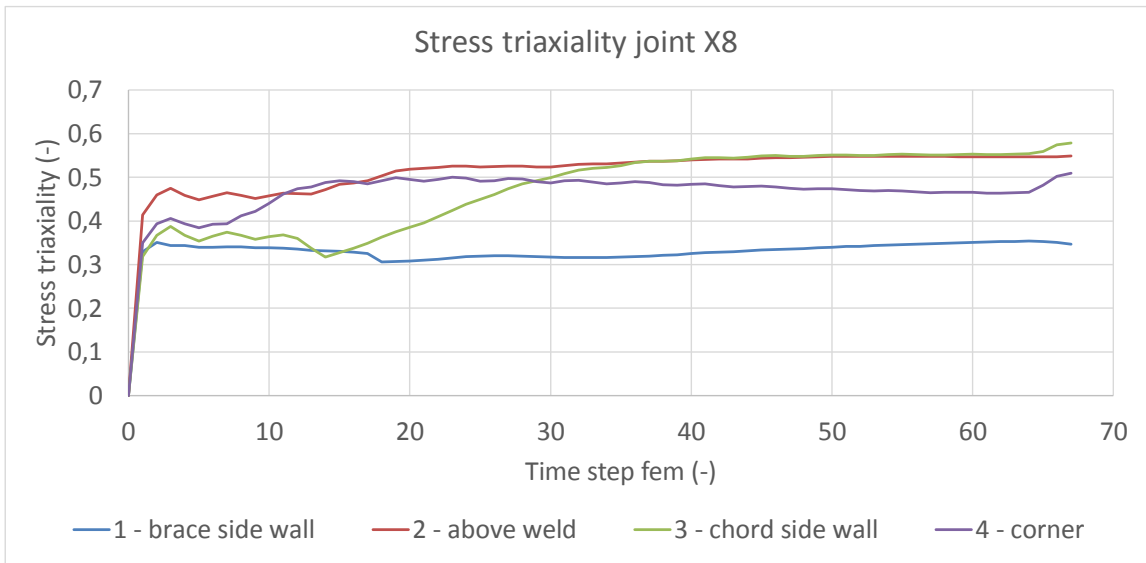


Figure 5.13: Stress triaxiality of joint X8

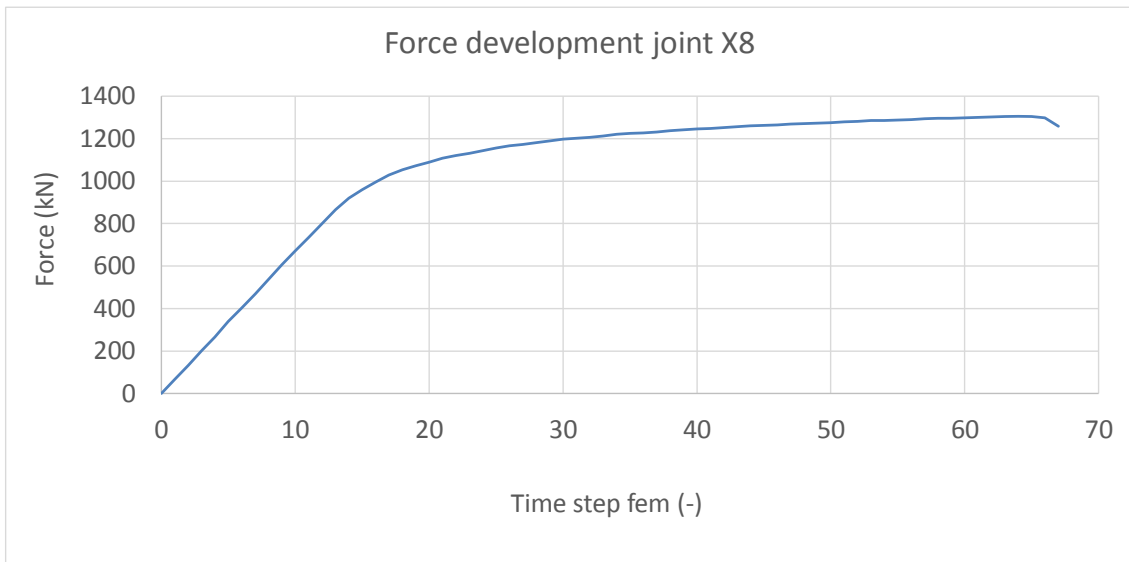


Figure 5.14: Force development against time steps FEM of joint X8

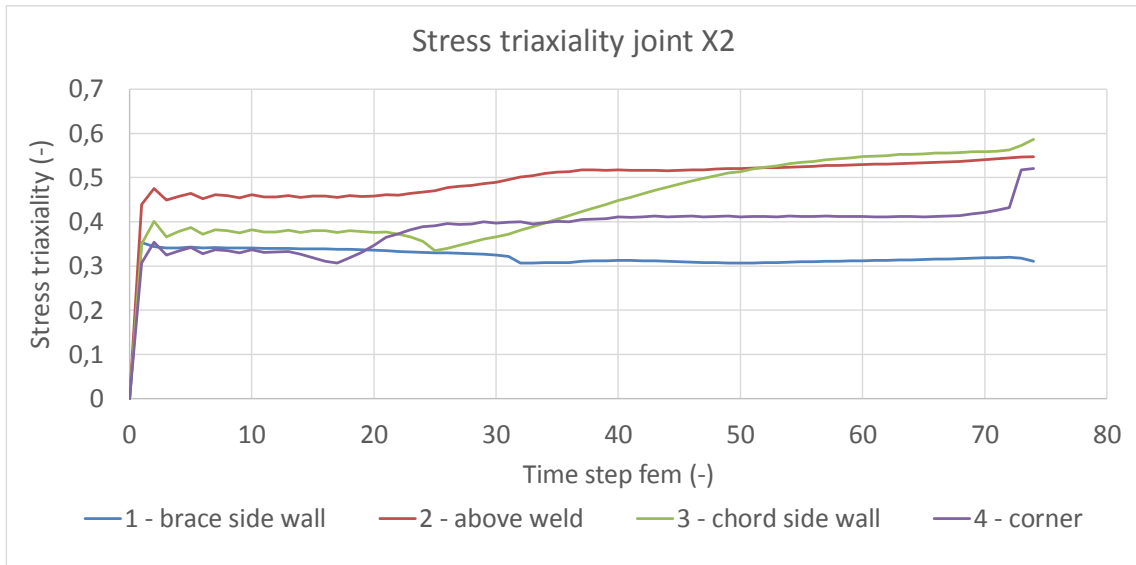


Figure 5.15: Stress triaxiality of joint X2

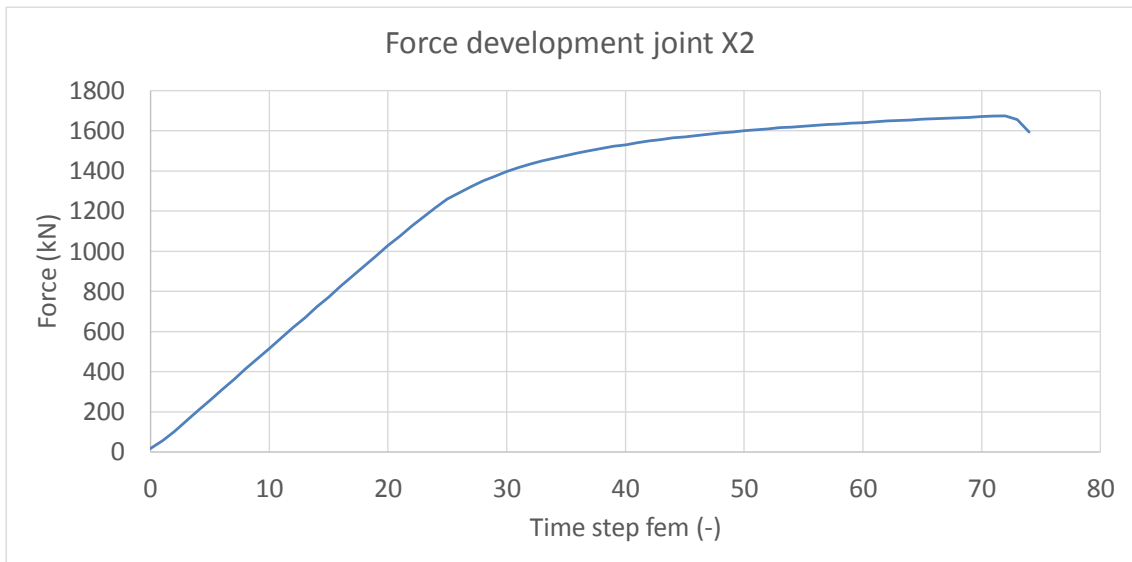


Figure 5.16: Force development against time steps FEM of joint X2

5.6 Conclusions finite element analysis and experiments X2 and X8

An overview of the obtained results is presented in Table 5.7. The governing resistance, either the ultimate resistance or the 3% deformation limit, is 1713 kN for joint X2 and 1362 kN for joint X8. The finite elements results confirm the experimental data with obtained differences in the joint resistance of 2,3% and 4,8% for joints X2 and X8. It is observed that different failure modes occur with different steel grades, S355 results in chord side wall failure while S500 results in brace failure.

Table 5.7: Overview results joints X2 and X8

Joint	Steel grade	F_{exp}	F_{fem}	F_{exp}/F_{fem}	ϵ_f	Failure mode
		[kN]	[kN]	[-]	[%]	
X2	S500	1713	1674	1,023	17	BF
X8	S355	1362	1300	1,048	38	CSWF

The fracture strain, which is evaluated by DIC, is 17% for joint X2 and 38% for joint X8. The small fracture strain of joint X2 is due to the brittle failure in the heat affected zone. The observed fracture strain in the coupon experiments (104%-108%) is significantly larger than the observed fracture strain for joint X8 (38%). The obtained values of the stress triaxiality, around 0,5 for joint X8 and 0,33 for the coupon experiments, support the lower observed fracture strain for joint X8 in comparison with the coupon experiments.

Table 5.8: Overview results X joint experiments compared to Eurocode [19] prediction

		F_{exp}	F_{EC3}	F_{exp}/F_{EC3}
		[kN]	[kN]	[-]
X2 - S500	real σ_y , incl. C_f	1713	1169	1,47
	real σ_y , excl. C_f	1713	1328	1,29
	nominal σ_y , incl. C_f	1713	1022	1,67
	nominal σ_y , excl. C_f	1713	1080	1,59
X8 - S355	real σ_y , incl. C_f	1362	964	1,41
	real σ_y , excl. C_f	1362	974	1,40
	nominal σ_y , incl. C_f	1362	767	1,78
	nominal σ_y , excl. C_f	1362	767	1,78

Table 5.8 shows the comparison between the experiments and the values predicted by the Eurocode [19]. The predictions are based on the (real or nominal) yield strength and (including or excluding) the material reduction factor (C_f). In all cases is the obtained resistance by experiments larger than the predicted resistance by Eurocode. The obtained resistance by experiments is 47% and 41%

larger than the Eurocode prediction for joints X2 and X8, based on the real measured yield strength and including the material reduction factor. These experiments indicate that for equal width SHS X joints (β of 1,0), the material reduction factors for steel grades S355 (σ_y is 451 MPa) and S500 (σ_y is 615 MPa) are not necessary.

The failure mode for joint X2, brace failure, is not correctly predicted by the finite element model. This can be explained by not including the real properties of the heat affected zone and filler metal in the finite element model. The failure mode of joint X8, chord side wall failure, is correctly predicted by the finite element model.

The results of the finite element model shows a good agreement with the experiment of joint X2. For joint X8, a lower deformation is observed when compared to the experiment. This is due to the incorrectly implemented material properties after the point of necking. The contribution of the localized deformation to the total displacement is more significant for joint X8 when compared to joint X2, respectively 30% against 13%. This explains the lower obtained deformation for joint X8 in the finite element model in comparison to the experimental result.

Chapter 6

Parametric study

This chapter describes a parametric study of square hollow section X joint connections. The ABAQUS software is used to perform the finite element analyses. The explicit solver is applied in this analysis. The design equations for hollow section joints that are provided by the newly proposed Eurocode [19] are validated for MSS. The new Eurocode applies the material reduction factors (C_f) to use the MSS validated formulas also for HSS up to S700. This parametric study intends to validate the design equation according to the standard.

6.1 Parameters

The parametric study investigates the behaviour of square hollow section X joints. Two parameters are varied in the parametric study, respectively the brace-to-chord width ratio (β) and the material properties.

The brace-to-chord width ratio greatly influences the strength of the connection. An increase in β will result in an increase in stiffness and strength. In total three β values are used in this parametric study varied from 0,3 to 0,7.

The material properties that are used in this parametric study range from S355 to S960. S960 is not a standard steel grade and is not included in the newly proposed Eurocode [19]. Nevertheless is this steel grade included in the parametric study. The parametric values used in this parametric study are presented in Table 6.1.

The following parameters are kept as constants: thickness chord (t_0), thickness brace (t_1), ratio of chord width to chord thickness (2γ). Fillet welds are adopted which are designed as single-sided full strength-welds.

Table 6.1: Parameters used in parametric study

Steel grade	S355, S460, S500, S700, S960
β -value	$\beta = 0,3, 0,5, 0,7$

6.2 Finite element model

6.2.1 Geometry

The geometry for the X joint is visible in Figure 2.29. The joint geometry used in the parametric study is visible in Table 6.2. To save calculation time, only a quarter of the full X joint is modelled in combination with symmetry conditions. The length of the brace members is based on 5 times the width (b_i) of the specific member. This length is used to make sure that the boundary conditions are not influencing the stresses in the critical zone [36].

Table 6.2: Parametric study joint geometry

β	h_0 [mm]	b_0 [mm]	t_0 [mm]	h_1 [mm]	b_1 [mm]	t_1 [mm]	$2\gamma = b_0/t_0$ [-]	$\tau = t_1/t_0$ [-]
0,3	200	200	6	60	60	6	33	1
0,5	200	200	6	100	100	6	33	1
0,7	200	200	6	140	140	6	33	1

Fillet welds are used to connect the brace members to the chord member. Full-strength welds are applied to ensure sufficient rotation and deformation capacity. The required throat thickness for single-sided filled welds, see equation 6.1 (section 2.3.2), is calculated and transformed to the minimal leg length of the weld (t_w). The calculation is made for materials '-1' and '-2' and assumed to be sufficient for the real obtained material properties by coupon experiments, see section 6.2.3. The values for β_w can be seen in Table 2.4. The Eurocode does not provide a β_w -value for S960. The value for S960 is obtained by linear interpolation [36]. The calculation is presented in Table 6.3. To save time during the modelling in ABAQUS, there is chosen to apply a fillet weld with a leg length of 13 mm for steel grades S355, S460 and S500. For steel grades S700 and S960 a fillet weld with a leg length of 18 mm is adopted. A numerical gap of 0,15 mm is used to ensure that the brace member is not in contact with the chord member.

$$a \geq 1,77 * \frac{\beta_w}{(f_u/f_y)} * t \quad (6.1)$$

Table 6.3: Full-strength weld calculation

	S355-1	S355-2	S460-1	S460-2	S500-1	S500-2	S700-1	S700-2	S960-1	S960-2
β_w [-]	0,90	0,90	0,85	0,85	0,90	0,90	1,10	1,10	1,24	1,24
f_u/f_y [-]	1,10	1,40	1,10	1,25	1,05	1,10	1,05	1,10	1,05	1,10
$a/t \geq$ [mm]	1,45	1,14	1,37	1,20	1,52	1,45	1,85	1,77	2,09	2,00
$a \geq$ [mm]	8,69	6,83	8,21	7,22	9,10	8,69	11,13	10,62	12,54	11,97
$t_w \geq$ [mm]	12,29	9,66	11,61	10,21	12,87	12,29	15,73	15,02	17,74	16,93

6.2.2 Boundary, loading and symmetry conditions

Figure 6.1 shows the boundary conditions of the finite element model. The boundary and loading condition are applied using MPC constraints of type BEAM. A reference point at the centre location of the full brace member is used. The surface of the brace member is used as slave surface. At the bottom brace member, a pinned boundary conditions is applied. At the top brace member, is the loading condition modelled by applying a displacement in Y/U2-direction. All the other degrees of freedom (U1, U3, UR1, UR2, UR3) at the reference point where the load is applied, are set to zero to make sure that the load is applied correctly on the quarter model. Symmetry conditions are applied to make sure that the quarter model represents the full X joint connection. These conditions are applied in X- and Z-direction, see Figure 6.1.

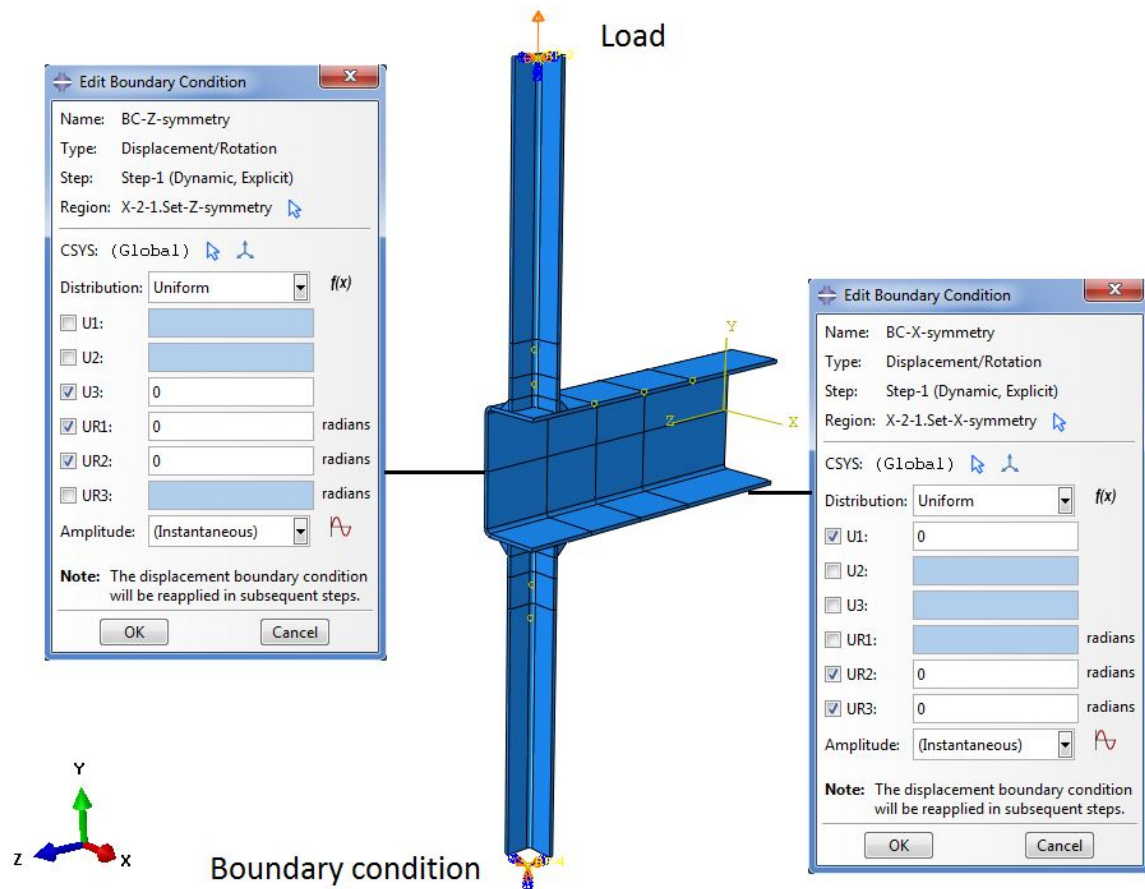


Figure 6.1: Boundary, loading and symmetry conditions FEM

6.2.3 Material properties

The material property is one of the parameters that is investigated in this study. The study contains steel grades ranging from S355 up to and including S960. For each steel grade, 2 alternatives are investigated. The first alternative, are the minimum requirements according to the Eurocodes, respectively EN1993-1-1 [14] and EN1993-1-12 [18]. This alternative is indicated by '-1'. So for example, the properties of steel grade S355 based on the minimum requirements of the Eurocode is indicated by S355-1. The second alternative for each steel grade is based on the nominal values from the standards. These properties are indicated by '-2'. The material properties are based on the properties used by Pavlović and Veljković [50]. The characteristic values of the material properties are given in Table 6.4. f_y is the yield strength, f_u is the tensile strength, $A_g (= 15\epsilon_y)$ is the strain at maximum stress and A_5 is the strain at fracture. The modulus of elasticity (210 GPa) is introduced for material-1 and material-2.

Besides these 2 options, the real material properties obtained from coupon experiments for steel grades S355, S500 and S700 are investigated as well, see Section 3.11.1. These properties are indicated by '-c'.

For all three material options is the Poisson's ratio (0,3) and density (7850 kg/mm³) introduced in the model. Non-linear geometry effects are included in the analysis

The engineering stress-strain curves are presented in Appendix E in Figures E.1 and E.2.

Table 6.4: Characteristic values material properties

Steel grade	f_y [MPa]	f_u [MPa]	f_u/f_y [-]	A_g [%]	A_5 [%]
S355-1	355	392	1,10	2,5	10
S355-2	355	497	1,40	15	30
S355-c	451	518	1,15	12	28
S460-1	460	507	1,10	3,3	15
S460-2	460	575	1,25	10	20
S500-1	500	525	1,05	3,6	10
S500-2	500	550	1,10	3,6	10
S500-c	615	673	1,09	5,6	22
S700-1	700	735	1,05	5,0	10
S700-2	700	770	1,10	5,0	10
S700-c	732	884	1,21	1,8	13
S960-1	960	1008	1,05	6,9	10
S960-2	960	1056	1,10	6,9	10

6.2.4 Meshing

The applied meshing of the X joint with a β of 0,5 is visible in Figure 6.2. The meshing contains 8-node linear brick elements with reduced integration (C3D8R). For the thickness of the tubular sections four elements are applied in through-thickness direction. Partitioning is applied to increase the mesh size to save calculation time. In the region where the braces are connected to the chord member a fine mesh of 3 mm (half the thickness of the tubular members) is applied. This dense mesh is gradually increased.

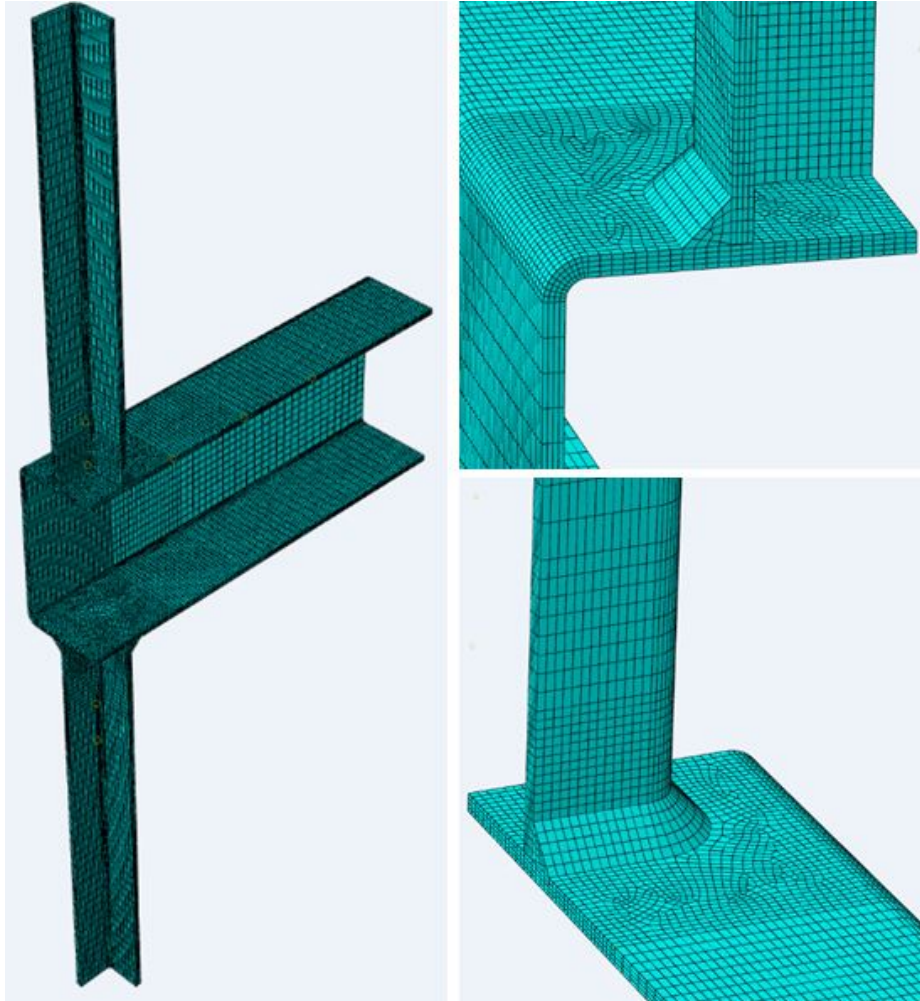


Figure 6.2: FEM meshing of X joint with $\beta = 0,5$

6.3 Finite element results

6.3.1 Effect of the material properties

The load-displacement curves are presented in Appendix E. An overview and detailed figure up to 4% deformation is presented for each β -value. The results of material-1 are presented in Figures E.3, E.4 and E.5. The results of material-2 are presented in Figures E.6, E.7 and E.8. The results of material-c are presented in Figures E.9, E.10 and E.11.

Table 6.5: FEM results influence of material property on numerical resistance

	$\beta = 0,3$	$\beta = 0,5$	$\beta = 0,7$	$\beta = 0,3$	$\beta = 0,5$	$\beta = 0,7$	r_4
	F_{fem}	F_{fem}	F_{fem}	r_1	r_2	r_3	
	[kN]	[kN]	[kN]	[%]	[%]	[%]	
S355-1	78	138	340	-	-	-	-
S460-1	94	170	429	21	23	26	23
S500-1	99	179	418	27	30	23	27
S700-1	139	271	672	78	96	98	91
S960-1	161	347	875	109	151	157	138
S355-2	78	139	362	-	-	-	-
S460-2	94	171	448	21	23	24	23
S500-2	100	184	430	28	32	19	26
S700-2	140	278	696	79	101	92	91
S960-2	162	355	899	108	155	148	137
S355-c	89	169	442	-	-	-	-
S500-c	108	211	567	21	25	28	25
S700-c	146	313	784	64	85	77	75

The governing joint resistance from the finite element model are indicated by F_{fem} . This value represent either the value of the 3% deformation limit, if this value is reached, or the ultimate resistance of the joint. To look at the influence of the material property, the joint resistance ($F_{fem,i}$) is compared to the joint resistance obtained for steel grade S355 ($F_{fem,S355}$), where i is S460, S500, S700 and S960. Table 6.5 gives an overview of the results. The following ratios are identified in the table:

1. $r_1 = F_{fem,i}/F_{fem,S355}$: for $\beta = 0,3$;
2. $r_2 = F_{fem,i}/F_{fem,S355}$: for $\beta = 0,5$;
3. $r_3 = F_{fem,i}/F_{fem,S355}$: for $\beta = 0,7$;
4. $r_4 = F_{fem,i}/F_{fem,S355}$: averaged for all β -values.

The numerical resistance increases with 23%, 26%, 86% and 138% for steel grades S460, S500, S700 and S960 when compared to the resistance of S355. It is reasonable that higher steel grades lead to a higher ultimate resistance. These results are the average values of ratio r_4 for each steel grade from Table 6.5.

The results from material-1, based on the minimum requirements of the Eurocode, are set as standard. Material-2 and material-c are compared to the values obtained by material-1. The results are presented in Table 6.6. The following ratios are defined in the table:

1. $r_5 = F_{fem,i}/F_{fem,mat-1}$: for $\beta = 0,3$;
2. $r_6 = F_{fem,i}/F_{fem,mat-1}$: for $\beta = 0,5$;
3. $r_7 = F_{fem,i}/F_{fem,mat-1}$: for $\beta = 0,7$.

Where i represents the value based on material-2 or material-c for that specific steel grade. When comparing material-2 to material-1, ratios show an increase between 0% and 6% for all steel grades. These results indicate that both the material properties based on the minimum requirements (material-1) and the nominal requirements (material-2) of the standards result in approximately the same numerical resistance.

Table 6.6: FEM results of material-2 and material-c compared to material-1

	$\beta = 0,3$	$\beta = 0,5$	$\beta = 0,7$	$\beta = 0,3$	$\beta = 0,5$	$\beta = 0,7$
	F_{fem}	F_{fem}	F_{fem}	r_5	r_6	r_7
	[kN]	[kN]	[kN]	[%]	[%]	[%]
S355-1	78	138	340	-	-	-
S355-2	78	139	362	0	1	6
S355-c	89	169	442	19	22	30
S460-1	94	170	429	-	-	-
S460-2	94	171	448	0	1	4
S500-1	99	179	418	-	-	-
S500-2	100	184	430	1	3	4
S500-c	108	211	567	9	18	36
S700-1	139	271	672	-	-	-
S700-2	140	278	696	1	3	4
S700-c	146	313	784	5	15	17
S960-1	161	347	875	-	-	-
S960-2	162	355	899	1	2	3

Material-c results in an increase in the range of 5% and 36% when compared to material-1. The result from the material properties based on the coupon experiments (material-c) result in larger

resistances. This can be explained by the larger yield strength obtained in the coupon experiments in comparison to the values used for material-1.

When the initial stiffness of the X joints is compared, see Figure 6.3, a difference is observed between the 'lower' steel grades (S355, S460 and S500) and the 'higher' steel grades (S700 and S960). This difference is supported by the results presented in Table 6.7. The difference between the 'lower' and 'higher' steel grades is 17%, 38% and 54% for β is 0,3, 0,5 and 0,7. The difference increases with an increase in β . The reason for this difference is the different weld size applied in the models for these different 'groups' of steel grades, respectively 13 and 18 mm leg length fillet welds.

Table 6.7: FEM results of the initial stiffness

	$\beta = 0,3$	$\beta = 0,5$	$\beta = 0,7$
	[kN/mm]	[kN/mm]	[kN/mm]
S355/S460/S500	26,6	72,4	282,3
S700/S960	31,2	99,9	435,5
Difference [%]	17	38	54

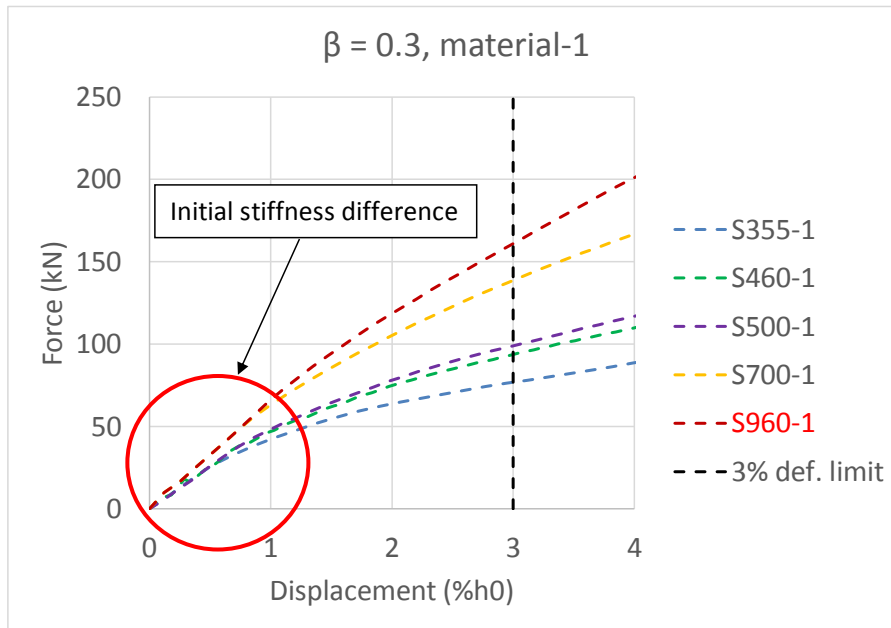


Figure 6.3: Initial stiffness difference

6.3.2 Visual results

Visual results from the finite element analysis are presented below for material S500-1. Figure 6.4 shows the von Mises stress distribution at the governing load for all three β -values. The governing load for β equals 0,3 and 0,5 is the load obtained by the 3% deformation limit. For β equals 0,7 is the deformation limit not reached before final failure occurred.

Figure 6.5 represents the von Mises stress at the moment the ultimate load is reached for all three β -values. From this figure it is visible that a lower β -value results in a larger deformation of the chord face.

Figure 6.6 represents the PEEQ strain distribution at the governing load.

Chord face failure is the governing failure mode in all models, this is due to the use of a maximum β -value of 0,7.

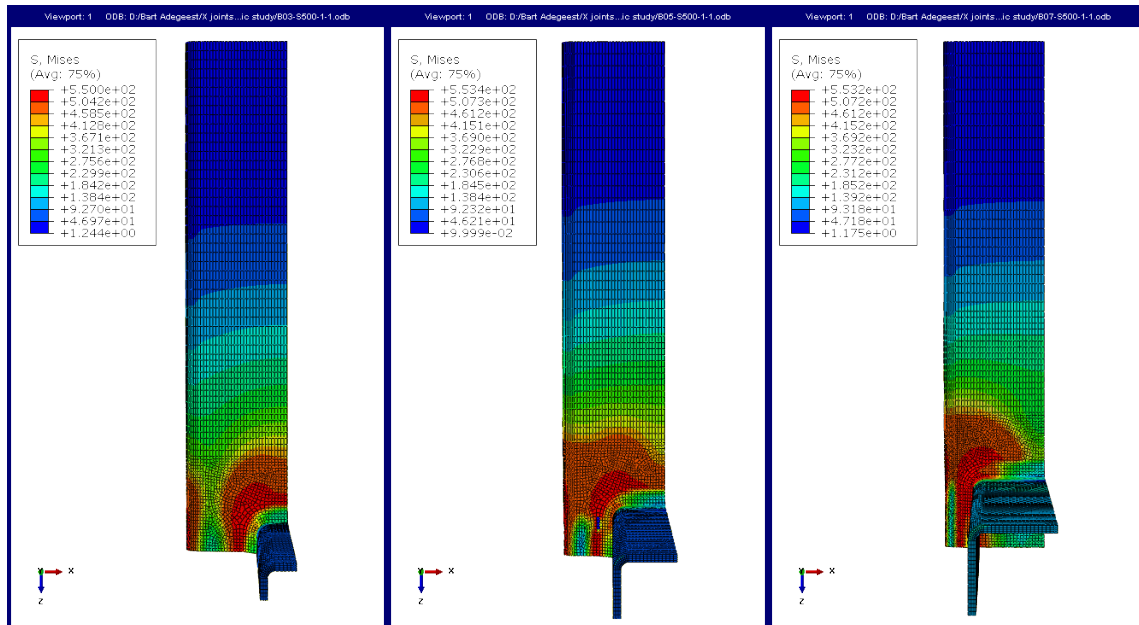


Figure 6.4: Von Mises stress distribution at the governing load of steel grade S500-1 for $\beta=0,3$ (left), $\beta=0,5$ (centre) and $\beta=0,7$ (right)

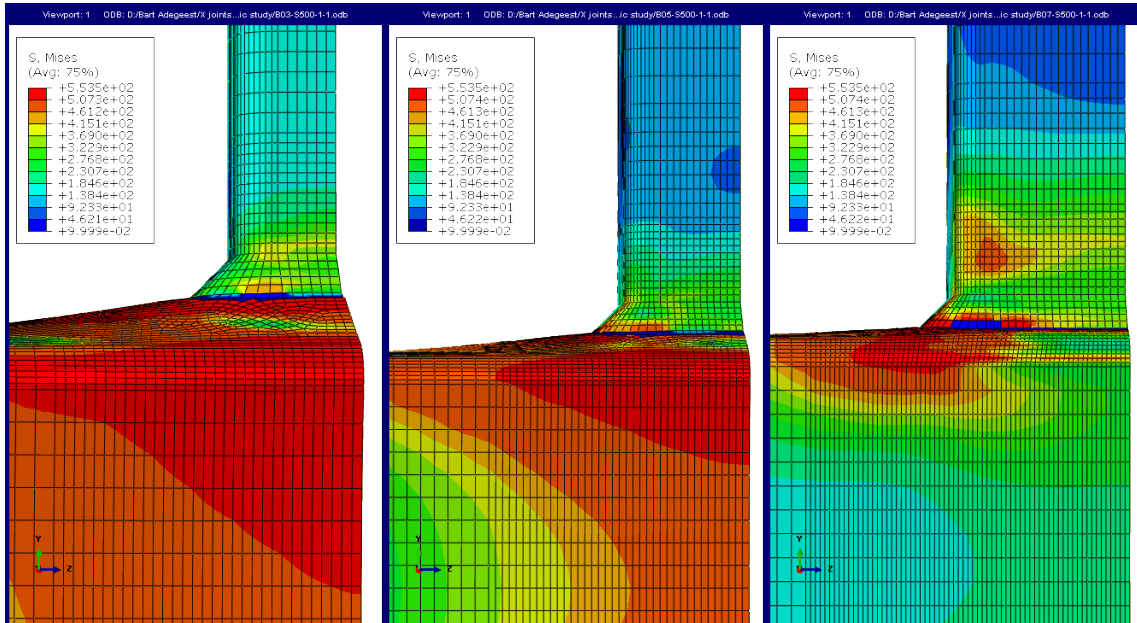


Figure 6.5: Von Mises stress distribution at the maximum load of steel grade S500-1 for $\beta=0,3$ (left), $\beta=0,5$ (centre) and $\beta=0,7$ (right)

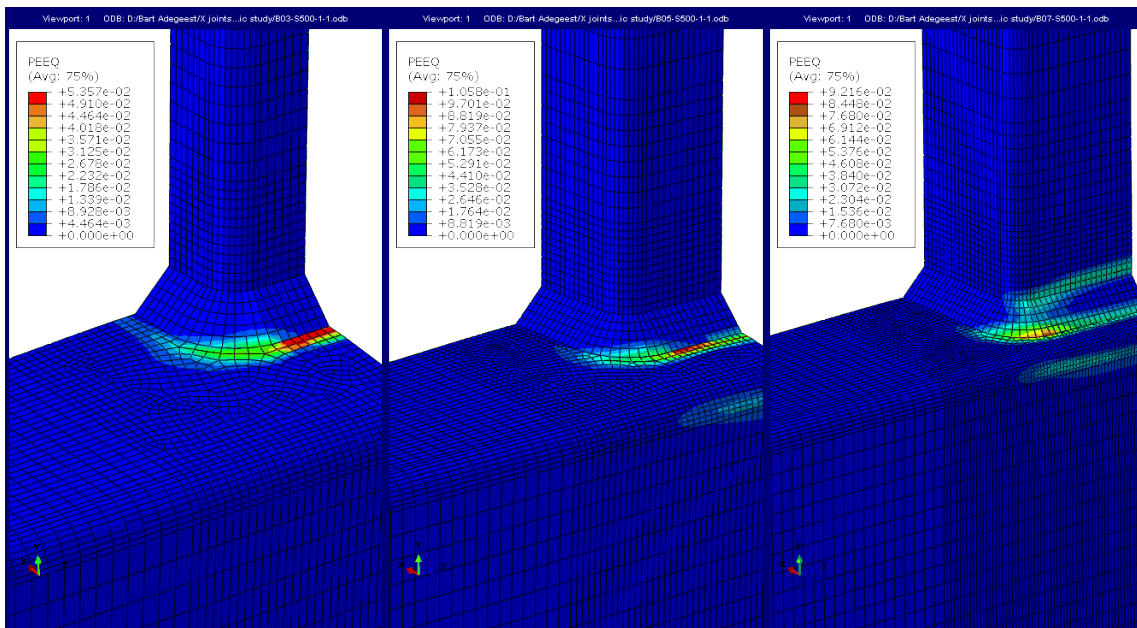


Figure 6.6: PEEQ strain distribution at the governing load of steel grade S500-1 for $\beta=0,3$ (left), $\beta=0,5$ (centre) and $\beta=0,7$ (right)

6.3.3 Comparison to the Eurocode prediction

The obtained numerical resistance is compared to the design resistances according to the Eurocode. It has to be noted that the range of validity for β equals 0,3 is not met, see Table E.1. Steel grade S960 is not included in the standards [14, 18] and is therefore indicated with a red colour in the figures that present the results. The design resistance according to the Eurocode is determined including ($F_{EC3,Cf}$) and excluding (F_{EC3}) the material reduction factor, see Table E.2. Table 6.8 presents the applied material reduction factor for each material and is based on the yield strength, these parameters are in accordance with [19].

Table 6.8: Used material reduction factors for design strength Eurocode ($F_{EC3,Cf}$)

	C_f								
S355-1	1,0	S460-1	0,9	S500-1	0,86	S700-1	0,8	S960-1	0,8
S355-2	1,0	S460-2	0,9	S500-2	0,86	S700-2	0,8	S960-2	0,8
S355-c	0,9			S500-c	0,8	S700-c	0,8		

The numerical resistance is compared to the Eurocode prediction including ($F_{EC3,Cf}$) and excluding (F_{EC3}) material reduction factor. The results are presented in Appendix E in Tables E.3, E.4 and E.5 for β equals 0,3, 0,5 and 0,7, respectively. Ratio d_1 is the numerical resistance divided by the Eurocode prediction without (excluding) the material reduction factor, ratio d_2 represents the numerical resistance divided by the Eurocode prediction including the material reduction factor.

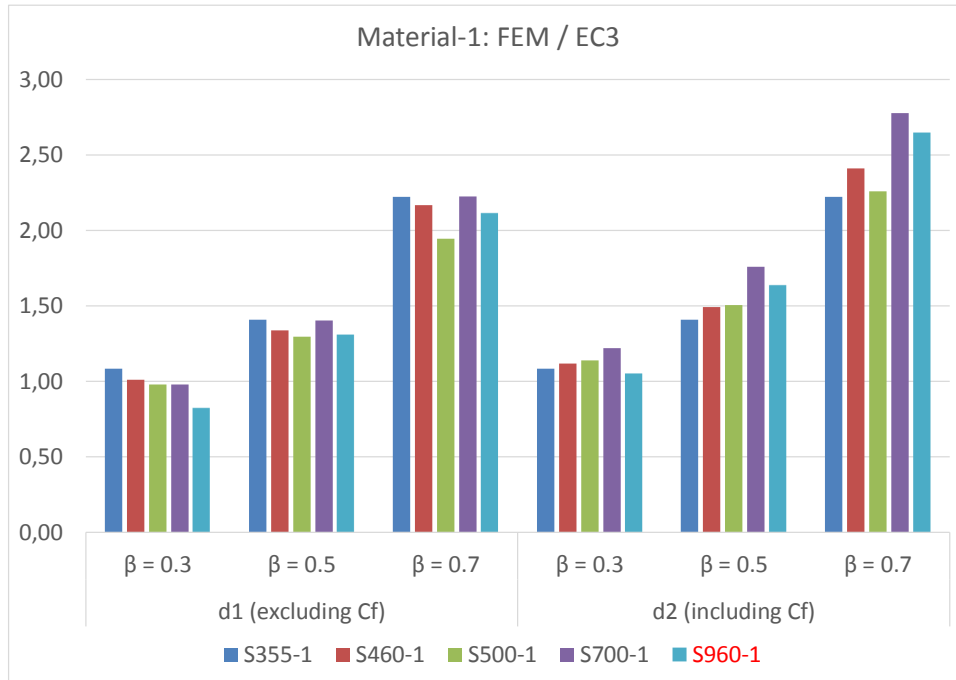


Figure 6.7: Results of material-1: FEM resistance over EC3 resistance

The results for material-1 are presented in Figure 6.7. If the ratio is above 1,0 this means that the numerical resistance exceeds the predicted Eurocode value. An increasing trend in the ratio is observed with an increase in β . This indicates that the design equation becomes more conservative for larger β -values of 0,5 and 0,7.

When the material reduction factor is not taken into account (d_1). For the same β -value, a small decreasing trend can be observed in the ratio of steel grades S355-1, S460-1 and S500-1. Steel grade S700-1 results in a jump in the ratio for β equals 0,5 and 0,7. The ratio remains constant for steel grades S500-1 and S700-1 for β equals 0,3. This result is contradicting with the observed decreasing trend and this can be explained by the difference in the used weld geometry. This results indicate that a larger applied fillet weld results in an increase in initial stiffness and corresponding governing resistance. The same trend is observed for material-2 and material-c, see Figures 6.8 and 6.9.

For the ratios including the material reduction factor (d_2), a decreasing trend is replaced by a more increasing trend. This is due to the use of the material reduction factor. Higher steel grades lead to larger ratios because of the larger value of the material reduction factors applicable for these steel grades. This trend is observed for all three material types.

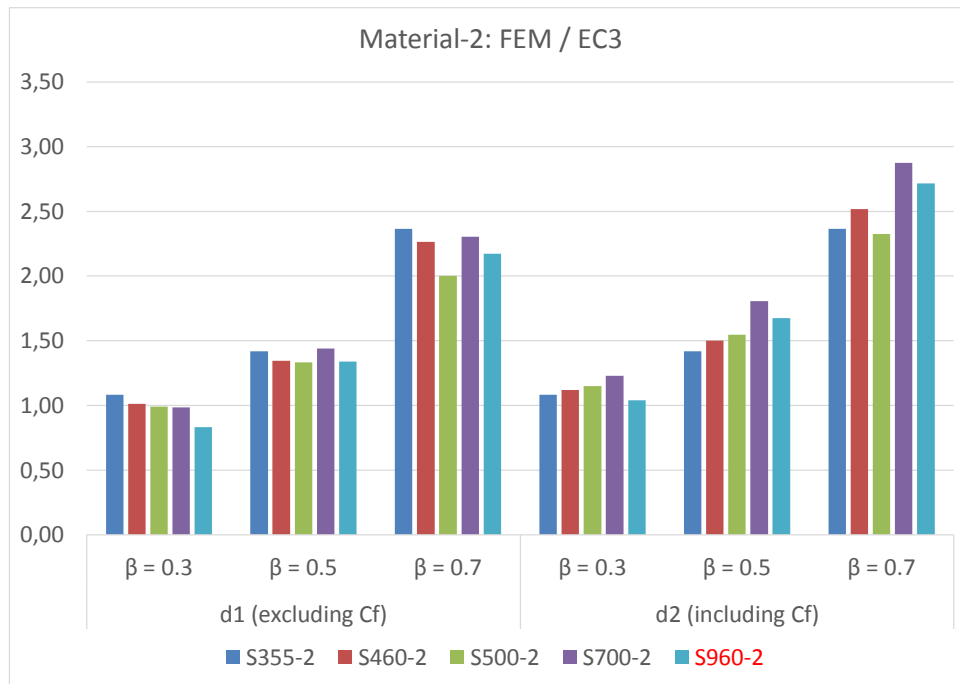


Figure 6.8: Results of material-2: FEM resistance over EC3 resistance

The obtained ratios for material-2, see Figure 6.8, are approximately the same as the ratios obtained for material-1. The maximum deviation observed between the ratios of material-2 and material-1 is 6,8%, where the average deviation is 2,0%.

The results for material-c are presented in Figure 6.9. The obtained ratios are in line with the ratios observed for material-1 and material-2. The maximum deviation observed between the ratios

of material-c and material-1 is 38% with an average deviation of 6,7%.

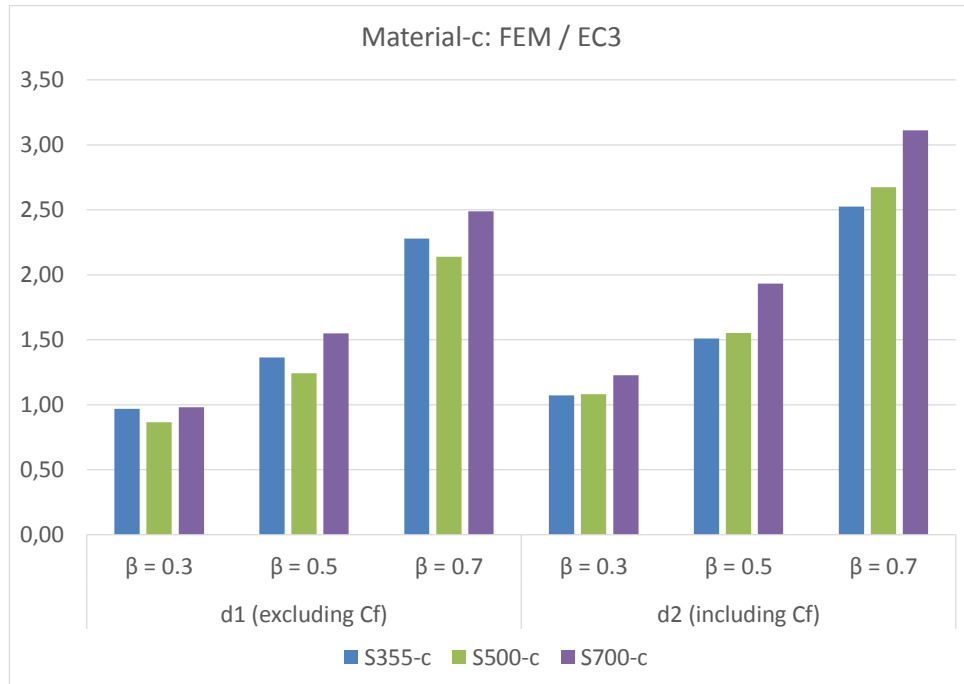


Figure 6.9: Results of material-c: FEM resistance over EC3 resistance

6.4 Summary parametric study

This parametric study is executed to investigate the validity of the material reduction factors for high strength steels. Three different type of material properties are investigated: properties based on the minimum requirements according to the Eurocodes (material-1), properties based on the nominal values from the Eurocodes (material-2) and real material properties obtained from coupon experiments (material-c). Besides the different material properties the β -value is varied between 0,3 and 0,7. This resulted in a total of 39 different models. Full-strength single-sided fillet welds are adopted in the analysis and a numerical gap between the brace and chord member of 0,15 mm is applied. Chord face failure is governing in all models. In most cases is the 3% deformation limit governing. The observations made are summarized.

6.4.1 Effect of the material properties

The numerical resistance for steel grades S460, S500, S700 and S960 increases with 23%, 26%, 86% and 138% in comparison with the resistance obtained with steel grade S355. It is reasonable that higher steel grades lead to higher resistances.

The material based on the minimum requirements of the Eurocode (material-1) and based on the nominal parameters of the Eurocode (material-2) show similar numerical resistances. When the

results of material-2 are compared to material-1 an increase is observed in the range of 0%-6%. This indicates that material-1 and material-2 result in approximately the same numerical resistance.

The real material properties based on the coupon experiments (material-c) result in larger resistances when compared to material-1, respectively an increase is observed in the range of 5%-36%. This is due to the larger yield strengths obtained in the coupon experiments in comparison to the values used for material-1.

The initial stiffness obtained from the finite element models show a difference between the 'lower' steel grades (S355, S460 and S500) and 'higher' steel grades (S700 and S960). The difference between the 'lower' and 'higher' steel grades are 17%, 38% and 54% for β equals 0,3, 0,5 and 0,7, respectively. The difference increases with an increase in β . This difference is due to the use of different weld sizes, respectively 13 and 18 mm leg length for the fillet welds of these two groups of steel grades. The fillet weld size influences the initial stiffness and corresponding governing resistance.

6.4.2 Comparison to the Eurocode prediction

The numerical resistances obtained by finite element method are compared to the predicted resistance according to Eurocode including and excluding the material reduction factor (C_f). It has to be noted that the joint with β equals 0,3 does not meet the range of validity equations according to the Eurocode [19]. Steel grade S960 is outside of the scope of the standard.

The ranges of the ratios for the three β -values including and excluding the material reduction factor are presented in Table 6.9. An increasing trend is observed between the ratio with an increase in β . The ranges of ratios increase when the material reduction factor is included.

Table 6.9: An overview of the resulted numerical resistance compared to the Eurocode

	$\beta = 0,3$	$\beta = 0,5$	$\beta = 0,7$
FEM / EC3, excluding C_f	0,83 - 1,08	1,24 - 1,55	1,94 - 2,49
FEM / EC3, including C_f	1,04 - 1,23	1,41 - 1,93	2,22 - 3,11

The results indicate that the material reduction factors might be necessary for joints with β equals 0,3, considering that the range of validity of the standard is not met. Joints with β equals 0,5 and 0,7 show significant higher numerical results compared to the design resistances from the Eurocode. This results indicate that for β -values of 0,5 and 0,7 the material reduction factors may not be necessary.

Chapter 7

Conclusions and recommendations

This research intends to investigate the behaviour of cold-formed geometrically identical X joints made from different steel grades. The necessity of the material reduction factors (C_f) applicable for different grades of high strength steels are investigated and the conclusions obtained from this research are presented in this chapter. Finally, recommendations are suggested for future research.

7.1 Conclusions

The scope of the experimental program is equal-width squared hollow section X joints made of steel grades S355 (X8) and S500 (X2). The brace and chord members consist of 150x150x6 mm cold-formed tubular section. The following conclusions can be drawn:

- The experiments resulted in higher resistances compared to the predicted value according to Eurocode [19] with ratios of 1,465 and 1,413 for joints X2 and X8, respectively, see Table 7.1. The governing resistance of joint X2 is the ultimate resistance, while the governing resistance of joint X8 is the 3% deformation limit. The experimental results are confirmed by the finite element results, with obtained ratios for the governing resistance of 1,023 and 1,048 for joints X2 and X8, respectively. It can be concluded that the Eurocode is conservative compared to the experiments. Therefore, the material reduction factors are not validated for equal-width SHS X joints made of steel grades S355 and S500.

Table 7.1: Results joints X2 and X8

Joint	Steel grade	F_{exp}	F_{fem}	F_{EC3}	ϵ_f	Failure mode	F_{exp}/F_{fem}	F_{exp}/F_{EC3}
		[kN]	[kN]	[kN]	[%]		[-]	[-]
X2	S500	1713	1674	1169	17	BF	1,023	1,465
X8	S355	1362	1300	964	38	CSWF	1,048	1,413

- Different failure modes are obtained in the experiments for identical SHS X joints with varying steel grades, respectively S355 and S500. Steel grade S355 results in chord side wall failure, while S500 results in brace failure. The fracture strain, evaluated by DIC, is 17% for joint

X2 and 38% for joint X8. The fracture strain for joint X2 is allocated to the failure in the heat affected zone of the weld. The fracture strain of joint X8 is allocated to the ductile chord side wall failure. The observed fracture strain in the coupon experiments, 104%-108%, is significantly higher than the fracture strain of joint X8. The obtained values of the stress triaxiality, around 0,5 for joint X8 and 0,33 for the coupon experiments, support the lower observed fracture strain for joint X8 in comparison with the coupon experiments.

The scope of the parametric study is squared hollow section X joints including three β -values (0,3, 0,5 and 0,7) with steel grades ranging from S355 up to and including S960. Material properties are based on the minimum requirements according to the standards, nominal values according to the standards and results from coupon experiments. The following conclusions can be drawn from the parametric study:

- The numerical resistance for steel grades S460, S500, S700 and S960 increases with 23%, 26%, 86% and 138% in comparison with the resistance obtained with steel grade S355.
- The resistance obtained with the nominal material properties is approximately the same as the resistance obtained with the minimum requirements according to the standards, a difference is observed in the range of 0% to 6%. The resistance obtained with the material properties based on the coupon experiments are 5% to 36% larger than the resistance obtained with the minimum requirements according to the standards.
- Different fillet weld sizes are implemented in the finite element models. For steel grades S355, S460 and S500 a fillet weld leg length of 13 mm is used ('lower' steel grades). For steel grades S700 and S960 a fillet weld leg length of 18 mm is used ('higher' steel grades). These values are based on the full-strength method. The 'higher' steel grades lead to an increase in stiffness of 17%, 38% and 54% for β is 0,3, 0,5 and 0,7. It can be concluded that the fillet weld size influences the initial stiffness of the X joint.
- Table 7.2 present the ratios of the numerical resistance compared to the predicted value according to Eurocode [19]. Ratios are presented including and excluding the material reduction factor. It has to be noted that for β equals 0,3 the range of validity of the standard is not met. Also, steel grade S960 is outside the range of the standard. The ratios indicate that a material reduction factor might be necessary for β equals 0,3. Without considering the material reduction factor, β equals 0,5 and 0,7 results in ratios in the range of 1,24-1,55 and 1,94-2,49, respectively. Therefore, it can be concluded that the material reduction factors might not be necessary for SHS X joints with β -values of 0,5 and 0,7.

Table 7.2: Results parametric study

	$\beta = 0,3$	$\beta = 0,5$	$\beta = 0,7$
FEM / EC3, excluding C_f	0,83 - 1,08	1,24 - 1,55	1,94 - 2,49
FEM / EC3, including C_f	1,04 - 1,23	1,41 - 1,93	2,22 - 3,11

7.2 Recommendations

The following recommendations are suggested for future research:

- Two experiments are included in this research. More experiments should be performed, which is in progress at TU Delft, to obtain a comprehensive test program and investigate if the material reduction factors according to the Eurocode are validated for X joints loaded in tension.
- The cold-forming process leads to different material properties in the cross-section. The influence of the position of the coupon specimens in the cross-section of the tubular cold-formed section needs to be evaluated more thoroughly. Ideally, a relationship should be obtained between the material properties obtained from coupon specimens of a specific position (opposite or adjacent side to the longitudinal seam weld) and the full cross-sectional material properties.
- In the finite element model only one material property is introduced for the full model. The model should be further developed to make a distinction between the base material, heat affected zone and weld material and implement the appropriate material properties for each region. Furthermore, the finite element model should be improved by implementing damage modelling. These two improvements could lead to the correct failure mode and deformation after necking.
- The parametric study showed the influence of the weld size on the initial stiffness of the X joint. Further research should be done to investigate the influence of the weld size on the stiffness of X joints.

Bibliography

- [1] S. Afshan, B. Rossi, and L. Gardner. Strength enhancements in cold-formed structural sections - Part I: Material testing. *Journal of Constructional Steel Research*, 83:177–188, 2013. <https://doi.org/10.1016/j.jcsr.2012.12.008>.
- [2] M. Amraei, H. Jiao, X.-L. Zhao, and L.-W. Tong. Fatigue testing of butt-welded high strength square hollow sections strengthened with CFRP. *Thin-Walled Structures*, 120:260–268, 2017. <https://doi.org/10.1016/j.tws.2017.09.004>.
- [3] Y. Bai. *Effect of Loading History on Necking and Fracture*. PhD thesis, Massachusetts Institute of Technology, 2008.
- [4] Y. Bao and T. Wierzbicki. On the cut-off value of negative triaxiality for fracture. *Engineering Fracture Mechanics*, 72(7):1049–1069, 2005. <https://doi.org/10.1016/j.engfracmech.2004.07.011>.
- [5] J. Becque and T. Wilkinson. The capacity of grade C450 cold-formed rectangular hollow section T and X connections: An experimental investigation. *Journal of Constructional Steel Research*, 133:345–359, 2017. <https://doi.org/10.1016/j.jcsr.2017.02.032>.
- [6] J. Billingham, J. V. Sharp, J. Spurrier, and P. J. Kilgallon. *Review of the performance of high strength steels used in offshore*. Cranfield University, 2003.
- [7] T. Björk, A. Ahola, and N. Tuominen. *On the design of fillet welds made of UHSS*. Lappeenranta University of Technology, IIW-Doc, XV-1547-17, 2017.
- [8] T. Björk and H. Saastamoinen. Capacity of CFRHS X-joints made of double-grade S420 steel. *Tubular Structures XIV*, pages 167–176, 2012.
- [9] D. W. Blom. *The strength of welded connections using overmatched filler metals*. Master’s thesis, Delft University of Technology, 2019.
- [10] P. W. Bridgman. *Studies in large plastic flow and fracture*. Cambridge, MA, Harvard University Press, 1964.
- [11] M. Bruneau, C.-M. Uang, and R. Sabelli. *Ductile Design of Steel Structures*. McGraw-Hill Companies, Inc., 2nd edition, 2011.
- [12] CEN. *EN10002-1. Metallic materials - Tensile testing - Part 1: Method of test at ambient temperatures*. 2001.
- [13] CEN. *EN1011-2. Welding - Recommendations for welding of metallic materials - Part 2: Arc welding of ferritic steels*. 2003.

- [14] CEN. *EN1993-1-1. Eurocode 3: Design of steel structures - Part 1-1: General rules and rules for buildings*. 2005.
- [15] CEN. *EN1993-1-10. Eurocode 3: Design of steel structures - Part 1-10: Material toughness and through-thickness properties*. 2005.
- [16] CEN. *EN1993-1-8. Eurocode 3: Design of steel structures - Part 1-8: Design of joints*. 2005.
- [17] CEN. *EN10219-1. Cold formed welded structural hollow sections of non-alloy and fine grain steels - Part 1: Technical delivery conditions*. 2006.
- [18] CEN. *EN1993-1-12. Eurocode 3: Design of steel structures - Part 1-12: Additional rules for the extension of EN1993 up to steel grades S700*. 2007.
- [19] CEN. *EN1993-1-8. Eurocode 3: Design of steel structures - Part 1-8: Design of joints*. 2020.
- [20] C. Chen, S.-P. Chiew, M.-S. Zhao, and T.-C. Fung. Welding effect on tensile strength of grade S690Q steel butt joint. *Journal of Constructional Steel Research*, 153:153–168, 2019.
- [21] M.-T. Chen and B. Young. Tests of cold-formed normal and high strength steel tubes under tension. *Thin-Walled Structures*, 153, 2020. <https://doi.org/10.1016/j.tws.2020.106844>.
- [22] DS Simulia Corp. *ABAQUS 2016 - GETTING STARTED WITH ABAQUS/CAE*.
- [23] M. Feldmann, N. Schillo, S. Schaffrath, K. Viridi, T. Björk, N. Tuominen, M. Veljkovic, M. Pavlovic, P. Manoleas, M. Heinisuo, K. Mela, P. Ongelin, I. Valkonen, J. Minkkinen, J. Erkkilä, E. Pétursson, M. Clarin, A. Seyr, L. Horváth, B. Kövesdi, P. Turán, and B. Somodi. *Rules On High Strength Steel (RUOSTE)*. Research Fund for Coal and Steel, European Commission, 2016.
- [24] F. B. Gang Shi, M. Veljković, and Xuhong Qiang. *First Workshop Proceedings of High Performance Steel Structures Research Council (HPSSRC)*. Delft University of Technology, 2018.
- [25] E. Gogou. *Use of High Strength Steel Grades for Economical Bridge Design*. Master’s thesis, Delft University of Technology, 2012.
- [26] A. M. Gresnigt and C. M. Steenhuis. High strength steels. *Progress in Structural Engineering and Materials*, 1(1):31–41, 1997.
- [27] G. Hancock, T. Wilkinson, and L. Teh. *Welded Connections in High Strength Cold-Formed Steels*. University of Sydney, 2006.
- [28] O. Hechler, G. Axmann, and B. Donnay. The right choice of steel - according to the Eurocode. *Economical Bridge Solutions based on innovative composite dowels and integrated abutments*, pages 21–43, 2014. https://doi.org/10.1007/978-3-658-06417-4_2.
- [29] M. Heinisuo, K. Mela, and M. Kierros. *SSAB High Strength Structural Hollow Sections. Handbook for Steel Structures*. 2017.
- [30] A. F. Hobbacher, M. Karpenko, S. J. Hicks, P. Schneider, and B. Uy. Establishing new brittle fracture provisions for the Australasian steel structures standards. *Journal of Constructional Steel Research*, 155:20–32, 2019.

- [31] F. Hochhauser, W. Ernst, R. Rauch, R. Vallant, and N. Enzinger. Influence of the soft zone on the strength of welded modern HSLA steels. *Welding in the World*, 56(5-6):77–85, 2012.
- [32] P. Hradil and A. Talja. *Ductility limits of high strength steels*. VTT Technical Research Centre of Finland, 2017.
- [33] J.-P. Jaspart and K. Weynand. *Design of Joints in Steel and Composite Structures*. ECCS, 2016.
- [34] F. Javidan, A. Heidarpour, X.-L. Zhao, C. R. Hutchinson, and J. Minkinen. Effect of weld on the mechanical properties of high strength and ultra-high strength steel tubes in fabricated hybrid sections. *Engineering Structures*, 118:16–27, 2016. <https://doi.org/10.1016/j.engstruct.2016.03.046>.
- [35] J. H. Kim. *Experimental and Analytical Study of RHS X-Joints under Axial Compression*. Master’s thesis, Seoul National University, 2018.
- [36] P. S. Kisoensingh. *Secondary Bending Stresses in High-Strength Hollow Section Joints*. Master’s thesis, Delft University of Technology, 2019.
- [37] X. Lan and T. M. Chan. Recent research advances of high strength steel welded hollow section joints. *Structures*, 17:58–65, 2019. <https://doi.org/10.1016/j.istruc.2018.11.015>.
- [38] X. Lan, T.-M. Chan, and B. Young. Structural behaviour and design of chord plastification in high strength steel CHS X-joints. *Construction and Building Materials*, 191:1252–1267, 2018. <https://doi.org/10.1016/j.conbuildmat.2018.10.065>.
- [39] X. Lan, T.-M. Chan, and B. Young. Structural behaviour and design of high strength steel RHS X-joints. *Engineering Structures*, 200:1–23, 2019. <https://doi.org/10.1016/j.engstruct.2019.109494>.
- [40] H. Levanger. *Simulating Ductile Fracture in Steel using the Finite Element Method: Comparison of Two Models For Describing Local Instability due to Ductile Fracture*. Master’s thesis, University of Oslo, 2012.
- [41] L. H. Lu, G. D. de Winkel, Y. Yu, and J. Wardenier. Deformation limit for the ultimate strength of hollow section joints. *Tubular Structures VI*, pages 341–347, 1994.
- [42] J.-L. Ma, T.-M. Chan, and B. Young. Material properties and residual stresses of cold-formed high strength steel hollow sections. *Journal of Constructional Steel Research*, 109:152–165, 2015. <https://doi.org/10.1016/j.jcsr.2015.02.006>.
- [43] J.-L. Ma, T.-M. Chan, and B. Young. Tests on high-strength steel hollow sections: a review. *Proceedings of the Institution of Civil Engineers - Structures and Buildings*, 170(9):621–630, 2017.
- [44] W. Maurer, W. Ernst, R. Rauch, S. Kapl, R. Vallant, and N. Enzinger. Numerical simulation on the effect of haz softening on static tensile strength of hsla steel welds. *Mathematical Modelling of Weld Phenomena*, 10:669–690, 2012.
- [45] M. Mohan and T. Wilkinson. FEA of T & X joints in grade C450 steel. *Tubular Structures XIV*, pages 185–194, 2012.

- [46] M. Mohan and T. Wilkinson. Finite element simulations of 450 grade cold-formed K and N joints. *Tubular Structures XV*, pages 449–456, 2015.
- [47] J. Nseir. *Development of a new design method for the cross-section capacity of steel hollow sections*. PHD thesis, University de Liege, 2015.
- [48] M. Pandey and B. Young. High strength steel tubular X-joints - an experimental insight under axial compression. *Tubular Structures XV*, pages 223–230, 2017.
- [49] M. Pandey and B. Young. Tests of cold-formed high strength steel tubular T-joints. *Thin-Walled Structures*, 143, 2019. <https://doi.org/10.1016/j.tws.2019.106200>.
- [50] M. Pavlović and M. Veljković. Compact cross-sections of mild and high-strength steel hollow-section beams. *Proceedings of the Institution of Civil Engineers - Structures and Buildings*, 170(11):825–840, 2017. <https://doi.org/10.1680/jstbu.16.00124>.
- [51] M. Pirinen, Yu. Martikainen, P. D. Layus, V. A. Karkhin, and S. Y. Ivanov. Effect of heat input on the mechanical properties of welded joints in high-strength steels. *Welding International*, 30(2):129–132, 2015.
- [52] P. Ritakallio and T. Björk. Low-temperature ductility and structural behaviour of cold-formed hollow section structures - progress during the past two decades. *Steel Construction*, 7(2):107–115, 2014.
- [53] G. Selacek and C. Müller. *The use of very high strength steels in metallic construction*. Institute of Steel Construction, RWTH Aachen, Germany.
- [54] J. Siltanen, S. Tihinen, and J. Kömi. Laser and laser gas-metal-arc hybrid welding of 960 MPa direct-quenched structural steel in a butt joint configuration. *Journal of Laser Applications*, 27(S2), 2015. <https://doi.org/10.2351/1.4906386>.
- [55] SSAB. *Welding of Domex*, 2013.
- [56] SSAB. *Welding of Strenx*, 2017.
- [57] R. Stroetmann, T. Kästner, A. Hälsig, and P. Mayr. Influence of the cooling time on the mechanical properties of welded HSS-joints. *Steel Construction*, 11(4):264–271, 2018. <https://doi.org/10.1002/stco.201800019>.
- [58] R. Stroetmann, T. Kästner, A. Hälsig, and P. Mayr. Mechanical properties and a new design approach for welded joints at high strength steels. *Hong Kong: Engineering Research and Practice for Steel Construction*, pages 79–90, 2018.
- [59] N. Tuominen and T. Björk. *Ultimate capacity of welded joints made of cold formed S460 steel grade rectangular hollow sections*. Master’s thesis, Lappeenranta University of Technology (in Finnish), 2016.
- [60] J. Wang, S. Afshan, N. Schillo, M. Theofanous, M. Feldmann, and L. Gardner. Material properties and compressive local buckling response of high strength steel square and rectangular hollow sections. *Engineering Structures*, 130:297–315, 2017. <https://doi.org/10.1016/j.engstruct.2016.10.023>.
- [61] J. Wardenier, J. A. Packer, X.-L. Zhao, and G. J. van der Vegte. *Hollow sections in structural application*. 2010.

- [62] J. Wardenier and R. Puthli. *Recommended actions for CHS and RHS joints for steel grades S420 up to S690*. 2017.
- [63] M. R. Wenman and P. R. Chard-Tuckey. Modelling and experimental characterisation of the Lüders strain in complex loaded ferritic steel compact tension specimens. *International Journal of Plasticity*, 26(7):1013–1028, 2010. <https://doi.org/10.1016/j.ijplas.2009.12.005>.
- [64] M. S. Zhao, C. K. Lee, T. C. Fung, and S. P. Chiew. Impact of welding on the strength of high performance steel T-stub joints. *Journal of Constructional Steel Research*, 131:110–121, 2017. <https://doi.org/10.1016/j.jcsr.2016.12.023>.
- [65] Y.-L. Zhao, J. Shi, W.-Q. Cao, M.-Q. Wang, and G. Xie. Effect of direct quenching on microstructure and mechanical properties of medium-carbon Nb-bearing steel. *Journal of Zhejiang University-SCIENCE A*, 11(10):776–781, 2010.

Appendix A

Strain development along coupon specimen

Table A.1: Characteristic points

1	Elastic stage
2	Yield point
3	Plastic behaviour
4	Ultimate stress
5	Post-necking behaviour
6	Post-necking behaviour
7	Fracture point

A.1 X2-N-C - S500

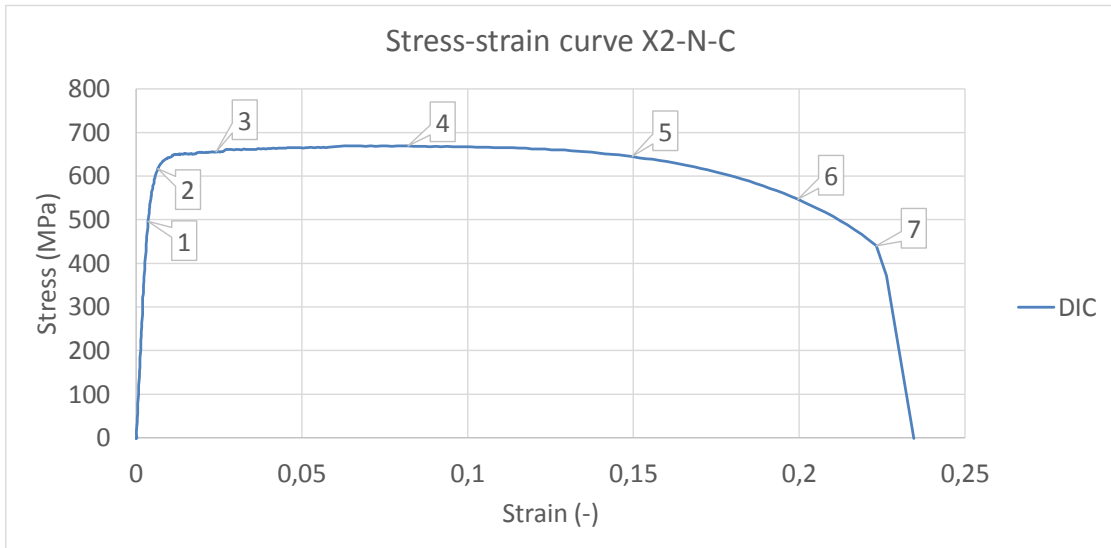


Figure A.1: Stress-strain curve X2-N-C with characteristic points (S500)

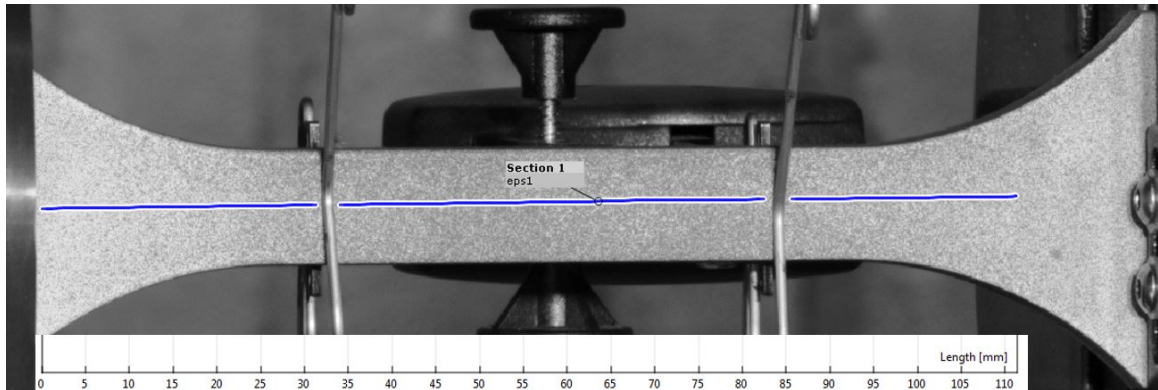


Figure A.2: Section line along which the strains are extracted with length scale X2-N-C (S500)

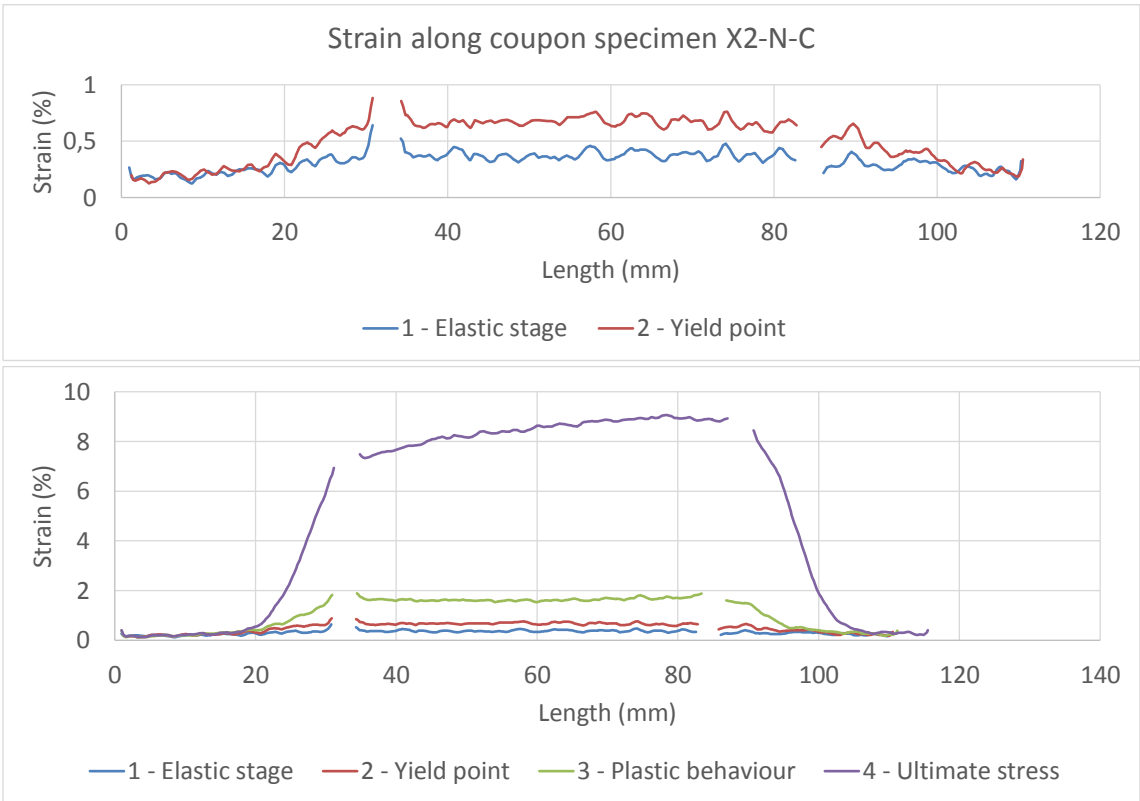


Figure A.3: Strain development X2-N-C for points 1 to 4 (S500)

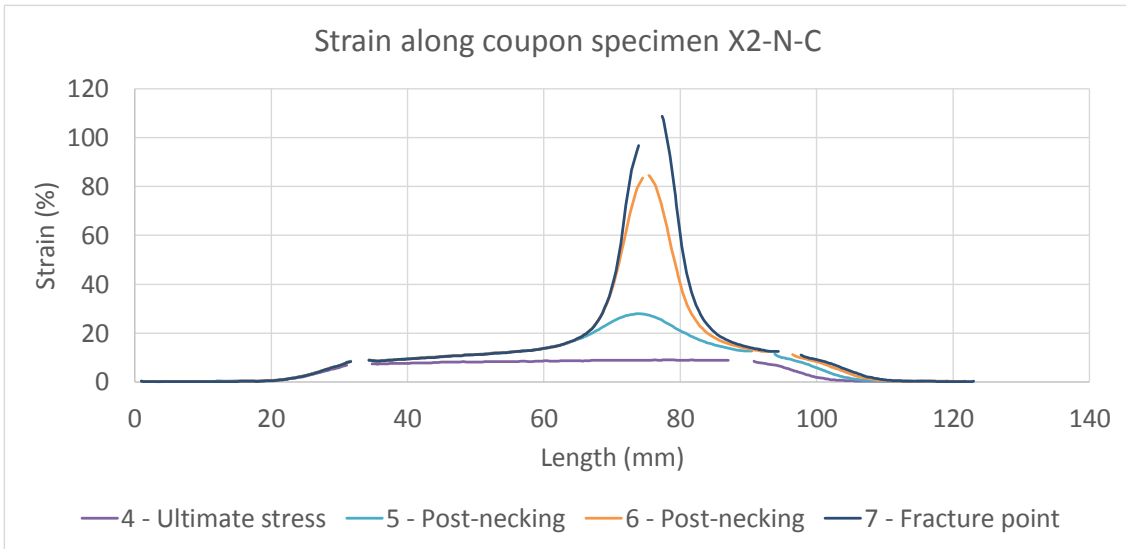


Figure A.4: Strain development X2-N-C for points 4 to 7 (S500)

A.2 T103-A - S700

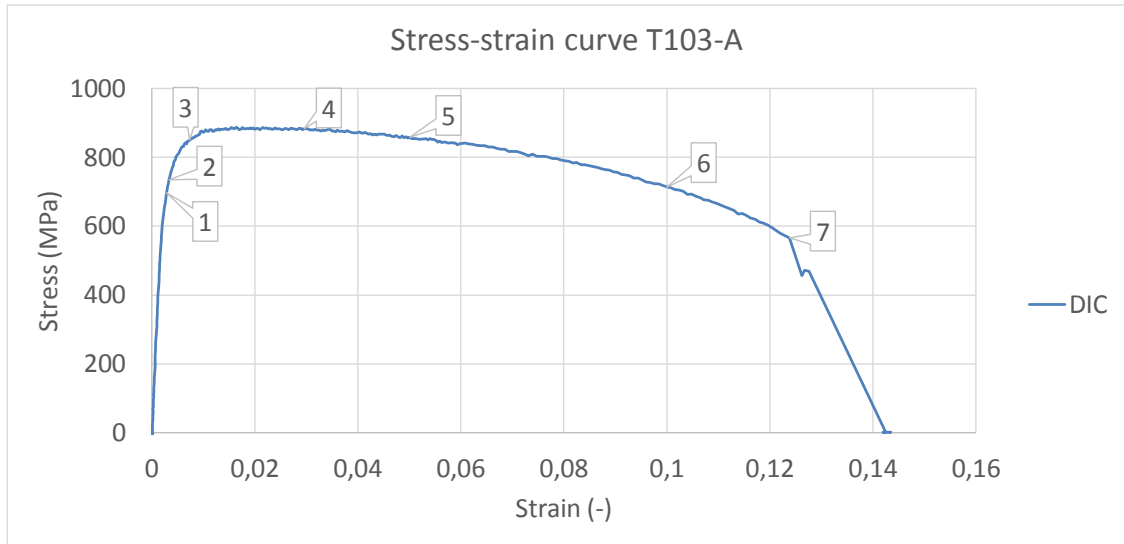


Figure A.5: Stress-strain curve T103-A with characteristic points (S700)

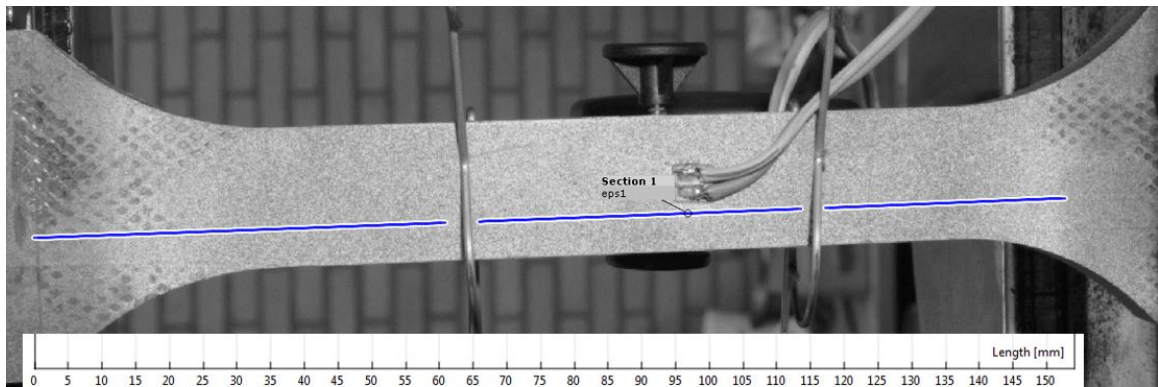


Figure A.6: Section line along which the strains are extracted with length scale T103-A (S700)

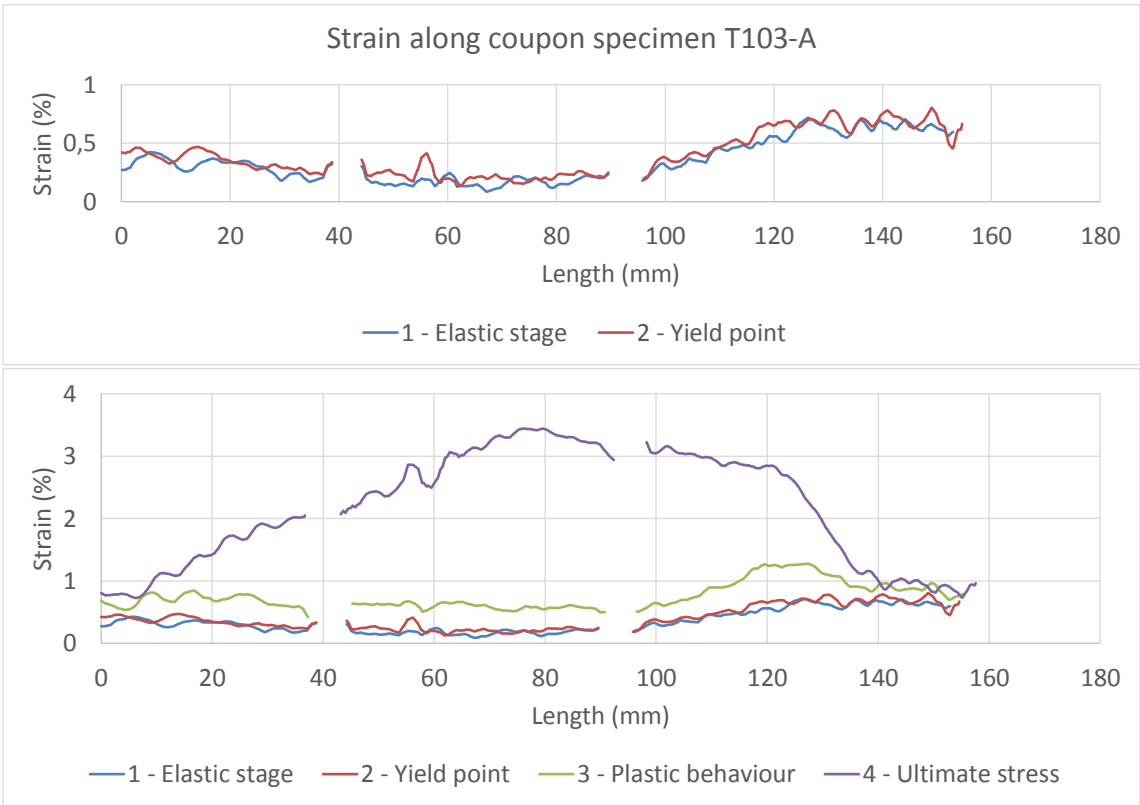


Figure A.7: Strain development T103-A for points 1 to 4 (S700)

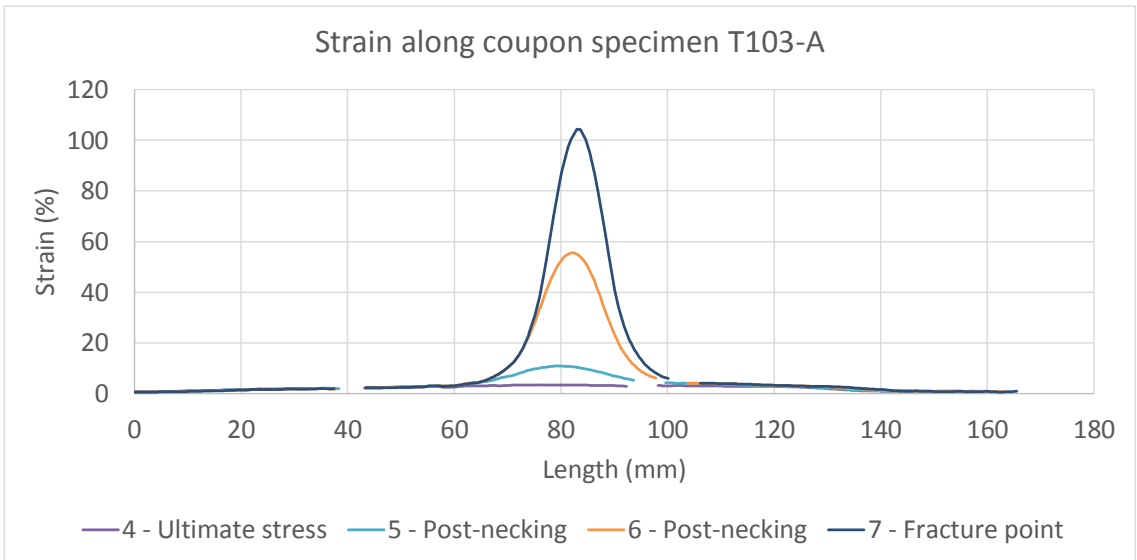


Figure A.8: Strain development T103-A for points 4 to 7 (S700)

Appendix B

Hand calculation according to EN1993-1-8:2020

In this Annex is the hand calculation of the X joints described. There is one type of X joint configuration (X2/X8) which consists of tubular sections of 150x150x6 mm. The method according to EN1993-1-8:2020 [19] is applied. The parameters of the X joints are described in Table B.1. To apply the design method described in the new standard, the joint needs to fulfil certain range of validity equations. These equations are described in Table 9.10 of the standard for welded joints between RHS chord and brace members, see Table 2.10. If these conditions are met, the design equations of Table 9.13 have to be applied, see Table 2.13. Table 9.13 describes the equations for chord face failure (CFF), chord side wall failure (CSWF), brace failure (BF) and punching shear failure (PSF). For welded connections between SHS chord and brace members additional conditions are given in Table 9.11 of the standard, see Table 2.10. In the case of SHS chord and brace members, and both the conditions of Table 9.10 and 9.11 are met, only chord face failure has to be checked according to Table 9.12 of the standard, see Table 2.12.

Table B.1: Parameters X joint calculation

	Chord	Brace	Steel grade	$\beta = b_1/b_0$	$2\gamma = b_0/t_0$	$\tau = t_1/t_0$
	$h_0 : b_0 : t_0$ [mm]	$h_1 : b_1 : t_1$ [mm]	-	-	-	-
X2	150x150x6	150x150x6	S500	1	25	1
X8	150x150x6	150x150x6	S355	1	25	1

The validity of the X joint configuration is checked and summarized in Table B.2. The braces have an angle of 90° and therefore fulfil the condition of a minimum angle of 30°. All joints have no eccentricity and therefore fulfil the upper eccentricity limit of e/h_0 . The range of validity equations are met. The specific X joint configuration consists of SHS braces and chord and therefore needs to be checked on the additional conditions according to Table 9.11. These additional conditions are not met. Therefore, the equations according to Table 9.13 need to be applied and not Table 9.12.

A summary of the results of the calculation for joints X2 (S500) and X8 (S355) is given in Table B.3. The full calculation per X joint is described in sections B.1 and B.2. The design resistance

is based on the material properties obtained from the coupon experiments of joints X2 and X8, see Section 5.3. Material S355 has a yield strength of 451 MPa which results in a material reduction factor C_f of 0,9. Material S500 has a yield strength of 615 MPa which results in a C_f of 0,8. This is in agreement with Table 1.1.

Table B.2: Range of validity check

Range of validity conditions	
Table 9.10 EC3	
$b_1/b_0 \geq 0,1 + 0,01*b_0/t_0$, but $\geq 0,25$	$1,0 > 0,35 > 0,25$
$0,5 \leq h_0/b_0 \leq 2,0$	$0,5 < 1,0 < 2,0$
$0,5 \leq h_1/b_1 \leq 2,0$	$0,5 < 1,0 < 2,0$
$b_0/t_0 \leq 35$	$25 < 35$
$h_0/t_0 \leq 35$	$25 < 35$
$b_1/t_1 \leq 35$	$25 < 35$
$h_1/t_1 \leq 35$	$25 < 35$
Conditions met? (Yes or No)	Yes, check add. cond.
Additional conditions	
Table 9.11 EC3	
$b_1/b_0 \leq 0,85$	$1,0 > 0,85$
Conditions met? (Yes or No)	No, use Table 9.13

Table B.3: Hand calculation results joint X2 and X8

	Steel grade	σ_y [MPa]	C_f [-]	CFE [kN]	CSWF [kN]	BF [kN]	PSF [kN]	Predicted failure mode
X2	S500	615	0,8	-	1328	1169	-	BF
X8	S355	451	0,9	-	974	964	-	BF/CSWF

B.1 Joint X2 (steel grade S500)

Chord face failure

$$\beta = \frac{b_1}{b_0} = \frac{150}{150} = 1,0 > 0,85 \quad (\text{B.1})$$

Because β is 1,0, chord face failure will not occur.

Chord side wall failure

The chord stress parameter n is 0. C_1 is equal to 0,10 for $n \geq 0$. This leads to the following stress function Q_f for X joints:

$$Q_f = (1 - |n|)^{C_1} = (1 - 0)^{0,1} = 1,0 \geq 0,4 \quad (\text{B.2})$$

$$f_b = f_{y0} = 615 \text{ MPa} \quad (\text{B.3})$$

$$\gamma_{m5} = 1,0 \quad (\text{B.4})$$

$$N_{1,rd} = \frac{f_b * t_0}{\sin \theta_1} * \left(\frac{2 * h_1}{\sin \theta_1} + 10 * t_0 \right) * \frac{Q_f}{\gamma_{m5}} = \frac{615 * 6}{\sin 90} * \left(\frac{2 * 150}{\sin 90} + 10 * 6 \right) * \frac{1,0}{1,0} = 1328 \text{ kN} \quad (\text{B.5})$$

Brace failure

$$b_{eff} = \frac{10}{\frac{b_0}{t_0}} * \frac{f_{y0} * t_0}{f_{y1} * t_1} * b_1 = \frac{10}{\frac{150}{6}} * \frac{615 * 6}{615 * 6} * 150 = 60 \text{ mm} \leq b_1 = 150 \text{ mm} \quad (\text{B.6})$$

$$N_{1,rd} = \frac{C_f}{\gamma_{m5}} * f_{y1} * t_1 * (2 * h_1 - 4 * t_1 + 2 * b_{eff}) = \frac{0,8}{1,0} * 615 * 6 * (2 * 150 - 4 * 6 + 2 * 60) = 1169 \text{ kN} \quad (\text{B.7})$$

Punching shear failure

$$\gamma = \frac{b_0}{2 * t_0} = \frac{150}{2 * 6} = 12,5 \quad (\text{B.8})$$

$$\beta \leq \left(1 - \frac{1}{\gamma} \right) \quad (\text{B.9})$$

$$\beta = 1,0 > \left(1 - \frac{1}{\gamma} \right) = \left(1 - \frac{1}{12,5} \right) = 0,92 \quad (\text{B.10})$$

This condition is not met. Therefore, punching shear failure will not occur.

B.2 Joint X8 (steel grade S355)

Chord face failure

$$\beta = \frac{b_1}{b_0} = \frac{150}{150} = 1,0 > 0,85 \quad (\text{B.11})$$

Because β is 1,0, chord face failure will not occur.

Chord side wall failure

The chord stress parameter n is 0. C_1 is equal to 0,10 for $n \geq 0$. This leads to the following stress function Q_f for X joints:

$$Q_f = (1 - |n|)^{C_1} = (1 - 0)^{0,1} = 1,0 \geq 0,4 \quad (\text{B.12})$$

$$f_b = f_{y0} = 451 \text{ MPa} \quad (\text{B.13})$$

$$\gamma_{m5} = 1,0 \quad (\text{B.14})$$

$$N_{1,rd} = \frac{f_b * t_0}{\sin \theta_1} * \left(\frac{2 * h_1}{\sin \theta_1} + 10 * t_0 \right) * \frac{Q_f}{\gamma_{m5}} = \frac{451 * 6}{\sin 90} * \left(\frac{2 * 150}{\sin 90} + 10 * 6 \right) * \frac{1,0}{1,0} = 974 \text{ kN} \quad (\text{B.15})$$

Brace failure

$$b_{eff} = \frac{10}{\frac{b_0}{t_0}} * \frac{f_{y0} * t_0}{f_{y1} * t_1} * b_1 = \frac{10}{\frac{150}{6}} * \frac{451 * 6}{451 * 6} * 150 = 60 \text{ mm} \leq b_1 = 150 \text{ mm} \quad (\text{B.16})$$

$$N_{1,rd} = \frac{C_f}{\gamma_{m5}} * f_{y1} * t_1 * (2 * h_1 - 4 * t_1 + 2 * b_{eff}) = \frac{0,9}{1,0} * 451 * 6 * (2 * 150 - 4 * 6 + 2 * 60) = 964 \text{ kN} \quad (\text{B.17})$$

Punching shear failure

$$\gamma = \frac{b_0}{2 * t_0} = \frac{150}{2 * 6} = 12,5 \quad (\text{B.18})$$

$$\beta \leq \left(1 - \frac{1}{\gamma}\right) \quad (\text{B.19})$$

$$\beta = 1,0 < \left(1 - \frac{1}{\gamma}\right) = \left(1 - \frac{1}{12,5}\right) = 0,92 \quad (\text{B.20})$$

This condition is not met. Therefore, punching shear failure will not occur.

Appendix C

Finite element analysis X joints

During the finite element simulations convergency problems occurred when the implicit solver was used. To prevent these problems, there is chosen to use the explicit solver. After completing all the finite element analysis, an implicit model is created to validate the results obtained by the explicit solver. The input used in the models are in agreement with Figures 3.24 and 3.25 for the implicit and explicit solver. It is observed that the implicit solver gives the same results as the used explicit solver. The proof is given in Figures C.1 and C.2. Figure C.1 shows the experimental results, obtained by the LVDTs located on the steel frame for joint X2, and the FEM results obtained by the explicit and implicit solver. Figure C.2 shows the force-deformation curve for the experimental results, obtained by DIC for joint X2, and the FEM results obtained by the explicit and implicit solver. The explicit solver results in a slightly larger displacement when compared to the implicit solver.

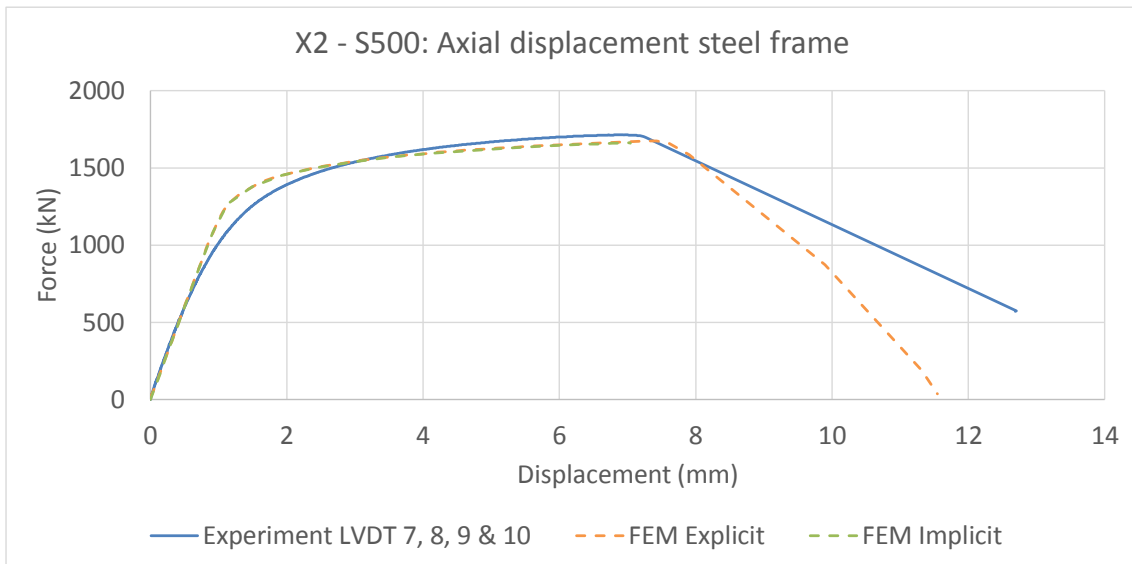


Figure C.1: Axial displacement steel frame joint X2

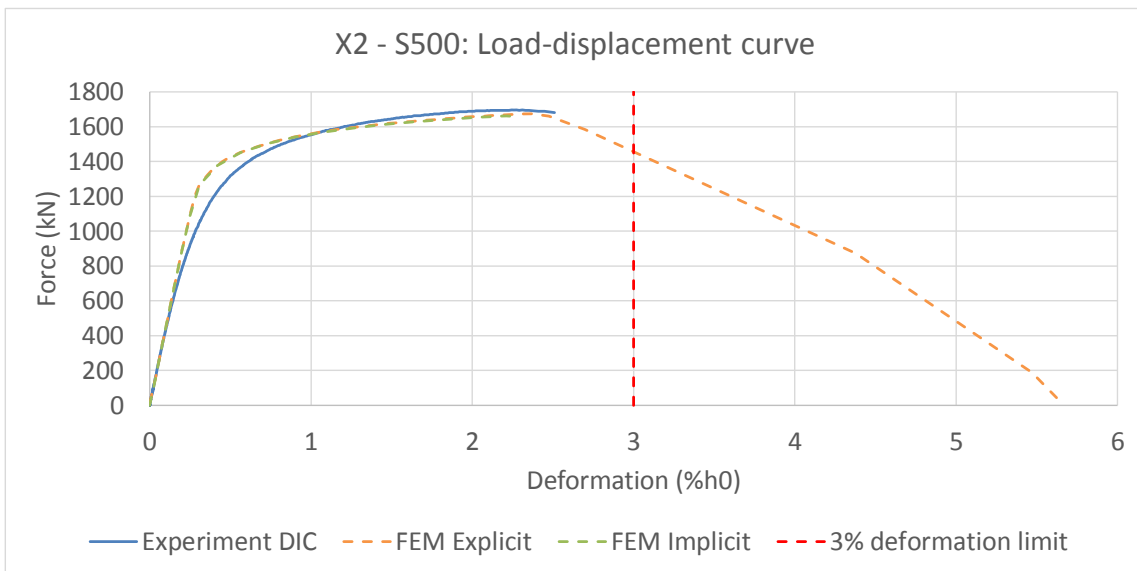


Figure C.2: Load-deformation curves joint X2

Appendix D

Stress triaxiality X joints

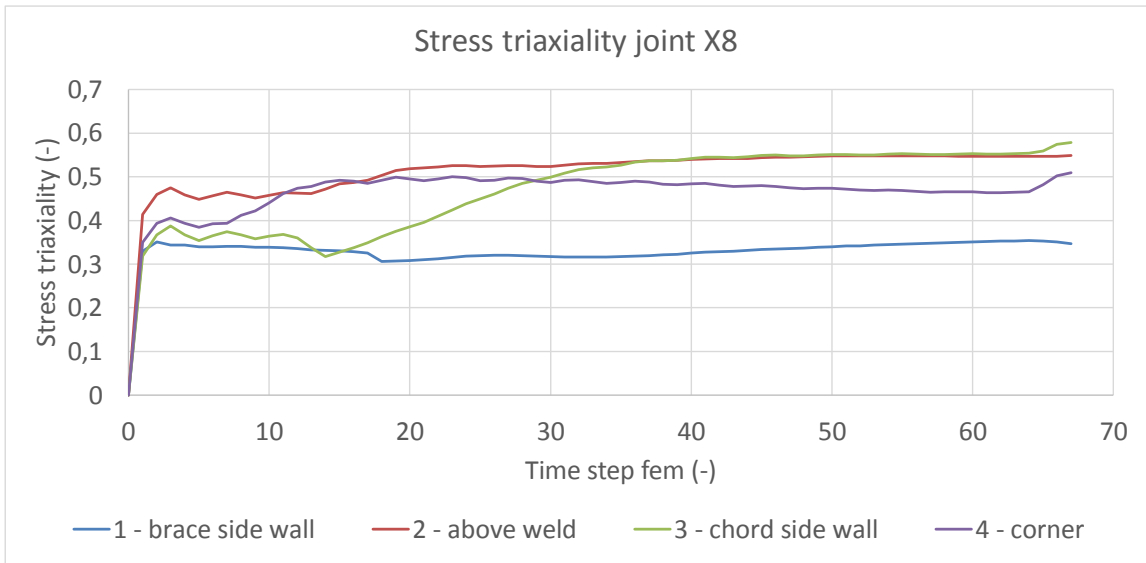


Figure D.1: Stress triaxiality joint X8 (S355)

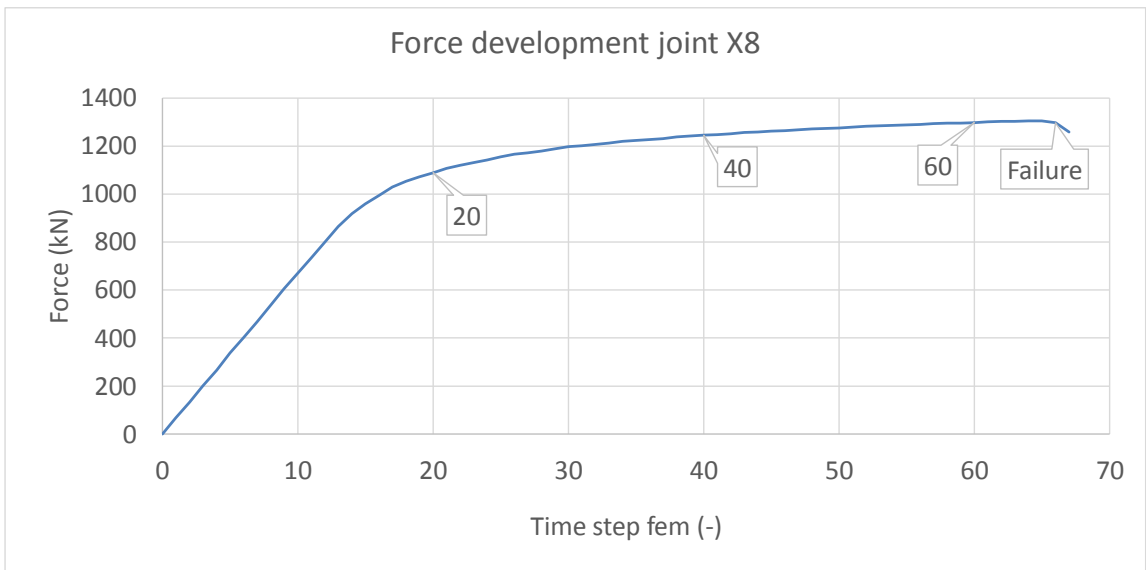


Figure D.2: Force development against time steps FEM for joint X8 (S355)

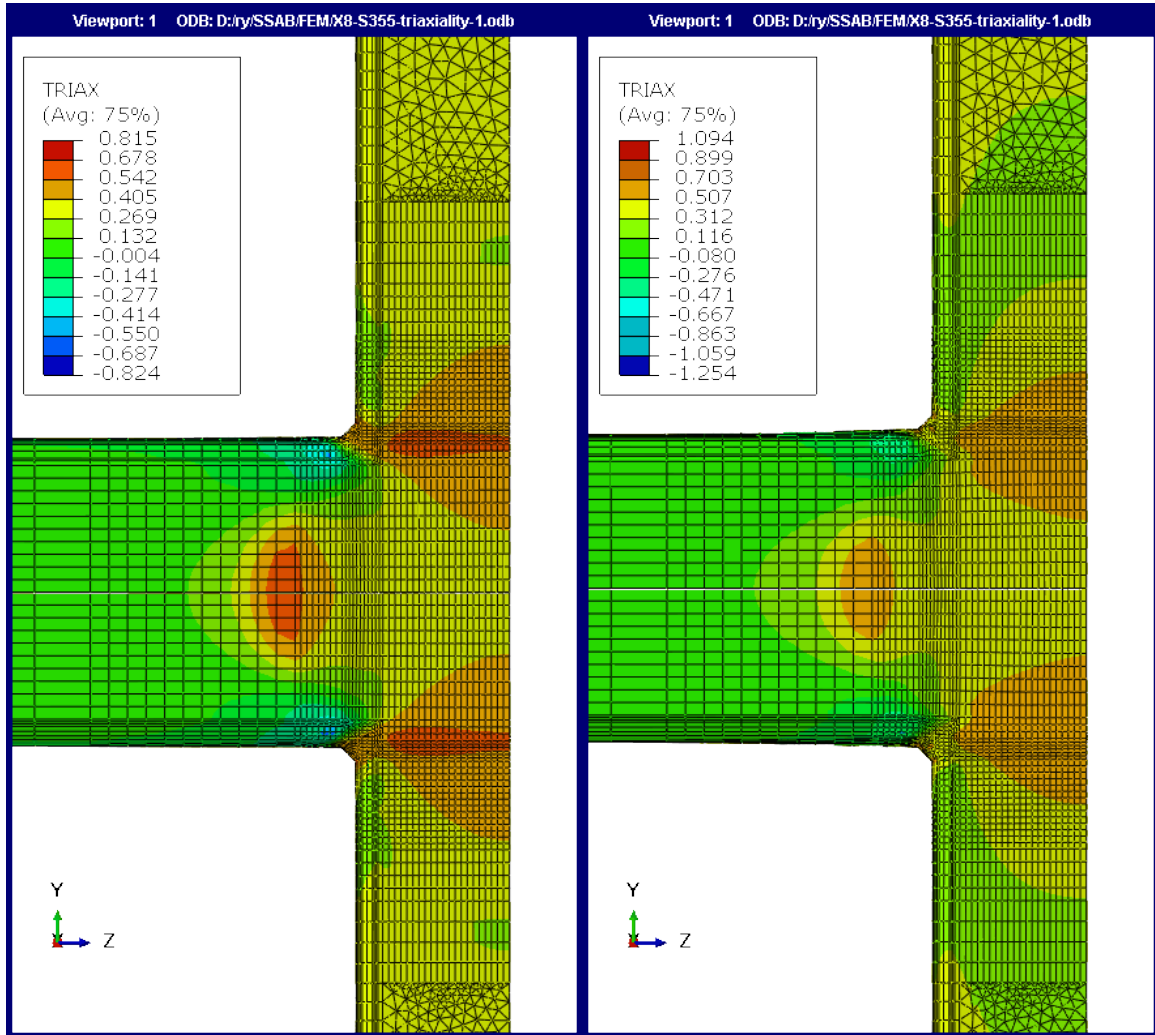


Figure D.3: Stress triaxiality distribution joint X8 (S355) for time step 20 (left) and 40 (right)

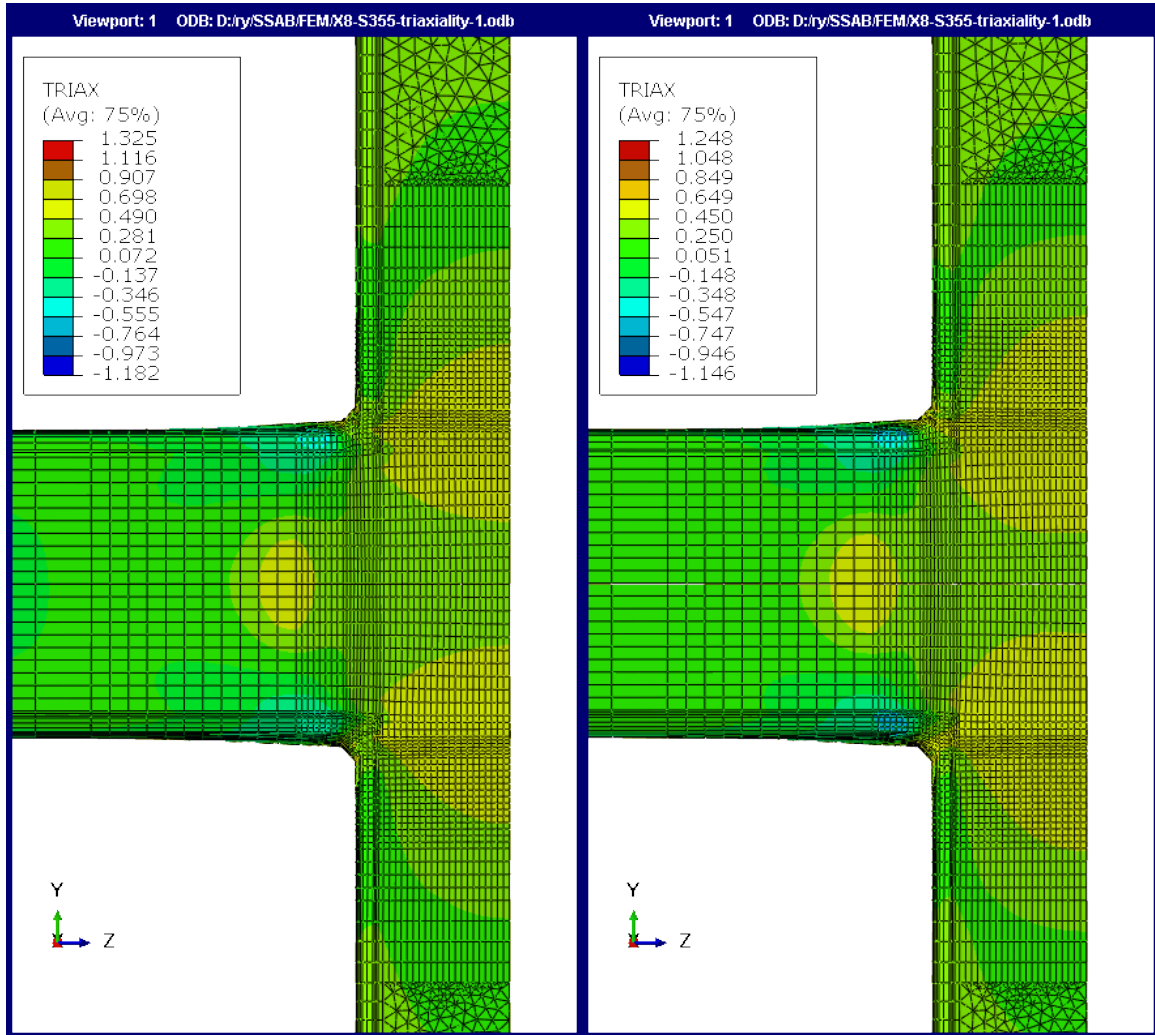


Figure D.4: Stress triaxiality distribution joint X8 (S355) for time step 60 (left) and failure (right)

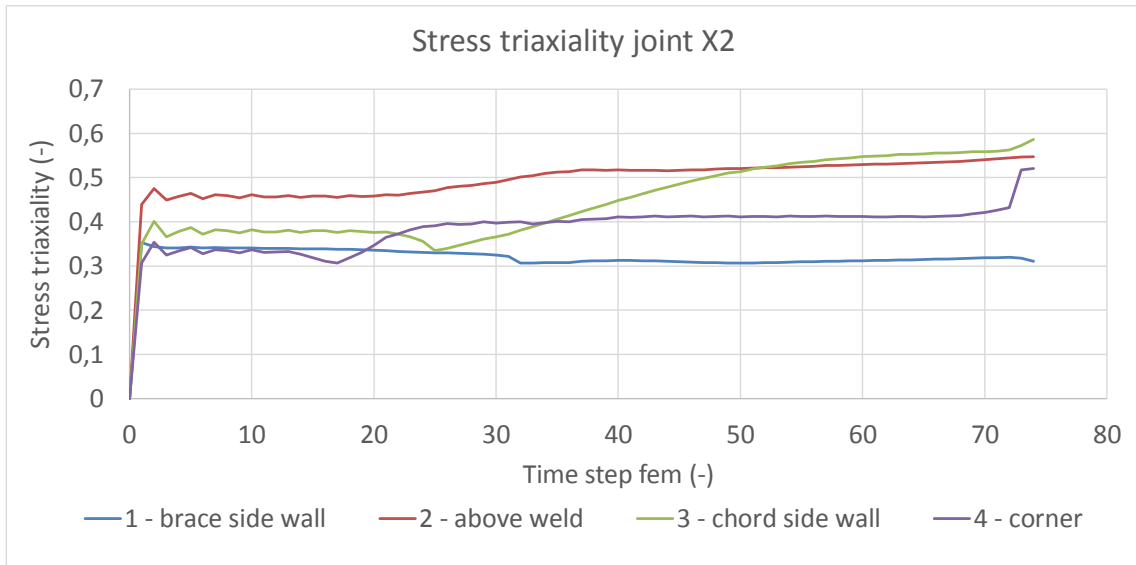


Figure D.5: Stress triaxiality joint X2 (S500)

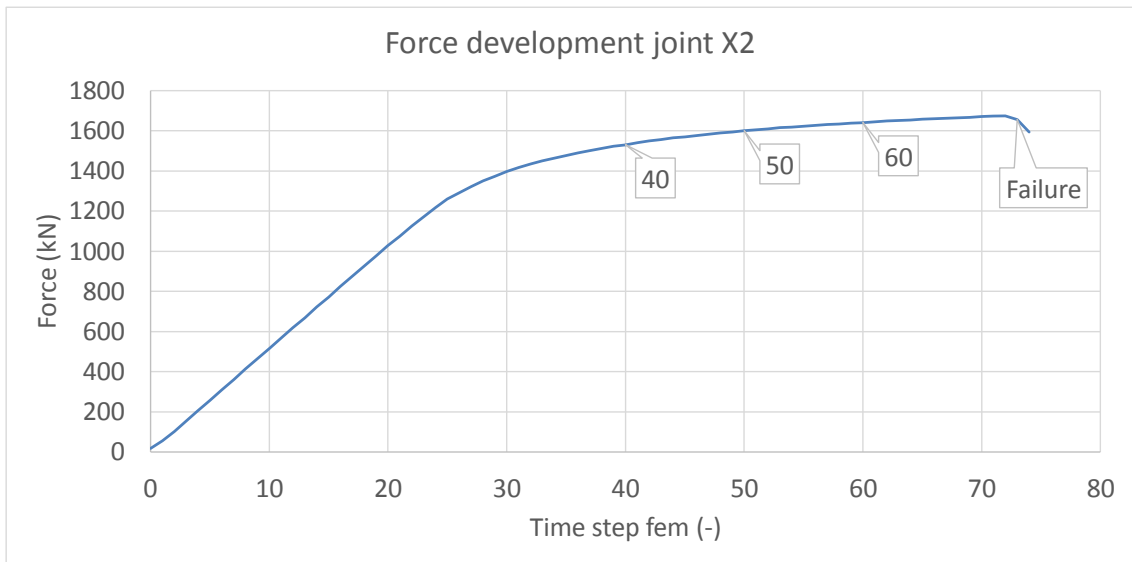


Figure D.6: Force development against time steps FEM for joint X2 (S500)

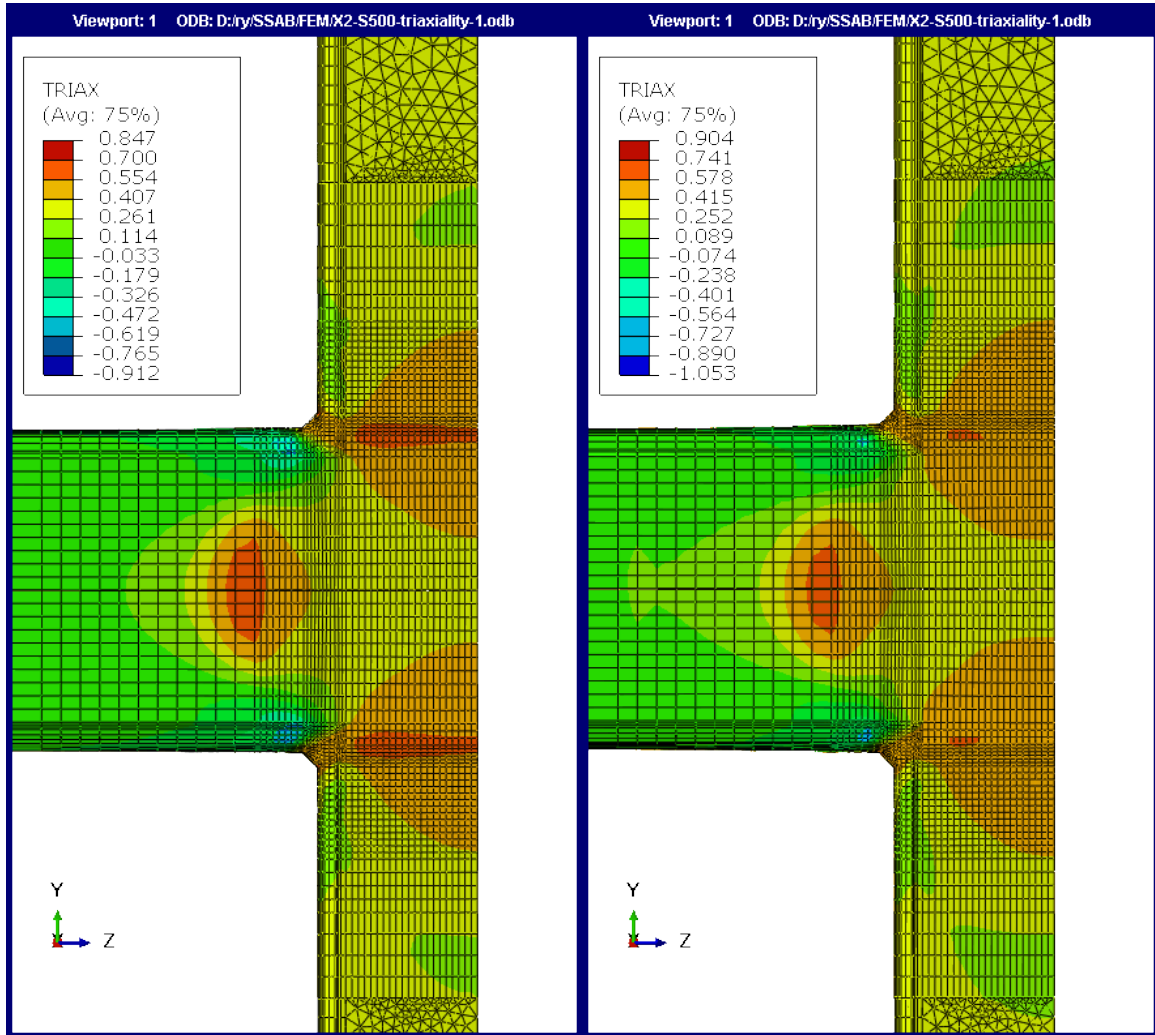


Figure D.7: Stress triaxiality distribution joint X2 (S500) for time step 40 (left) and 50 (right)

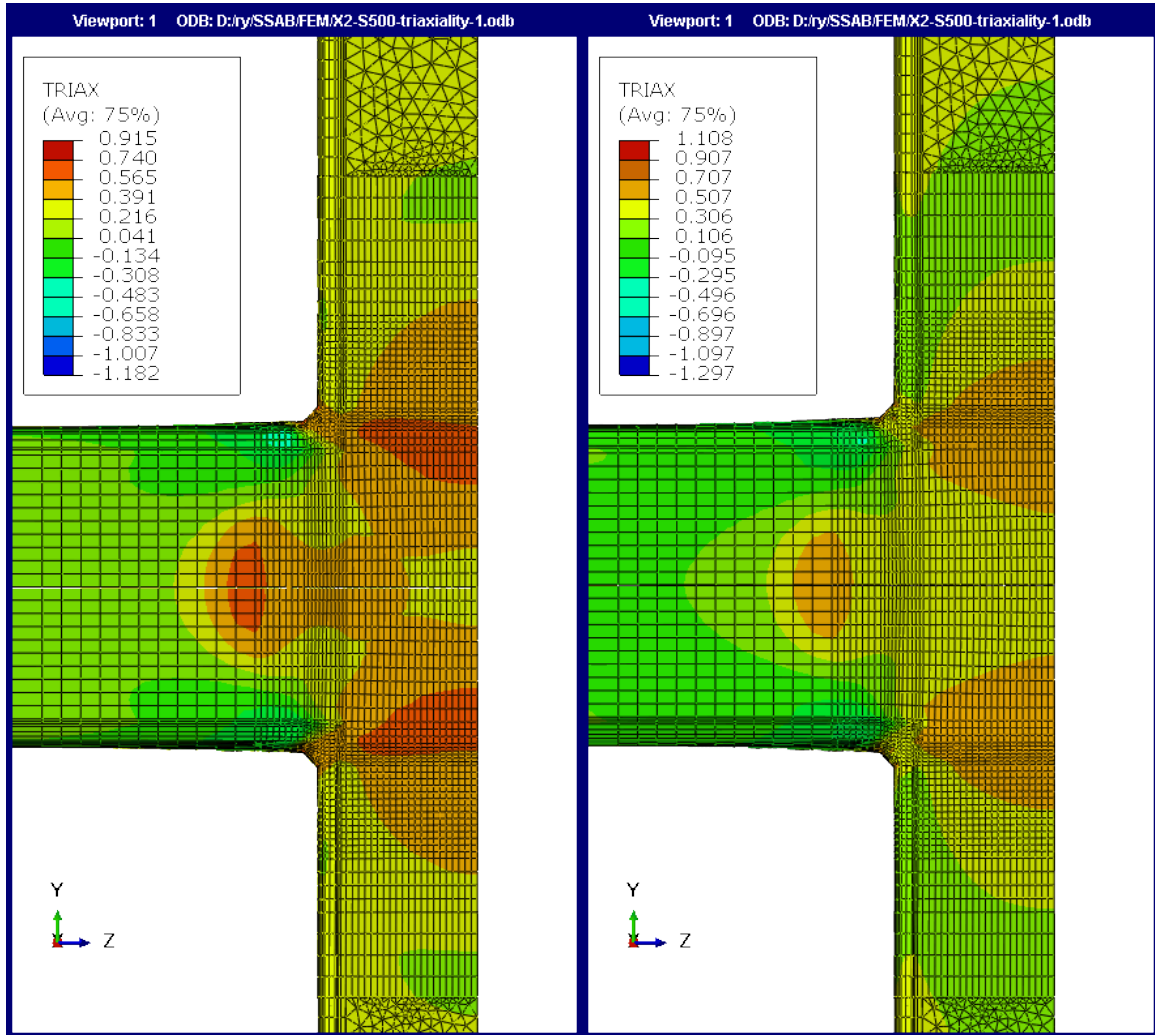


Figure D.8: Stress triaxiality distribution joint X2 (S500) for time step 60 (left) and failure (right)

Appendix E

Parametric study

Table E.1: Range of validity parametric study FEM [19]

Conditions	$\beta = 0,3$		$\beta = 0,5$		$\beta = 0,7$	
$\theta_i \geq 30^\circ$	90°	good	90°	good	90°	good
$e/h_0 \leq 0,25$	0	good	0	good	0	good
$b_i/b_0 \geq 0,1 + 0,01 * b_0/t_0$, but $\geq 0,25$	0,3 < 0,43	not good	0,5 > 0,43	good	0,7 > 0,43	good
$0,5 \leq h_i/b_i \leq 2,0$	1,0	good	1,0	good	1,0	good
$b_0/t_0 \leq 35$	33	good	33	good	33	good
$h_0/t_0 \leq 35$	33	good	33	good	33	good
$b_1/t_1 \leq 35$	10	good	16,7	good	23,3	good
$h_1/t_1 \leq 35$	10	good	16,7	good	23,3	good
Conditions met?	no		yes		yes	

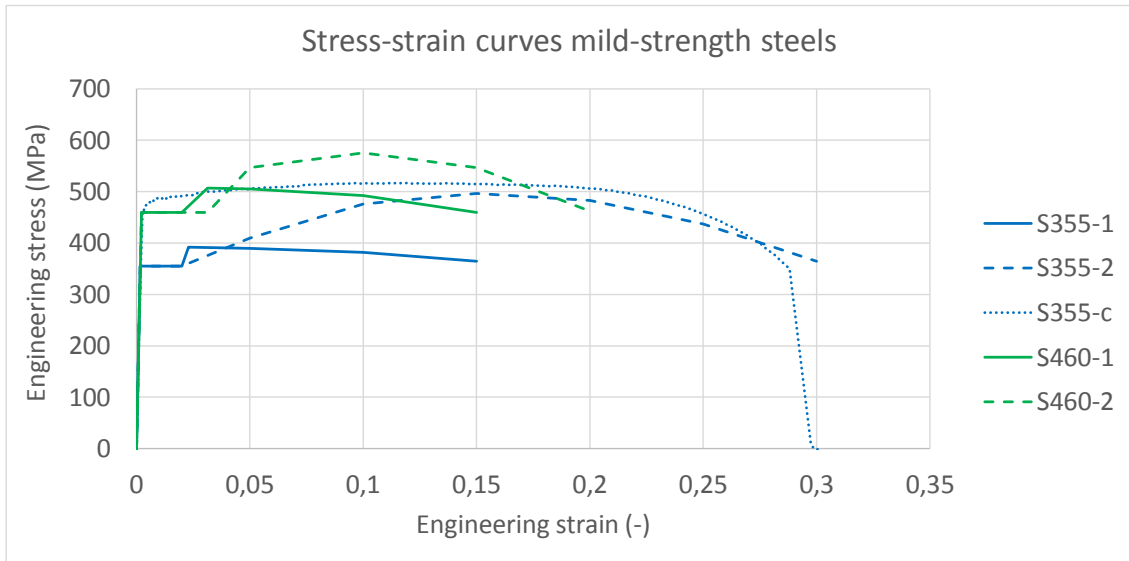


Figure E.1: Engineering stress-strain curves mild strength steels

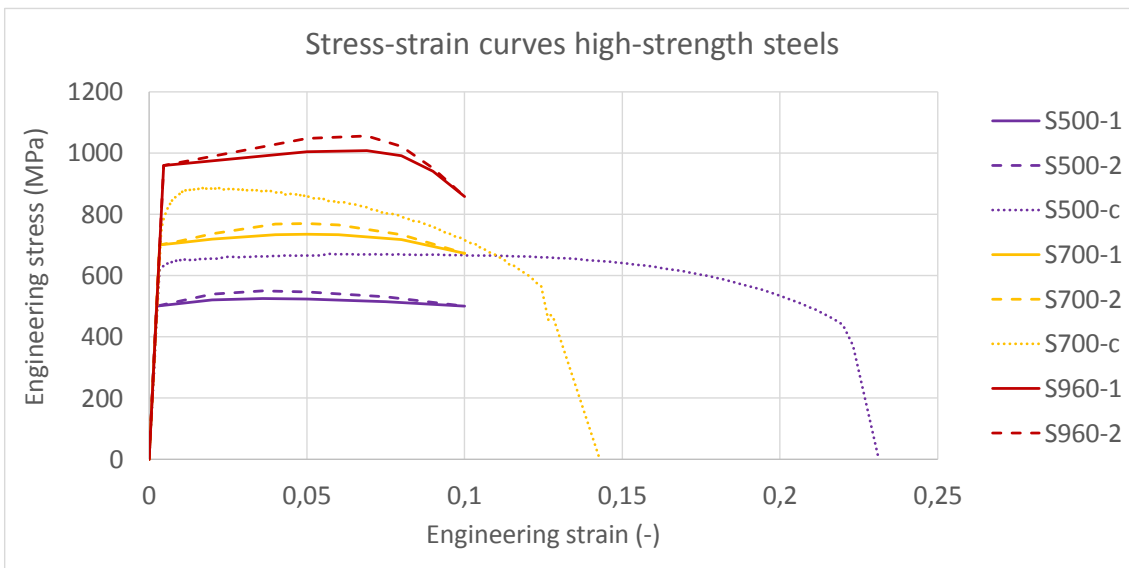


Figure E.2: Engineering stress-strain curves high strength steels

Table E.2: Design resistances parametric study FEM according to EN1993-1-8:2020 [19]

Steel grade	C_f [-]	f_{y0} [MPa]	t_0 [mm]	θ_i [°]	$\eta = h_1/b_0$ [-]	β [-]	n [-]	$C1$ [-]	Q_f [-]	γ_{m5} [-]	F_{EC3} [kN]	$F_{EC3,Cf}$ [kN]
$\beta = 0,3$												
S355-1 & S355-2	1	355	6	90	0,3	0,3	0	0,10	1	1	72	72
S355-c	0,9	451	6	90	0,3	0,3	0	0,10	1	1	92	83
S460-1 & S460-2	0,9	460	6	90	0,3	0,3	0	0,10	1	1	93	84
S500-1 & S500-2	0,86	500	6	90	0,3	0,3	0	0,10	1	1	101	87
S500-c	0,8	615	6	90	0,3	0,3	0	0,10	1	1	125	100
S700-1 & S700-2	0,8	700	6	90	0,3	0,3	0	0,10	1	1	142	114
S700-c	0,8	732	6	90	0,3	0,3	0	0,10	1	1	149	119
S960-1 & S960-2	0,8	960	6	90	0,3	0,3	0	0,10	1	1	195	156
$\beta = 0,5$												
S355-1 & S355-2	1	355	6	90	0,5	0,5	0	0,10	1	1	98	98
S355-c	0,9	451	6	90	0,5	0,5	0	0,10	1	1	124	112
S460-1 & S460-2	0,9	460	6	90	0,5	0,5	0	0,10	1	1	127	114
S500-1 & S500-2	0,86	500	6	90	0,5	0,5	0	0,10	1	1	138	119
S500-c	0,8	615	6	90	0,5	0,5	0	0,10	1	1	170	136
S700-1 & S700-2	0,8	700	6	90	0,5	0,5	0	0,10	1	1	193	154
S700-c	0,8	732	6	90	0,5	0,5	0	0,10	1	1	202	162
S960-1 & S960-2	0,8	960	6	90	0,5	0,5	0	0,10	1	1	265	212
$\beta = 0,7$												
S355-1 & S355-2	1	355	6	90	0,7	0,7	0	0,10	1	1	153	153
S355-c	0,9	451	6	90	0,7	0,7	0	0,10	1	1	194	175
S460-1 & S460-2	0,9	460	6	90	0,7	0,7	0	0,10	1	1	198	178
S500-1 & S500-2	0,86	500	6	90	0,7	0,7	0	0,10	1	1	215	185
S500-c	0,8	615	6	90	0,7	0,7	0	0,10	1	1	265	212
S700-1 & S700-2	0,8	700	6	90	0,7	0,7	0	0,10	1	1	302	242
S700-c	0,8	732	6	90	0,7	0,7	0	0,10	1	1	315	252
S960-1 & S960-2	0,8	960	6	90	0,7	0,7	0	0,10	1	1	414	331

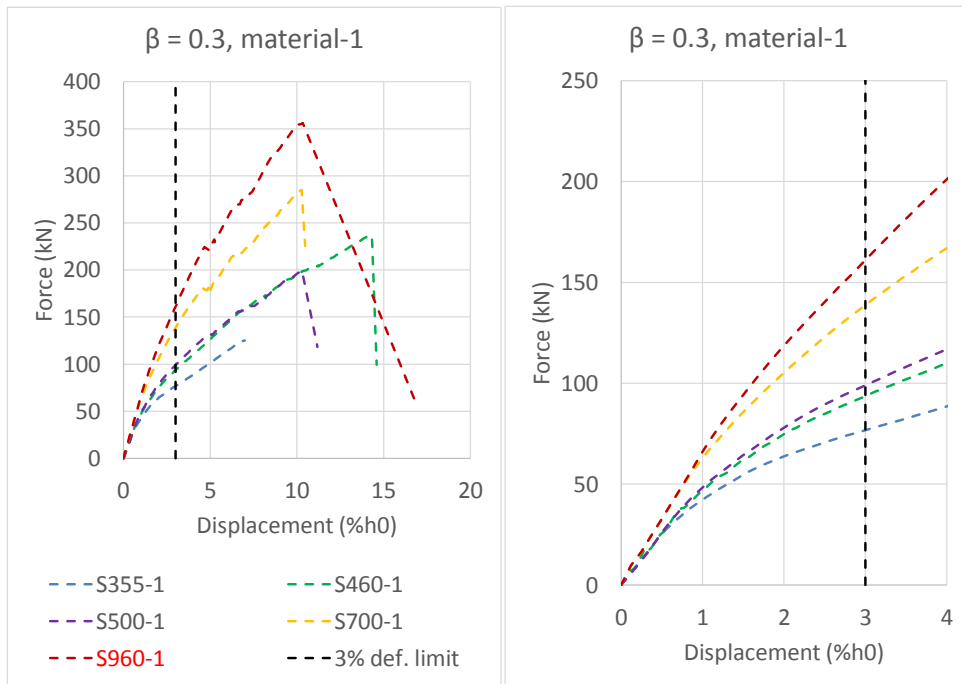


Figure E.3: Force-displacement curve material-1 for β equals 0,3: overview (left) and detail (right)

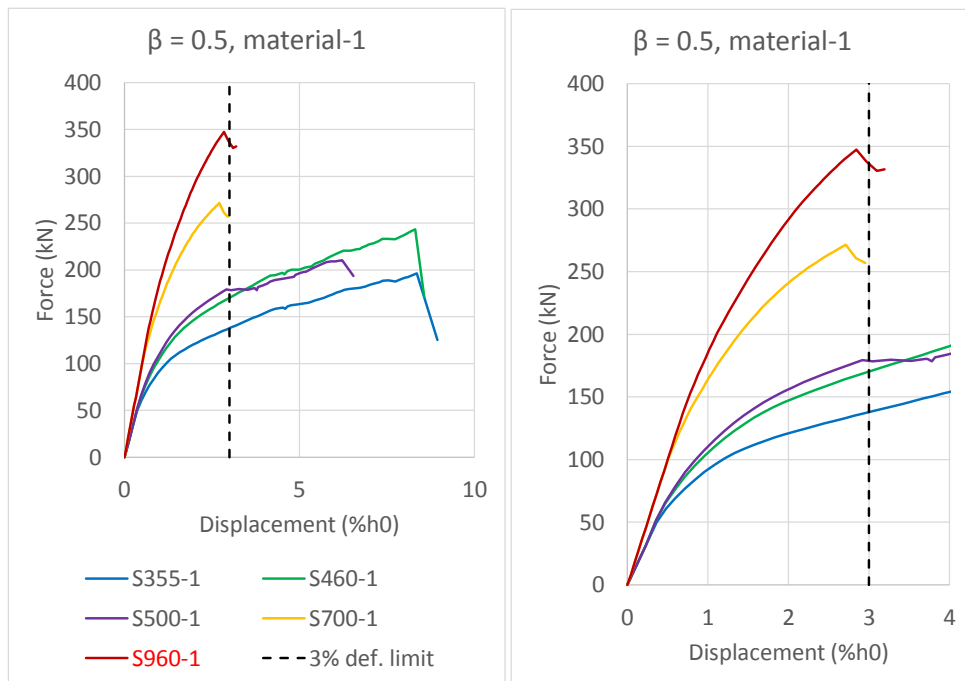


Figure E.4: Force-displacement curve material-1 for β equals 0,5: overview (left) and detail (right)

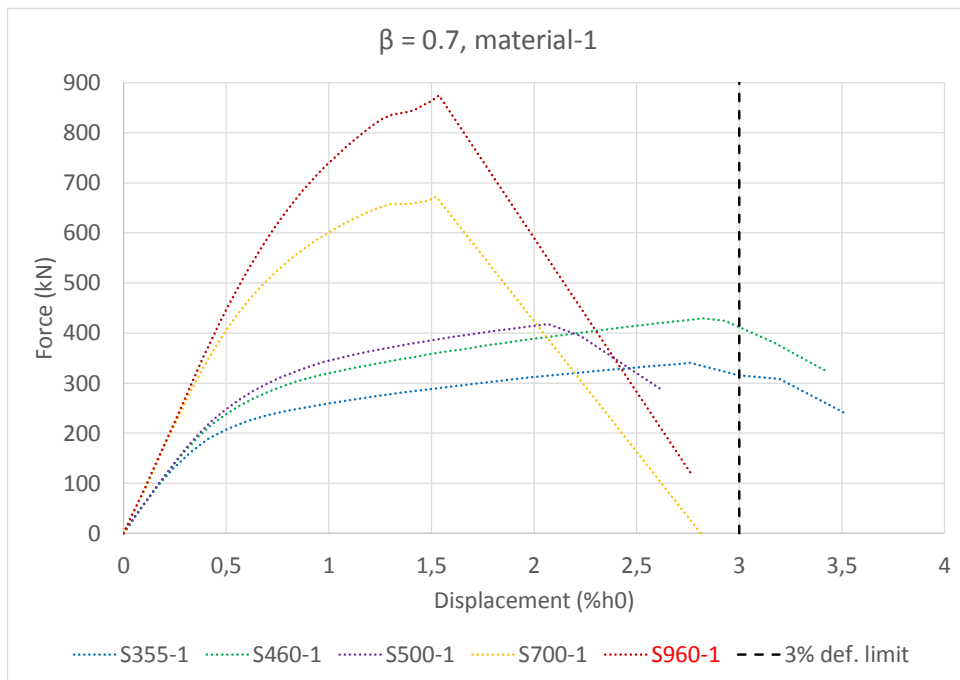


Figure E.5: Force-displacement curve material-1 for β equals 0,7

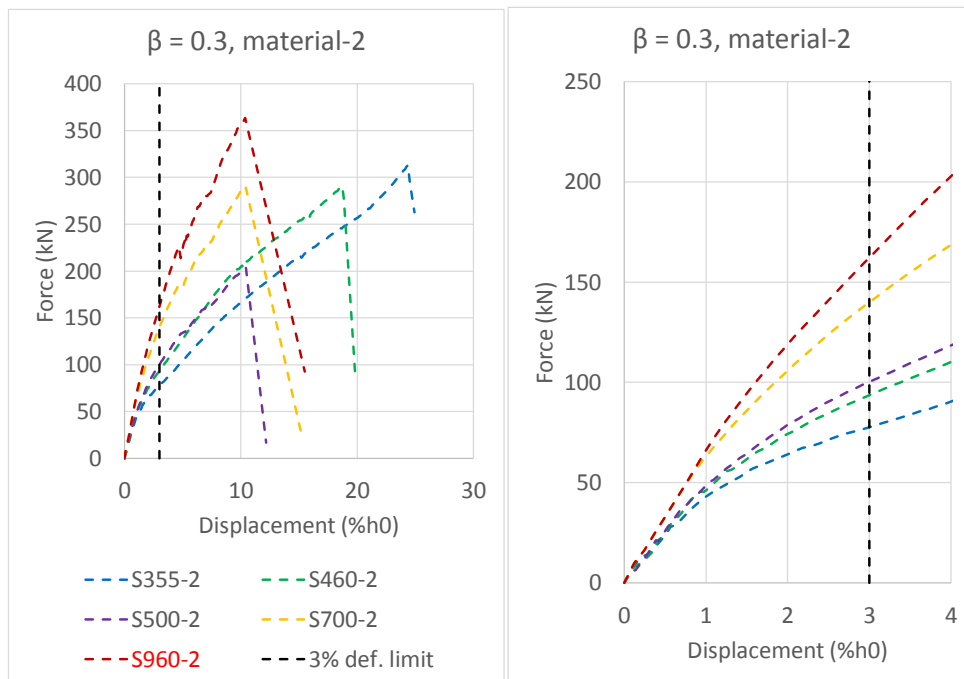


Figure E.6: Force-displacement curve material-2 for β equals 0,3: overview (left) and detail (right)

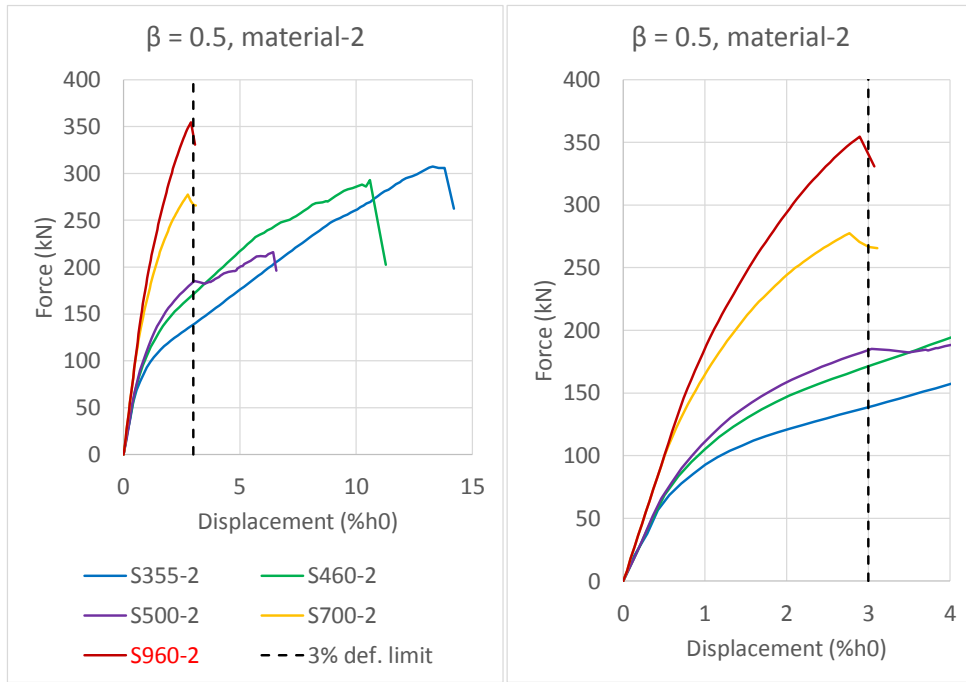


Figure E.7: Force-displacement curve material-2 for β equals 0,5: overview (left) and detail (right)

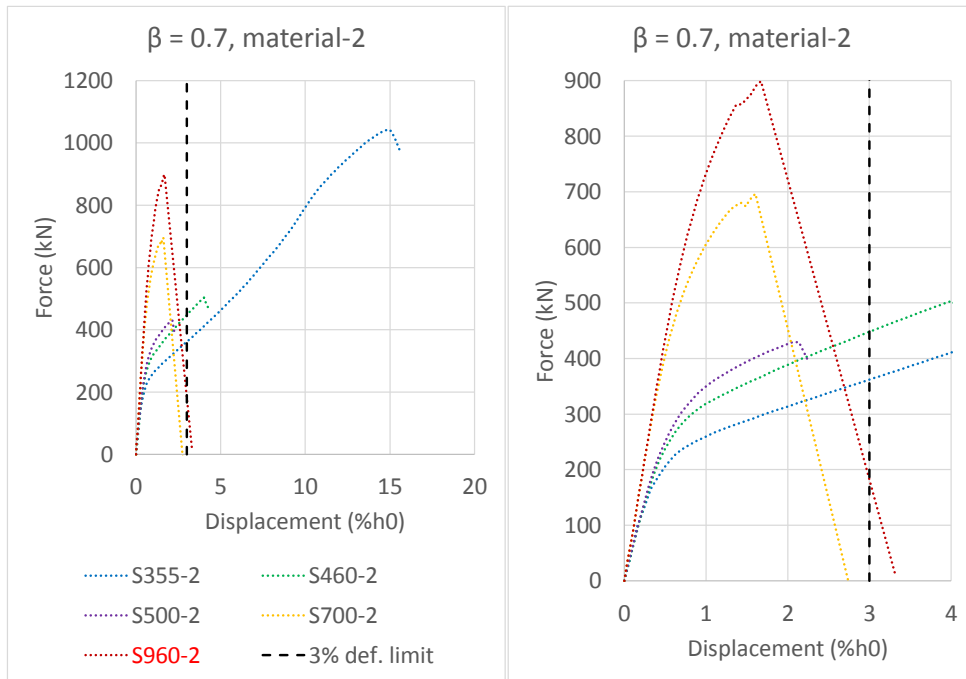


Figure E.8: Force-displacement curve material-2 for β equals 0,7: overview (left) and detail (right)

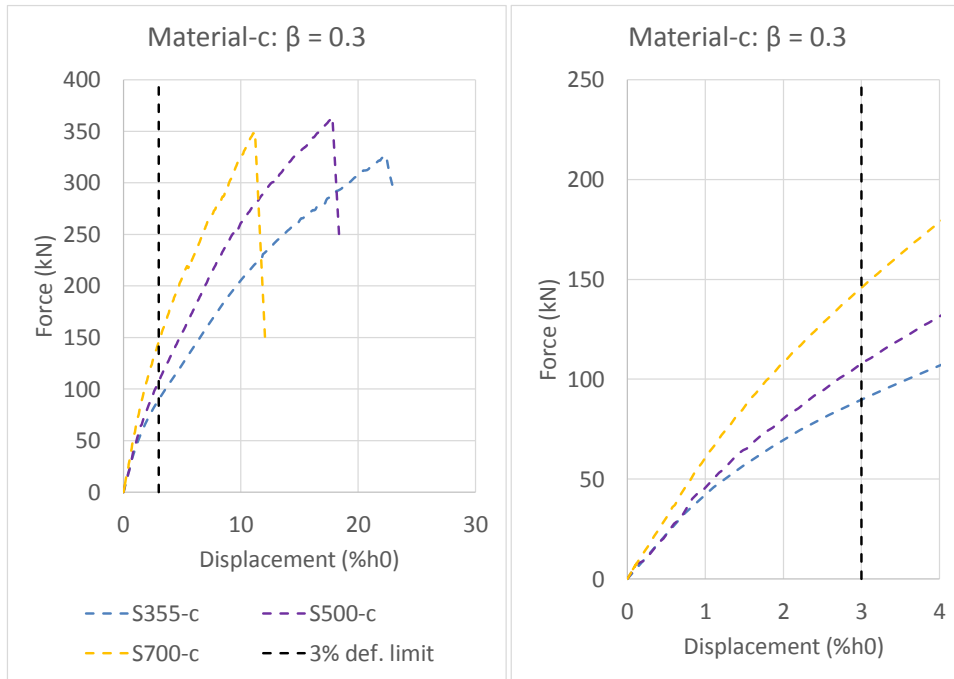


Figure E.9: Force-displacement curve material-c for β equals 0,3: overview (left) and detail (right)

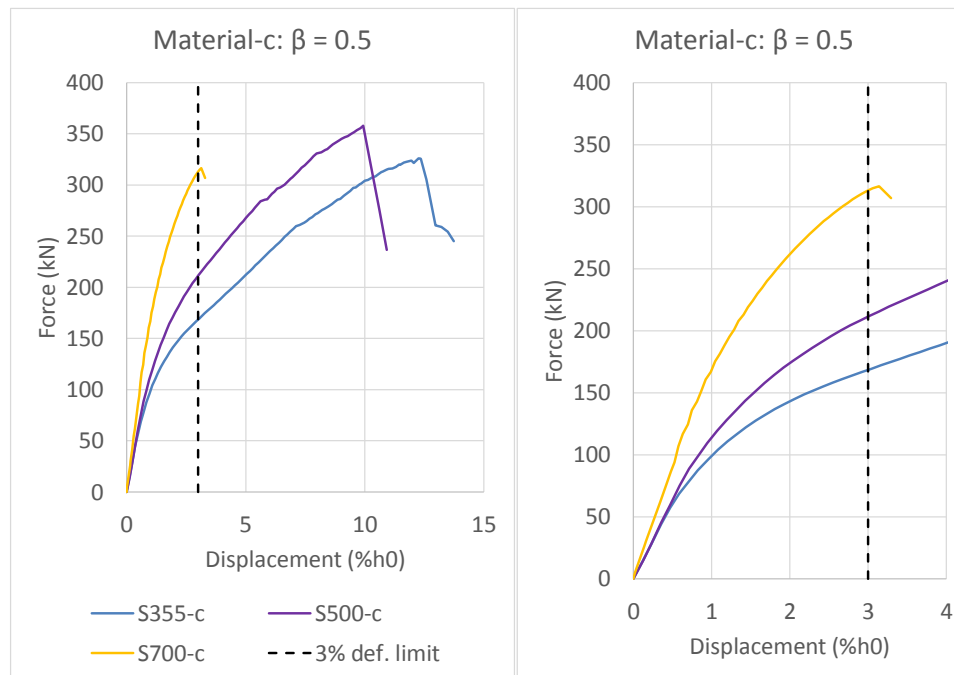


Figure E.10: Force-displacement curve material-c for β equals 0,5: overview (left) and detail (right)

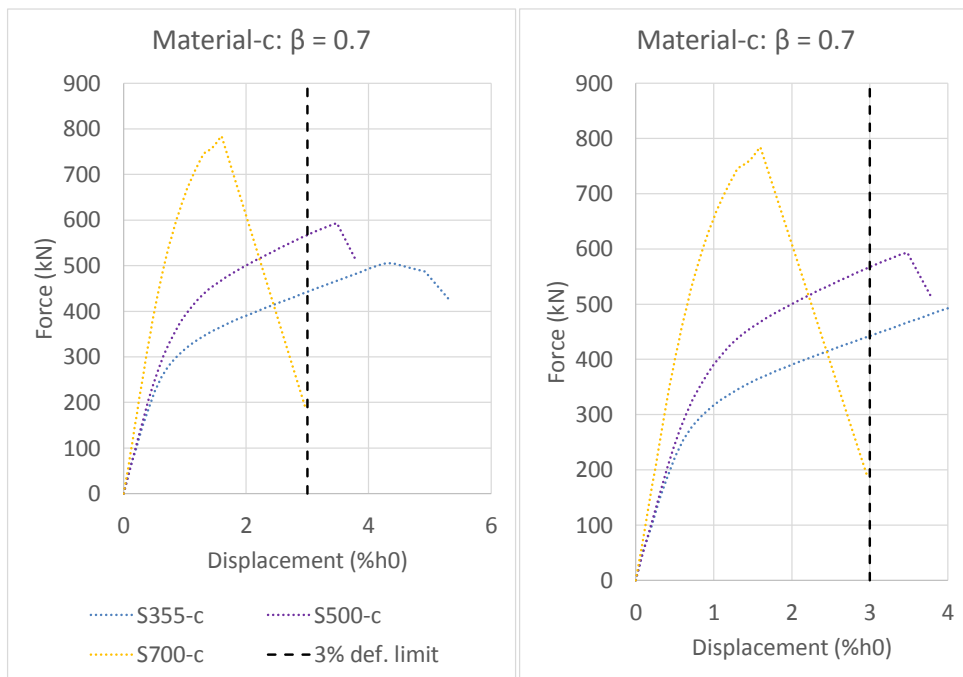


Figure E.11: Force-displacement curve material-c for β equals 0,7: overview (left) and detail (right)

Table E.3: Results FEM and Eurocode prediction for β equals 0,3

$\beta = 0,3$	F_{fem} [kN]	F_{EC3} [kN]	$F_{EC3,Cf}$ [kN]	$d_1 = F_{fem}/F_{EC3}$ [-]	$d_2 = F_{fem}/F_{EC3,Cf}$ [-]
S355-1	78	72	72	1,08	1,08
S460-1	94	93	84	1,01	1,12
S500-1	99	101	87	0,98	1,14
S700-1	139	142	114	0,98	1,22
S960-1	161	195	153	0,83	1,05
S355-2	78	72	72	1,08	1,08
S460-2	94	93	84	1,01	1,12
S500-2	100	101	87	0,99	1,15
S700-2	140	142	114	0,99	1,23
S960-2	162	195	156	0,83	1,04
S355-c	89	92	83	0,97	1,07
S500-c	108	125	100	0,86	1,08
S700-c	146	149	119	0,98	1,23

Table E.4: Results FEM and Eurocode prediction for β equals 0,5

$\beta = 0,5$	F_{fem} [kN]	F_{EC3} [kN]	$F_{EC3,Cf}$ [kN]	$d_1 = F_{fem}/F_{EC3}$ [-]	$d_2 = F_{fem}/F_{EC3,Cf}$ [-]
S355-1	138	98	98	1,41	1,41
S460-1	170	127	114	1,34	1,49
S500-1	179	138	119	1,30	1,50
S700-1	271	193	154	1,40	1,76
S960-1	347	265	212	1,31	1,64
S355-2	139	98	98	1,42	1,42
S460-2	171	127	114	1,35	1,50
S500-2	184	138	119	1,33	1,55
S700-2	278	193	154	1,44	1,81
S960-2	355	265	212	1,34	1,67
S355-c	169	124	112	1,36	1,51
S500-c	211	170	136	1,24	1,55
S700-c	313	202	162	1,55	1,93

Table E.5: Results FEM and Eurocode prediction for β equals 0,7

$\beta = 0,7$	F_{fem} [kN]	F_{EC3} [kN]	$F_{EC3,Cf}$ [kN]	$d_1 = F_{fem}/F_{EC3}$ [-]	$d_2 = F_{fem}/F_{EC3,Cf}$ [-]
S355-1	340	153	153	2,22	2,22
S460-1	429	198	178	2,17	2,41
S500-1	418	215	185	1,94	2,26
S700-1	672	302	242	2,23	2,78
S960-1	875	414	331	2,11	2,64
S355-2	362	153	153	2,37	2,37
S460-2	448	198	178	2,26	2,52
S500-2	430	215	185	2,00	2,32
S700-2	696	302	242	2,30	2,88
S960-2	899	414	331	2,17	2,72
S355-c	442	194	175	2,28	2,53
S500-c	567	265	212	2,14	2,67
S700-c	784	315	252	2,49	3,11